2020

Influence of transdermal current flow in tDCS-induced cutaneous adverse events

Niranjan Khadka
CUNY City College

Influence of transdermal current flow in tDCS-induced cutaneous adverse events

by

Niranjan Khadka

A dissertation submitted to the Graduate Faculty in Engineering
in partial fulfillment the requirements for the degree of

Doctor of Philosophy

The City College of New York, City University of New York

2020

This manuscript has been read and accepted for the Graduate Faculty in Engineering in satisfaction of the dissertation requirement for the degree of Doctor of Philosophy

Marom Bikson, Chair of Examining Committee	Date
Ardie D. Walser, Associate Dean for Academic Affairs	Date

EXAMINING COMMITTEE

Prof. Marom Bikson, Dept. of Biomedical Engineering, The City College of New York

Prof. Lucas Parra, Dept. of Biomedical Engineering, The City College of New York

Prof. Jacek Dmochowski, Dept of Biomedical Engineering, The City College of New York

Prof. Leigh E. Charvet, Department of Neurology, NYU Grossman School of Medicine

Prof. John Tarbell, Dept. of Biomedical Engineering, The City College of New York

THE CITY COLLEGE OF THE CITY UNIVERSITY OF NEW YORK

Abstract

Significant contributors to the broad application of transcranial direct current stimulation (tDCS) are portability, ease-of-use, and tolerability; with adverse events limited to transient and mild cutaneous sensations (e.g. perception of burning, itching, and tingling) and erythema. However, the fundamental questions remain about the mechanism of transdermal current flow during transcranial electrical stimulation, including tDCS. Example of previously unexplained questions in tDCS include: 1) the relationship between tDCS-induced skin reddening (erythema) profile and local current density profile predicted by the model; 2) the source of burning sensation during tDCS and whether it is related to an actual skin heating; 3) the role of skin multi-layers and ultrastructures (blood vessels, sweat glands, and hair follicles) in current flow. The finite element modeling (FEM) of current flow using simplified tissue geometries predict higher current density at the electrode edge, but the experimental evidences for the cutaneous effects of tDCS (skin heating or skin reddening) are unclear. Prior skin models of cutaneous current flow lacked anatomical details that will a priori be expected to govern current flow patterns.

In this dissertation we address the aforementioned questions by: first quantifying tDCS-induced skin erythema profile alongside FEM predicting local current density profile; then assess the extent of skin heating during tDCS, including the role of joule heating, and relate temperature increase (if any) to burning sensation; and finally develop a realistic skin model to address the role of complex skin tissue layers and ultrastructures in current flow. In the first study, we conclude that the tDCS-induced skin reddening profile is diffuse, higher in active stimulation than sham stimulation, and does not occur at the electrode edges suggesting two alternate hypothesis: 1) skin reddening profile is not related to local current density; and 2) skin current density is relatively uniform, so prior FEM models are incorrect. Next, we conduct phantom measurement suggesting

no significant temperature increase due to joule heat as expected at the skin during tDCS. The *in vitro* human skin temperature measurement suggests that independent of tDCS polarity, temperature increases by about 1^{o}C; an increase during tDCS that is less than the cooling produced following a room-temperature sponge application during the set-up. We conclude that any incremental temperature increase by tDCS may reflect vascular flare response due to current flow, cannot exceed the core body temperature, and is more than the offset by sponge-material coolness, thus, the sensation of skin "burning" during tDCS is not related to an actual increase in temperature. In the final study, we develop a detailed multi-layer skin model including sweat glands, hair follicles, and vasculature, and assess the role of multi-layers and ultrastructures in current flow. The FEM analysis predict that sweat glands eliminates localized current density around the electrode edges, and blood vessels uniformly distribution current across the modeled vasculature under the electrode. We expect that a current flow and bioheat model of such a detailed skin would increase the uniformity of current density and temperature predicted at the skin - consistent with the experimental measurement of skin reddening and skin heating.

Dedication

To my beloved grandmother, Alaichi Khadka and mother, Nirmala Khadka

Whatever I am today is just because of you and your sacrifice.

Acknowledgements

First and foremost, I would like to thank my advisor, Dr. Marom Bikson, for his support, patience, and encouragement throughout my PhD studies. Words fell short to express my gratitude to Dr. Bikson for countless insightful discussions that were just a knock on his office door away. He is an excellent teacher whose intellectual explanations stimulated the through process. His enthusiasm for research is truly contagious and I am grateful to have him as my advisor, mentor, and a role model.

I owe special thanks to my committee members, Dr. Lucas Parra, Dr. Jacek Dmochowski, Dr. Leigh Chervet, and Dr. John Tarbell, for their valuable suggestions and discussion to my proposal and defense. It was their comments that helped me to ponder upon a problem beyond my normal thinking.

I cannot thank more to my peers and colleagues who have contributed to this work in various ways. Preet Minhas, my first mentor since I joined the lab in 2011, helped with segmentation. Dennis shared his knowledge of COMSOL and assisted me with image processing in projects where we both co-authored. Discussions with Dennis Truong was always helpful and encouraged me at every aspect of my research projects dating from 2011. He was always even after his own PhD defense to answer my questions regarding my ongoing projects. Yu Huang (Andy) was always available to discuss anything that he was proficient at. Asif Rahman and Belen Lafon encouraged me to learn new things and choose right career path since my undergraduate studies. Chris Sarantos shared his knowledge of LABVIEW to design a virtual programming environment for designing waveform and acquiring signals from human. Dr. Luis Cardoso shared his knowledge of SolidWorks and assisted me in some designs. Bhaskar Paneri provided technical

supports for my studies. Brian Aguilar Avila helped me keep track of my degree requirements, track, and other administrative stuffs. Dennis Arce from Soterix Medical Inc. helped with electrodes and devices for my experiments. I want to offer my gratitude to the many talented and fun-loving members of the Neural Engineering Lab at the City College of New York, who enriched my life in graduate school academically and socially. All my co-authors and interns helped shape my all publications.

My deepest gratitude goes to my late grandmother (Alaichi Khadka), mother (Nirmala Khadka), and sisters (Renu Khadka and Shreejana Khadka) for their unconditional love and support. I want to extend my sincere gratitude to Rinzi Tamang and the family for encouraging me and treating me like their own.

I would like to acknowledge the following individuals who contributed to my thesis and and/or publication included in this thesis: Adantchede L Zannou, Adriano H. Moffa, Alexandre Costa, Andre R Brunoni, Andres M. Lozano, Asif Rahman, Bernardo de Sampaio-Junior, Brad Hershey, Byunggik Kim, Chris Sarantos, Dennis Q. Truong, Electra Nassis, Evan Rogers, Fatima Zunara, Felipe Fregni, Fernando Ezquerro, Hans Zander, Helen Borges, Hyeongseob Choi, Irene E. Harmsen, Isabela M. Bensenor, Jacek Dmochowski, Jaiti Swami, John H. Martin, Jongmin Jang, Kiwon Lee, Launa VM Aparicio, Paulo A Lotufo, Preston Williams, Rosana Esteller, Scott F. Lempka, Seonghoon Kim, Tianhe Zhang, Trynia Kaufman, and Xijie Liu.

This work was supported by National Institutes of Mental Health (1R01MH111896), National Institute of Neurological Disorders and Stroke (1R01NS101362), National Cancer Institute (U54CA137788/ U54CA132378), NYS Department of Health (DOH01-C31291GG), PSC CUNY (Cycle 50), and Boston Scientific Inc.

Table of Contents

List of Tables

List of Figures

Chapter 1: Introduction and Overview

1.1 Transcranial direct current stimulation

Transcranial Direct Current Stimulation (tDCS) is investigated for treating a range of neuropsychiatric disorders, rehabilitation, and altering cognitive performance (Bikson et al., 2016; Brunoni et al., 2012; Nitsche et al., 2008). Significant contributors to the broad adaptation of tDCS are the portability and ease-of-use along with the tolerability profile of tDCS - adverse events limited to transient cutaneous sensations (e.g. perception of warmth, itching, and tingling) and erythema (Dundas et al., 2007a; Fertonani et al., 2015). However, fundamental questions remain about the mechanisms of transdermal current passage during tDCS.

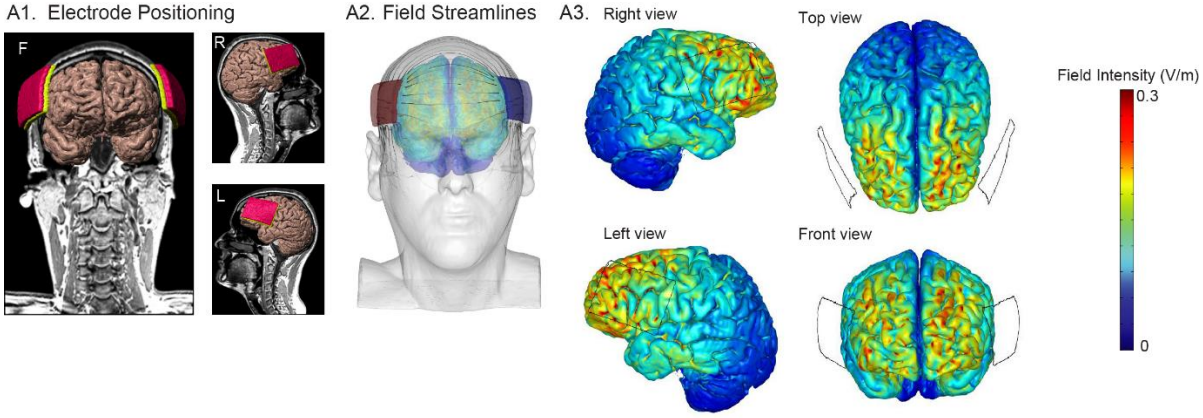

Figure 1: Computational FEM head model and predicted electric field using a dual-hemisphere tDCS montage. (A1) 3D image of a segmented brain generated from an MRI scan of a healthy adult and different views (F, L, R) of electrode placement over the inferior frontal gyrus. (A2) represent an orientation of magnitude controlled electric field streamlines inside the head tissue layers during tES. (A3) Volume plot of predicted field intensity and different views of brain under stimulation conditions. Predicted results plotted at same color range (Peak= 0.3 V/m) indicated comparable field intensity under both anode and cathode.

Previous studies have not well documented whether localized current density causes skin reddening. Although adverse events of tDCS are mild and transients, the source of burning sensation during tDCS is still unknow. Prior models have predicted no harmful skin temperature increase during tDCS but experimentally the extent of temperature rise during 20 min 2 mA tDCS is not quantified. tDCS-induced skin heating (if any) can answer whether the burning sensation is thermal in nature. Past studies have outlined the influence of electrical properties of skin in the performance and controllability of stimulation (Luna et al., 2015) suggesting a better understanding of the influence of skin anatomy, electrical properties of its structure, and an ability to predict skin current flow pattern under controlled stimulation are imperative for better clinical outcomes.

The common modality of transcranial electrical stimulation is to modulate brain functions by applying electrical stimulus (treatment specific range of current or voltage) across pairs of electrodes (sponges, gel, or adhesive pads) placed on the skin surface (Bohm, 1978). Central to the application of tES is the stimulation parameters such as intensity, duration, waveform, and electrode montage which shape the amount of current that can be safely delivered through skin to a desired target. For the case of tDCS, the waveform is direct current.

Regardless of the level of target (central or peripheral nervous system), current must flow through the skin. Transient cutaneous sensation (tingling, itchiness) and erythema (stimulation induced skin redness) normally occurs at the skin level, which are considered the main adverse events of tDCS (Minhas et al., 2011), except paresthesia (transcutaneous electrical nerve stimulation (tENS)) (Tonezzer et al., 2017). Thus, it is imperative to quantify whether erythema profile and skin heating are related to local current density, investigate whether tDCS produces

skin heating and if any skin heating is due to joule heat, and analyze the role of skin-ultrastructures such as sweat glands, hair follicles, and blood vessels in skin current flow.

1.2 Common adverse events of tDCS

Transient cutaneous sensation (e.g., itching, tingling, warmth) and skin erythema (so called "flare") are the primary reported adverse events of tDCS (Nitsche et al., 2008). tDCS-induced skin reddening is observed immediately under the site of stimulation after tDCS. Prior studies reported that it is observed more in active conditions than sham. Only in cases using nonoptimal materials and procedures can more severe or lasting skin irritation be observed (Bikson et al., 2009; Poreisz et al., 2007). Across trials, there are variations in the intensity and duration of reported adverse events (Brunoni et al., 2011; Dobbs et al., 2018; Matsumoto and Ugawa, 2017). These adverse skin responses can be readily minimized by following established protocols in dose and electrode preparation (Brunoni et al., 2012; Woods et al., 2016), monitoring electrode resistance (Khadka et al., 2015a; Merrill et al., 2005), and using proven electrode designs (Brunoni et al., 2011; Woods et al., 2016) or more advanced electrode techniques (Kempe et al., 2014; Khadka et al., 2015b).

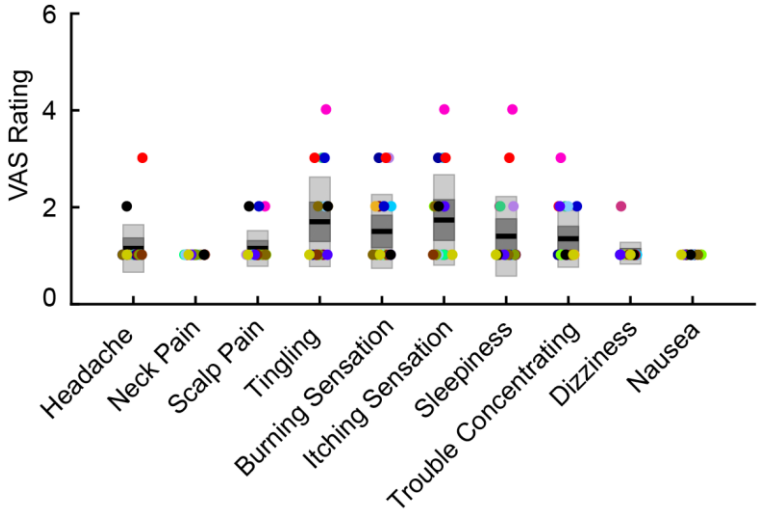

Figure 2: Adverse events reported during tDCS using a VAS rating scale (1-10; 0: absent, 1=severe).

Since sensations also determine effective blinding, tDCS electrodes are critical for blinding reliability. To the extent tDCS electrodes design shapes current flow through the skin, proper electrode selection and monitoring are critical for the reproducibility of efficacy. Monitoring of electrode resistance before and during tDCS is considered important for tolerability (DaSilva et al., 2011; Khadka et al., 2015a) where an unusually high electrode resistance is indicative of undesired electrochemical changes and/or poor skin contact conditions. However, monitoring of electrode impedance in no way reduces the need and importance of proper electrode selection and set-up- in the sense that poor electrodes conditions may be associated with a low resistance and, conversely, in some cases (e.g. subjects with high resistance scalp) good contact may be associated with a moderately high resistance. Skin irritation and discomfort may be associated with high resistance, but not necessarily. Thus, monitoring of resistance is an adjunct tool to detect not only ideal conditions at the electrode skin interface, but also a substitute for quality electrode design and strict protocol adherence (Khadka et al., 2015a; Woods et al., 2016).

As noted, direct contact between the metal or conductive rubber electrode (site for electrochemical reaction) and the skin can trigger skin irritation (Merrill et al., 2005). Hence, sufficient electrolytic gel, cream or saline should be used as a buffer in between. The shape or size of tES electrodes also significantly alter the distribution of current delivered to the brain (Kronberg and Bikson, 2012; Minhas et al., 2011). Variation in the electrode assemblies or particularly electrode size, results in differences in the distribution of the current across the surface area of the scalp and to the brain (Kronberg and Bikson, 2012; Minhas et al., 2011). Thus, it is critical for investigators to consistently report not only the current intensity applied and the amount of contact medium used but also the shape and size of the electrode assembly.

1.3 Unexplained Questions in tDCS

It is still unclear whether the source of tDCS-induced skin redness (erythema) is related to local current density or some other processes activated by current flow. The skin reddening is inevitable after tDCS and the spatial profile has not been explicitly studied before (Guarienti et al., 2015; O'Connell et al., 2012). Experimentally, it is currently not possible to measure current density with precision in an intact skin to validate the pattern of current density. Prior models predicted higher current density at the electrode edges (Minhas et al., 2011; Miranda et al., 2006). If local skin reddening is directly related to local current density then there should be a correlation between them: essentially, one would expect localized skin reddening around the perimeter of electrode. But the prior models are not validated, and the prediction cannot be conclusive. Burning sensation is one of the commonly reported adverse events in tDCS, but the source of burning sensation remains unaddressed. It is still unclear whether the skin is actually heating during tDCS or rather if the stimulation is activating heat-sensitive nerve fibers thus creating the burning sensation.

It is not well established whether current always concentrates around the edges or skin ultra-structures (hair follicles, sweat glands, and blood vessels). Prior modeling studies have not modeled skin accurately and all of the prior skin models predict higher current density around the electrode edges. How predicted current flow pattern changes with adding details such as multiple skin layers and/or ultra-structure has not be adequately addressed.

Another important question is whether tDCS strictly require an electrolyte soaked-sponge electrode or fluid-hydrogel, or there is a "dry" alternative for this. Finally, there is a growing interest of implementing higher current in clinical trials of tDCS. The major question is whether

we can safely increase the stimulation intensity up to 4 mA. These are some unexplained questions which underpinned the research approach and aims of this thesis.

1.4 Hypothesis and Aims

Aim 1: Characterize whether the profile of tDCS-induced skin reddening (erythema) profile matches predicted current density by the FEM model. The main hypothesis is that tDCS-induced skin reddening profile matches the current density profile as predicted by the FEM model, and the sub-hypothesis is that there is a difference in skin reddening between active and sham. Skin reddening (erythema) is important because it is one of the most evident side-effects in DCS trials. Redness resolve spontaneously after stimulation and is not inherently injurious; so, in the context of clinical acceptability, skin reddening is not a serious concern. None the less, it is the most obvious outcome of tDCS and may be linked to and inform skin current flow optimization. The sources of tDCS-induced erythema include but is not limited to stimulation current, electrochemical reaction, pressure by headgear, vascular flare response, or joule heat (O'Connell et al., 2012). Electrode design and thickness, gender, skin type, nature of stimulation (anodal or cathodal), and intensity of stimulation have been suggest to mediate the degree of erythema (Dundas et al., 2007b; Guarienti et al., 2014; Guleyupoglu et al., 2014).

An overarching question related to the source of skin redness is its relationship with local skin current density. Prior current flow models predict peak current density at the electrode edges (Gomez-Tames et al., 2016; Kronberg and Bikson, 2012; Minhas et al., 2011; Miranda et al., 2006; Opitz et al., 2015; Saturnino et al., 2015). In controlled tDCS trials, skin reddening might directly affect subject or operators blinded to active vs sham, if skin reddening depends on current flow. There is a lack of quantitative assessment of the skin reddening profile during or after tDCS. Existing skin reddening assessments is typically based on visual observation, using either a

questionnaire (presence of redness: yes; absence of redness: no) or, rarely, Draize erythema rating scale (Guarienti et al., 2015). For example, Guarienti et al., 2015 applied an anti-inflammatory paste (2 % ketoprofen) to minimize skin reddening related to any inflammatory reaction at the surface of skin during tDCS. In this dissertation, we quantitatively analyzed erythema under the site of stimulation by estimating the probability heatmap of erythema distribution and a ROI-based assessment of relative erythema spatial profile. This approach also revisits suggestions from prior studies (Guarienti et al., 2015; O'Connell et al., 2012; Palm et al., 2013) that significant skin redness is observed during sham stimulation, possibly induced by 1) a brief period of active stimulation at the session onset; 2) pressure of the sponge pad, depending on how it is fixed; and 3) irritation of the skin due to the sponge or saline solution.

Aim 2: Assess whether there is any significant skin heating during tDCS and if joule heating contributes to any skin heating. The main hypothesis is that tDCS produces skin heating, and the sub-hypothesis is that tDCS produces skin heating due to joule heat. Burning sensation is a common adverse events and skin heating during tDCS is speculated as the main cause for this sensation. In addition, prior works have suggested that even small changes in the skin temperature during tDCS might influence current flow patterns to the brain. (Gholami-Boroujeny et al., 2015). However, there is a lack of systematic studies on the exact mechanism (source) of burning sensation during tDCS. It is unclear whether burning sensation is related to actual skin heating, any temperature increase during tDCS is polarity specific, contributed by passive heating, or vascular flare response, remains to be studied. Skin temperature may confound blinding and decrease the validity of tDCS trials. If the sensation of warmth is based on real temperature change then it could confound both subject and operator blinding. Nitsche and Paulus, 2000 measured skin temperature during a relatively brief 5 min stimulation and reported no change in skin temperature

during and after. However, tDCS is typically applied for 20 min or more, and the extent of temperature increase during this stimulation period was not addressed before. Some prior computational modeling studies with homogenous skin model or two-layer skin model predicted negligible temperature increase at the skin (A. Datta et al., 2009; Gomez-Tames et al., 2016). In this dissertation, we address whether there is any skin heating during tDCS and if any skin heating is due to joule heat. We first conducted phantom study to isolate joule heat generated during tDCS. The phantom was a homogeneous volume which mimics how the skin is typically modeled. It is not feasible to build a skin phantom that reproduces skin multi-layers (note the thickness of epidermis (0.1 mm)) and ultra-structures (hair follicles, sweat glands, and blood vessels). Next, we conducted human experiment to investigate if the skin surface warms during tDCS. Since the prior homogenous skin model predicted negligible temperature increase, we modeled the phantom to verify that prior simplistic skin models would not reliability predict temperature increase due to joule heat. We then developed a multi-layer skin model (epidermis, dermis, and fat) incorporating blood perfusion and metabolism to predict any temperature increase during tDCS due to joule heat.

Aim 3: Develop a high-resolution skin model incorporating skin-ultrastructures such as sweat glands, hair follicles, blood vessels, and complex tissue layers to describe their role in skin reddening and skin heating. This is a technical aim. We first used the multi-layer skin model adapted from Aim 2 and predicted the current flow pattern. Since the predicted current flow pattern was not uniform (current concentration was higher around the epidermis and dermis), we added moderately-realistic (e.g. geometric) ultra-structures sequentially to address their role in current flow pattern. Finally, based on the prediction from the multi-layer skin model with moderately-realistic ultra-structures, we developed the first high-resolution anatomically realistic and detailed

skin model considering complex mosaic skin layer, skin-ultrastructure (hair follicles, sweat glands, and complex vasculature network), and experimentally measured skin electrical properties.

1.5 Outline of Chapters

Chapter 2 describes tDCS-induced skin reddening profile and confirms whether this profile matches with the current density profile predicted by the FEM model (Aim 1). In this study, we developed an image-based skin reddening (erythema) approach to generate a probability heatmap of erythema (skin reddening) distribution at the skin surface for active and sham conditions and quantified the erythema spatial profile.

Chapter 3 tests whether there is any skin heating during tDCS and if any heating is related to joule heat (Aim 2). In this study, we conducted phantom study (a controlled experiment) to isolate if there is any joule heat during the stimulation assuming the skin respond like a homogenous structure. After establishing the extent of joule heat produced on the phantom study, we conducted human study by stimulating readily accessible human skin (forearm). There was no significant temperature increase due to joule heat in phantom or in a model of the phantom – which can suggest either prior attempts to model the skin as a simple structure do not capture joule, or that joule heat is in any case not significant. To try and distinguish these two possibilities, we developed a multi-layer skin model incorporating Penn's heat transfer multiphysics to specifically predict in a more realistic skin model the impact of joule heat during tDCS.

Chapter 4 presents the first realistic and anatomically detailed skin model incorporating skin ultrastructures such as sweat glands, hair follicles, and blood vessels, and complex tissue layers to describe their role in current flow (Aim 3). In this computational study, we transitioned from a multi-layer skin model (Aim 2) to a high-resolution anatomically realistic and detailed skin model with ultra-structures. In this chapter we predicted the role of each ultrastructure in current

flow pattern through skin which could in turn be related to experimental skin reddening or skin heating.

Appendix 1 describes a method to isolate individual electrode resistance during tDCS. High electrode resistance is an indicative of poor electrode conditions or non-optimal conditions at the skin or electrode skin interface. Thus, monitoring electrodes during tDCS promote tolerated stimulation. In this study, we proposed a novel method to monitor individual electrode resistance during tDCS using a super-position of direct current with a test-signal (low intensity and low frequency sinusoid with electrode-specific frequencies) and a sentinel electrode (not used for DC). Assumptions were tested and parameterized in participants using the forearm stimulation combining tDCS (2 mA) and test-signals (38 and 76 µA peak-peak at 1,10, and 100 Hz) and in vitro test (creating electrode failure modes). The DC and AC components voltages across the electrodes were compared and the participants' subjective pain was rated using a VAS scale.

Appendix 2 validates the performance of the first "dry" electrode for tDCS against the state-of-the-art conventional wet sponge-electrode to test the hypothesis that whether tDCS can be applied with dry electrode that has comparable tolerability profile as conventional "wet" techniques. Multilayer hydrogel composite (MHC) dry-electrode performance was verified using a skin-phantom, including mapping voltage at the phantom surface and mapping current inside the electrode using a novel biocompatible flexible printed circuit board current sensor matrix. MHC dry-electrode performance was validated in human study including tolerability (VAS and adverse events), skin redness (erythema), and electrode current mapping. Experimental data form the skin-phantom stimulation was compared against a finite element method (FEM) model.

Appendix 3 presents a new electrode design validation and an adaptive controller to provide tDCS up to 4 mA, while managing tolerability. In this parallel-group participant-blind

design with 50 healthy subjects, we used specialized electrodes to administer 3 daily session of tDCS for 11 min, with a lexical decision task as a distractor, in the five study conditions: adaptive 4 mA, adaptive 4 mA with Relax-button, adaptive 4 mA with historical-Relax-button, 2 mA, and sham. A tablet-based stimulator with a participant interface regularly queried VAS pain score and also limited current based on impedance and tolerability. An Abort-button provided in all conditions stopped the stimulation. In the adaptive 4 mA with Relax-button and adaptive 4 mA with historical-Relax-button conditions, participants could trigger a Relax-mode ad libitum, in the latter case with incrementally longer current reductions. Primary outcome was the average current delivered during each session, VAS pain score, and adverse event questionnaires. The delivered current was analyzed either excluding or including dropouts who activated Abort (scored as 0 current).

Appendix 4 presents a concept of a technology called Within Electrode Current Steering (WECS) that enhances the sophistication of electrode design to further enhance tolerability and promote broad (e.g., home) use of tDCS. The WECS adjusts current between electrodes not in contact with the tissue but rather embedded in an electrolyte on the body surface with the goal of not altering the brain current flow but rather compensate for nonideal conditions at the skin. This technology leverages our technique for independently isolating electrode impedance and overpotential during multichannel electrical stimulation. Here, we demonstrated the principles of WECS using an exemplary electrode design typical for tDCS (four rivet-electrodes sponge) and extremes of current steering (from uniform in all rivets to a single rivet). Through FEM simulation of this illustrative case, we validated the underlying assumptions of WECS: steering current within electrodes but without altering current distribution in brain target. This idea supports future studies

in optimization of electrode design, automation of algorithms to control current (including using impedance measurement), and ultimately validation under experiment conditions.

Appendix 5 describes the first approach to establish the role of tissue heating in kilohertz spinal cord stimulation (kHz-SCS). We hypothesized that kHz-SCS increases local tissue temperature by joule heat which may influence the clinical outcomes. Temperature increases were quantified in an experimental bath phantom and these data were used to verify a SCS lead heat-transfer model based on joule heat. Temperature increases were then predicted in a seven-compartment (soft tissue, vertebral bone, fat, intervertebral disc, meninges, spinal cord with nerve roots) geometric human spinal cord model under varied parameterization. The experimentally constrained bio-heat model shows kHz-SCS waveform (waveform RMS) determines tissue heating which increases supralinearly with stimulation power and is sensitive to incremental changes in SCS waveform parameters (pulse compression).

Appendix 6 proposes a general theory called quasi-uniform assumption in spinal cord stimulation that postulates local electric field predicts neuronal activation. We developed a finite element models of cat and rat SCS, and brain slice alongside human SCS models. Clinically and across animals, electric fields change abruptly over small distance compared to the neuronal morphology, such that each neuron is exposed to the multiple electric fields. Per unit current, electric fields generally decrease with body mass, but not necessarily and proportionally across the tissues.

Appendix 7 is about the 10 kHz-DBS which build upon our earlier hypothesis that kHz-frequency SCS (10 kHz) modulates neuronal function through moderate local tissue heating. To establish the role of tissue heating in 10 kHz-DBS, as the first decisive step, we characterize the range of temperature changes during clinical kHz-DBS protocols. We developed a high-resolution

MRI-derived DBS model incorporating joule-heat coupled bio-heat multi-physics to establish the role of tissue heating. Volume of Tissue Activated (VTA) under assumptions of activating-function (for 130 Hz) or heating (for 10 kHz) based neuromodulation were contrasted. We found that DBS waveform power (waveform RMS) determine joule heating at the deep brain tissues. Peak heating was supra-linearly dependent on the stimulation RMS. Tissue parameter analysis predicted that subthalamic nucleus (STN) heating was especially sensitive to decrease in enCAP electrical conductivity and decreases in STN thermal conductivity. Subject to validation with in vivo measurements, neuromodulation through a heating mechanism of action by the 10 kHz-DBS can indicate novel therapeutic pathways and strategies for dose optimization.

Appendix 8 proposes an open-source spinal cord model with precision in the anatomical details to serve as a standard for the SCS simulation. We developed a sophisticated SCS modeling platform, named Realistic Anatomically Detailed Open-Source Spinal Cord Stimulation (RADO-SCS) model. This platform consists of realistic and detailed spinal cord and ancillary tissues anatomy derived based on prior imaging and cadaveric studies. In our finite element model of the T9-T11 spine levels, we represented the following tissues: vertebrae, intervertebral disc, epidural space, epidural space vasculature, dura mater, dural sac, intraforaminal tissue, cerebrospinal fluid (CSF), whitematter, spinal cord vasculature, Lissauer's tract, gray matter, dorsal and ventral roots and rootlets, dorsal root ganglion (DRG), sympathetic chain (trunk and ganglion), thoracic aorta and its branching, peripheral vasculature, and soft tissues (thorax). As an exemplary application to illustrate the model workflow, we simulated a bipolar SCS montage and calculated the corresponding activation thresholds for individual axons populating the spinal cord. RADO-SCS provides precision across 19 tissue compartments. The resulting model calculations of the electric fields generated in the white-matter and gray matter, and the axonal activation thresholds are

broadly consistent with prior simulations. The RADO-SCS can be used to simulate any SCS approach with both unprecedented resolution (precision) and transparency (reproducibility). Freely-available online, the RADO-SCS will be updated continuously with version control.

The final section of this dissertation summarizes the main findings of the Aims, proposes general considerations for reconciling the experiments with model predictions, and discusses the future directions. In addition, we also consider how the novel hypotheses, techniques, and tools developed in the Appendices could be tested in future.

Chapter 2: The influence of Skin Redness on Blinding in Transcranial Direct Current Stimulation Studies

2.1. Outline

This chapter describes Aim 1 of the thesis where we used a novel approach of quantifying skin reddening profile and assessed whether the tDCS-induced skin reddening profile matches the local current density profile predicted by the FEM model. A version of the experimental component has been published (Ezquerro et al., 2017). In this chapter, we aimed to analyze whether there is a correlation between the experimental skin reddening profile and the model predicted local current density profile by generating a spatial reddening profile on a population level.

2.2. Introduction

Transcranial direct current stimulation (tDCS) is a non-invasive brain stimulation technique that involves delivery of a weak, direct current to the brain through electrodes placed over the subject's scalp (Brunoni et al., 2012). TDCS has been increasingly investigated as a possible treatment for diverse neuropsychiatric disorders (Sampaio-Junior et al., 2018). Not with-standing the presence of well-designed and conducted trials (Tortella, 2015), the overall number of studies is still small, especially studies with moderate to large sample sizes. Thus, improved techniques and protocols are warranted to enhance internal validity and research quality (Khadka et al., 2015a; Niranjan Khadka et al., 2019d; Woods et al., 2016). Optimal blinding techniques remain a concern in tDCS trials. In a canonical study, Gandiga et al. 2006 used a sham method that consisted of a brief period of 1mA stimulation followed by no stimulation until the end of the session, concluding that sham tDCS could be successfully used in double-blind trials, as subjects

were not able to distinguish between real and sham stimulation. However, recent evidence suggested that Gandigaet al.'s method is in adequate in some contexts, such as rater's blinding, 2 mA current intensity, cross-over designs and non-naive tDCS subjects (O'Connell et al., 2012). Skin redness (erythema) after tDCS is one reason for inadequate investigator blinding. Palm and collaborators (Palm et al., 2013) found that operators, even when blinded using tDCS devices with a number code that automatically delivers active or sham stimulation, were able to differentiate between active and sham stimulation based on skin reddening after active tDCS. Causes for tDCS erythema may include irritation by the saline, iontophoresis of substances present in skin prior to stimulation (makeup, sunscreen, cleansing substances, etc.), pressure by headgear, and the stimulation itself; whereas electrode design and thickness, gender, skin type, nature of stimulation (anodal or cathodal), and amperage of stimulation may mediate its intensity (Dundas et al., 2007a; Guarienti et al., 2015; Guleyupoglu et al., 2014). Although subjects' blinding can be managed by avoiding self-inspection of the forehead immediately after stimulation, this can be particularly troublesome for raters who are assessing outcomes immediately after the end of stimulation. For instance, (O'Connell et al., 2012) reported that erythema was noted after 60% of active stimulation sessions, compared to 1% after sham; moreover, 98% of the investigators associated noticeable skin redness with active stimulation. The authors also noticed that some skin redness persisted for several minutes beyond the end of stimulation. Recent studies have been conducted to characterize and control tDCS-induced erythema. Prior study has reported that skin pretreatment with ketoprofen reduces tDCS-induced erythema (Guarienti et al., 2015), although such approach inconveniently increases the preparation time. In addition, electrode-sponge geometry (rectangular vs. round-shaped) was explored as a method for improving bias (Ambrus et al., 2011); however, no difference was observed on the potential for blinding. Larger electrode size was also found to

be associated with cutaneous discomfort (Turi et al., 2014). However, no study hitherto has objectively evaluated the influence of tDCS-induced erythema on investigator blinding, or whether it is dependent on specific brands of available electrodes. Therefore, this issue was investigated in the present study.

The main objective of this study was to explore whether tDCS-induced skin reddening profile tracks model predicted current density profile at the skin. The hypothesis was that tDCS-induced skin reddening profile matches the current density profile as predicted by the prior models. In addition, we proposed two sub-hypotheses: 1) Skin reddening profile is different between sham and active stimulation; 2) Skin reddening profile is electrode type dependent. To this end, we used high-definition skin photographs of tDCS-induced erythema, presented at random to investigator, and used semi-automated image processing to determine redness and simulated a probability skin heatmap, and surface area coverage of redness using image processing software.

2.3. Materials and methods

2.3.1. Subjects

We recruited 26 healthy volunteers (21 women and 5 male) aged between 18 and 45 years (M = 526.2; SD = 54.7) who were naive to tDCS applications and presented no active dermatosis, skin allergy, skin marks, recent exposure to intense sunlight or artificial tanning, systemic skin treatment or topical skin treatment in the region where the electrodes were placed. We further categorized the volunteers based on their skin tone using Fitzpatrick scale. Out of the 26 volunteers, 21 were Caucasian (Fitzpatrick scale: Type II), 4 were Mediterranean Caucasian (Fitzpatrick scale: Type III), and 1 was African-American (Fitzpatrick scale: Type IV). The local

and national ethics committees approved the study and all participants provided written informed consent.

2.3.2. Materials

We used two different sets of sponges in this study: “thick” sponges (5.6 mm thickness), manufactured by Soterix Medical (Soterix Medical Inc., NY, USA) and “thin” sponges (1.5 mm thickness), manufactured by Neuroconn (Neuroconn GmbH, Munich, Germany). These sponges are commonly used in tDCS trials, both being cellulose-based, 535 cm wide, and behave similarly to absorb saline.

2.3.3. Design

Our independent variable was stimulation condition (3 levels: thick-active, thin-active, and sham). Dependent variables included the region-of-interest probability heatmap for erythema.

Following a within-subject design, participants received three stimulation sessions separated by one-week intervals: active tDCS with thick sponge, active tDCS with thin sponge and sham stimulation (in this case, in half of sham sessions we used thin sponges and, in the other half, thick sponges). The sequence was “active thick” on week 1, then “sham” on week 2, and finally “active thin” on week 3.

2.3.4. Procedures

The study was conducted in rooms with controlled temperature and humidity (temperature 20 ^{o}C ± 2^{o}C, relative humidity 50 % ± 5 relative humidity) as to ensure standardization of the dermatologic evaluation. As participants presented to the study, they were inter-viewed for exclusion criteria, demographics, medical history, use of contraceptives and other medications,

sun exposure and other life habits since childhood. High-resolution skin images were acquired before tDCS sessions, then again 5, 15, and 30 min after. Each day, stimulations were per-formed after gentle cleansing of forehead with ethanol. In case the participant wore make-up, a thorough face wash was requested with a 30 min interval for the beginning of procedures (including the baseline photograph).

2.3.5. tDCS Protocol

The anode was placed in the right supraorbital (SO) region. The electrode location was standardized with positioning according to the following parameters: the uppermost limit of the right eyebrow, in the line of the pupil, was the downmost inferior limit to place the inferior border of the electrode; transversally, the medial border of the electrode corresponded to the medial limit of the eyebrow. The anode was held by plastic straps in such a way to assure an even amount of pressure across the whole area of the electrode. The cathode was placed over the vertex area and its position was fixed by plastic straps. The rationale for this was that we aimed for optimal image acquisition and the most even electrode placement over de skin with littlest inter-subject anatomical bone surface variation; the right side was an arbitrary standard. Only anodal stimulation was tested in this study, based on previous finding of our group showing that anodic DCS generates more intense erythema (Guarienti et al., 2015) and to keep consistent across conditions. Stimulations were carried out using 131 tDCS devices (Soterix Medical Inc., New York, NY, USA). The active stimulation consisted of 30 min of a 2 mA current intensity plateau, with ramp-up and ramp-down periods of 45 sec and 15 sec, respectively. Sham stimulation consisted of a 30-min interval with no current, with a brief period (60 sec) of 2 mA stimulation at the beginning of the session, with ramp-up and ramp-down periods of 45 sec and 15 sec, respectively. The sponges were soaked with saline solution (NaCl 0.9%).

2.3.6. Image Data Protocol

A VISIA imaging System (Canfield Scientific, Fairfield, NJ, USA) was used to photograph the forehead of the subjects using a combi-nation of regular white light, 365 nm wavelength UV light and cross-polarized lightning flashes. A total of 292 photos from 26participants were obtained (4 per session per subject except for 20(<6.5%) images that were missed due to technical reasons). The photographed images are of very high definition (21 Megapixel resolution, 3433 x 4171 pixels size, image DPI 96 pixels/inch, file size 8.4 MB); 145mm (width) per 175 mm (height). They were then presented in a random order to the naïve rater.

The high definition images of subjects' forehead photographed before and 5, 15, and 30 min after the stimulation for active stimulation and sham phase (both using thin and thick electrode) were analyzed for erythema distribution using customized MATLAB (MathWorks, MA, USA) based image processing graphical user interface (GUI). Images corresponding to each phase were first randomized and were loaded in the GUI, which was designed to define a 5 x 5 cm region of interest (ROI) (corresponds to the length of the supraorbital (SO)) (Fig. 3A1a). Erythema beyond the ROI was not included in the analysis. Images were then filtered using Lab color space; the most accurate means of representing color, is device independent, and includes all of colors in the spectrum, as well as colors outside of human perception. Using a freehand tool enabled in the GUI, erythema inside the ROI was traced (Fig. 3A1b-d). The same rater traced erythema in all images for both active and sham stimulation cases. Erythema was separately traced as "mild" and "strong" inside the ROI. Assignment of the traces as "mild" and "strong" was based on comparison of natural tone of the facial skin (non-stimulated area) to the skin tone under the ROI. Traces of erythema were then binarized and normalized within the ROI (Fig. 3A2). Binary images were re-categorized to their respective sections: thin, thick, and sham, as mild and strong erythema. Surface

area of erythema trace inside the binary ROI was estimated first by finding the perimeter of the erythema distribution. Pixels that were part of the perimeter were only nonzero (1s) and were at least connected to one zero-valued pixel (0s). The default connectivity was 4 for a given 2D binary ROI. All the white pixels representing the erythema traces inside the ROI was enumerated and summed up to get surface area in pixels. Finally using a calibration factor, are in pixels was converted to area in centimeter square. The percentage erythema was calculated by dividing the ROI by erythema area, but the ROI is the same in each case. Mean of the combined, mild, and strong erythema distribution for active and sham phases was calculated (Fig. 3A3) and a probability heatmap of the distribution was generated (Fig. 3A4).

To analyze the spatial profile of erythema distribution, we defined multiple regions of interest (ROIs) at the edges (4), center (1), and hotspots (2). The size of each ROIs was 10% of the image size. Mean probability of skin reddening across the center ROIs and hot spot ROIs were compared.

2.3.7. Statistical Analysis

The normality was tested using Shapiro-Wilk test and when normally distributed a corresponding parametric test otherwise a nonparametric test was used to establish significance. Non-parametric Wilcoxon rank sum test was used to compare erythema intensity between groups. Critical value of $P < 0.01$ was accepted as statistically significant difference between groups.

2.4. Results

For the results section, “sham group” indicates sham tDCS, “thin sponge” indicates active tDCS with thin sponge and “thick sponge” indicates active tDCS with thick sponge.

The calculated probability heatmap across active stimulation (using thin and thick electrode) and sham condition indicated that erythema was diffused across the ROI. For the "thin" sponge, the maximum likelihood of observing erythema was 69.88%; 51.81 % for mild and 21.69 % for strong (Fig. 3B*1*). For "Thick" electrode, the maximum probability of erythema was 72.83 %: 44.57% for mild and 34.78 % for strong (Fig. 3B*2*). In case of "sham" stimulation, the maximum probability of erythema in combined was 41.43 %; 31.43 % for mild and 8.57 % for strong (Fig. 3B*3*).

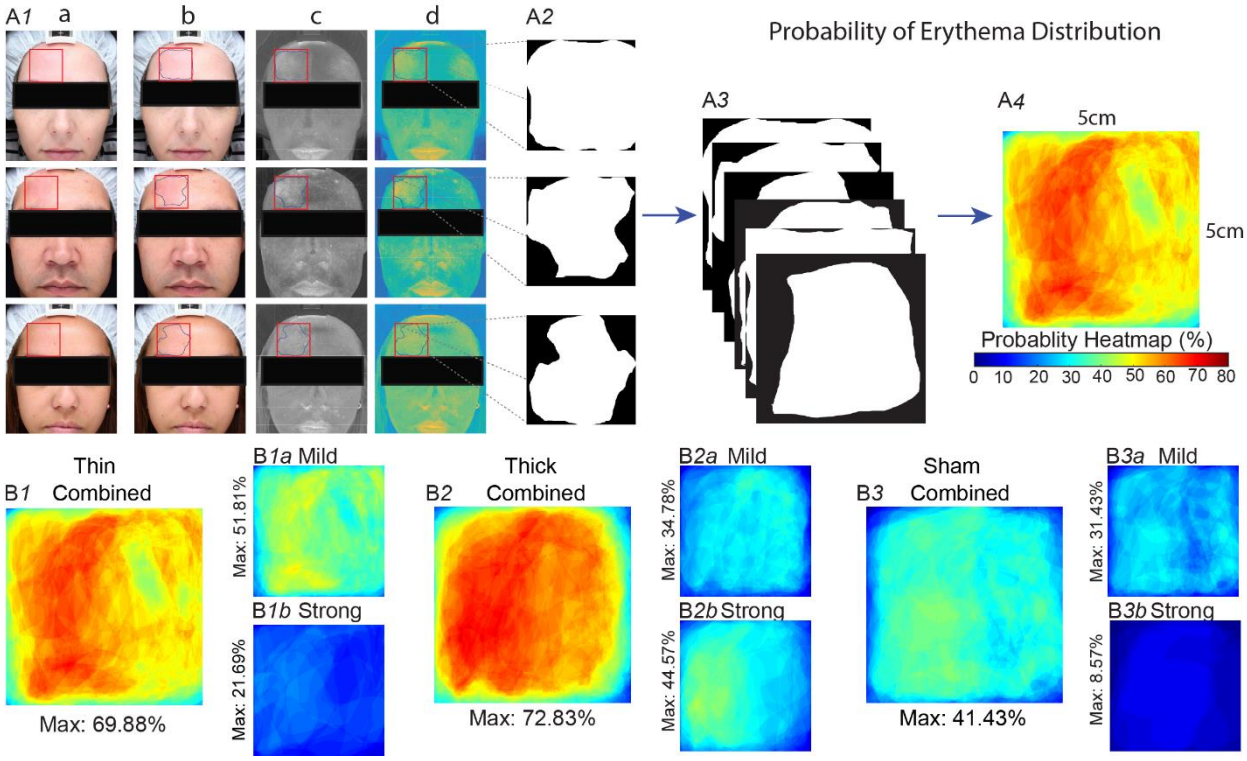

Figure 3: Erythema distribution analysis in the region of interest (site of stimulation) for active (using thin and thick sponges) and sham stimulation. (A1a) Illustration of high definition images of subject photographed before and after the stimulation. (A1b) represents region of interest (ROI) and traced erythema distribution. (A1c and A1d) Representation of filtered Images using Lab color space to isolate erythema from regular skin color tone. (A2) illustrates binary image of erythema traces in the ROI. (A3) Illustration of the probability of erythema distribution calculation via stacking equidimensional binary

images. (A4) Probability heatmap of erythema distribution (in percentage) across the ROI. (B1) Graphical illustration of the calculated maximum combined probability of erythema distribution for the "thin" sponge. Distribution was diffused across the ROI. Mild erythema distribution (B1a) had higher probability than strong (B1b). (B2) represents a maximum combined probability of erythema distribution for "thick" electrode. Mild erythema distribution (B2b) was slightly higher than strong (B2a). (B3) Illustration of the maximum combined probability of erythema distribution for "sham" stimulation. Probability of the erythema distribution compared to the active stimulation sponge types was significantly lower. Mild erythema (B3a) had higher probability than strong erythema (B3b).

To answer the question whether local current density pattern tracks the skin reddening profile, we analyzed the erythema probability within multiple square ROIs including edges and center of the electrode-skin interface (Fig. 4, black, gray, and blue squares). ROIs were defined at the edges, middle, and hotspots to compare the mean erythema probability across ROIs. Across all stimulation groups, the sampled average erythema probability at the edge (Thin: 0.30; Thick: 0.21; Sham: 0.10) was lower than the middle (Thin: 0.54; Thick: 0.60; Sham: 0.34) ($P < 0.01, Z = -133.68; P < 0.01, Z = -137.87; P < 0.01, Z = -126.89$) and the hotspots (Thin: 0.65; Thick: 0.67; Sham: 0.35) ($P < 0.01, Z = -147.94; P < 0.01, Z = -148.16; P < 0.01, Z = -153.22$. This analysis concluded that unlike local current concentration at the edge, erythema is higher in the non-edge region (not uniform at the skin-electrode interface).

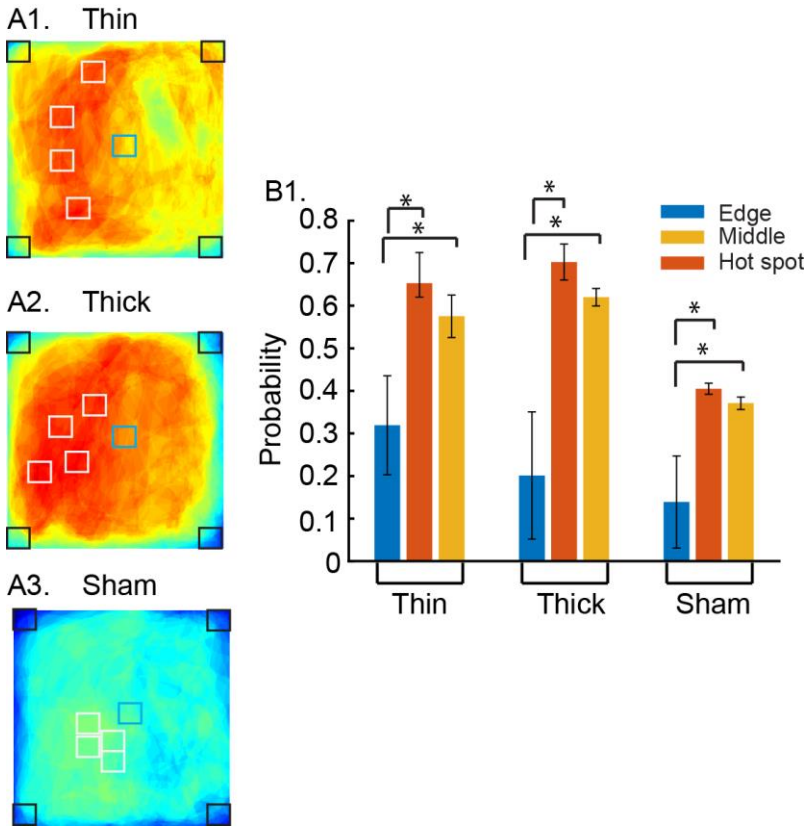

Figure 4: Regional analysis of erythema probability for different stimulation modalities. (A1, A2, A2) overall erythema probability and multiple ROIs (edges: 4 (green), hotspot: 2 (gray), and center: 1 (cyan)) defined to contrast the difference in erythema probability across regions. (B1) shows average erythema intensity for different ROIs (region color coded). Erythema at the non-edge regions were higher than edges.

Next, we assessed difference in erythema probability for active stimulation and sham stimulation. Histograms of mean erythema distribution (probability) across groups were generated for combined, mild, and strong cases, and skewness or kurtosis values were reported (Fig. 5). Across all groups, the combined histograms for each group were negatively skewed (Thin: -0.98; Thick: -0.86; Sham: -1.16) indicating that mean and median erythema intensity were less than mode. There was a significant difference in erythema distribution (probability) between the active stimulation and sham stimulation (Combined Thin Vs Sham: $P < 0.01$; $Z = 5.6$; Combined Thick Vs Sham: $P < 0.01$, $Z = 6.69$). Active stimulation have higher likelihood of both mild (Thin vs

sham: $P < 0.01$, $Z = 1234$; Thick vs sham: $P < 0.01$, $Z = 1258$) and strong (Thin vs sham: $P < 0.01$, $Z = 961$; Thick vs sham: $P < 0.01$, $Z = 254.72$) skin reddening compared to sham.

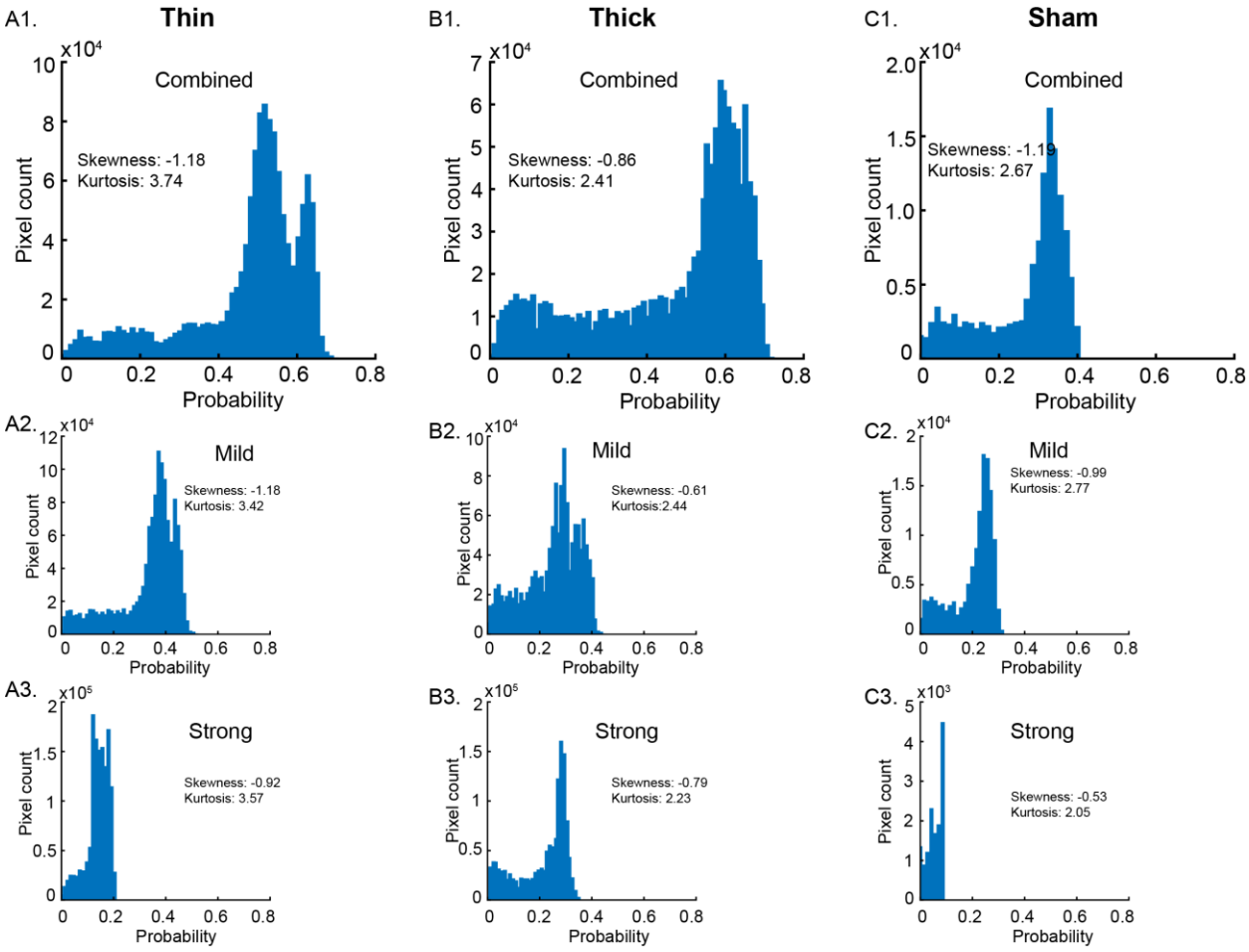

Figure 5: Histograms of mean erythema distribution for thin, thick, and sham group, categorized into combined, mild, and strong erythema. (A1, A2, A3) shows mean erythema distribution as combined, mild and strong (intensity vs number of pixels) for Thin electrode group, (B1, B2, B3) shows mean erythema distribution for Thick electrode group, and (C1, C2, C3) shows erythema distribution for Sham group.

We further assessed the difference in mean erythema distribution (probability) between active stimulation and sham stimulation (Fig. 6). This analysis also confirmed that active conditions produces higher skin reddening compared to sham, and the skin reddening is not

concentrated around the perimeter. Thus, the skin reddening profile does not track the current density profile predicted by the skin FEM model.

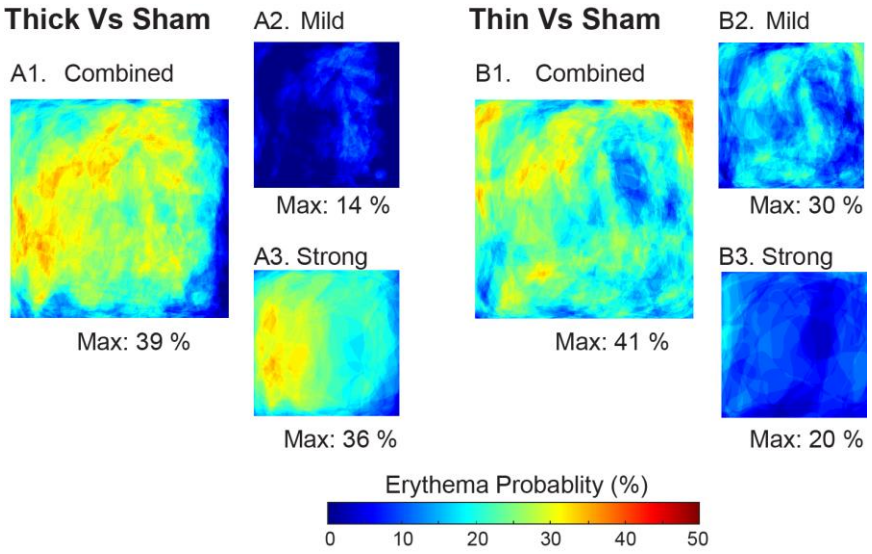

Figure 6: Erythema distribution difference across stimulation conditions. (A1, A2, A3) represents difference in probability of skin reddening between Thick Vs Sham and (B1, B2, B3) represents difference in probability between Thin Vs Sham. The spatial profile does not track local current density profile predicted by skin model.

In a separate analysis, we compared the erythema coverage across stimulation group. The mean erythema area (converted from pixels to cm^2 using a calibration factor (3.6 cm reference length in each image)) was higher in active groups compared to sham (Thin: 9.49 ± 0.5797; Thick: 9.67 ± 0.5756; Sham: 5.53 ± 0.70); Thin vs Sham: $P < 0.01$, $Z = 4.06$; Thick vs Sham: $P < 0.01$; $Z = 4.52$.

2.5. Discussion

In this within-subjects study enrolling 26 healthy volunteers, we found that tDCS-induced erythema is generally mild to moderate. Interestingly, a very mild erythema occurred after sham

stimulation although erythema was significantly higher after active stimulation, and even higher for the thick compared to thin sponge.

Our image processing analyses confirm that sham is significantly different from active tDCS stimulation. This study presented a new approach semi-automated image analysis approach to evaluate erythema spatial profile. In previous studies, investigators quantified erythema by examining site of stimulation site and rated erythema intensity (O'Connell et al., 2012). Even if investigators are blinded to the stimulation allocation group, they will be aware of the timing of stimulation (before vs. after stimulation). Moreover, non-verbal cues can break blinding during erythema examination (e.g., scratching during examination) and subjects can inadvertently report other adverse events to the investigators. By asking investigators to evaluate erythema through high-definition skin photographs presented at random, we were able to eliminate this source of bias. Conversely, in our study, erythema evaluation might be overestimated compared to the usual trial where investigators only do a quick visual inspection of the skin.

We implemented a novel approach of analyzing erythema using images acquired using high-resolution imaging system, and estimated a probability heatmap on the skin area, which presumably represents the erythema distribution under the electrode. This model also corroborated with prior observation of skin redness visible after sham stimulation. This might have occurred for some reasons such as 1) the brief period of active stimulation at the session onset;2) pressure of the pad, depending on how it is fixed; and 3) irritation of the skin due to the saline solution. Erythema was mild across stimulation groups which is in agreement with prior observations (O'Connell et al., 2012; Palm et al., 2013). In the active groups, there was no difference in erythema. Moreover, redness does not concentrate around pad edges, but it is rather diffuse (non-uniform) under the electrode. Assuming that the electric current causes redness, it seems that

current density is non-uniform below the pad (profile does not match with FEM predicted current density), and redness would be caused by an increase in blood perfusion among the tissue (Durand et al., 2002). This is in contrast to a previous modeling study that predicted higher current density at the center of a thin sponge and higher current density at the edges with thick sponge (Miranda et al., 2006; Wagner et al., 2007). However, that model did not fully capture the inhomogeneity and anisotropy within the skin; for instance, skin/scalp was considered a combined mass of muscle, skin, fat and connective tissues. A more recent model also estimated higher current densities at the edges when conductivity is high (Saturnino et al., 2015). Nonetheless, our finding reinforces the need to validate modeling studies empirically.

The implications of our erythema results in informing tDCS trial design should be taken with caution. First, our results are specific to the headgear (e.g., presuming sham erythema reflects pressure), electrode technologies, electrolyte (gel/saline/cream) used, subject demographics, and waveforms tested. We in fact show a dependence on electrode design and skin type. Trial-specific considerations would determine the need and value to mitigate erythema-related sham concerns. At a minimum, researchers should be rigorous in controlling and reporting relevant headgear and electrode, as well as other factors that could induce erythema. Simple methods to conceal exposed skin areas can be implemented. If appropriate, erythema intensity can be reduced by topic ketoprofen2% before stimulation (Guarienti et al., 2015). Triple-blind studies where the raters do not apply tDCS reduce confound of operator unblinding. Importantly, our protocol involved either trained operators or quantified segmentation, with optimal lighting and image capture, and with the targeted intention to identify erythema difference across arms, something impractical for regular use in tDCS trials.

Our findings, therefore, do not necessarily contradict conventional experience in tDCS trials where sham was found effective by operator and subject reports, but rather raise the alert for more detailed report of procedures used in future research to conceal stimulation group allocation, since it is now well documented that erythema is an independent factor for breaking investigator blinding in within-subjects design.

Chapter 3: Minimal Heating at the Skin Surface During Transcranial Direct Current Stimulation

3.1. Outline

This chapter describes Aim 2 of the thesis where we investigated whether tDCS produces significant skin heating and if any skin heating is due to joule heat. A version of this study has been published (Khadka et al., 2018b). In this chapter, we aimed to measure temperature increase at the skin surface during tDCS using multiple temperature sensors positioned around the perimeter and the center of sponge pad. In addition, a standard phantom was used to measure any temperature increase due to joule heat. The modeling of the phantom served to verify the simple model assumption which did not reflect accurate skin heating due to joule heat. Therefore, we developed a multi-layer skin model (epidermis, dermis, and fat) incorporating blood perfusion and metabolism to reliably predict temperature increase due to joule heat (through resistivities of skin layers).

3.2. Introduction

Transcranial Direct Current Stimulation (tDCS) is investigated as a non-invasive neuromodulation tool in healthy and patient populations (Nitsche and Paulus, 2000). Transient cutaneous sensation (e.g. itching, tingling, warmth) and skin erythema (so called “flare”) are the primary reported side effects of tDCS (Nitsche et al., 2008). Only using non-optimal materials and procedures cause severe skin irritation (Bikson et al., 2009; Poreisz et al., 2007). These adverse skin responses can be minimized by following established protocols in dose and electrode preparation (Brunoni et al., 2012; Woods et al., 2016), monitoring electrode resistance (Khadka et

al., 2015a; Merrill et al., 2005), and using proven electrode designs (Brunoni et al., 2011; Woods et al., 2016) or more advanced electrode techniques (Kempe et al., 2014; Khadka et al., 2015b).

One of the concerns to be addressed during the tDCS stimulation is the change in temperature at the skin surface. These changes might be stimulation polarity (anode or cathode) specific, contributed due to passive heating (joule heat), or due to change in blood perfusion. Small non-injurious changes in skin temperature during tDCS may influence cutaneous sensation (Lagopoulos and Degabriele, 2008) and even influence current flow patterns to the brain (DaSilva et al., 2011; Gholami-Boroujeny et al., 2015). Such changes may also confound blinding of subjects (e.g. sensation of warmth that is based on real temperature changes) or operators (e.g. in the active case sponges are warmer). However, the exact mechanism of burning sensation in still unknown. If the burning sensation was related to temperature, it could be polarity specific (under anode or cathode), contributed by passive heating, or vascular flare response. Although higher temperature changes may be injurious and contribute to less tolerable treatment, prior experimental and finite element method (FEM) modeling studies have curtailed a role for significant temperature increases during tDCS (A. Datta et al., 2009; Palm et al., 2008). Prior works have inadequately addressed skin temperature during tDCS. Nitsche and Paulus (Nitsche and Paulus, 2000) measured skin temperature during a 5 min 1 mA tDCS but didn't report any temperature increase. FEM models have predicted no temperature increase at the skin (Datta et al., 2009; Gomez et al., 2016). These models were basic/simplistic and didn't capture the realistic anatomy and detailed tissue layers.

This current study also builds upon the prior study by Datta et al., 2009 where no significant temperature rise at the sponge- electrode and the scalp interface was predicted by the FEM

simulation of 2 mA 4 X 1 ring HD-tDCS and conventional tDCS. tDCS produces skin heating and it is due to joule heat is the hypothesis of this study. Here, using an array of precise thermocouples, we measured temperature changes at the electrode-sponge and the agar phantom interface, and the skin interface, on an easily accessible area of skin such as forearms, during anodal, cathodal, and sham stimulation. Though systemic (centrally mediated) temperature changes during tDCS have not been observed (Raimundo et al., 2012), we none-the-less stimulated subjects' forearms to remove a central confound.

As a first demonstration, we implemented detailed experimental measures along with computational FEM model of an agar phantom (control experiment where vasculature is absent) and a skin (that included a vascular flare response (Dusch et al., 2009, 2007; Guarienti et al., 2015)) to determine the role of joule heating versus vascular flare (explained in discussion section) on any temperature changes.

3.3. Materials and Methods

This study involves experimental measurements in phantom and participant, and FEM simulation for stimulation (anode or cathode) and control cases.

3.3.1. Participants

Twenty healthy subjects (14 males and 6 females; age range 20-30 years; mean age 23.5 ± 2.5) volunteered in the study. Participants with any form of skin disorders or preexisting injuries at the sites of stimulation were excluded. The CCNY local Ethics Committee granted approval for this study and a written informed consent from the participants was collected before conducting the experiment. Participants were seated in a relaxed position.

3.3.2. Stimulation and Temperature Measurement

A constant current stimulator (1x1 tDCS, Soterix Medical Inc., NY, USA) was used to administer direct current for all trials through a pair of rubber electrodes (2 x 3 cm) placed into two saline (0.9% NaCl) soaked sponge pockets (35 cm^2 skin contact area, EasyPads, Soterix Medical Inc., NY, USA). Direct current intensity of 2 mA was applied for 20 min with an additional linear ramp up and down of 30s at the beginning and at the end of stimulation. Eight type- K thermocouples probes (Digi-Key Electronics, MN, USA) sensed by three dual input digital thermometers (~ ± [0.05% of reading + 0.3 ^{0}C] accuracy, 52II, Fluke Corporation, WA, USA) were positioned under the center and periphery of the anode, cathode, and control sponge-electrode to measure the temperature during stimulation (anode, cathode) and control (non-stimulation) electrode cases. Temperature was measured during stimulation (20 min), and pre-stimulation and post-stimulation (5 min each) phases for every minute. Measurement of temperature under the anode, cathode, and control was conducted during the same stimulation session – with the control electrode positioned on the opposite arm or at a distance location on the phantom. Experiments were conducted at the bench top in a temperature-controlled room and the ambient temperature was continuously monitored during the experiment using 2 similar type- K thermocouples as mentioned above. The ambient room temperature during the entire study remained nearly unchanged (22 ± 1.5 ^{0}C).

3.3.3. Phantom study

Agar *phantom* (2 % agar by weight; 20 gm agar ash and 1 gm NaCl to 1000 ml water, A7002, Sigma-Aldrich, MO, USA) was prepared using established standard protocols (Smith, 1993). While conducting temperature measurement on the phantom, sponge-electrodes were positioned approximately 10.2 cm apart on a thin coated layer (~ 0.5 cm) of conductive electrode

gel (Signa gel, Parker Laboratories Inc., NJ, USA). Assigned electrode distance was based on our earlier study [8]. The electrode-sponge distance in the phantom study matched the *in vivo* study. Conductive gel layer was used to maintain consistent contact between the sponge-electrode and the gel. For stimulation case, a 2 mA DC was injected from the 1X1 tDCS stimulator via sponge electrodes and corresponding temperature under the electrodes were measured whereas for the control case, sponge electrodes were positioned on the phantom but not connected to the stimulator.

3.3.4. In vivo study

For *in vivo* study, skin was cleaned with dilute saline prior to the electrode placement. The sponge electrodes were then secured on the forearm of the participants using rubber straps (Elastic Fasteners "Blue", Soterix Medical Inc., NY, USA) and were positioned proximal and distal to the forearm (Khadka et al., 2015a). Stimulation and control cases, and the corresponding temperature measurement were conducted following the aforementioned procedure.

3.3.5. Temperature Analysis

Temperature measurements at every minute during pre-stimulation, stimulation, and post-stimulation phases for both phantom and *in vivo* studies were averaged across phantoms and subjects, and were normalized with respect to the initial temperature, which was considered a baseline (0^0C) as shown in Fig. 7A. Since the initial temperature upon the placement of the sponge-electrodes at the skin or the phantom varied with the initial temperature of the saline soaked sponges and the ambient temperature, we considered initiation of the tDCS stimulation (t=5 min) as the "initial temperature" for normalizing temperature data. Temperature difference (ΔT) was

calculated across all subjects and phantom studies for both stimulation and control cases. In case of the FEM simulations, ΔT was calculated at the given instant (t= 5, 10, 15, and 20 min).

3.3.6. Computational model and solution method

3.3.6.1. Heat Transfer

Human skin was modeled as an inhomogeneous medium comprising three layers; epidermis, dermis, and subcutaneous layer (fat and connective tissue) where epidermis was superficial and avascular (presence of stratum corneum (SC)), while the underlying dermis and subdermal tissues were rich in vasculature (Wilson and Spence, 1988a). Each layer of the skin was modeled as a homogeneous and isotropic volume conductor and thickness values were based from prior literature (Wilson and Spence, 1988a). The anodal case was considered for the FEM multi-physics (current flow and bioheat) model, however, none of the physics considered for the computational model were polarity specific. Heat transfer and temperature fields in the human skin was modeled using time-dependent bioheat equation Pennes equation as mentioned below:

$$\rho C_p \nabla T = \nabla.(\kappa \nabla T) - \rho_b C_b \omega_b (T - T_b) + Q_{met} \quad (1)$$

where ρ, C_p, T, κ, and Q_{met} represent tissue density, specific heat, temperature, thermal conductivity and metabolic heat generation respectively. Similarly,ρ_b, C_b, ω_b, and T_b are density of the blood, specific heat of the blood, blood perfusion rate, and temperature of arterial blood. Blood perfusion was constant in all vascular skin layers and the values for the properties of blood were assigned as:$\rho_b = 1060\ kg/m^3$(Duck, 1990); $C_b = 3770\ J\ /(kg.K)$; $T_b = 37\ ^0C$ (Torvi and Dale, 1994). In order to account for the heat generation during electrical stimulation, equation (1) was further modified to include joule heating ($Laplace\ equation\ \nabla(\sigma \nabla V) = 0$ where V: potential and σ: conductivity) and was given by:

$$\rho C_p \nabla T = \nabla.(\kappa \nabla T) - \rho_b C_b \omega_b (T - T_b) + Q_{met} + \sigma |\nabla V^2| \quad (2)$$

3.3.6.2. Boundary and initial conditions

The boundary condition at the top surface of the skin and sponge was simulated as convective heat loss to the ambient air, without explicitly considering heat loss to the surrounding due to evaporation. Therefore, the boundary conditions at the top surface of the skin and sponge electrode was

$$q = h(T_{amb} - T) \quad (3)$$

$$h = 5\ W/m^2.K\ , \quad T_{amb} = 24\ ^0C\ (air\ temperature)$$

where *h* is the convective heat transfer coefficient and T_{amb} was ambient temperature (averaged from *in vivo* study). Bottom surface of subcutaneous layer was set to be at core temperature (T_{core}) and the boundary condition was (T_{core}= 37 ^{0}C).

Initial temperatures (T_0) for electrode-sponge (22.5 ^{0}C), top layer of skin (surrounding epidermis=32.5 ^{0}C, and epidermis section underpad =29.02 ^{0}C) were based on experimental measurement. The underlying dermis (33 ^{0}C) and subcutaneous layer (33 ^{0}C) temperature was set slightly higher than the epidermis due to vasculature and proximity to the core (Wilson and Spence, 1988a).

For electrical stimulation, boundary conditions were applied as normal current density (inward current flow:J_{norm}) at the top exposed surface of anode and ground at the bottom surface of subcutaneous layer. Uniform current density corresponding to 2 mA intensity was applied through a rubber electrode (σ=0.947 *S/m*; *κ*=0.2 *W/(m.K)*, (Khanam et al., 2015)), embedded inside sponge pocket (σ = 1.4 *S/m*; *κ =0.6 W/(m.K)*, (Minhas et al., 2011). All other external surfaces of the model were electrically insulated. Dimensions of rubber electrode and sponge were set according to the experimental protocol.

The thermophysical parameters of biological tissue layers were based on average of prior literature (Duck, 1990; Pavšelj et al., 2007; Torvi and Dale, 1994; Werner and Buse, 1988; Wilson and Spence, 1988a). Epidermis under the wet sponge (σ = 0.16 *S/m*; κ =0.235 *W/(m.K)*) was assigned higher conductivity compared to the surrounding dry epidermis (σ = 0.0004 *S/m*; κ = 0.235 *W/(m.K)*) due to the water content in the saline. Blood perfusion in the vascular tissues was increased with current density, simulating stimulation-induced erythema (flare response). Dermis (σ = 0.23 *S/m*; κ = 0.450 *W/(m.K)*, ω_b= 0.0020 s^{-1}, Q_{met}= 400 Wm^{-3}) and subcutaneous layer (σ = 0.02 *S/m*; κ = 0.185 *W/(m.K)*, ω_b= 0.001 s^{-1}, Q_{met}= 400 Wm^{-3}) have blood perfusion due to vasculature, hence metabolic heat generation.

The phantom was modeled using equation (1) and (2) neglecting the biological tissue parameters. The boundary and initial temperatures of the phantom were set based on experimental measurement (T_{core}=T_0 =24 ^0C). The electrical conductivity and thermal conductivity of agar phantom were 0.05 *S/m* and 0.07 *W/(m.K)* respectively (Bennett, 2011).

3.3.6.3. Computational Method

Computer aided design (CAD) models of skin layer geometry consisting epidermis, dermis, subcutaneous layer, sponge, and electrode (Figure 2B_1) were assembled in SolidWorks 2013 (Dassault Systemes Americas Corp., MA, USA) and were imported as an assembly in COMSOL Multiphysics 4.3 (COMSOL Inc., MA, USA) to solve the model using a finite element technique. The phantom model was solved implementing the same methods as the skin model. Volumetric meshes for the skin and the phantom model were generated as *Physic-controlled mesh* with an average element quality of greater than 0.5. The final FEM skin model was solved for greater than 2,000,000 degrees of freedom and had greater than 1,700,000 tetrahedral elements whereas in the

phantom model, the degrees of freedom was greater 600,000 and had greater than 400,000 tetrahedral elements. In our study, we considered the steady-state solution (temperature obtained by evaluating the model under non stimulation condition) as the initial conditions for the time-dependent study (20 min stimulation with a time step of 0.01 sec) of temperature elevation. Bio-heat transfer physics in biological tissues (for the skin) and solid (for the phantom) were solved for stimulation and non- stimulation cases and the temperature were predicted. Current density streamlines were generated for the stimulation case (skin) to illustrate the distribution of current on the surface and through different tissue layers (Fig. $7B_2$). Streamlines were seeded uniformly from the top surface of the rubber electrode and were proportional to the logarithm of current density magnitude.

Datasets from the computational result of the skin and the phantom volume plots (non-stimulation and stimulation cases) were exported from COMSOL and were analyzed in MATLAB R2016a (MathWorks, MA, USA) to calculate the temperature difference (ΔT). Since the FEM model was first solved under steady-state condition and later its solutions were used as the initial conditions for the time-dependent study, we considered temperature at t=1 min as the initial temperature for the ΔT computation of both phantom and skin model.

3.3.7. Statistical analysis

Analyses were performed using Shapiro-Wilk test to access normality of temperature difference across active stimulation (anodal, cathodal) and control groups. Statistically significant differences ($p < 0.01$) in ΔT between polarities (anode, cathode, and control) were probed using a non-parametric analysis. Specifically, a Wilcoxon signed-rank test was used to analyze the t temperature difference (ΔT) under the control, compared to the anode and cathode, and also to investigate an interaction between control and stimulation cases. Calculated p-values were

corrected using the false discovery rate (FDR) where the discovery signifies the rejection of the null hypothesis that there is no difference between the temperature change at the polarities (anode, cathode, and control). A critical value of less than 0.01 was accepted as a significant difference between the groups.

3.4. Results

Temperature changes at the skin surfaced under electrodes during active direct current stimulation (2 mA, 20 minutes) and control (0 mA, 20 minute) conditions were recorded on subject forearms and a specially constructed phantom. Additionally, temperature increases were also simulated using bio-heat FEM models of the skin and phantom surface. In both phantom and subjects, we observed a dynamic temperature variation reflecting difference in the initial temperature at the skin electrode interface when the sponges were initially placed on the forearm at a given ambient room temperature in all cases. Therefore, all analysis was performed relative to the temperature at the surface of the skin, 5 minutes after the sponge was initially placed; corresponding to when stimulation was initiated in the active stimulation case (Fig. $7C_1$ and $7D_1$).

Average temperature difference (ΔT) across stimulation group and control in the phantom was less than $0.1^{O}C$ (Fig. $7C_1$). The temperature difference (ΔT) in the phantom was not significantly different under both anode (*Mdn =0.0687 ^{O}C*) and cathode (*Mdn = 0.046 ^{O}C*), compared to control (*Mdn = 0.0260 ^{O}C*) (*P = 0.0771*, *P = 0.4126*). Furthermore, ΔT was independent of electrode polarity (anode (*Mdn = 0.0687 ^{O}C*), cathode (*Mdn = 0.0460 ^{O}C*), *P = 0.2036*, Fig. $7C_1$).

Stimulation of subjects resulted in a gradual increase in temperature under both anode and cathode, compared to control (for example at t = 20 min: ΔT_{anode} = 0.9 ^{0}C, $\Delta T_{cathode}$ = 1.1 ^{0}C, $\Delta T_{control}$ = 0.05 ^{0}C as shown in Fig. $7D_1$). The ΔT under cathode (*Mdn=0.6327 ^{0}C*) was

significantly higher than control (*Mdn = 0.0442 ^0C*) at $t \geq 10$ min, Z = -2.6133, P = 0.0090, r = 0.58. Similarly, ΔT at $t \geq 14$ min under the anode (*Mdn = 0.4769 ^0C)* compared to the control (*Mdn=0.0442 ^0C*) was also significant, Z = -2.389, P = 0.0169, r = 0.53 (Fig. 7D_1). Interaction of ΔT at the anode and the cathode was not significant, Z = -0.5973, P = 0.5503, r = 0.133.

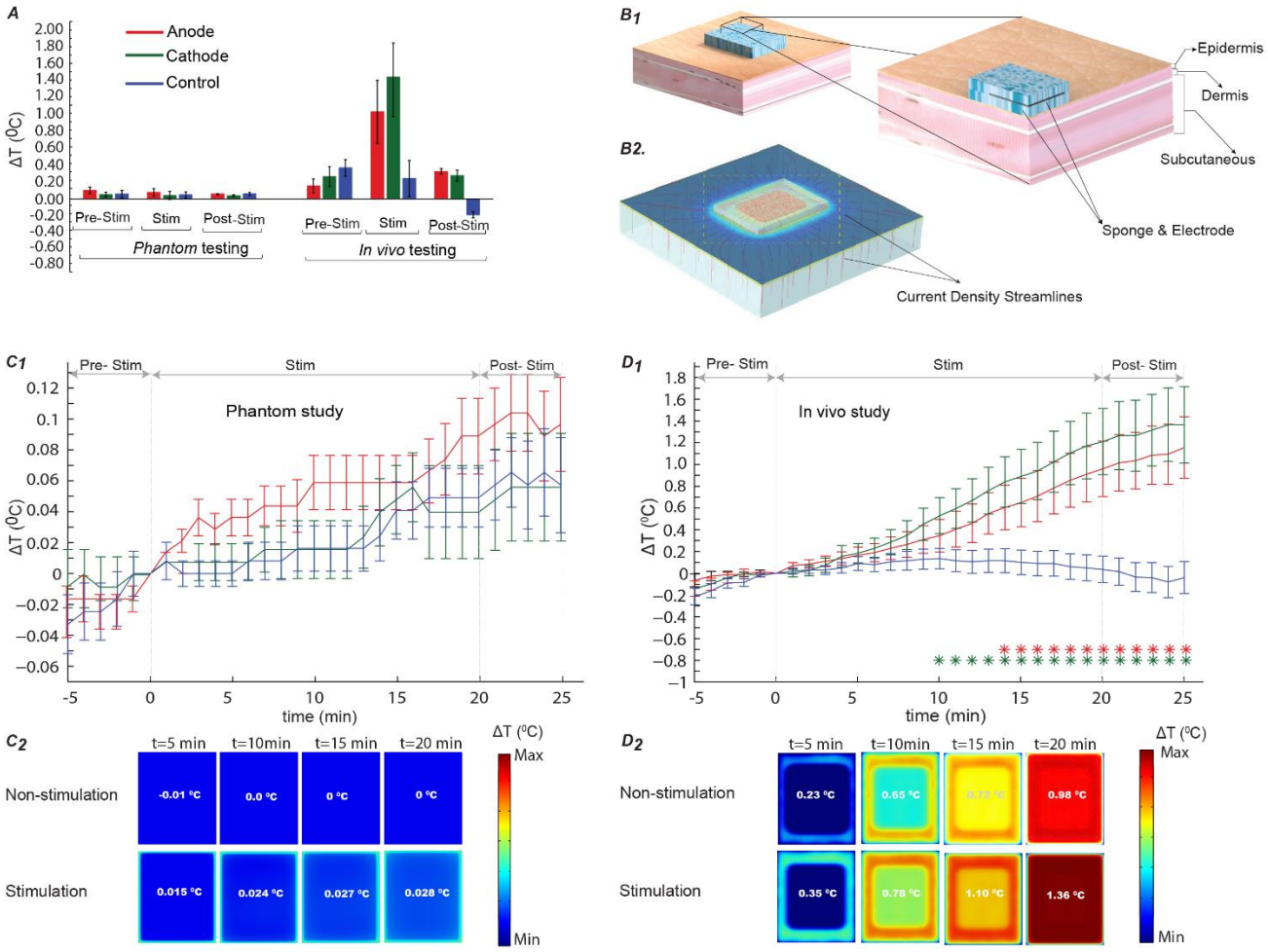

Figure 7: Skin surface temperature changes under tDCS electrodes during pre-stimulation, stimulation, and post-stimulation phases in the phantom from in vivo studies, and FEM simulations. (A) Average temperature change in subjects (right) and phantom (left) normalized to temperature at t= 0. The error bars indicate standard error of mean (SEM). In the phantom, ΔT was approximately same across test samples and mode of stimulation, whereas in the in vivo study, maximum ΔT was measured under the

active electrode (max. under cathode) during stimulation compared to the control. (B1) Architecture of a skin model showing skin layers (epidermis, dermis, and subcutaneous layers) and electrode positioning on the skin surface. (B2) represents an orientation of current density flow streamlines inside the different skin tissue layers. (C1) Analysis of normalized average ΔT in the phantom study ($p < 0.01$). No significant difference in ΔT was found in the control, compared to the anode and the cathode. (C2) Illustration of predicted ΔT for the non- stimulation (control) and stimulation cases in the FEM phantom model. Predicted results indicated no significant effect of stimulation on the phantom. (D1) In vivo analysis of temperature difference over time within subjects during pre-stimulation, stimulation, and post-stimulation. Red and green asterisks symbolize statistically significant difference ($p < 0.01$) between anode and control, and cathode and control respectively. There was a significant difference in ΔT under the anode ($p < 0.01$) and the cathode ($p < 0.01$), compared to the control. Temperature under both anode and cathode gradually increased due to stimulation, compared to that of control. (D2) FEM representation of the predicted ΔT in the skin model. Maximum ΔT of 1.36 ^{0}C was predicted during direct current stimulation by the FEM model.

The FEM model of stimulation on the skin and phantom predicted current flow pattern produced across the tissue/phantom (Fig. $7B_2$) and the coupled change in heat and blood flow (for the case of the skin). The phantom FEM model predicted a comparable maximum ΔT of 0.027 ^{0}C and 0.028 ^{0}C (at *t= 20 min*) for the non-stimulation (control) and stimulation (anode/cathode) cases respectively (Fig. $7C_2$). A maximum ΔT of 0.98 ^{0}C was predicated by the FEM skin model at *t=20 min* for the non-stimulation case, whereas for the stimulation case, ΔT was 1.36 ^{0}C (Fig. $7D_2$). Compared to the control case, tDCS induced a moderate temperature rise (ΔT = 0.38 ^{0}C) at the skin surface, as predicted by the FEM skin model (*t=20 min*).

3.5. Discussion

Any electrical stimulation might produce temperature changes; reflecting complex interactions between joule heat due to applied current across resistive tissue, changes in

metabolism (neuronal activation) or perfusion (flare), and heat conduction (Abram et al., 1980; Maged M. Elwassif et al., 2006a). Evidently, the results of our study are relevant only for the specific technology, dose, and subject conditions tested (c.f. transcranial magnetic stimulation (rTMS) in the presence of a heating clip (Hsieh et al., 2012)). Temperature changes in the body are typically considered unimportant in the efficacy or safety of neuromodulation technologies (Balogun et al., 1996; Cramp et al., 2000). We observed only incremental temperature changes at the skin surface during tDCS, independent of stimulation polarity and results from stimulation. Since changes were absent in the phantom, we propose that temperature elevation increases the anode/cathode reflected stimulation induced flare – a heating induced skin response due to increased blood flow. Skin surface temperature changes of ~1 ^{0}C are none injurious and within normal variation (e.g. due to exercise, environment; (Maged M. Elwassif et al., 2006a; Scudds et al., 1995)). Moreover, as this small increment is in fact compensating for a reduction in surface temperature following application of room-temperature sponges, and since perfusion-based heating is limited by the core body temperature of the blood, this mechanism is not hazardous.

Our results are consistent with the tDCS perception of warmth being attributed to electrical nerve activation rather than heating (Abram et al., 1980; Cramp et al., 2000), and any significant skin irritation (that occurs only when standard protocols are not followed) being electrochemical in nature (Minhas et al., 2010). We analyzed temperature change at the surface of the skin (*in vivo* study) during stimulation (20 min) relative to the temperature after the pre-stimulation duration (5 min) to account for the dynamic temperature changes reflecting difference in the initial temperature at the skin-electrode interface relative to the skin and room temperature (Fig. 7D$_1$). Similarly, to account for such dynamic temperature variation due to natural cooling of the skin when exposed to the ambient temperature, we solved our FEM models first under steady-state

conditions and then used its solution as an initial condition for the time-dependent analysis. Any warming of sponges observed by subjects or operators touching the electrode surface would reflect passive heating from the body and it is unlikely that the difference between active and sham can be resolved, hence, not a confound to blinding. Our result does not address temperature changes inside the body (e.g. at the brain), temperature changes outside of the period evaluated (up to 5 min post tDCS), microscopic changes (e.g. at sweat pores) or changes following abnormal tDCS dose (e.g. 100 mA), and repeated sessions. We speculate the flare response, already a well-known consequence of tDCS from inspection of skin erythema (Ezquerro et al., 2017; Guarienti et al., 2015), along with the associated skin temperature change indicated here, may influence current flow patterns through the skin, and so indirectly tolerability (Khadka et al., 2017). For future research, this approach can be extended to a realistic head model or a microscopic level skin model.

Chapter 4: Role of complex skin tissue layers and ultrastructures in transdermal current flow during tDCS

4.1. Outline

This chapter describes the Aim 3 of the thesis (Technical Aim) where we developed a high-resolution skin model to address the current flow pattern and relate whether the model aligns with experimental results of the skin reddening or skin heating. In Aim 1, the local current density predicted by the homogenous FEM model did not match the skin experimental reddening profile (main hypothesis was rejected). We then proposed an alternative hypothesis that experimental skin current density is indeed (relatively) uniform, and the homogenous model prediction is therefore incorrect. Prior simplistic (e.g. homogenous or two-layer) models lack relevant details of skin structures and thus did not directly align with experimental findings such as skin reddening. In order to address this possibility, in this Aim, we modeled the skin with multi-layers (epidermis, dermis, and fat), with or without additional ultra-structures (hair follicles, sweat glands, and blood vessels).

4.2. Introduction

4.2.1. Cutaneous current flow during transcranial electrical stimulation

Transcranial electrical stimulation, including tDCS is a noninvasive electrotherapeutic tool used to modulate brain functioning by delivering weak current to the brain via two electrodes positioned at the scalp/skin (Bikson et al., 2016; Nitsche et al., 2008). tDCS is well tolerated with common mild adverse events such as transient cutaneous sensations (tingling, itching, burning) and erythema (Antal et al., 2017; Aparício et al., 2016; Bikson et al., 2016; Fertonani et al., 2015; Paneri et al., 2016). However, if the established standard protocols are not strictly followed

(Woods et al., 2016), tDCS can produce significant skin irritation (Bikson et al., 2009; Poreisz et al., 2007; Shiozawa et al., 2013; Wang et al., 2015). Though these adverse events outline the need for a strict adherence to the stimulation protocols and an optimal electrode design for efficacy and safe cutaneous electrical stimulation (evaluated by the current density distribution under the electrode), the underlying electrical properties of the skin might not be totally affected by an external control of these stimulation parameters. The commonly reported adverse events such as erythema and burning sensation (if related to skin heating) are often related to current density under the electrode. Prior simplistic (e.g. homogeneous or two-layer) skin models predict higher current density at the electrode edges (A. Datta et al., 2009; Gomez-Tames et al., 2016; Miranda et al., 2006; Saturnino et al., 2015). However, these models lack relevant details of skin complex layers and realistic ultrastructures (sweat glands, hair follicles, and blood vessels) and thus did not align with the experimental findings such as skin reddening (Ezquerro et al., 2017) and skin heating (Khadka et al., 2018b).

4.2.2. Experimental studies of skin electrical properties and lumped-parameter models

The electrical properties of skin can be altered, including by the degree of hydration, pH, salinity, temperature, stimulation waveform type, perspiration, skin diseases, emotional state, and most importantly, the electrical stimulus intensity (current, voltage, power) (Kalia and Guy, 1995). Decreased skin resistance often correlates with an enhanced skin permeability (Björklund et al., 2013). Given the sensitivity of skin electrical properties to an environment (e.g. room temperature) and preparation (e.g. cleaning) conditions along with the electrode design, it is important to interpret the experimental studies as specific to and in light of these limitations.

4.2.2.1 Skin impedance

The influence of complex skin tissue layers including stratum corneum has been previously documented using skin stripping experiments. Successive stripping of the stratum corneum (keratinized superficial layer of epidermis) decreased skin resistivity by up to a factor of 300 compared to the intact skin, which can be related to the removal of a resistive pathway (Lykken, 1970; Tregear, 1966). In 1953, Mueller and colleagues studied the role of sweat duct in current flow using a multicontact electrode, and demonstrated that current is conducted through discrete channels in dry skin underneath a contact electrode (Mueller et al., 1953). In 1974, Saunders observed a discrete pattern of Ag (silver) deposition on a forearm after an electroplating experiment, confirming that during stimulation, current enters into the deeper skin tissue layers from the epidermis through a discrete sweat gland pathway (Systems et al., 1974).

In 1955, Suchi confirmed that a wet skin or ducts filled with sweat has 10x lower impedance compared to a dry skin (Suchi, 1955). Martinsen et al., 1997 measured a galvanic skin response using electrical admittance meter on a blister skin and wart (pure stratum corneum (SC) without sweat ducts)), and concluded that the electrical properties of keratinized tissues like SC contribute to overall skin conductance, and below 10 Hz, skin demonstrate frequency independent electrical conductance (Martinsen et al., 1997). In 1976, Mason and Mackay demonstrated a gradual drop in skin impedance over time by placing an electrode over the skin (dry and wet skin (treated with tap water or conductive electrode paste)) and stimulating with a pulsed current (0.1 - 1 mA, 4 Hz, 1 ms pulse width, and 2 ms interpulse width). In the dry skin, impedance significantly dropped (150 kΩ to 110 kΩ) with rapid fluctuations during the first minute of stimulation and then continued to drop asymptotically for 20 to 30 min. This drop phenomenon might have occurred due to a gradual hydration of SC from the sweat (equivalent to saline conductivity) build up

underneath the electrode. In the tap water treated skin, impedance at the start of stimulation was lower (90 kΩ), but matched the dry skin impedance after 20 min (~ 65 kΩ), whereas for the skin pretreated with a conductive electrode paste, impedance was initially low (24 kΩ), but gradually increased to a maximum magnitude (~ 28 kΩ) and then descended below initial impedance (< 24 kΩ) after 1 min of stimulation (Mason and MacKay, 1976).

4.2.2.2 Skin capacitance

Several experiments have confirmed that skin capacitance lies in the SC. In 1966, Schwan demonstrated that at α relaxation frequencies (0.1 - 1000 Hz), the capacitance of the skin is predominantly due to the SC (Schwan, 1966). The capacity of stratum corneum has also been demonstrated using stripping experiments, where with every successive stripping, the skin capacitance dropped compared to its intact value- dropped lower than its intact value when all SC was removed (Edelberg, 1977; Lykken, 1970). However, the lumped circuit models have not yet captured this observation when considering SC/epidermis as a pure dielectric material sandwiched between electrode and dermis. If the model's prediction is right based on the physics (parallel plate capacitor), the capacitance should increase with a decrease in SC thickness. In 1977, Edelberg experimentally measured the skin's capacity using a corneometer and reported that the skin's capacity lies in a range of 0.02 to 0.06 μF/cm^2 (Edelberg, 1977), which is considered higher than the theoretically calculated value. For example, consider a 10 μm thick SC with dielectric constant of 2.5. Its theoretical capacitance will be 2 x 10^{-4} μF/cm^2, smaller than the experimental values. Schwan et al., 1966 addressed this anomaly in skin capacitance using the concept of polarization capacitance- stored charge that appears around an electrode when placed in an electrolyte, thus forming an ionic capacitor (Schwan, 1966). Furthermore, Tregear in 1966 used a complex lump circuit model and addressed that the skin capacitance is contributed by individual cell membranes

(Tregear, 1966). For example, consider the epidermis has 200 cell layers and each cell have a capacitance of 5 μF/cm^2. Each cell is a bilayer, and thus the total capacitance will be ~ 0.05 μF/cm^2, which is close to the experimental measurement (0.02 - 0.06 μF/cm^2). In 1996, Gabriel reported that the skin conductivity increases with frequency, and the skin capacitance decreases with frequency (Gabriel et al., 1996a). Franchimont and colleagues in 2015 characterized the skin capacitance using a skin capacitance mapping (SCM) system. Through an optic based imaging system, they photographed participants' skin at rest and 10 min after physical exercise. They concluded that the calculated SCM score of the skin after physical exercise was higher (sweat production) than the skin at rest suggesting that sweat glands governs the skin capacitance (Pierard-Franchimont and Pierard, 2015).

4.2.2.3 Skin nonlinearity

Numerous prior studies (Grimnes, 1983; Mason and MacKay, 1976; Yamamoto and Yamamoto, 1981) demonstrated a nonlinear phenomenon (non-dielectric mechanism or a dielectric breakdown mechanism) as a time dependent impedance changes by applying voltage (600 to 1000 V), while limiting the current. Above a critical voltage, these studies reported significant skin non-linearity (for a 15 μm dry -excised SC sample) due to sudden dielectric breakdown of impedance (at ~ 450 V). However, for an intact living skin, this breakdown phenomenon was observed at significantly lower voltages than that of the excised SC. In 1977, Edelberg suggested that linear region for skin current density lies below 2 mA/cm^2 (Edelberg, 1977). Saunder and colleagues in 1974 studied the nonlinear voltage/current relationship using a 5 μs pulse and hypothesized that during a brief time interval, the capacitive coupling to dermis might bypass the SC resistance and the nonlinear properties were exhibited by the skin (nonlinear breakdown occurring at 150 to 250 V) (Systems et al., 1974).

In 1934, Freiberger observed a nonlinear skin response to the waveform shape (sinusoidal at 50 Hz) as a distortion in the measured voltage for an injected current. Transient distortions (less than a minute) occurred as an instantaneous nonlinear response within the individual cycles, whereas the extensive nonlinearities were observed as a gradual decay in the impedance (Freiberger, 1934). In 1966, Schwan reported that skin impedance decreases with increasing frequency of the stimulating current. The capacitive properties of the skin predominantly account for its frequency dependent (0 to 2 kHz) nature (Schwan, 1966). Biegelmeier and colleagues in 1980, demonstrated that skin impedance drops as much as ~ 750 Ω of its initial impedance at the highest frequency (Beigelmeier and Miksch ,1980).

The extent of dielectric breakdown on a dry skin is also modulated by an electrode size. Freiberger in 1934 observed the breakdown ($V \geq 100$ V) occurring within less than a second with a smaller electrode stimulation whereas with a larger electrode, the breakdown was above 200 V (Freiberger, 1934). Through a mockup parallel plate capacitor and a variable DC voltage source in series with the capacitor, Mason and MacKay in 1976 noticed a sharp increase in current recorded in the circuit at 600 V (DC) signaling a skin breakdown (onset of pain). Few small darkened punctures were observed following a prickling pain at the site of stimulation in dry skin, however there was no evidence of punctures when skin was pretreated with tap water or electrode paste (wet skin). This observation suggested current concentration at the discrete channels on the surface of skin, but not necessarily addressed the dielectric breakdown phenomenon. Grimnes et al., 1983 addressed dielectric breakdown mechanism of the human skin *in vivo* using a small electrode (0.018 mm^2) in a low-admittance point (i.e. the dorsal side of the hand to avoid humidity build up under the electrode) and a positive stimulation potential. The dielectric breakdown progressed in a stepwise manner when a positive 600 V was applied through the series resistor

(150 MΩ) with an initial skin impedance of 6000 MΩ. At the higher potentials, the breakdown was immediate. With repeated square wave potential, the breakdown occurred in the second pulse and a new current level was attained after the next period of a zero current, suggesting the result of a permanent skin damage (Grimnes, 1983).

4.2.3. Prior Skin FEM Models of Electrical Stimulation

The FEM modelling serves as a powerful tool to predict current flow or study of any related electric properties of skin-electrode system. As an alternative to conventional lump circuit model or 1D electrical network simulation, the FEM method can yield higher accuracy, is less time consuming, and have better parameter control to emulate realistic conditions. The modeling of skin evolved over time, but the level of details and sophistication is still lacking in the existing FEM models. Prior skin models are simplistic (homogeneous or three layers) (Miranda et al., 2006; Sha et al., 2008; Abhishek Datta et al., 2009; Gomez-Tames et al., 2016), fail to capture the detailed anatomy of the complex tissue layers and ultrastructures (hair follicles, sweat glands, and blood vessels), and address their role in cutaneous current flow pattern. We expect these details to profoundly change the current flow pattern. The safety and tolerability of tDCS has been widely investigating by designing an optimal electrode or optimizing the waveform parameters to minimize cutaneous adverse events (Hahn et al., 2013; Khadka et al., 2015a, 2018a; Niranjan Khadka et al., 2019b; Minhas et al., 2010). However, without understanding the physiological electrical properties of the skin and its ultrastructures, the waveform or electrode optimization alone cannot ensure better stimulation outcome.

Panescu and colleagues modeled the first non-linear 2D skin FEM model for current flow prediction (Panescu et al., 1993). The nonlinearity was addressed by simulating dynamic skin conductivity (conductivity dependent upon the voltage), and by modelling 10 different nonlinear

sub-regions mimicking the mosaic skin structure (epidermis) of five different breakdown voltages. In 2006, Miranda and colleagues constructed a sphere model (representation of human head) to predict the spatial profile of the magnitude and direction of the current density in human head during tDCS. This model predicted highly non-uniform current density at the electrode/scalp interface (higher at the electrode perimeter) (Miranda et al., 2006). Sha et al., 2008 developed a 2D FEM model of skin with stratum corneum, fat, muscles, and a single sweat duct to identify role of electrode on current distribution through the skin. The model predicted that peak current density was concentrated at the sweat gland, and high resistivity electrode produced lower peak current density (Sha et al., 2008). Datta and colleagues in 2009 demonstrated through an anatomical head model with simplified skin representation that tDCS induces negligible skin heating (A. Datta et al., 2009). In 2016, Gomez-Tames and colleagues developed a three layer skin model with non-realistic hair follicles and sweat glands (geometric shapes of equal dimension) to investigate their effect in electrical and thermal analysis of tDCS. They did not include blood vessels into the model. The predicted electric field at the epidermis was uniform (edge effect was eliminated) when the hair follicle/sweat gland was assigned saline conductivity (conductive), whereas when the hair follicles/sweat gland was assigned hair conductivity (resistive than epidermis), the electric field around the electrode perimeter was not uniform (high electric field around the electrode perimeter) (Gomez-Tames et al., 2016).

We previously developed a multi-layer skin model (in Aim 2) without ultrastructures to predict skin heating during tDCS (Khadka et al., 2018c). This model predicted a non-uniform temperature change across different locations under the sponge pad for few minutes after the onset of stimulation. However, near the end time of stimulation (t =20 min), the temperature change across different locations were uniform, suggesting that model match experimental distribution of

temperature only near the end of stimulation. The multi-layer skin model predicted ~ 0.38 OC temperature increase due to joule heat (the difference between peak temperature in the active case compared to no-stimulation (t=20 min) which is less than the experimental measurement of ~1.3 OC (t=20 min)). We expect that adding skin ultrastructures such as hair follicles, sweat glands, and blood vessels will increase uniformity of temperature predicted at the surface of the skin during the entire stimulation period- consistent with the experimental measurement of skin temperature.

In our prior study on tDCS-induced skin reddening profile, we hypothesized that skin reddening (erythema) profile matches local current density profile predicted by the skin model. However, the experimental skin reddening profile did not match the model predicted local current density profile (skin reddening was diffused, not concentrated around the electrode perimeter). Therefore, we proposed an alternative hypothesis that experimental skin current density is indeed (relatively) uniform, and the homogeneous/multi-layer skin prediction is incorrect. In order to address this possibility, we need to model multi-layer skin with additional ultra-structures.

To this end, we will develop the first high-resolution anatomically realistic and detailed skin model accounting complex tissue layer, ultrastructures, and their physiological electrical properties, to predict current flow pattern through the skin layers and address whether cutaneous adverse events such as skin reddening or skin heating aligns with the experiment.

4.3. Methods

4.3.1. Computational Model and Solution Method

a. Skin anatomy

Skin is a complex mosaic layer of tissues uniformly perforated by sweat ducts and hair follicles with different characteristics (Panescu et al., 1993). Epidermis, the outermost layer of the

skin, overlays the dermis and consists of predominantly keratin cells (dead cells). Epidermis thickness ranges from 50 - 150 μm and has a greater density of sweat glands (Kolarsick et al., 2011; Yousef and Sharma, 2018). Sweat ducts are filled with sweat which has an electrical conductivity equivalent to 0.1 - 0.4 % saline solution (Suchi, 1955). The density of sweat glands varies across different skin surfaces (for example, on the forearm: 160 /cm^2 ; on the palmer and planter surfaces of the hand and feet: ~ 370 /cm^2) (Edelberg, 1977; Tregear, 1966). The most superficial layer of the epidermis is stratum corneum (10-15 μm thickness) which is relatively a poor conductor of electricity (Yamamoto and Yamamoto, 1976). Dermis is the immediate layer following epidermis and contains living cells with greater blood vessels density that provide nutrition to the skin and maintain thermoregulation (Luna et al., 2015). The remaining tissue layer of the skin is subcutaneous and it consists of fat, adipose tissue, connective tissues, and muscles (Kolarsick et al., 2011; Yousef and Sharma, 2018).

We modelled three variations of skin model namely basic (homogeneous), intermediate (multi-layer with or without ultrastructures), and advanced (high-resolution with realistic anatomy). The basic skin model, like the prior skin model (Khadka et al., 2018b; Kronberg and Bikson, 2012; Minhas et al., 2011; Miranda et al., 2006; Saturnino et al., 2015), is a homogeneous block representing combined mass of the skin tissues. The intermediate model, which is already developed in Aim 2, captures the common skin multi-layers (epidermis, dermis, and subcutaneous fat). We assessed the role of the skin ultrastructures by successively adding moderately-realistic (solid cylinders) hair follicles (diameter: 1 mm), sweat glands (diameter: 1 mm), and blood vessels (diameter: 10 mm) into the multi-layer skin model. Finally, based on the prediction from the multi-layer skin with non-realistic ultrastructures, we developed a high-resolution anatomically realistic and detailed skin model. The anatomical shape (mosaic pattern, folding, and ridge patterns (mainly

in stratum corneum or epidermis)), tissue dimensions (thickness and diameter), and densities of hair follicles, sweat glands, and blood vessels were based on the prior cadaver study (Kolarsick et al., 2011; Yousef and Sharma, 2018) and imaging data (Hussain et al., 2017; Mogensen et al., 2009; Olsen et al., 2015; Welzel, 2001). Specifically, the thickness of the epidermis, dermis, and fat were 0.1 mm, 2 mm, and 4 mm, respectively. The diameter of the hair follicles and sweat glands were 0.2 mm and 0.05 mm, with a spatial density of 1-2 per cm^2 for the both ultrastructures. We only modeled the lumen of the blood vessels. The diameter of the blood vessel was 0.12 mm and the intercapillary distance was 50 µm. The location of hair follicles and sweat glands were allocated arbitrarily.

b. Model construction and computational method

All variations of the skin models were modeled as computer-aided design (CAD) files in SolidWorks (Dassault Systemes Americas Corp., MA, USA) and imported into Simpleware (Synopsys, CA, USA) to generate an adaptive tetrahedral mesh using a built-in voxel-based meshing algorithm. The models were refined to a finer mesh density until additional refinement produced less than 1% difference in voltage at the surface of the skin. The resulting models consisted of > 6 million, >28 million, and > 70 million tetrahedral elements for the homogeneous, multi-layer with or without moderately realistic ultrastructures, and the high-resolution skin models, respectively. The models were imported into COMSOL Multiphysics 5.1 (COMSOL Inc., MA, USA) to computationally solve the FEM under steady-state assumption. Respective isotropic electrical conductivities (including variations) were assigned to each model domain as: epidermis: 0.465 S/m, 0.12 S/m, or 1.05×10^{-5} S/m; dermis: 0.23 S/m; and subcutaneous (fat): 2.0×10^{-4} S/m; hair follicles: 1.65×10^{-5} S/m; sweat gland: 1.4 S/m; and blood vessels: 0.7 S/m (A. Datta et al., 2009; Duck, 1990; Gabriel et al., 1996a; Gomez-Tames et al., 2016; Khadka et al., 2018b; Pavšelj

et al., 2007; Torvi and Dale, 1994; Wagner et al., 2007; Wake et al., 2016; Werner and Buse, 1988; Wilson and Spence, 1988b; Yamamoto and Yamamoto, 1976). For the boundary conditions, a static inward normal current density (J_{norm}) corresponding to 1 mA DC was applied through the anode sponge (σ = 1.4 S/m) positioned dorsal to the skin voxel while the ventral surface of the skin voxel was grounded, with the remaining external boundaries electrically insulated. Laplace equation ($\nabla(\sigma\nabla V) = 0$) for voltage (and in turn electric field and current density) was applied and solved as the field equations to determine the current densities at different skin layers and ultrastructures. The role of detailed anatomical structures in transcutaneous current flow was assessed based on the model predictions.

4.4. Results

4.4.1. Current flow in a homogeneous skin with varied conductivities

To understand the role of physiological electrical properties of skin in current flow pattern, we first modeled a homogeneous skin model with varied electrical conductivities (Fig. 8A1). We considered three electrical conductivities of skin- 1) resistive ($\sigma = 1.05 \times 10^{-5}$ S/m, Fig. 8A2a); 2) moderately resistive (σ = 0.12 S/m, Fig. 8A2b); and 3) conductive (σ = 0.465 S/m, Fig. 8A2c) (A. Datta et al., 2009; Kessler et al., 2013; Leite et al., 2018; Truong et al., 2013). The first two conductivity values were averaged based on prior literature values (Çetingül and Herman, 2010; Gomez-Tames et al., 2016; Hodson et al., 1989a; Hua et al., 1993; Khadka et al., 2018c; Panescu et al., 1994; Pavšelj et al., 2007; Sha et al., 2008; Torvi and Dale, 1994; Wilson and Spence, 1988b). Models were constructed such that current density was insensitive to the modeled tissue exterior boundary size (see Methods). We quantified the distribution of current density profile diagonally from edge-to-edge at the surface of the skin by normalizing the local current density to

the peak current density (at the edges) (Fig. 8B1). Compared to our prior model prediction, the peak current density predicted by the moderately resistive skin and the resistive skin was ~ 8 % and ~ 11% lower (Fig. 8A2a, A2b, A2c). However, all models predicted higher current concentration around the edges.

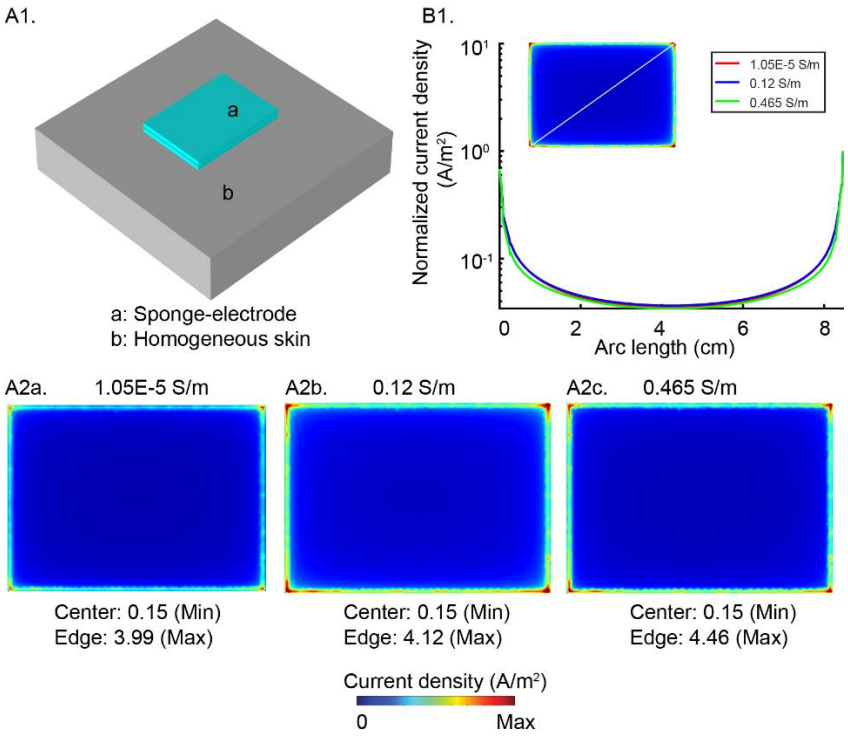

Figure 8: Homogenous skin model and current flow. (A) Illustration of homogeneous skin model with conventional tDCS electrode. (B1) Diagonal (edge-to-edge) current density normalized to the current density at the edge for 1.05×10^{-5} S/m, 0.12 S/m, and 0.465 S/m (color coded). Current density plots for the three variants of skin electrical conductivity (A2a, A2b, and A2c). Current density across the simulations were higher at the edges.

4.4.2. Role of skin multi-layers in current flow

Simplistic homogenous skin model with varied conductivities did not address the current concentration at the electrode edges. Therefore, we used the multi-layer skin model from Aim 2

and predicted the role of multi-layers in current flow pattern through the skin (Fig. 9A1). We compared the model prediction by simulating two epidermis resistivities (resistive ($\sigma = 1.05 \times 10^{-5}$ S/m) and moderately resistive ($\sigma = 0.12$ S/m)), and standard dermis and fat conductivities (dermis: $\sigma = 0.12$ S/m; fat: $\sigma = 2 \times 10^{-4}$ S/m). The resistive epidermis (Fig. 9B1, B2, B3) and moderately resistive epidermis (Fig. 9C1, C2, C3) models predicted higher current density around the electrode perimeter in the epidermis compared to the center (~ 2x and ~ 6x), however, the magnitude of the peak current density was significantly lower than the homogeneous model (0.42 A/m^2 vs 4.46 A/m^2 and 0.77 A/m^2 vs 4.46 A/m^2). In the dermis layer, the current density was still higher at the edges for both resistivity models, however at the fat layer, the current density edge effect was eliminated (Fig. 9A2, B2, B3, C2, C3).

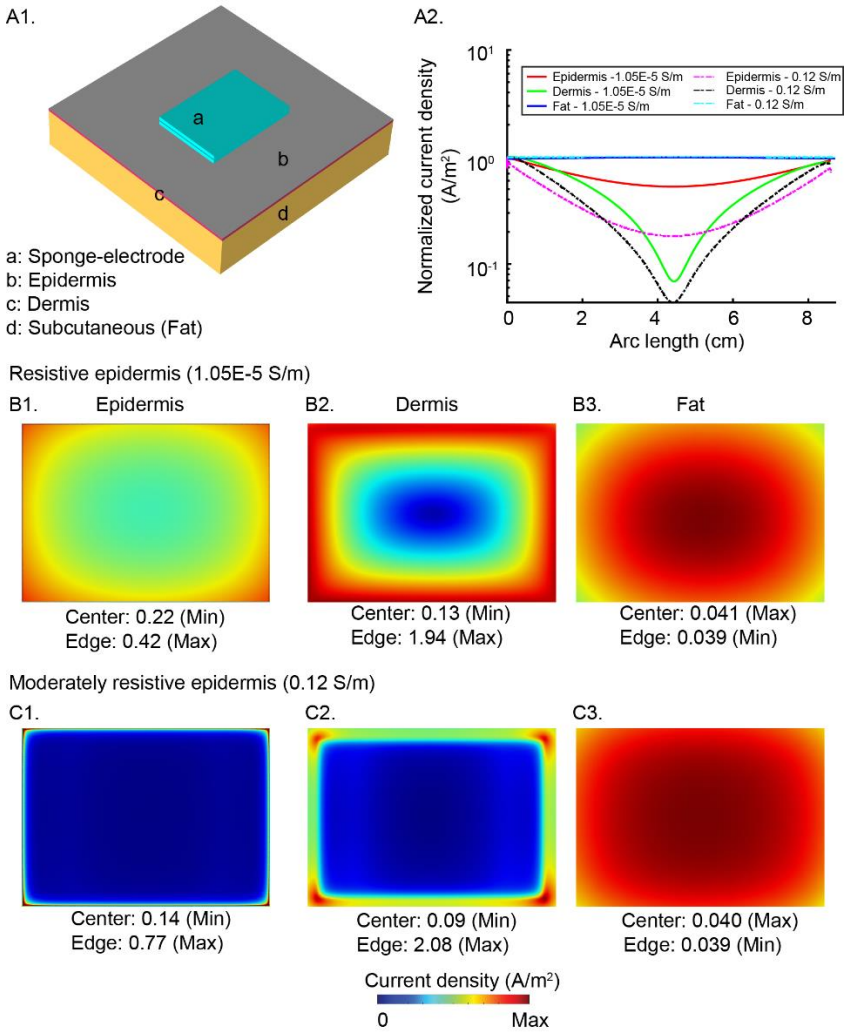

Figure 9: Multi-layer skin model and current flow. (A1) Illustration of a multi-layer skin model (epidermis, dermis, and fat). (B1, B2, B3) and (C1, C2, C3) represent predicted current density at the surface of epidermis, dermis, and fat for resistive and moderately resistive epidermis. (A2) shows normalized diagonal current density distribution. Compared to the homogeneous skin model, the peak current density at the epidermis was relatively lower in both variant of resistive epidermis. Current concentration was higher around the edges in epidermis and dermis, but in the fat layer, it was comparable.

Furthermore, we conducted an exploratory sensitivity analysis in the multi-layer skin model using different combinations of electrical conductivities for the multi-layers to search for the best possible conductivities combination that results in a prediction of a uniform current density

at the surface of the skin (epidermis). We simulated ~ 65 different combinations of electrical conductivities of epidermis, dermis, and fat, and 17 combinations resulted in a prediction of a uniform current density profile at the epidermis (Fig. 10). The normalized current density profile across different tissue layers were comparable in the 17 conductivity combinations. This sensitivity analysis concluded that increasing the epidermis resistivity and decreasing the dermis resistivity results in a uniform current density prediction at the surface of skin.

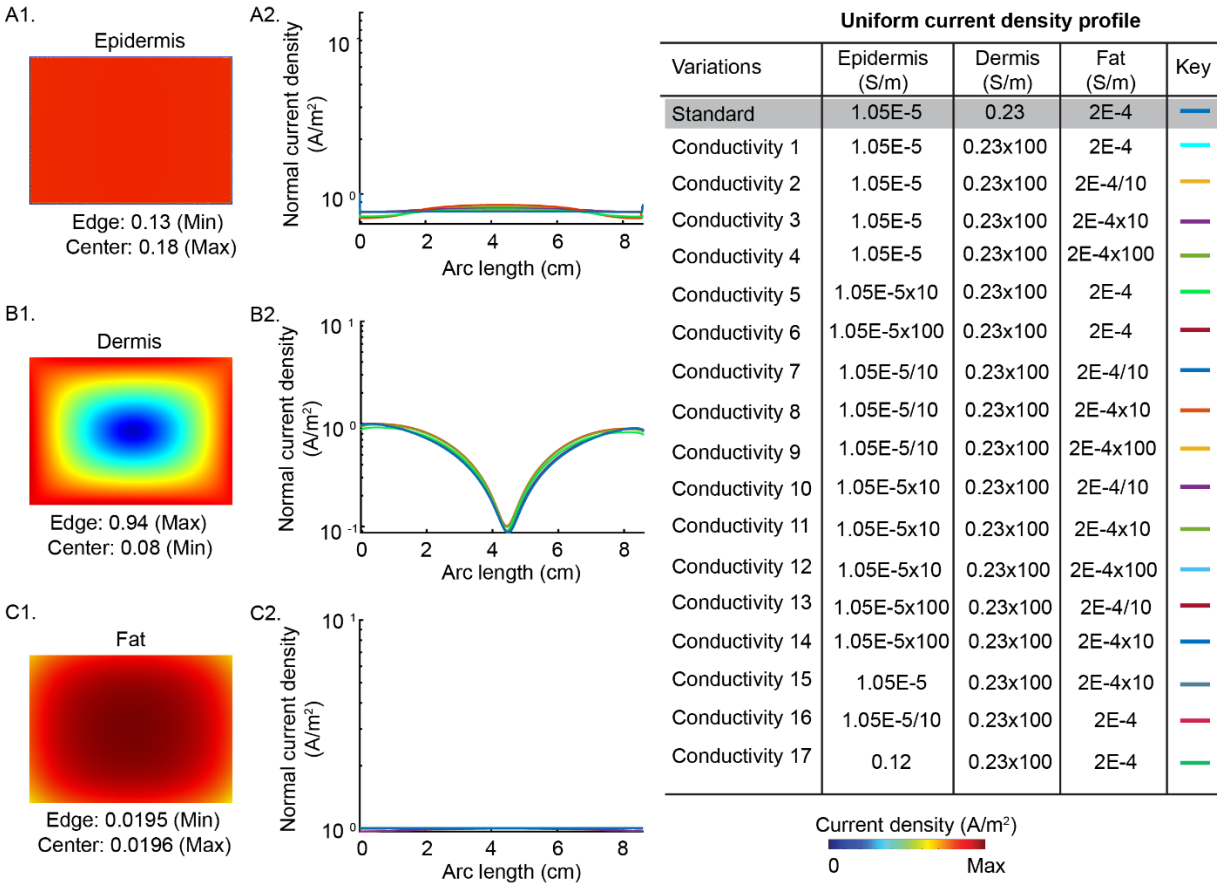

Uniform current density profile

Variations	Epidermis (S/m)	Dermis (S/m)	Fat (S/m)	Key
Standard	1.05E-5	0.23	2E-4	
Conductivity 1	1.05E-5	0.23x100	2E-4	
Conductivity 2	1.05E-5	0.23x100	2E-4/10	
Conductivity 3	1.05E-5	0.23x100	2E-4x10	
Conductivity 4	1.05E-5	0.23x100	2E-4x100	
Conductivity 5	1.05E-5x10	0.23x100	2E-4	
Conductivity 6	1.05E-5x100	0.23x100	2E-4	
Conductivity 7	1.05E-5/10	0.23x100	2E-4/10	
Conductivity 8	1.05E-5/10	0.23x100	2E-4x10	
Conductivity 9	1.05E-5/10	0.23x100	2E-4x100	
Conductivity 10	1.05E-5x10	0.23x100	2E-4/10	
Conductivity 11	1.05E-5x10	0.23x100	2E-4x10	
Conductivity 12	1.05E-5x10	0.23x100	2E-4x100	
Conductivity 13	1.05E-5x100	0.23x100	2E-4/10	
Conductivity 14	1.05E-5x100	0.23x100	2E-4x10	
Conductivity 15	1.05E-5	0.23x100	2E-4x10	
Conductivity 16	1.05E-5/10	0.23x100	2E-4	
Conductivity 17	0.12	0.23x100	2E-4	

Figure 10: Sensitivity analysis on electrical conductivities of multi-layers that result a uniform current density profile prediction at the skin surface. The 17 variations of conductivity combinations (out of 65) of multi-layer skin model resulted in a uniform current density at the epidermis.

4.4.3. Role of skin multi-layers and ultrastructures in current flow

We analyzed the role of hair follicles, sweat glands, and blood vessels in current flow by successively adding each ultrastructure into the multi-layer skin model. Skin ultrastructures were modeled as a solid cylinder with moderately-realistic dimensions (diameter of sweat gland and hair follicle: 1 mm, and blood vessels: 10 mm). In this and the remaining other analysis, we used the standard resistive epidermis (1.05×10^{-5} S/m) and standard dermis (0.12 S/m) and fat (2×10^{-4} S/m) conductivities. The current densities at the surface of epidermis, dermis, and fat, and across the ultrastructures were compared across the model variations.

The addition of only hair follicles (Fig. 11D1, D2, D3) into the multi-layer skin model resulted in the prediction of higher current density at the edges of epidermis and dermis, but it was uniform at the fat. We also observed current concentration around the hair follicles (not across the hair follicles) because hair follicles act as a resistive pathway ($\sigma = 1.6 \times 10^{-5}$ S/m). The addition of sweat glands (σ =1.4 S/m) (Fig. 11E1, E2, E3) resulted in the prediction of peak current density around the sweat glands in both the epidermis and dermis. These current density hotspots were consistent (uniform) across the sweat glands, both near and far from the electrode edges. At the fat layer, the current density was uniform. Further addition of only blood vessels into the multi-layer skin model resulted in the prediction of higher current density around the edges in the epidermis and upper dermis. However, at the lower dermis and fat, current density was uniform across the blood vessels under the electrode, both near and far from the electrode edges. The normalized current density plots show diagonal distribution of current density (edge-to-edge).

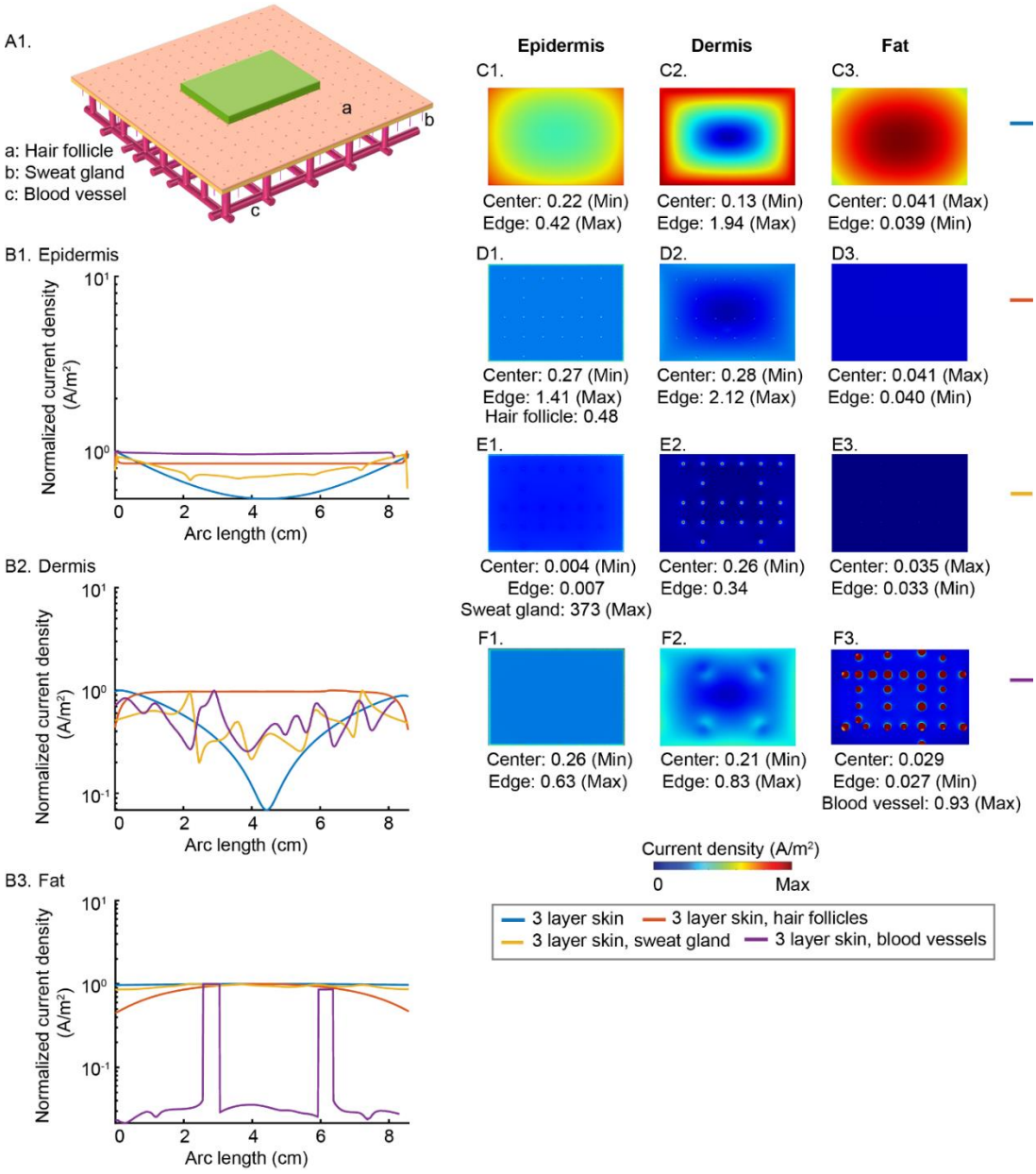

Figure 11: Successive addition of non-realistic skin ultrastructures (hair follicles, sweat glands, and blood vessels) into the multi-layer skin model. (A1) Illustration of skin model with sweat glands, hair follicles, and blood vessels. (B1, B2, B3) shows normalized current density distribution at the surface of epidermis ($\sigma = 1.05 \times 10^{-5}$ S/m), dermis ($\sigma = 0.12$ S/m), and fat ($\sigma = 2 \times 10^{-4}$ S/m) for different model variations. (C1, C2, C3) shows current density plots for multi-layer skin model without ultrastructures. (D1,

D2, D3) represents current density prediction with the addition of only hair follicles, (E1, E2, E3) with the addition of only sweat glands, and (F1, F2, F3) with the addition of only blood vessels. Sweat glands and blood vessels provides conductive pathway for transcutaneous current flow to deeper skin layers, reflected by uniform current density across them.

4.4.4. Role of anatomically realistic and detailed skin multi-layers and ultrastructures in current flow

The multi-layer skin model with moderately-realistic ultrastructures resulted in the prediction of different current flow pattern (in some cases, higher current density across the sweat glands in the epidermis, and uniform current density across the blood vessels in the lower dermis and fat) compared to the multi-layer skin model, suggesting that ultrastructures have profound effect in cutaneous current flow. Therefore, based on these predictions, we developed the first high-resolution anatomically realistic and detailed skin model to assess how the realistic tissue layers and ultrastructures fundamentally change current flow pattern depending upon the parameters.

We simulated the realistic skin model with four variations of electrical conductivities of the epidermis and dermis with the goal of predicting a uniform current density at the surface of the skin. With the moderately resistive epidermis (0.12 S/m) and dermis (0.23 S/m) conductivities, the predicted current density was higher at the edges in the epidermis, similar to the prediction of homogeneous model or intermediate model. The current concentration was still higher at the edges compared to the center in the dermis, however, in the fat, there was no current density edge effects (Fig. 12 B1). The resistive epidermis and 100x conductive dermis model predicted peak current density across the sweat glands in the epidermis (3.5 A/m^2). The current density was still higher across the sweat glands in the dermis, however at the fat layer, current density profile was uniform

(Fig. 12B2). In the resistive epidermis and dermis (/100) model, the peak current density was across the sweat glands in the epidermis and dermis layer. In the fat layer, current density was localized at the blood vessels (Fig. 12B3). In the resistive epidermis and standard dermis conductivity model, the current density was higher across the sweat glands in the epidermis and dermis. In the fat layer, current density was mainly concentrated across the blood vessels (Fig. 12B4). The normalized current density profiles at the epidermis was comparable for all the resistive epidermis simulation condition (Fig. 12C1) except for the conductive epidermis condition (Fig. 12B1). Note that the fluctuations in current density at the epidermis and dermis are due to the mosaic morphology of epidermis and dermis, and the presence of the sweat glands and blood vessels along the current density trajectory (current density is higher across sweat gland and blood vessel) (Fig. 12C1, C2). Overall, the results emphasize that complex tissue layers and ultrastructures of the skin can fundamentally change the current flow pattern depending upon the electrical conductivities.

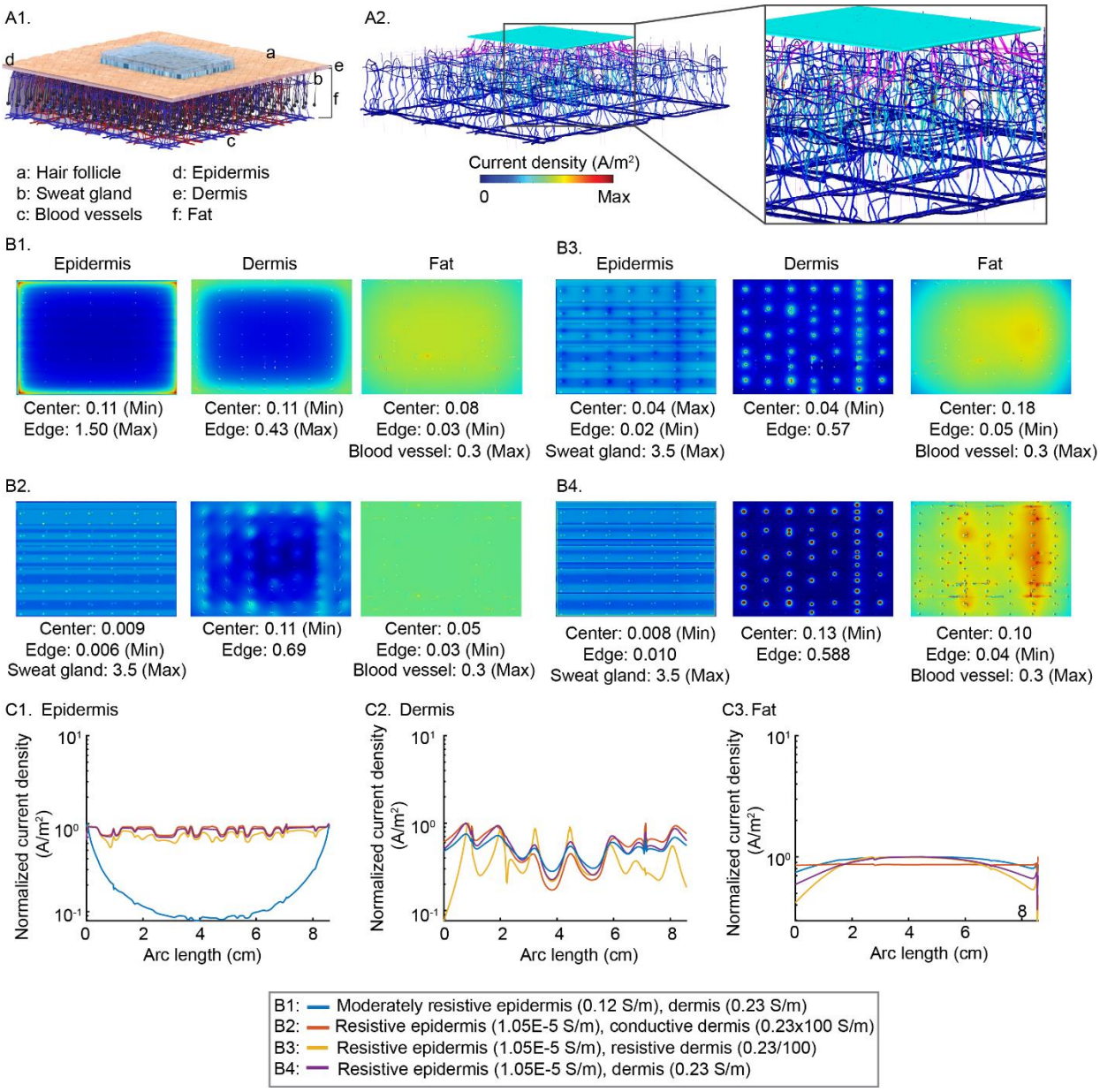

Figure 12: High-resolution anatomically realistic and detailed skin model and current flow prediction. (A1) Illustration of the realistic skin model with detailed skin layers (with mosaic morphology), hair follicles, sweat glands, and blood vessels. (A2) current flow from electrode to deeper tissues with inset showing current density streamlines through the blood vessels and the sweat glands. (B1, B2, B3, B4) show predicted current density at the epidermis, dermis, and fat under varied epidermis and dermis electrical properties. B2, B3, and B4 modeling conditions produced a uniform current density at the surface of epidermis compared to the B1 condition. The sweat gland and blood vessels provide a conductive pathway

for the current flow to deeper tissues (current density hotspot around sweat gland and blood vessels). (C1, C2, C3) shows normalized current density profile at the epidermis, dermis, and fat, respectively. Noticeable fluctuations in current density at the epidermis and dermis emphasizes the influence of skin anatomy and ultrastructures in skin current flow pattern.

4.5. Discussion

Prior studies, including through computational modeling studies have well established that during electrical stimulation, current distribution is not uniform at the skin surface, with high current density at the electrode edges (Miranda et al., 2006; Opitz et al., 2015). Higher current density at the electrode edges is generally considered undesirable for safety reasons (especially for implanted electrodes (Merrill et al., 2005); and may increase sensation during transdermal electrical stimulation. Note that any subsequent current dispersion across deeper tissues results in no evidence of electrode-edge related current concentrations at the brain during transcranial electrical stimulation (Datta et al., 2009; Miranda et al., 2006; Datta et al., 2009). Prior efforts on strategies for normalizing current distribution at the electrode-skin interface (skin) have focused on electrode design (shape and/material)(Gilad et al., 2007; Krasteva and Papazov, 2002; Minhas et al., 2010).

Here, we modeled three variants of skin models- 1) homogeneous (Basic); 2) multi-layer (Intermedia); and 3) high-resolution (Advanced) to analyze the role of skin multi-layers and ultrastructures in uniformly dispersing current through the skin. Consistent with the previous modeling studies, the rectangular electrode produced higher electrode edges in the homogeneous skin model- moderately lower current concentration with the resistive skin conductivity compared to our standard skin conductivity (Fig. 8). We further implemented the multi-layer skin model previously developed in Aim 2 to predict the current flow pattern across the tissue layers. The

addition of multi-layers significantly lowered the current concentration at the electrode-edges, lower for the resistive epidermis (1.05 $x10^{-5}$ S/m) than the moderately resistive epidermis (0.12 S/m) (Fig. 9). A broader parametric sweep through different conductivities combination concluded that resistive epidermis and conductive dermis results in a uniform current distribution at the electrode-skin interface. Inhomogeneity and anisotropy within the skin (such as sweat glands, hair follicles) plays an important role in current dispersion from the skin surface to deeper tissues (Gomez-Tames et al., 2016; Piérard-Franchimont et al., 2016; Sha et al., 2008; Suchi, 1955). We modelled the multi-layer skin (resistive epidermis) with the non-realistic (cylindrical) hair follicle, sweat gland, and blood vessels to assess their role in current distribution. The model prediction suggested that sweat glands and blood vessels act as conductive pathway for current dispersion to deeper tissues and the hot spots of current density around the sweat glands and blood vessels are the region of susceptibility but not the electrode edges. Finally, we developed the first high-resolution anatomically detailed skin model incorporating mosaic epidermis morphology, realistic vasculature, hair follicles, and sweat glands, which predicted that depending upon parameters and detailed anatomy, the current flow through the skin is significantly altered.

Prior simplistic models lack relevant details of skin structures and thus they did not align with experimental findings such as skin reddening and skin heating. Adding details resulted in the predictions of current flow patterns that are consistent with the experimental observations of skin reddening and heating (uniform profile under the sponge pad). The addition of sweat glands removes current concentration at the electrode edges and the addition of blood vessels uniformly distributes current density across the modeled vasculature under the electrode. We considered range of model details and parameters and could not conclude the “ideal” model parameter. However, in the real skin, the ultrastructure and the multilayers are present and incorporating these

details will address the experimental observations of reddening (uniform current flow dilates blood vessels and causes vascular flare or blood flow related skin reddening (Dusch et al., 2009, 2007)). Since the addition of sweat glands and blood vessels into the multi-layer skin model eliminated or reduced current density edge effect, we expect that a bioheat model of the realistic skin model would increase the uniformity of predicted temperature at the surface of the skin. Moreover, these ultrastructures may increase joule heat by producing local hotspots of current to reconcile the predicted temperature with the experimental measurement of temperature rise (Khadka et al., 2018c).

In conclusion, it is important to emphasize that skin needs to be empirically modeled to address the current flow pattern through the skin and explain the experimental findings of burns, skin reddening, or cutaneous sensations such as burning sensation. Though prior efforts outline the need to optimize and refine current technology and protocols in tDCS to produce a uniform current distribution, without appropriately modeling the skin, these technologies cannot alone address current flow and rapid prototype testing.

Appendix 1: Methods for Specific Electrode Resistance Measurement during Transcranial Direct Current Stimulation

1.1. Outline

This Appendix describes a novel method to isolate individual electrode resistance during tDCS by using a super-position of direct current with a test-signal (low-intensity and low frequency sinusoids with electrode-specific frequencies) and a sentinel electrode (not used for DC). A version of this study has been published (Khadka et al., 2015a). We concluded that a sentinel electrode is required to isolate an electrode resistance in a two-electrode or multi-electrode system where cross talk aggravated with electrode proximity and resistance, mismatches in multi-electrode resistance tracking and could be corrected using the proposed approaches, and a test signal can predict DC electrode resistance since unique test frequencies can be used at each tDCS electrode for any number of stimulating channels.

1.2. Introduction

Transcranial Direct Current Stimulation (tDCS) is investigated to treat a range of neuropsychiatric disorders, for rehabilitation, and for altering cognitive performance (Brunoni et al., 2012; Nitsche et al., 2008). When standard protocols are followed, tDCS is well tolerated with common adverse events limited to transient skin sensation and erythema. When established protocols are not followed, tDCS can produce significant skin irritation. Given that skin-sensation (Dundas et al., 2007b; Minhas et al., 2011; Turi et al., 2014) and skin irritation are the primary risks of tDCS (Poreisz et al., 2007; Shiozawa et al., 2013), proper electrode preparation and then monitoring of electrode resistance are important to ensure the stimulation is reproducible and well tolerated (as well as sham reliability in clinical trials). The monitoring of electrode resistance before and during tDCS is considered important for tolerability and safety (DaSilva et al., 2011;

Merrill et al., 2005; Nitsche et al., 2008), where an unusually high electrode resistance is indicative of undesired electrochemical changes (Minhas et al., 2010) or poor skin contact conditions. Yet, conventional methods to monitor electrode resistance are flawed conceptually and technically.

"Electrode resistance" during tDCS in fact reflects an aggregate metric of conditions in the electrodes (e.g. over-potential; (Merrill et al., 2005)) and skin (see discussion for terminology). Resistance is conventionally measured between two electrodes by applying a test current before tDCS or measuring voltage during tDCS and dividing the voltage by the current (Hahn et al., 2013). While convenient, this method does not distinguish the contribution from each electrode. Non-linear tissue impedance and tissue generated potentials, themselves a function of the applied current, also confound measurement. Moreover, when multiple electrodes are used (as in HD-tDCS) the problem is aggravated with cross talk across electrodes making concurrent resistance monitoring unreliable. Here we present the first approach that allows measurement of individual electrode resistance using any number of electrodes or electrode configurations.

The need to combine electrode resistance measurement with current flow for neuromodulation raises special concerns not previously addressed. For example, electrode resistance measurement during EEG is achieved by testing individual pairs of electrodes sequentially (Ferree et al., 2001; Kappenman and Luck, 2010), such that at any given instant only one pair is activated. While this approach could be applied prior to tDCS, during tDCS all electrodes need to be active for neuromodulation. A potential solution is a super-position of direct current stimulation with a test-signal; but, to be meaningful, such a test signal should provide information related to DC-resistance of the electrodes. Similarly, in Electrode-Impedance-Tomography (EIT refer to measuring tissue resistance using electrodes, not measuring electrode resistance), electrode pairs can be tested sequentially and independently, and care is taken to avoid

changing or measuring the resistance of electrodes (Gaggero et al., 2012; Grychtol and Adler, 2013; Khan et al., 2013). Continuous direct current is avoided in all these applications because it generates changes in electrode impedance, and it precludes time or frequency multiplexing. Thus, methods for using a low-intensity test signal in combination with direct current stimulation remains to be proposed and tested. Here we validated methodology for monitoring of individual electrode resistance during two or multi-channel tDCS by using a low-intensity low-frequency test signal (sinusoids) with electrode-specific frequencies and an additional sentinel electrode that is not used for direct current stimulation.

1.3. Materials and Methods

1.3.1. Participants

Six healthy volunteers (all male; age range 20-30 years; mean age 22.8 ± 2.4) participated in this study. The experiment was conducted after receiving approval from the CCNY local Ethics Committee and all participants gave written informed consent before participating in the experiment. They were seated in a relaxed position with their stimulated arm on a bench top.

1.3.2. Stimulation

The main input signal superimposed a direct current source (2 mA) with an alternating current source (38 µA and 76 µA pk-pk at 1 Hz, 10 Hz, and 100 Hz) applied on the subjects' arm for 4 min. We aimed to establish a relationship between the DC and the test signal (AC) to predict electrode resistance (as defined in discussion). A sentinel (none DC current carrying) electrode was used to isolate electrode impedance and eliminate tissue resistance contamination from one or more sources. A trapezoidal current input composed of a 30 s test signal (AC, 38 µA or 76 µA) followed by a DC ramp up to 2 mA (30 s duration), a 2 min stimulation phase composed of superimposed AC and DC signal (main input signal), a DC ramp down (30 s), and a post

stimulation test signal (AC, 30 s) was applied through tin electrodes (EASYCAP, Herrsching, Germany) on the subjects' forearm. The LabVIEW (National Instruments, TX, USA) generated voltage signal output from a NI 9263 cDAQ Module (National Instruments (NI), TX, USA) was converted to a constant current through an analog current controller (A-M Systems Analog Stimulus Isolator, WA, USA).

1.3.3. Subject experimental procedures

A combined DC and test-signal was used to stimulate forearms of the six healthy participants under different current amplitudes (38 µA and 76 µA) and frequencies (1 Hz, 10 Hz, and 100 Hz). Prior to simulation, the skin was cleaned with dilute saline. Rubber straps and electrode holders from Soterix Medical Inc. (NY, USA) were secured on the forearm (10.2 cm apart) and uniformly filled with a conductive gel (Signa, NJ, USA). The anode and cathode electrodes were positioned proximal and distal to the hand, respectively, and connected to the analog current isolator/stimulator. Voltage was recorded across the stimulator. A manual switch was placed in series with the circuit to avoid transient current spikes and ensure that the skin impedance doesn't change until the stimulation session begins.

1.3.4. In vitro electrode testing

While conducting in vitro electrodes testing on parafilm sheets, the electrodes were positioned on top of conductive gel (Signa). In case of Type A error and method of correction using a sentinel electrode, 2 mA DC (Source 1 (S1)) was passed through anode and cathode and a test signal (38 µA pk-pk at 10 Hz as Source 2 (S2)) was passed through the anode (shared) and sentinel. Voltage was recorded across sentinel and shared anode. In Type B error and method for correction using sinusoidal test signal, first source (S1) with test signal (38 µA at 10 Hz) superimposed on top of DC (0.5 mA) energized anode1 and cathode1 and a DC current (second

source (S2)) of 2 mA was passed through anode 2 and cathode 2. Voltage across anode 1 and cathode 1 was acquired for this approach.

1.3.5. Data recording and Impedance analysis

Unless otherwise stated, voltage data from stimulation were acquired using NI 9229; an analog input module and Lab VIEW. In experiment where independent current sources were used, data were collected using multi-meters. Acquired voltage signal (Fig. 15A) was first isolated into test signal (sinusoid) voltage using high pass filter (Fig. 15B) and DC signal using low pass filter (Fig. 15E). Specific cut-off frequencies were selected for all stimulation frequencies. Test signal was converted into RMS (root mean squared) voltage (Fig. 15C) and divided by the RMS current to calculate the AC-impedance (Fig. 15D). DC-resistance was determined by dividing DC voltage component by the DC current (Fig. 15F).

1.3.6. Pain analysis

Subjective pain was acceded by asking every participant to rate their pain level during every 30 s of stimulation phase excluding pre and post-stimulation. Participants rated their skin sensation in the scale of 1-10; visual analogue scale (VAS) (Poreisz et al., 2007).

1.3.7. Statistical analysis

The data were evaluated using MATLAB (MA, USA). Two-way repeated measures ANOVAs (analysis of variance) were used for each output measures (pain sensation, average voltage and DC-resistance to AC- impedance ratio) with current intensities and frequencies as factors to analyze interactions between the two factors and to account testing within each participant. Critical value < 0.05 was accepted as a statistical difference between groups.

1.4. Results

In the first part of results, we define the problem - which is unrecognized in current tDCS and HD-tDCS - and our proposed solution. This also allows us to identify assumptions of our solution. The second part tests those assumptions experimentally. The third part illustrates the solution through experiment.

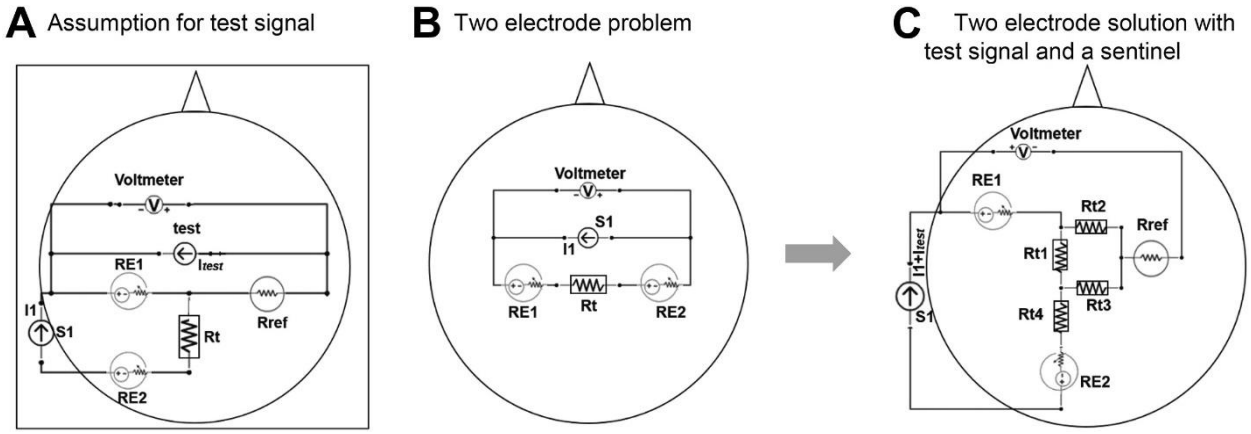

Figure 13. Lumped circuit analysis of transcranial Direct Current Stimulation (tDCS) using two electrodes with an additional sentinel electrode that does not carry direct current. (A) Illustrates our assumption of using a test signal (test) and a sentinel (Rref) to predict DC voltage. This example includes two sources, S1 (DC) and a test AC signal, two active electrodes used for DC simulation: RE1 and RE2, and a sentinel electrode (Rref). We assume that the AC voltage detected across RE1 and Rref can predict the DC voltage (hence DC-resistance) of RE1. (B) Illustrates the need for methodology to detect single electrode resistance changes. The schematic has two electrodes (RE1 & RE2) and a DC source (S1). The resulting voltage drop across these electrodes is function of tissue impedance (Rt) and the resistance of both electrodes. (C) Presents a solution for the problem indicated in (B) based on the assumptions outlined in A, where a sentinel electrode (Rref) is used to selectively monitor an stimulating electrode (in this case RE1) of interest. In this case a single source produced a combined direct current with superimposed test AC signal. And sentinel electrode (not used for DC stimulation) is required, but not additional current sources.

Part 1: Problem Definition, Solution, and Assumptions to be tested

a. The non-triviality of resistance measurement during two electrode tDCS

Fig. 13B is a simplified lumped parameter model of electrode resistance during tDCS. The complete "cell" across which net resistance can be measured (at the output terminals of the stimulator) includes two electrodes and tissue. The stimulator (current source, S1) generates current (I1) across the cell and the resulting voltage is measured (voltmeter) as indicative of electrode resistance. The presence of multiple elements in itself makes it impossible to determine the contributing element to a resistance increase (e.g. is electrode 1, electrode 2, and/or tissue) as shown in the following equation.

$$Vt = I1\ (RE1 + Rt + RE2) \text{ -------- (i)}$$

where the total voltage (Vt) measured across two active electrodes (RE1 & RE2) is found assuming a linear relationship between current I1 and sum of electrodes resistance and tissue impedance (Rt). The matter is further complicated by the complex non-linear impedance of each electrode reflecting the electrochemistry as the electrode surface before and during direct current stimulation (Minhas et al., 2010). For illustration, we simplify this electrode resistance (as defined in discussion) as a voltage source, reflecting electrode over-potential, and a non-linear resistance, reflecting how current application produces a further voltage across the electrode. Tissues (skin, bone, fat, brain, etc.) also offer complex impedances (current and time dependent) and generate potentials, but for convenience are also considered a resistance. Equation (i) is thus not strictly valid. Simplistically, the "resistance" reported during tDCS (see discussion) is the measured voltage (Vt) divided by the applied current (I1). But the voltage measured across the cell, before or during direct current stimulation is not a trivial function of "electrode resistance". For example, the electrode over-potential contributes to Vt and the impedance is itself a function of the amount of current applied (Hahn et al., 2013). Our purpose here is to simply develop a measure to resolve

the voltage across a single resistance (e.g. the voltage across RE1) during two and multi-electrode tDCS.

b. Use of test signal and sentinel electrode

Fig. 13 C illustrates a schematic for our basic solution. The use of a third "sentinel" electrode (Rref) that is not involved in stimulation is common in electrochemical analysis (Michael and Borland, 2007). The potential measured between any given active electrode and the sentinel electrode, reflects only voltage drop across that active electrode and tissue voltage contribution as shown in the equation below:

$$Vt = (I1 + Itest)\left(\frac{Rt1.Rt2}{(Rt1+Rt2+Rt3)} + RE1\right) \quad \text{(ii)}$$

where Rt1, Rt2, and Rt3 are tissue resistances and Vt reflect the voltage drop across RE1. This step in itself enhances the fidelity of electrode resistance measurement by isolating a single electrode. If RE1 is significantly larger than the tissue impedances, then Vt is assumed to largely reflect the impedance of RE1 ($Vt = (I1 + Itest)RE1$). More generally, assuming linear relation, equation (ii) cannot be applied.

Up to this point we have considered application of only direct current and measurement of the resulting voltage. We proposed the addition of a further current ("I*test*" in Fig. 13 C), a low-intensity and frequency test signal that generates a characteristic voltage across the active electrode, which in turn will be a sinusoid component in Vt superimposed on the voltage generated by the direct current stimulation. The central assumption of this report is that this sinusoidal voltage is representative in magnitude of the voltage generated across RE1 by the passage of direct current. This assumption is trivial where one assumes Ohmic current flow. But given the

complexity of the electrode interface, including electrode over-potential, this assumption requires validation.

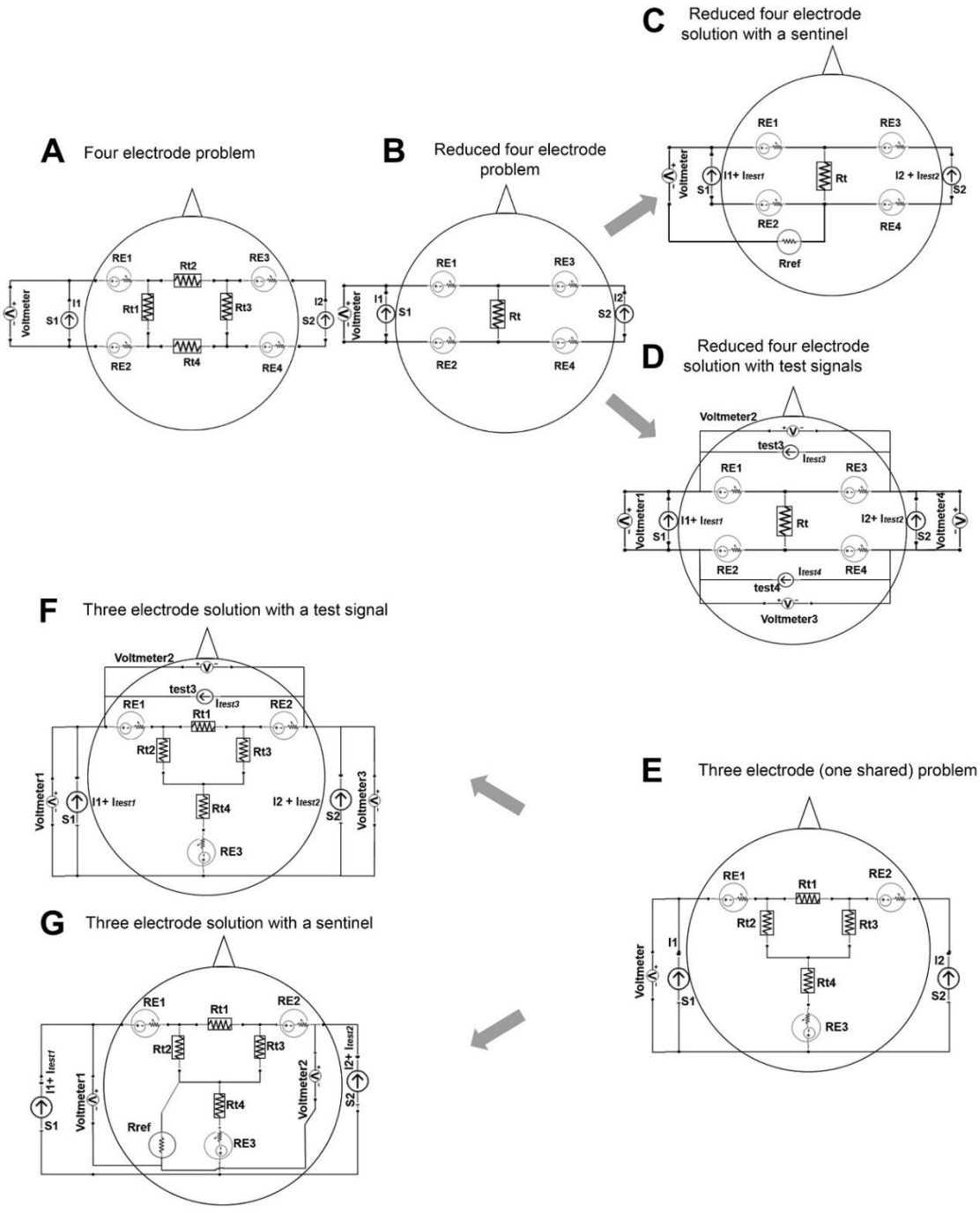

Figure 14. Lumped circuit analysis of transcranial Direct Current Stimulation (tDCS) using four or three DC stimulating electrodes with solutions for electrode resistance tracking solutions using either

an additional sentinel electrode or additional current sources. (A) Representation of a four-electrode arrangement problem which is reduced to a simpler form as shown in (B). (C) First solution for problem in (B) using a sentinel electrode and a test signal superimposed on an existing current source. (D) Second proposed solution with using an additional test current sources but no additional electrodes. (E) Representation of a stimulation montage using three electrodes when there are two independent electrodes (RE1 &RE2) and a common shared electrode (RE3). (F) Illustration of the first solution of problem situation in (E) where a test signal produced by additional current sources are passed across two active electrodes to resolve specific DC-electrode resistance. (G) Another solution of the same problem where a sentinel is used without requiring additional current sources. For all of the cases, confound of tissue resistance is also shown (see text).

Fig. 13 A rephrases the lump-parameter model to clarity this assumption. Passage of DC current (I1) by S1 produces complex over-potential and impedance changes in electrode RE1 and a direct voltage across RE1. This is the "DC impedance" of the electrode, which is the so-called "resistance" of interest in tDCS. Will a sinusoidal current simultaneously passed across RE1, produce a sinusoidal voltage that is related to this direct voltage? At face value, the addition of a test signal does *not* provide more information in a two electrode system, however if this test signal predicts DC resistance of an electrode, it can be leveraged during multi-electrode tDCS, as explained next.

In exploring sinusoid test-signal tracking of DC resistance, we will test a range of frequencies and intensities. And we further will evaluate if the passage of sinusoidal current itself does *not* change the electrical performance of the electrode or skin impedance, as well as that the subject sensation is not a function of test signal intensity or frequency.

c. Further cross talk during resistance measurements in multi-electrode tDCS

Here, we represented two independent current sources (S1 and S2) though this analysis can be extended to any number of electrodes and sources (Fig. 14). In a four electrode example, each current source is connected to distinct two stimulating electrode (RE1, RE2 to S1 & RE3, RE4 to S2; Fig. 14A, 2B, 2C, & 2D) while in the three electrode example (RE1, RE2, RE3), one electrode (RE3) is shared by the stimulation sources (Fig. 14E, 2F, & 2G). Tissue impedance is again represented as multiple lumped parameters for the purpose of illustration (such as Rt, Rt1, Rt2, Rt3, Rt4, etc.). Voltage measurement can be obtained across the current sources (the voltage being produced by the current source accessible at the output leads) or using additional voltmeters and a sentinel electrode (Rref). For each electrode, the electrode potential and non-linear impedance are represented by a single lumped parameter, but we emphasize again these quantities are a complex function of time and current passage.

For two independent sources that do not share electrodes (Fig. 14A), the voltage measured across source S1, is also influenced by the current source S2 and a function of specific tissues impedances. Assuming linearity the voltage across S1 is:

$$Vt = I1\left(RE1 + \frac{Rt1\,(Rt2+Rt3+Rt4)}{(Rt1+Rt2+Rt3+Rt4)} + RE2\right) + I2\left(\frac{Rt3.Rt1}{(Rt1+Rt2+Rt3+Rt4)}\right) \quad \text{(iii)}$$

The degree of cross-talk from S2 to the voltage recording across S1 is a function of tissue resistivities. Depending on polarity, the voltage across S2 may be higher or lower. However, even for tissue resistivities leading to relatively low coupling (e.g. Rt3 << Rt2), a large S2 source (e.g. 2 mA) may contribute significantly to the voltage across a smaller S1 source (e.g. 0.1 mA). By further extension, for a multiple channel system (e.g. 10 sources with 0.2 mA) the voltage measured at any given source may be significantly contaminated by tissue coupling across other sources making “electrode impedance” calculation unreliable.

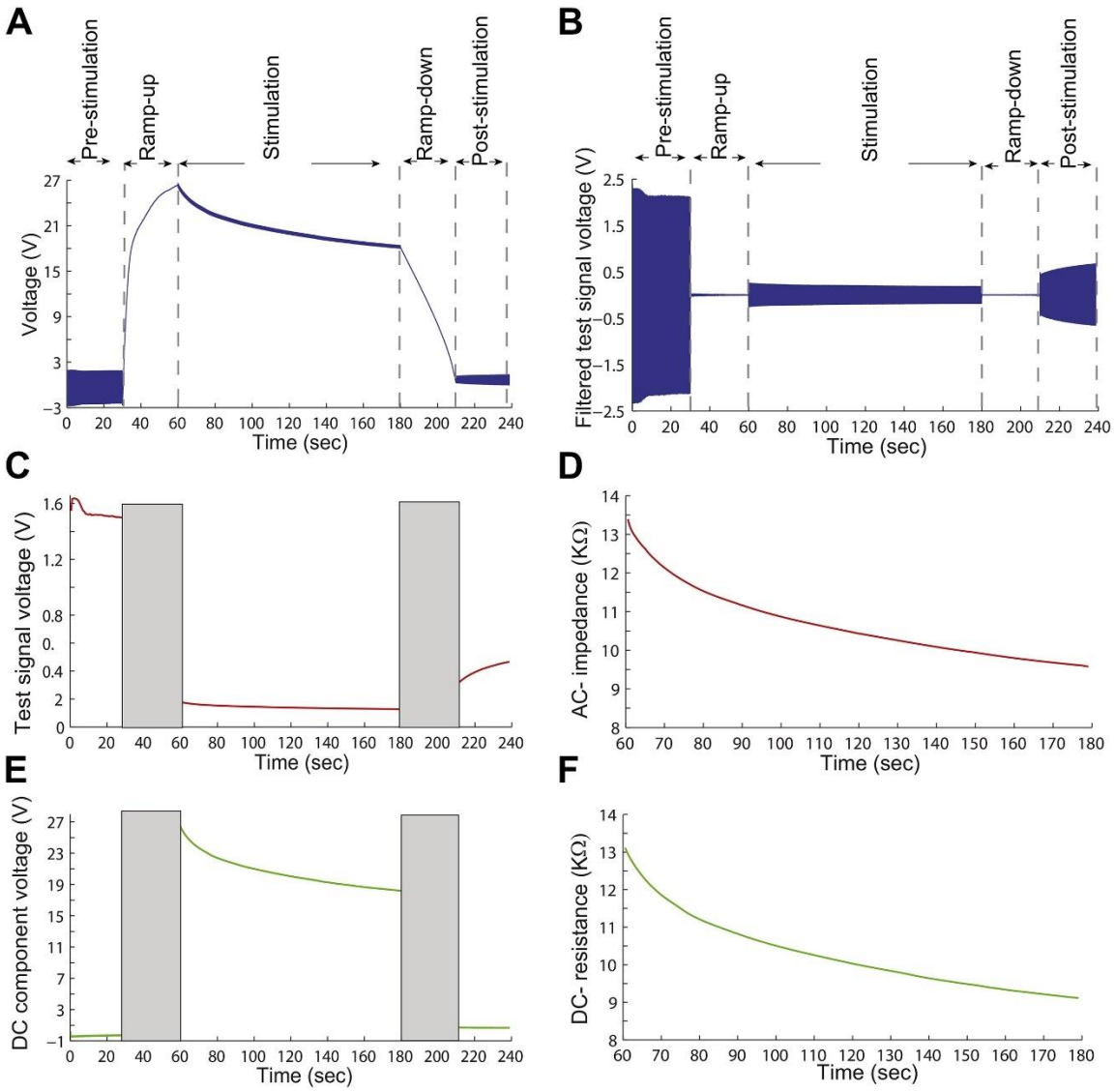

Figure 15. Representative analysis for combined DC resistance and AC-impedance measurement. (A) Voltage signal measured across the electrodes. 2 mA DC current is applied for2 min with an additional ramp up and ramp down across a subject's forearm. A 10 Hz, 38mA test sinusoidal current (pk-pk) is also applied prior, during (superimposed on the DC), and post-stimulation. (B) High pass filtered signal revealing the test signal: AC component. (C) RMS voltage of the AC component. (D) Calculated AC impedance. (E) Low pass (DC component) voltage filtered signal. (F) Calculated DC resistance.

To illustrate our solution, a further simplified four stimulating electrode lumped circuit is shown in Fig. 14B which is governed by the following equation assuming linearity:

$$Vt = I1\,(RE1 + RE2 + Rt) + I2\,(Rt) \quad \text{(iv)}$$

where DC current (I2) from S2, and by extension additional sources, would confound the voltage (Vt) reading across S1.

For the four-electrode example, two solutions that both remove this electrode-cross talk and furthermore allow isolation of single-electrode impedance are shown. The first solution using a test signal and sentinel electrode is shown in Fig. 14C, where the voltmeter (tuned to the frequency of test1) will detect the sinusoid test1, which under the assumptions explained above (illustrated in Fig. 13 A), would predict the DC electrode impedance of RE1. The total voltage across S1 assuming linearity is given by:

$$Vt = (I1 + Itest1)(RE1 + Rt) + (I2 + Itest2)\,Rt \quad \text{(v)}$$

But considering only the test frequency, the contributing voltage will be:

$$Vt\,(test) = Itest1\,(RE1 + Rt) + Itest2(Rt) \quad \text{(vi)}$$

Here, assuming RE1>>Rt, and our overall assumption, provide a measure of single electrode impedance. A similar approach (not shown) can be used to determine the DC electrode resistance of RE3. A test sinusoid signal, test2, can be applied across RE2 and RE3 but with a distinct frequency as test1, such that there is no cross talk across these test signals. The DC electrode impedance of RE3 and RE4 can be measured using a voltmeter across RE3 and RE4 or Rref, where that voltmeter is tuned to the frequency of test2. Some powerful analysis can be obtained from this solution: 1) only one additional electrode is needed (Rref); 2) no additional current sources are needed if a single current source can produce both DC and test signals; 3) as long as Rref does not fail, the system is robust to the failure of any given electrode.

For the four-electrode case, the second solution (Fig. 14D) does not involve the use of a sentinel electrode (no Rref electrode). Here, two additional current sources (test3, and test 4) generate test signals of unique frequencies, with associated voltmeters. Two test signals are also provided with the DC sources (test1 and test 2). A total of four voltmeters (four equations) and four electrodes (four unknowns) provide a substrate for solving for the impedance of each electrode where assuming linearity, the voltage across the S1 voltmeter is given by:

$$Vt = (I1 + Itest1)(RE1 + RE2 + Rt) + (I2 + Itest2)Rt + test3\ (RE1) \quad \text{(vii)}$$

A similar equation can be provided for each voltmeter and, after removing all tissue impendences under the assumption they are smaller than electrode impendences, all solves simultaneously to calculate the impedance of each electrode as:

$$Vt = (I1 + Itest1)(RE1 + RE2) + test3\ (RE1) \quad \text{(viii)}$$

Note that in this solution: 1) no additional electrodes are needed but additional current sources; 2) if any electrode fails completely (source open) it may not be possible to obtain a solution for any of the electrode impedances. The underlying assumption for test signal predicting DC-resistance is still required.

Finally, we considered the case of two current sources (S1 and S2) and three stimulating electrodes (RE1, RE2, RE3) such that one stimulating electrode (RE3) is shared by the two current sources (Fig. 14E). When a stimulating electrode is shared by two sources, two measurements (two voltages) and three key unknowns (three electrode impedances) arise and thus do not allow identification of faulty electrode responsible for any increase in resistance. Assuming linearity, the voltage across S1 is given by:

$$Vt = I1\left[Rt2\frac{Rt1+Rt3}{(Rt1+Rt2+Rt3)} + RE1 + RE3 + Rt4\right] + I2\left(\frac{Rt2.Rt3}{(Rt1+Rt2+Rt3)} + RE3 + Rt4\right) \quad \text{(ix)}$$

Again, if our assumption of electrode resistance being greater than that of tissue impedances is supported, this equation can be further reduced (assuming linearity) to:

$$Vt = I1\,(RE1 + RE3) + I2\,(RE3) \quad \text{(x)}$$

For this case, two solutions are illustrated with a sentinel electrode (Fig. 14G) and without a sentinel but with an extra current source (Fig. 14F). As with the four-electrode case, both solutions allow calculation of individual electrode resistance, but for the solution without a sentinel electrode, an additional test current sources are needed and must be connected across novel combinations of electrodes. For the first solution with the sentinel, the voltmeter across S1 will detect (assuming linearity):

$$Vt = (I1 + Itest1)\left[\frac{Rt2(Rt1+Rt3)}{Rt1+Rt2+Rt3} + RE1\right] + (I2 + Itest2)\left(\frac{Rt2.Rt3}{Rt1+Rt2+Rt3}\right)$$

(xi)

If one assumes RE1 is greater than any tissue resistance, and consider only the test1 frequency, this reduces to

$$Vt\,(test) = Itest1(RE1) \quad \text{(xii)}$$

For the second solution to the three-electrode case with*out* a sentinel, the S1 voltmeter will detect:

$$Vt = (I1 + Itest1)\left[\frac{Rt2(Rt1+Rt3)}{(Rt1+Rt2+Rt3)} + RE1 + RE3 + Rt4\right] + (I2 + Itest2)\left(\frac{Rt2.Rt3}{Rt1+Rt2+Rt3} + RE3 + Rt4\right) + test(RE1) \quad \text{(xiii)}$$

A similar equation can be provided for each voltmeter and, after removing all tissue resistance under the assumption they are smaller than electrode resistance, all can be solved simultaneously.

Part 2: Testing of assumptions, and identification of effective test signals

This section aims at testing the underlying assumptions of the proposed solution (not illustrating its application per se which is left for Part 3). The core assumption to be tested is the tracking of DC-resistance by the AC test signals; several intensities and frequencies are compared. Secondary assumptions include that the selected signals do not confound the application or tolerability of tDCS as indicated by average voltage and subjective pain (Fig. 16). Experiments were conducted on in a parafilm sheet (gel base) and on the forearms of subjects. All participants tolerated the stimulation hence none of the experimental sessions were interrupted.

a. Pain analysis during Stimulation

A two-way repeated measures ANOVA of current intensities (38 µA & 76 µA) and frequencies (1 Hz, 10 Hz, and 100 Hz) during stimulation was conducted. The main effect of current intensities and frequencies on pain sensation was not significant; $F(1, 5) = 2.8$, $p = 0.16$ & $F(2, 10) = 3.3$, $p = 0.08$ as shown in Fig. 16A. The interaction between these two factors was not significant, $F(2, 10) = 0.16$, $p = 0.86$.

b. Average voltage during Stimulation

Average voltage was independent of current intensities and stimulation frequencies, $F(1, 5) = 0.05$, $p = 0.83$ & $F(2, 10) = 0.7$, $p = 0.57$. The interaction was not significant, $F(2, 10) = 0.59$, $p = 0.57$ (Fig. 16B).

c. Comparing DC-resistance from AC-impedance on forearm

DC-resistance to AC-impedance ratio across stimulation frequencies was significantly different, $F(2, 10) = 31.03$, $p = 0.0001$ (Fig. 16C). The resistance ratio was slightly higher at 1 Hz ($DC:AC_{1\ Hz} = 1.14$) compared to that at 10 Hz ($DC:AC_{10\ Hz} = 1.02$) and 100 Hz ($DC:AC_{100\ Hz} = 1.12$).

No significant difference was found at the different current levels, F (1, 5) =1.46, p=0.28. Further analysis of the interaction between current intensities and frequencies was not significant, F (2, 10) =0.21, p=0.82.

d. Error percentage in Predicting Electrode Resistance

The error percentage ([predicted DC-resistance – actual DC-resistance]/actual DC-resistance, where the predicted DC-resistance = DC:AC ratio × actual AC-impedance) in predicting DC-resistance by AC-impedance was -2.56 ± 3.98 (mean ± SD) at 38 µA and -1.27 ± 1.72 at 76 µA (at the onset of the stimulation phase, 60 s), -1.09 ± 4.16 at 38 µA and 0.26 ± 0.34 at 76 µA (120 s after the onset of stimulation), and -0.74 ± 4.48 at 38 µA and 0.71 ± 1.22 at 76 µA (at the end of stimulation, 180 s). The inter-individual variability contributes to an over- or under-estimation of the prediction error as seen in Fig. 17 B1 and Fig. 17 B2.

e. DC-electrode resistance to AC-impedance ratio in gel, comparison with skin

The DC-resistance to AC-impedance ratio in forearm stimulation was found to be higher than that of the *in vitro* test (Wilcoxon rank sum test: $p<0.05$, Fig. 16D). Though interesting, our focus here is on application, so we do not diagnose here the source of this difference between forearm (*in vivo*) and gel (*in vitro*) testing; contribution may include frequency dependence of tissue impedance of tissue, which would decrease AC impedance (Dean et al., 2008), as well as tissue, namely skin, generated potentials (Grimnes et al., 2011) that would increase the DC potential. The precision of prediction (above) is thus specific to the DC- resistance to AC-impedance ratio determined from *in vivo* testing, while the *in vivo* to *in vitro* difference reinforces the complex nature of tissue impedance and the none-triviality of developing an approach to track electrode impedance during tDCS.

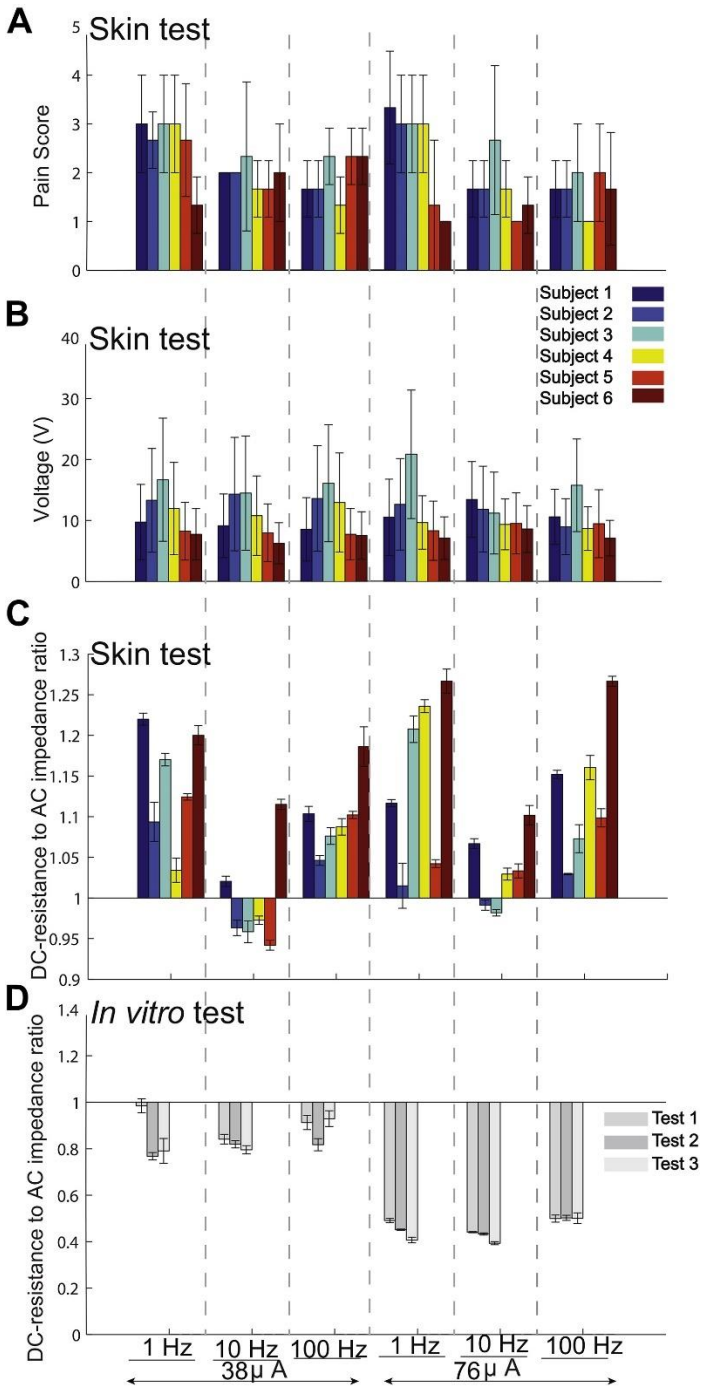

Figure 16. Interaction of AC test signal with electrical performance and subjective sensation. (A) Subjective average pain score, (B) average voltage, (C) average DC-resistance to AC-impedance ratio during forearm testing and (D) average DC-resistance to AC-impedance ratio during in vitro test. Values represent the average during the phase of constant current (excluding ramp up and ramp down). Average

pain scores were based on subjective VAS ratings. Results demonstrate that using AC test signal at different amplitudes and frequencies did not change pain score or the overall impedance trajectory. The averaged DC-resistance to AC-impedance ratio was also consistent (w1.08) across frequencies and intensities. The resistance ratio was found to be lower at 76mA (pk-pk) compared to 38mA (pk-pk) in vitro.

Part 3: Application of solutions in experiment

Using *in vitro* electrode testing, we consider two types of resistance measurement errors and test the correction provided by our invention: *Type A* errors related to cross talk across systems and *Type B* errors identifying failing electrode.

a. Correction of Type A error

Type A error result when a single electrode fails resulting in a voltage increase across the entire two-electrode system. We demonstrated this error and method of correction using three-electrode system (Fig. 18A1 & 18B1), where two electrodes are connected to a DC current source and a test sinusoid is passed between one of the active electrodes (shared) and a third sentinel electrode. This test was carried out with electrodes in conductive gel. We mimicked electrode failure (of the shared electrode) by using a corroded tin electrode and by reducing the contact area of this electrode and the conductive gel after 100 s of stimulation for about 20 s. Likewise, we also demonstrated another electrode failure condition (electrode connected to DC source only) after 145 s for 20 s too. While the measured voltages across the shared electrode and sentinel increased (shown in Fig. 18A1 in terms of DC- resistance), only by inspecting the test signal, it was possible to determine the electrode of interest was failing.

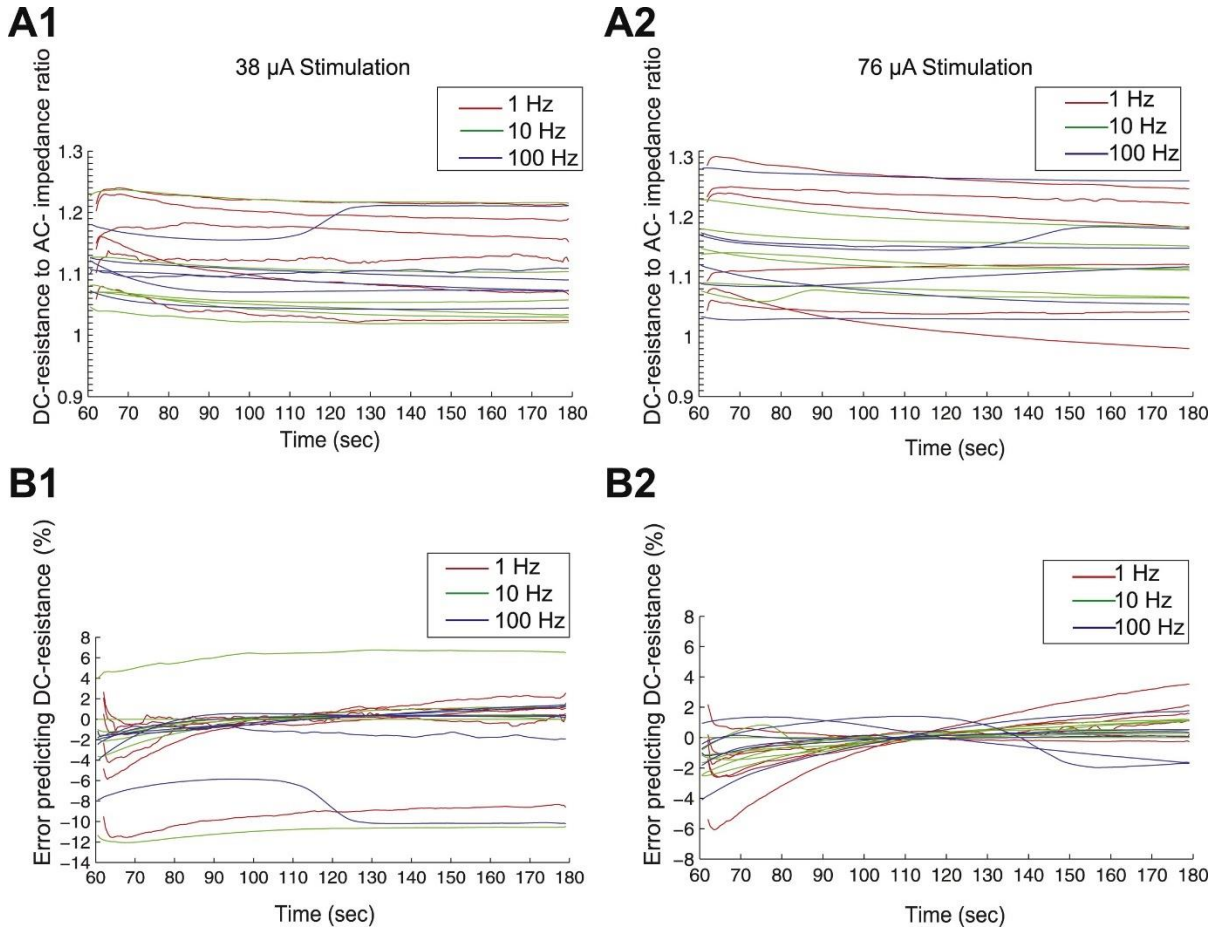

Figure 17. Reliability of predicting DC-resistance by AC-impedance. Average DC-resistance to AC-impedance ratio and error percentage in predicting DC-resistance at 38 mA (A1, B1) and at 76 mA (A2, B2) during forearm stimulation at different stimulation frequencies.

b. Correction of Type B error

Type B error are generated when two current sources are active and one current source produces a voltage that is detected by the other current source resulting in an error in resistance prediction – this error does not require that current source share an electrode when the error voltage is generated across tissue. We demonstrated this error and method for correction using a simple four electrode system (in conductive gel) with two independent current sources connected to four electrodes (Fig. 18A2 & 18B2). One current source (S1) has a superimposed test sinusoid on top

of DC while the other source was a tDCS. The test signal impedance did not change upon the introduction of a second source (Fig. 18B2). In contrast, the DC-impedance sharply increased (Fig. 18A2) as the second source (S2) was turned on (100-149 s) and decreased when S2 was turned off (150 s). Hence, an introduction of a second current source or a faulty electrode in a multi-channel stimulation can result in contaminated electrode impedance. Therefore, a test signal across electrodes can precisely predict DC-resistance correcting for *Type B* error.

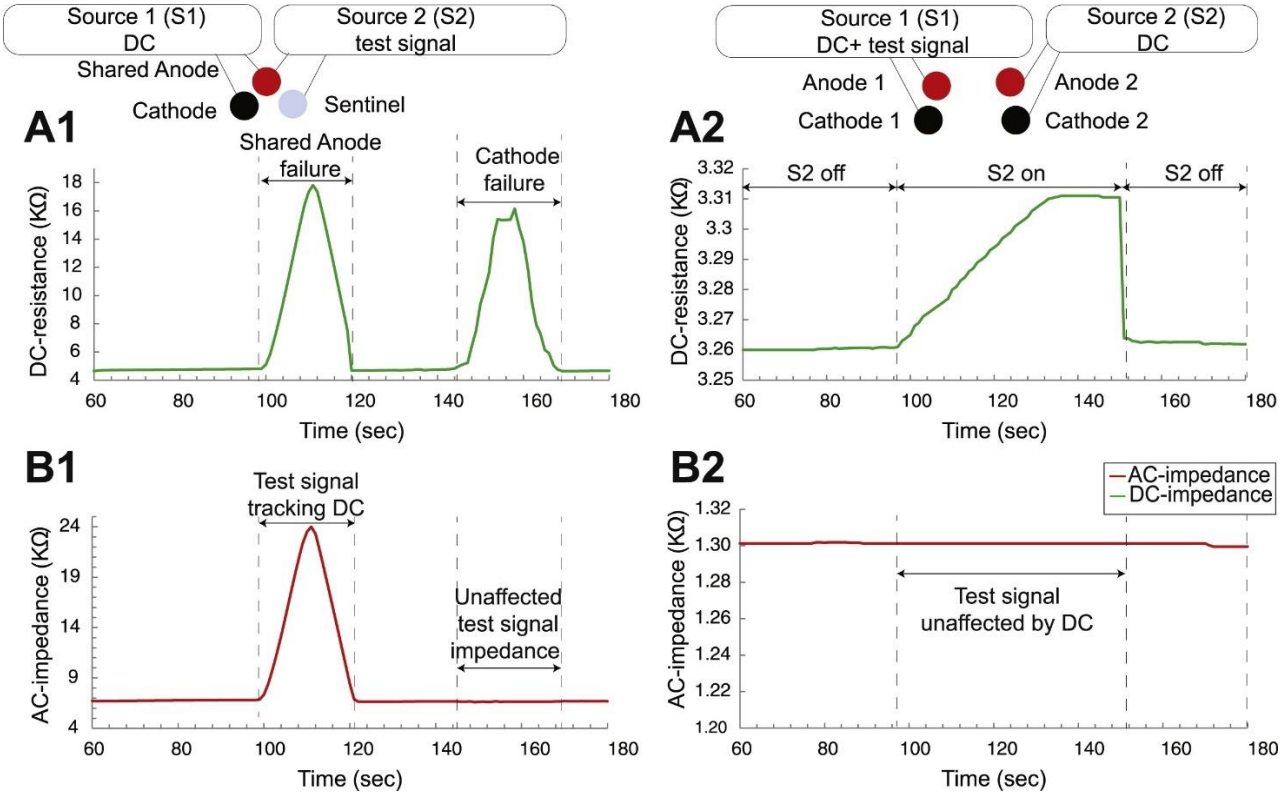

Figure 18. In vitro demonstration of failures to detect single electrode impedance changes (electrode faults) with specificity and methods to correct. (A1, B1) Type A error and method of correction using a sentinel electrode and test signal. A DC source (S1) energizes an anode and cathode with 2 mA. A second source (S2) passes a test sinusoidal current (38mA pk-to-pk at 10 Hz) between the anode (shared) and a sentinel electrode (not used for direct current). At any instance (here around 100- 120 s of stimulation; A1) when the anode electrode becomes faulty- in this case intentionally through reduced electrode gel contact area, the voltage/resistance increases across the DC current source and at the time the AC

voltage/impedance increases across the second test source. In contrast, when a fault is created at the cathode, DC-resistance across the first source again increases but AC-impedance at the second course is unaffected. (A2, B2) Type B error and method for correction using sinusoidal test signal. Two independent sources pass direct current (DC)across independent pairs of electrodes. Source 1 (S1) generates superimposed test signal (38 mA) on top of a DC (0.5 mA) while Source 2 (S2) generates 2 mA DC. S2 is activated transiently (around 100 - 150 s). Whereas the DC voltage/resistance across S1 is contaminated by the voltage produced when S2 is energized, the AC voltage/impedance is not affected.

1.5. Discussion

a. Clarification of "electrode resistance" during tDCS

The electrochemical performance of electrodes under DC, as well as tissue, has been addressed elsewhere (Merrill et al., 2005) - our focus here is on practical remedy rather than theory. None-the-less, context is necessary to inform rational design. tDCS is current controlled with the voltage output (also called here the total source-voltage) of the stimulator adjusted to maintain a controlled current application. In tDCS, when "resistance" is described, it is generally referring to the voltage at the output of the current source divided by the current applied – through the application of ohms law. However, the electrode and tissue are not simply resistive (e.g. explained by ohms law). "Impedance" refers to broader relation between current applied and the voltage associated with maintaining that current flow. Linear impedance includes frequency specific responses (e.g. the response to sinusoids of varied frequencies). The electrode and tissue are complex non-linear impedance. For example, the impedance may change over time and both electrodes and tissue may generate internal potentials. For electrodes, this is the over-potential from the electrode interface (Minhas et al., 2010) and for tissue this includes skin potentials (Nitsche and Paulus, 2000). How then does this complex system of impedance inform monitoring of "electrode resistance" for tDCS safety? It is accepted that during tDCS, significantly increased

voltage (at the current source output), which is associated with increased cell impedance, suggests a non-optimal condition at the electrode or electrode skin interface. This is biophysically justified since maintaining a low electrode over-potential voltage (see (Minhas et al., 2010) for detailed discussion) at the electrodes and high conductivity (e.g. good gel/saline contact with the electrode and skin) are associated with minimized chemical reactions and good contact. These in turn promote, but do no guarantee, tolerated stimulation. During tDCS, the voltage drop across a given electrode divided by the DC current across that electrode is what we refer to as the electrode resistance, while acknowledging it is not a simple resistance. Thus, we aimed to develop a system that allows measurement of a test-signal that is correlated with the electrode resistance during tDCS (passage of mA over minutes). We refer to electrode resistance equivalently as DC-electrode resistance to contrast with measurement derived from test signals. Our goal is further to resolve the electrode resistance of any given electrode during two or multi-channel tDCS.

b. Importance of electrode resistance measurement in tDCS and limitations of existing measurement approaches

The common adverse events associated with tDCS is skin irritation; conditions at the electrode are considered critical for tolerated stimulation (Minhas et al., 2011). The passage of electrical current across electrodes, and especially direct current, will strain electrode conditions that, if significant, can herald skin irritation. The most robust way to minimize skin irritation is through limiting current applied (e.g. total charge per session), use of well-designed electrodes (e.g. designed for tDCS), and following protocols for electrode assembly and skin preparation. None-the-less, nonideal conditions can arise. Subject reporting of sensation, general observation of electrode/skin conditions, and the monitoring of "electrode resistance" during stimulation are the only methods to monitor electrode conditions – and of these, electrode resistance is the only

device controlled and objective measures. Electrode resistance is thus universally relied on in tDCS.

However, as discussed above, the "electrode resistance" monitored is, in fact, the voltage at the current stimulator output (as the voltage is adjusted to maintain constant current) divided by the applied current. This voltage reflects many non-linear processes at both electrodes and the tissue (equations i to xiii). While valuable in tDCS monitoring, since large excursions in voltage are indicative of non-ideal electrode conditions, this is not a measure of *single* electrode resistance or even strictly resistance, since electrode over-potentials contribute as well. Rational development of tDCS can benefits from recognizing the none-triviality of this "electrode impedance" measurement.

Then multiple electrodes are used but the challenges in measuring *single* electrode resistance still exist where electrode impedances are confounded through cross talk. Measurements of "electrode resistance" (as extrapolated from the voltage as one of the current sources) may be misleading such that poor electrode conditions are not detected (false negative) or good electrode conditions as reported as poor (false positive). While our method for single electrode impedance is valuable for two electrode tDCS, for multi-electrode tDCS it becomes essential.

c. Commonalties and contrast with Electrode Impedance Tomography

Four electrode systems (tetra polar) are commonly used in tissue impedance measurements ("Bioimpedance and Bioelectricity Basics - 3rd Edition," n.d.; Pettersen and Høgetveit, 2011), and still more sophisticated multi-electrode methods do exist or have been developed for Electrode Impedance Tomography (EIT). But the application here is different in key regards. First, our measurand of interest is the electrode impedance with the goal to minimize contribution from

tissue, while in EIT the measurand of interest is tissue impedance with efforts taken to minimize contribution of electrodes. Second, significant current must be passed across electrodes for stimulation that results in changing electrode impedance, while in EIT minimal current is used. During tDCS, the changes in electrode impedance and electrode-over potential are particularly significant. None-the-less, to extend our solutions here, key techniques can be adapted from EIT including time or frequency multiplexing. What we demonstrated here is how to combine approaches used in EIT to resolve electrode impedance (more generally over-potential) during multi-channel direct current stimulation.

d. Assumptions to solution

The fundamental assumption to our solutions (both with and without a sentinel) is that the passage of a low-intensity and low-frequency sinusoidal current across an electrode (used for tDCS) produces a sinusoidal voltage across the electrode that predicts the DC-voltage across that same electrodes. Thus, the sinusoidal test impedance should predict the DC impedance of the electrode during tDCS.

A further assumption is that electrode resistance (at DC and also to the test signal) is greater than tissue resistance. We consider this assumption valid in the sense that poor electrode conditions will result in high electrode resistance and therefore will be detected. If a high resistance measurement is made, this is indicative of a poor electrode condition (not tissue conditions). If electrode resistance is low, and so comparable to tissue resistance, the resulting low measurement is regardless not of concern.

We also assumed and tested that the passage of the test current does not, in itself, confound either the tolerability of tDCS or electrode performance - meaning the test signal is presumed innocuous. These assumptions appear valid for the conditions tested here as physiological actions

on peripheral nerves or skin properties could be reflected by a chance in sensation or resistance, respectively. Since the current densities at the brain are much lower than the skin (DaSilva et al., 2011) where changes could not be detected, and experimentally based on prior neurophysiologic observations (Antal et al., 2008; Nitsche and Paulus, 2000), the test signals used here are predicted not to influence brain function.

Two distinct technological solutions are shown, both of which rely on our tested fundamental assumption, that AC-impedance can track DC-resistance. One approach requires the use of a single additional sentinel electrode, that is used a reference for AC voltage measurement across each stimulation electrode of interest. In this first approach, no additional current sources are needed, but existing current sources provide a small test AC current superimposed on DC, which is technically incremental. In the second approach, no additional electrodes are required but additional current sources providing only test signal are required at a number that is a function of the montage and stimulating source configuration, which is technically feasible. However, the first solution using a sentinel electrode may be advantageous as it is easily scalable, and the second approach may fail if a single electrode fails completely.

Appendix 2: Dry tDCS: Tolerability of a novel multilayer hydrogel composite non-adhesive electrode for transcranial Direct Current Stimulation

2.1. Outline

This Appendix validates the performance of the first "dry" electrode for tDCS which excludes 1) any saline or other electrolytes, that are prone to spread and leaving a residue; 2) any adhesive at the skin interface; or 3) any electrode preparation steps except the connection to the stimulator. A version of this study has been published (Khadka et al., 2018a). We concluded that dry (residue-free, non-spreading, non-adhesive, and no-preparation-needed) electrodes can be tolerated under the tested tDCS conditions, and possibly more broadly used in non-invasive electrical stimulation.

2.2. Introduction

Transcranial direct current stimulation (tDCS) is a non-invasive brain stimulation tool used in healthy and patient populations where a weak direct current (1-2 mA) is applied through two or more electrodes placed on the scalp (Bikson et al., 2018; Nitsche et al., 2008). A major contributor to the rapid and broad adoption of tDCS is portability and ease-of-use. tDCS is well tolerated with common mild side-effects such as transient cutaneous sensations (for e.g. as warmth, itching, and tingling) and erythema (Antal et al., 2017; Aparício et al., 2016; Bikson et al., 2016; Fertonani et al., 2015; Paneri et al., 2016). However, when (and only when) established standard protocols are not followed (Woods et al., 2016), tDCS can produce significant skin irritation (Bikson et al., 2009; Poreisz et al., 2007; Shiozawa et al., 2013; Wang et al., 2015). Given that cutaneous sensation and

irritation are the primary risks of tDCS (Antal et al., 2017; Brunoni et al., 2011; Fertonani et al., 2015; Minhas et al., 2011), proper electrode preparation and monitoring are vital for tolerability and reproducibility (Bikson et al., 2016; Brunoni et al., 2012; Paneri et al., 2016). Yet, the preparation and placement of tDCS electrodes remain the most cumbersome and prone-to-error steps (Fertonani et al., 2015). For example, both the level of sponge fluid saturation and head-gear tightness need to be titrated to balance good skin contact while avoiding of saline spread, and sponges can dehydrate or move (Woods et al., 2015) over an extended time. Thus, despite success with current research/clinical grade equipment and accessories, even for remote-supervised home use (Charvet et al., 2017), there is an interest to continue to enhance technology to deploy tDCS.

The sponge-pocket style electrode (25-35 cm^2) with conductive rubber insert, pin connectors, and saline application by the operator is the most traditional tDCS electrode used (Kronberg and Bikson, 2012; Woods et al., 2015), but most prone to preparation error, notably when poor materials are used by insufficiently trained users (DaSilva et al., 2011). Circular sponges do not appear to provide an advantage (Ambrus et al., 2011; Minhas et al., 2011). The introduction of pre-saline-saturated snap-connector sponge electrodes (Knotkova et al., 2019) automates most of the sponge electrode preparation process. Electrolyte gel or paste is used in specialized tDCS application (e.g. in MRI (Orlov et al., 2017)). Specialized adhesive hydrogels electrodes can support tDCS (Paneri et al., 2016). High-Definition electrodes with a distinct small form factor (~1 cm diameter (Abhishek Datta et al., 2009)) use specialized hydrogels (Minhas et al., 2010). What all these electrodes design share, is a "wet" electrode-skin-interface, where a fluid or viscous electrolyte is assumed to saturate the skin (Merrill et al., 2005), which in turn result in some residue on the skin.

Here, we validate the performance of the first "dry" electrodes for tDCS. Dry electrodes exclude: 1) any saline or other conductive hydrogel-based gel or paste, that are prone to leak or spread, and that leave a residue; 2) any adhesive at the skin, either around the electrode or part of the hydrogel; or 3) any electrode preparation steps by the operator except connection to the stimulator. A novel Multilayer Hydrogel Composite (MHC) electrode design fulfills these criteria. FEM models and a skin-phantom were used to verify electrode performance followed by tolerability validation in healthy subjects. Adverse events, erythema, and VAS pain were scored using established protocols (Brunoni et al., 2011; Fertonani et al., 2015; Paneri et al., 2016; Shiozawa et al., 2013). In addition, we developed a biocompatible flexible printed circuit board current sensor matrix (fPCB-CSM) to map current distribution inside the electrode during phantom or subject stimulation. In all experiments, MHC dry-electrode performance was compared against a state-of-the-art sponge electrode to address the hypothesis: can tDCS be applied with a dry electrode with comparable tolerability as conventional "wet" techniques.

2.3. Materials and Methods

This study involves experimental measures in phantom (voltage) and participants (via VAS and adverse events reporting questionnaire), computational FEM simulation in phantom, current mapping in the electrode, and an algorithm-based image processing of erythema distribution.

2.3.1. Participants

The study was conducted in accordance with the protocols and procedures approved by the Institutional Review Board of the City College of New York, CUNY. Twenty healthy participants (13 males and 7 females; age 19-34 years; mean age 24.7± 4.9) completed this study. Volunteers with any sign of skin disorder/sensitive skin (ex. eczema, severe rashes), blisters, open wounds,

burn including sunburns, cuts or irritation (e.g. due to shaving), or other skin defects which compromise the integrity of the skin at or near stimulation locations were excluded from this study. However, participants on mild acne medication with non-irritating skin disorders were not excluded. Similarly, prospective volunteers with any neuropsychiatric disorders or receiving medication for such disorders were excluded from this study. Participants volunteered in four different tDCS sessions using 1.5 mA and 2 mA current intensities plus an additional two sessions at 2 mA with the fPCB-CSM for both MHC dry and sponge-electrodes in a randomized order. All participants provided written informed consent to participate in the study. Participants were seated in an upright relaxed position and performed a lexical decision task throughout the duration of the stimulation.

2.3.2. Novel sensor array

The current sensor made up of a novel biocompatible flexible printed circuit board current sensor matrix (fPCB-CSM) comprises two units: 1) measuring unit (top view) and 2) sensor unit (bottom view) (Fig. 19, top middle and right panel). The measuring unit (rubber electrode positioning side) of the novel sensor array has an exposed gold (Au) plated uniform copper (Cu) metal surface, whereas on its distal side, there are twenty-five 50 Ω soldered resistors (5 rows and 5 columns of resistors) and five common grounds for each row. The sensor unit underneath the measuring unit (sponge/MHC-dry electrode side) has a high heat resistance polyimide insulating substrate that divides the conductive metal into twenty-five small sensor electrode arrays. Each of these twenty-five sensor arrays is connected independently to the twenty-five test resistors located at the measuring unit. Each end of the sensor array has a dimension of 5 cm x 5 cm x 0.03 cm (Fig.17). The entire sensor array is assembled into one compound unit using a biocompatible polyimide substrate.

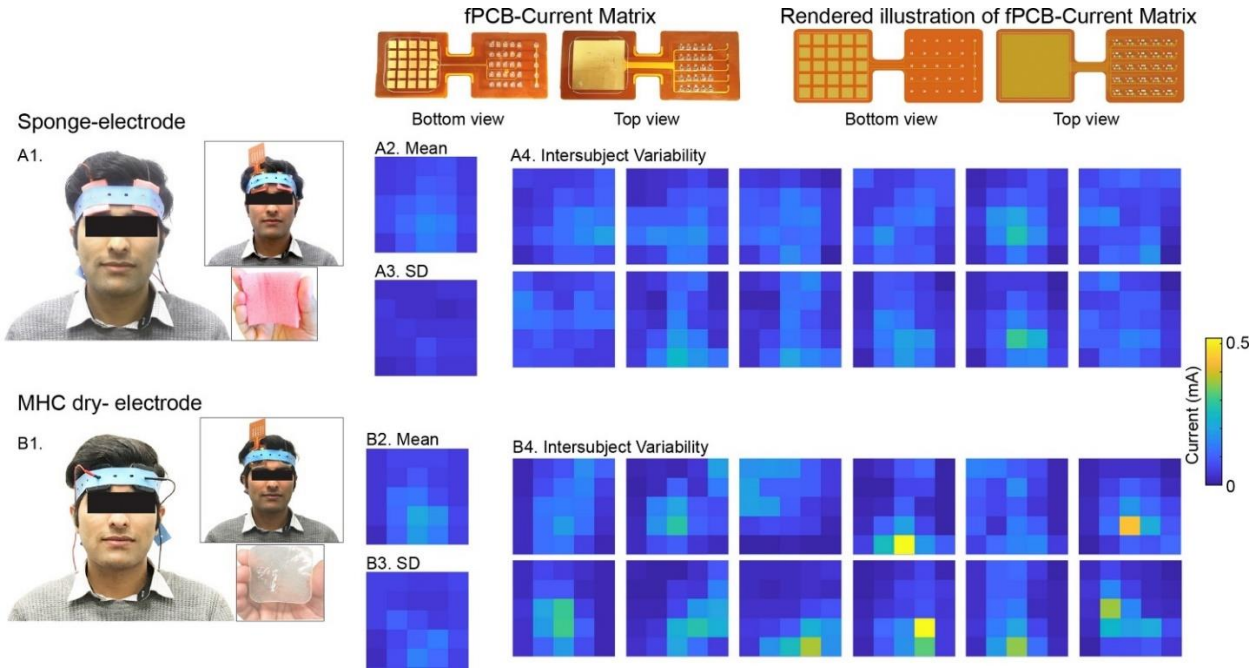

Figure 19. A configuration of conventional sponge and MHC-dry electrode, with and without fPCB within-electrode current mapping sensor. and voltage map represented as false colormap measured in the electrode using fPCB voltage sensor. (A1, B1) Electrical stimulation set-up on a participant's forehead using a bifrontal (left/right SO) montage electrode configuration. A biocompatible rubber strap secured both electrode types on the forehead and the electrodes were connected to the stimulator. In some experiments, a customize novel fPCB current mapping sensor array unit (bottom panel of B1) positioned inside the electrode mapped at the different location of electrode plane during tDCS. Current mapping data measured from 12 participants for either electrode type (false colormap for each sensor).

2.3.3. Voltage sensor array for Phantom study

Twenty-Five Ag/Agcl pellet shaped electrodes (diameter =1 mm) were embedded inside an agar phantom (based on (Khadka et al., 2018c; Smith, 1993)) such that the planar assembly mimics the shape of an overlaid 5 x 5 cm^2 tDCS electrode, and the position of each electrode corresponds to the center of the 25-small fPCB-CSM sensor arrays. An embedded reference

electrode placed 5 cm away from the twenty-five electrode array was used as a ground for voltage measurement across the recording electrodes.

2.3.4. MHC dry-electrode

The dual layer structure of the MHC dry-electrode includes independently optimized mechanical, electrical, and chemical properties of the hydrogel. The top layer (thickness, 0.6 mm) of the MHC dry-electrode was composed of an adhesive polymer hydrogel, whereas the bottom layer (thickness, 1 mm) had a non-adhesive bio-compatible polymer hydrogel containing Poly-Vinyl Alcohol (PVA) (Fig. 19). Both layers were optimized in a way that the top layer becomes less resistive to redistribute the injected current across the electrode plane, whereas the bottom layer becomes highly resistive layer and minimizes current clustering at the skin (Kronberg and Bikson, 2012). Furthermore, any electrochemical produced (e.g. pH changes) at the electrode (non-ionic/ionic conduction) interface within the electrodes were optimized using the top layer as a diffusion barrier (Merrill et al., 2005). The electrode components weight by percentage) were: cross-linked acrylic resin (top layer: 15 - 25; bottom layer: 15 - 25); polyhydric alcohol (top layer: 40-60; bottom layer: 30-60); NaCl as an electrolytic salt (top layer: < 10; bottom layer: < 8); additives / stabilizers (top layer: < 0.5; bottom layer: < 0.5); deionized water (top layer: 20 – 40; bottom layer: 20 - 40); polyvinyl alcohol resin (top layer: none; bottom layer: 1 - 5).

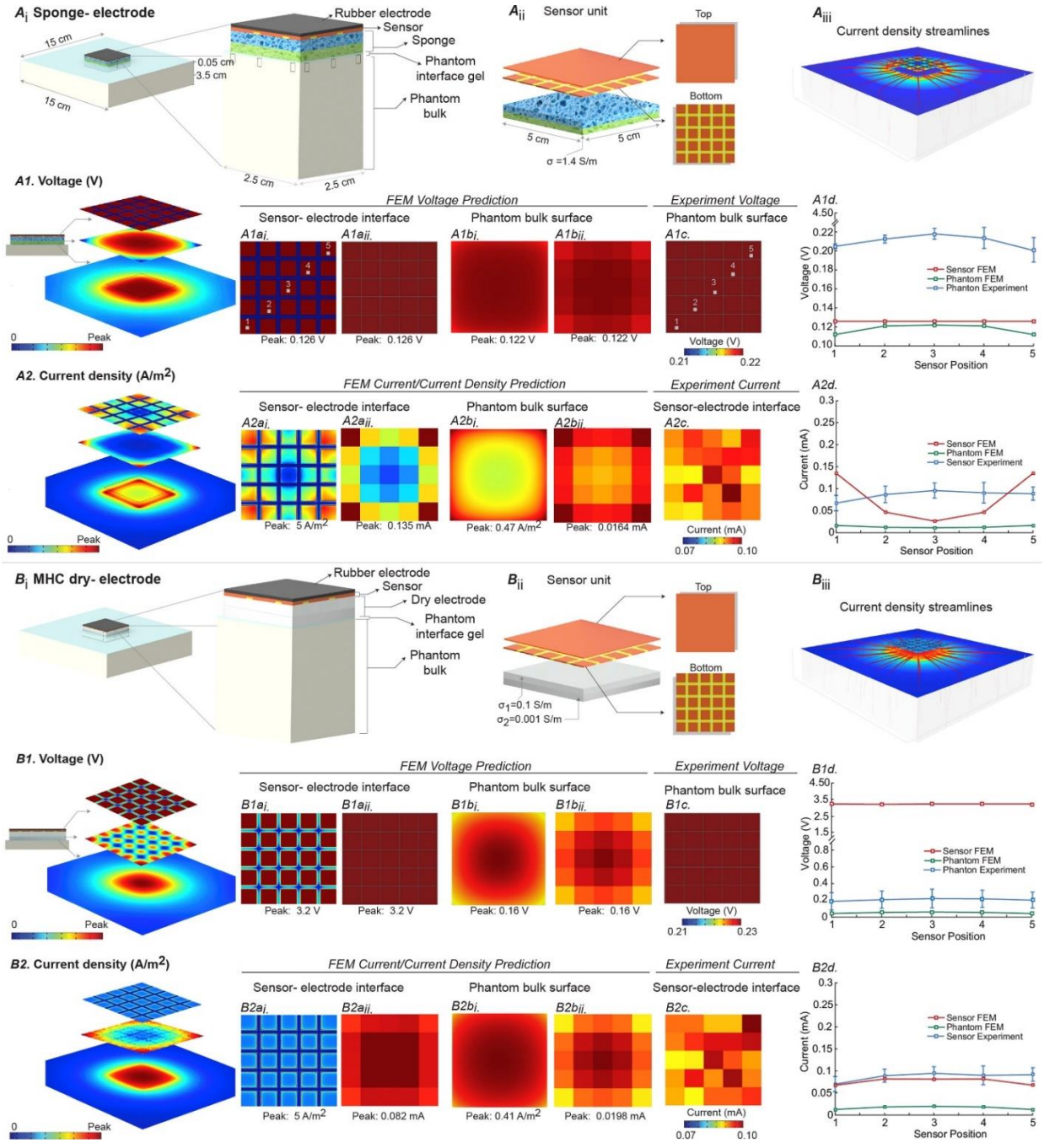

Figure 20. Electrical performance of conventional sponge-electrode and MHC dry electrode verified using a skin-phantom and FEM simulations. Phantom voltages and electrode currents were measured using the Ag/AgCl array or fPCB-CSM, respectively, with corresponding FEM prediction. (Ai) Architecture of a phantom model showing expanded cut off view of rubber electrode, sensor array, and sponge-electrode assembly on the phantom-gel surface. (Aii) illustration of fPCM-CSM sensor unit

positioned over sponge pad. (Aiii)represents an orientation of current density flow streamlines from inside of the electrode to the phantom. (A1) Voltage distribution measured experimentally and predicted by FEM simulation at the sensor-electrode interface and phantom bulk surface. The leftmost panel ofA1illustrates side-view of the electrode-sensor and phantom assembly, and predicted voltage distribution at the sensor-electrode interface (dorsal), within-sponges (medial), and phantom bulk surface (ventral). Middle row ofA1shows FEM prediction of voltage distribution at the sensor-electrode interface and phantom bulk surface using simulation result (A1ai,A1bi) and false voltage distribution map at each small squared surface that resemble the shape of the experimental sensor arrays (A1aii, A1bii) and the measured voltage from experimental measures (A1c). Peak FEM predicted voltage at the sensor-electrode interface was 0.126 V and 0.122 V at the phantom bulk surface. Experimental voltage measurement at the phantom bulk surface was 0.22 V (peak). (A1d) Graphical representation of voltage line graphs plotted from diagonal voltage components at the sensor-electrode interface and phantom bulk surface (FEM prediction results), and an experimental measure. Position of the sensors is represented as numbers in a diagonal fashion as illustrated inA1ai, A1bi and A1c. Results represents an overall distribution map of voltage. (A2) represents current/current density measured experimentally and predicted by the FEM simulation at the sensor-electrode interface and phantom bulk surface. Panel at the left ofA2showsstacked view of current density distribution from sensor-electrode interface (dorsal), within-sponges (medial), and phantom bulk surface (ventral). FEM prediction of current/current density and experimental measurement of current are shown in the middle panel ofA2. Peak current of 5 A/m^2 (A2a) and a peak current of 0.135 mA (A2aii) was predicted at the sensor-electrode interface, whereas at the phantom bulk surface FEM predicted a peak current density of 0.47 A/m^2 (A2bi) and a peak current of 0.0164 mA (A2bii). Current measured experimentally (A2c) at the sensor-electrode interface was almost uniform. (A2d) Representation of line plots of diagonal current measured experimentally and predicted by FEM at sensor-electrode interface and phantom bulk surface. (Bi) Illustration of MHC dry electrode positioning over the phantom-gel surface. (Bii) schematics of the sensor array rendered on top of the MHC dual-layered (top layer: 0.1 S/mand bottom layer:0.001 S/m) dry electrode. (Biii) represents uniformly seeded current density streamlines distribution

from the surface of rubber electrode to the phantom. Left panel ofB1shows slice view of electrode assembly and FEM predicted voltage at the sensor-electrode interface, within-MHC dry electrode, and phantom bulk surface. Middle panel ofB1is an illustration of voltage distribution as predicted by FEM simulation (Sensor-electrode interface: B1ai, B1aiiandphantom bulk surface: B1bi, B1bii) and measured experimentally (B1c). Peak predicted voltage was 3.2 V at the sensor-electrode interface and 0.16 V at the phantom bulk surface, whereas experimentally, a comparable peak voltage of 0.23 V was measured as that of the sponge-electrode. Line plots of voltages shows even voltage distribution in the diagonal direction. (B2) Stacked slices of current density distribution at the sensor-electrode interface, within the MHC electrode, and at the phantom bulk surface (left panel). A comparable peak current density of 5 A/m^2 as that in the sponge electrode was predicted at the sensor-electrode interface (B2ai) whereas mean peak current was 0.082 mA (B2aii). Predicted current density (B2bi) and current (B2bii) at the phantom bulk surface was comparable to that of the sponge-electrode and the distribution was almost uniform (slightly higher at the center but without edges). Comparable current as in the conventional sponge electrode was measured at the senor-electrode interface (B2c). Diagonal current distribution line graph was almost identical to that of conventional sponge electrode (B2d).

The effectiveness of the MHC dry-electrode was successfully evaluated not only as a current re-distribution layer but also as a diffusion barrier layer. In the diffusion barrier test, pH changes were measured at the entire conductive silicone rubber/top hydrogel layer, top/bottom hydrogel layer, and bottom hydrogel layer/skin interface after 2mA 30min stimulation. There was no pH change at the bottom/skin hydrogel interface. Only less than 0.3 % of the total electrode area showed pH change at the top/bottom hydrogel layer interface (n=30).

2.3.5. Electrode preparation and placement

The experiment was conducted on rectangular phantom bulks (15 cm x 8 cm x 5 cm; prepared using established standard protocols as discussed in (Khadka et al., 2018c; Smith, 1993)).

Prior to the electrode placement, a thin coat (~ 0.5 cm) of conductive electrode gel (Signa gel, Parker Laboratories Inc., NJ, USA) was applied over the agar phantom bulk. Conductive gel was used to maintain a consistent contact between the stimulation electrodes and the phantom. For the phantom study, the conventional sponge-electrode (5 x 5 cm) were first soaked with saline (0.9 % NaCl) and a conductive carbon rubber (5 x 5 cm, Carbon Rubber Electrode, Soterix medical Inc., NY, USA) was inserted inside the sponge pocket. While the whole assembly is often referred as an electrode in tDCS, the electrode is technically the conductive rubber and the saline/gel is technically the electrolyte (DaSilva et al., 2011). Two electrodes (anode and cathode; 5 x 5 cm each) were then positioned on the phantom with an interelectrode distance of 10 cm and connected to a tDCS stimulator (1x1 tDCS, Soterix Medical Inc., NY, USA). The non-adhesive bottom layer of the MHC dry-electrode was placed over the phantom bulk and a conductive silicone rubber was positioned on the top adhesive layer of the MHC-dry electrode which was connected to the tDCS device.

For the human study, a bifrontal montage (anode left and cathode right on the supraorbital (SO) region of a forehead) was used to place both type of electrodes. Note that we selected this particular montage to overcome the major limitation of the MHC dry-electrode- not applicable in hairy regions of scalp unlike the conventional "wet" sponge-electrode. Electrodes were positioned and secured over the brain region using an elastic fastener (Soterix Medical Elastic Fastener, Soterix Medical Inc., NY, USA).

When current at the electrode was measured, the fPCB-CSM array was placed in between the sponge or MHC dry-electrode (bottom) and the conductive carbon/silicone rubber electrode (top). Together they formed a stacked electrode configuration of rubber electrode, fPCS-CSM array, and sponge/MHC dry-electrode respectively.

2.3.6. Stimulation and Current/Voltage Measurement

A weak 1.5 or 2 mA direct current (with an additional linear ramp up and down of 30 s at the beginning and at the end of stimulation) from a tDCS stimulator was applied in both human and phantom studies through sponge or MHC dry-electrodes. In the human study, voltage was measured across each test resistor located at the measuring unit of the fPCB-CSM using a digital multimeter (Fluke 87 V Industrial Multimeter, Fluke Corporation, WA, USA) and the corresponding current was calculated using the Ohm's law. In the phantom bulk experiment, voltage was measured across the twenty-five embedded recording electrodes using a low power instrumentation amplifier (AD 620, Analog Devices, MA, USA), whereas current at the electrode was measured using the aforementioned procedure as in the human study. Note that for current measurement at the electrode in both human study and phantom study, the fPCB-CMS was positioned over the sponge or MHC dry-electrode and the carbon/silicone rubber electrode was placed on the top surface of the sensor.

		Adverse Events	Headache	Neck pain	Scalp pain	Tingling	Burning Sensation	Itching	Sleepiness	Trouble concentrating	Dizziness	Nausea
Sponge	1.5 mA	#Reports (%)	3 (15 %)	2 (10 %)	0	11 (55 %)	7 (35 %)	9 (45 %)	8 (40 %)	7 (35 %)	1 (5 %)	1 (5 %)
		Intensity (mean ± SD)	(1.20 ± 0.52)	(1.10 ± 0.30)	(1.0 ± 0)	(1.70 ± 0.73)	(1.50 ± 0.76)	(1.76 ± 0.83)	(1.60 ± 0.99)	(1.50 ± 0.82)	(1.05 ± 0.22)	(1.05 ± 0.24)
		Relation (mean ± SD)	(1.40 ± 0.99)	(1.20 ± 0.61)	(1.0 ± 0)	(2.45 ± 1.66)	(2.0 ± 1.52)	(2.35 ± 1.76)	(1.50 ± 1.14)	(1.60 ± 1.09)	(1.15 ± 0.67)	(1.0 ± 0)
	2 mA	#Reports (%)	2 (10 %)	0	3 (15 %)	9 (45 %)	7 (35 %)	9 (45 %)	5 (25 %)	6 (30 %)	1 (5 %)	0
		Intensity (mean ± SD)	(1.15 ± 0.48)	(1.0 ± 0)	(1.15 ± 0.36)	(1.70 ± 0.92)	(1.50 ± 0.76)	(1.73 ± 0.93)	(1.40 ± 0.82)	(1.35 ± 0.58)	(1.05 ± 0.22)	(1.0 ± 0)
		Relation (mean ± SD)	(1.05 ± 0.22)	(1.0 ± 0)	(1.40 ± 1.09)	(2.15 ± 1.63)	(1.80 ± 1.32)	(2.05 ± 1.54)	(1.1 ± 0.30)	(1.35 ± 0.74)	(1.05 ± 0.22)	(1.0 ± 0)
MHC Dry	1.5 mA	#Reports (%)	3 (15 %)	0	1 (5 %)	9 (45 %)	4 (20%)	8 (40 %)	5 (25 %)	5 (25 %)	0	1 (5 %)
		Intensity (mean ± SD)	(1.40 ± 0.52)	(1.0 ± 0)	(1.05 ± 0.22)	(1.50 ± 0.60)	(1.25 ± 0.55)	(1.64 ± 0.78)	(1.35 ± 0.74)	(1.25 ± 0.44)	(1.0 ± 0)	(1.05 ± 0.24)
		Relation (mean ± SD)	(1.05 ± 0.22)	(1.0 ± 0)	(1.0 ± 0.44)	(2.20 ± 1.50)	(1.55 ± 1.23)	(2.29 ± 1.64)	(1.05 ± 0.22)	(1.20 ± 0.69)	(1.0 ± 0)	(1.0 ± 0)
	2 mA	#Reports (%)	1 (5 %)	2 (10 %)	0	11 (55 %)	8 (40 %)	9 (45 %)	4 (20 %)	5 (25 %)	0	3 (15%)
		Intensity (mean ± SD)	(1.05 ± 0.22)	(1.10 ± 0.30)	(1.0 ± 0)	(1.65 ± 0.67)	(1.45 ± 0.60)	(1.73 ± 0.93)	(1.30 ± 0.73)	(1.30 ± 0.57)	(1.0 ± 0)	(1.15 ± 0.36)
		Relation (mean ± SD)	(1.0 ± 0)	(1.05 ± 0.22)	(1.0 ± 0)	(2.40 ± 1.53)	(2.10 ± 1.51)	(2.42 ± 1.74)	(1.05 ± 0.22)	(1.25 ± 0.71)	(1.0 ± 0)	(1.10 ± 0.30)

Table 1. Representation of adverse events as intensity and relationship to tDCS based on subjective reporting before and after stimulation (pre- and post). Reporting of adverse events (mean ± SD) were comparable across electrode types and stimulation intensities.

2.3.7. Pain and Adverse Events

Headache, neck pain, scalp pain, tingling, burning sensation, itching sensation, sleepiness, trouble concentrating, dizziness, and nausea were assessed through self-reporting questionnaires completed by the participants before and after each session (Table 1). The intensity of the events was rated from 1 - 4 (1 = absent, 2 = mild, 3 = moderate, and 4 = severe) and their relationship to tDCS was rated in a scale from 1 - 5 (1 = none, 2 = remote, 3 = possible, 4 = probable, and 5 = definite). A visual analogue scale (VAS) was used during the 20 min 1.5 mA or 2mA stimulations to report skin sensation or pain (if any) in a scale of 1-10 (1: no or minimum pain and 10: unbearable pain). Stimulation was aborted if a participant reported a VAS of 7 or above. The VAS for pain was collected during the stimulation, while the participants were performing the lexical decision task. The lexical decision task was presented as a mixture of words (e.g. house, ship, sleep, etc.) and pseudowords (nonsense strings that represented the phonotactic rules of a language, like trud in English) and participants reported whether the presented stimulus was a word or a pseudoword. The lexical decision task was paused every two minutes to allow participants time to report the VAS.

2.3.8. Computational Model and Solution Method

The phantom was modeled as a homogenous and isotropic volume conductor of dimension 15 cm x 15 cm x 3.55 cm (including a 0.5 mm thin layer of conductive gel). Computer-aided design models of phantom bulk, conductive gel, sponge or MHC dry- electrode, sensor arrays, and rubber electrode (Fig. 20, 22) were modeled in SolidWorks 2013 (Dassault Systemes Americas Corp.,

MA, USA) and were assembled in ScanIP software (Synopsys, Exeter, UK). Dimensions of rubber electrode, MHC dry-electrode, sponge, and sensor arrays were based on the experimental values. An adaptive tetrahedral meshing algorithm was implemented in ScanIP to generate meshes of the phantom bulk for both conventional sponge-electrode and MHC dry-electrode simulation cases. The finite element method (FEM) models of the volumetric meshes were then imported and solved in COMSOL Multiphysics 4.3 (COMSOL, Inc., MA, USA) using electric current physics at a steady-state assumption. The final FEM phantom model was solved for greater than 600,000 degrees of freedom and had greater than 400,000 tetrahedral elements. The phantom conductivities were based on prior literature [28]. The Laplace equation ($\nabla (\sigma \nabla V) = 0$ where 'V' is potential, 'σ' is conductivity) was solved to simulate direct current stimulation. Boundary conditions for phantom simulation were applied as uniform normal current density (inward current flow: Jnorm) at the top exposed surface of the anode (2 mA) and ground at the bottom surface of the phantom bulk layer. All other external surfaces of the phantom bulk model were electrically insulated. Two versions of MHC dry-electrodes with varying electrical conductivities of the top and bottom layers were simulated (MHC dry-electrode Variation I and II; Fig. 20, 22).

2.3.9. Image post processing and analysis

The photographs of participant's forehead (area under anode) taken immediately after stimulation were analyzed for erythema distribution using a customized MATLAB (MathWorks, MA, USA) based image processing graphical user interface (GUI) as previously illustrated in (Ezquerro et al., 2017) (Fig. 3).

2.3.10. Statistical Tests

Normality of the VAS, cumulative adverse events responses, and adverse events in relationship to tDCS were tested using Shapiro-Wilk tests with Lilliefors significance correction across electrode types (dry-electrode vs. sponge-electrode) and stimulation intensities (1.5 mA vs. 2 mA). A corresponding non-parametric test (Wilcoxon signed rank test) or a parametric test (repeated measures ANOVA) probed significance of the data. A critical value (α) of 0.05 was accepted as a significant difference between groups.

2.4. Results

Voltage and current density/current distribution at the sensor-electrode interface and phantom bulk surface during direct current stimulation (2 mA, 20 min) were predicted by FEM simulation (phantom) and measured experimentally (phantom gel and in vivo study) using both conventional sponge-electrode and MHC dry-electrode. In addition, VAS score, lexical decision task response, and adverse event analysis based on participants' rating and response were analyzed.

2.4.1. In vivo current mapping

The fPCB-CSM mapped the overall current distribution inside both sponge-electrode and MHC dry-electrode with 2 mA tDCS. The distribution was represented as a heat map (mean and standard deviation, or intersubject variability) where each square represents current at one sensor position (Fig.19A2, A3, A4: Sponge-electrode and Fig. 19B2, B3, B4: MHC dry-electrode). The total current across all fPCM-CSM sensors was 2 mA in all cases, as expected. Across individuals, there was no evident concentration of current at any fPCM-CSM sensor or sensors, for either MHC dry-electrode or sponge-electrode. On an individual basis, hot spots (e.g. 6x average) were detected but with no consistent pattern suggesting that it reflect idiosyncratic contact of the electrode with the skin surface or internal skin or electrode inhomogeneities. In any case, there

was no average or individual electrode observation of current concentration at the electrode edge (at sensors around the perimeter) as much be predicted based on prior models (Khadka et al., 2015b; Kronberg and Bikson, 2012; Minhas et al., 2011; Miranda et al., 2009; Opitz et al., 2015).

2.4.2. Erythema distribution

Erythema was diffused across the skin-electrode contact area in both MHC dry-electrode and sponge-electrode for both stimulation intensities as indicated by the probability heat map. For the MHC dry-electrode, the peak cumulative probability of erythema distribution for 1.5 mA was 50 %; 41.2 % for mild and 17.65 % for strong (Fig. 21B1) whereas for 2 mA (Fig. 21B2), the cumulative erythema percentage was 73.53 %; 52.9 % for mild and 32.35% for strong. Conventional sponge-electrode had the peak probability of 50 % erythema distribution for 1.5 mA (Fig. 21B3); 50 % for mild and 18.9 % for strong, and for 2 mA (Fig. 21B4), the peak cumulative erythema was 71.1 %; 57.9 % for mild and 26.32 % for strong. The mean probability of erythema distribution yielded by MHC dry-electrode and conventional sponge-electrode were comparable (Fig. 21).

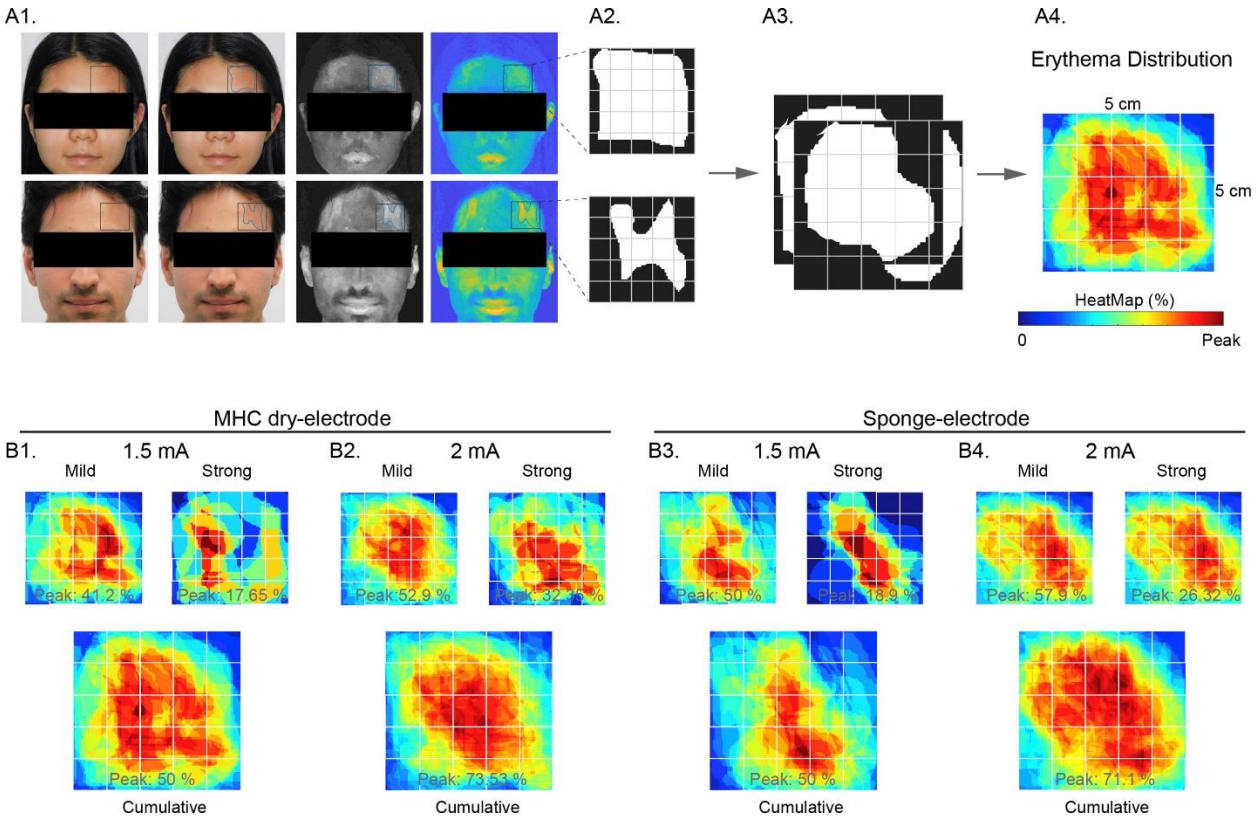

Figure 21: Graphical representation of skin redness (erythema) distribution over the site of stimulation after tDCS (20 min, 1.5 mA, and 2 mA). (A1) depicts the image analysis steps where photographs of participants taken immediately after stimulation were passed through series of filters to isolate erythema region from the site of stimulation by defining a region of interest (ROI). (A2) represents a binary mask of erythema image traced by the rater. (A3) shows steps of computing the probability of erythema distribution by stacking all binary erythema mask. (A4) illustrates the mean heatmap of erythema distribution across subjects represented as a percentage across the ROI. Peak represent 100% probability in the color bar and probability was depicted as mild, strong, and combined heatmaps. (B1, B2) are erythema heatmaps of 1.5 mA and 2 mA using MHC dry electrode and (B3, B4) represents heatmaps for sponge-electrode. Combined erythema distribution was widely diffused with a comparable peak probability of erythema in both electrode types.

2.4.3. Performance of conventional sponge-electrode and MHC dry-electrode with variations: FEM prediction and Experimental Measures

For Sponge-electrode, the FEM model predicted a peak voltage of 0.126 V at the sensor-electrode interface (Fig. 20A1ai, 20A1aii) and 0.122 V (peak) at the phantom bulk surface (Fig. 20A1bi, 20A1bii). An embedded electrode array positioned at the phantom bulk surface measured a maximum voltage of 0.22 V (Fig. 20A1c). Predicted voltage and experimentally measured voltage (Mean ± SD) distribution line plots were almost even across diagonal direction (Fig. 20A1d), however at the center of the phantom bulk surface, it was slightly higher. The FEM model of sponge-electrode predicted a peak current density of 5 A/m2 and a peak current of 0.135 mA at the sensor-electrode interface, whereas at the phantom bulk surface, the predicted peak current density and peak current were 0.47 A/m^2 (Fig. 20A2bi) and 0.0164 mA (Fig. 20A2bii) respectively. Maximum current measured experimentally at the sensor-electrode interface for sponge-electrode was 0.10 mA and the overall current distribution was uniform (Fig. 20A2c). However, the FEM model predicted somewhat higher current density/current at the edges (Fig. 20A2d).

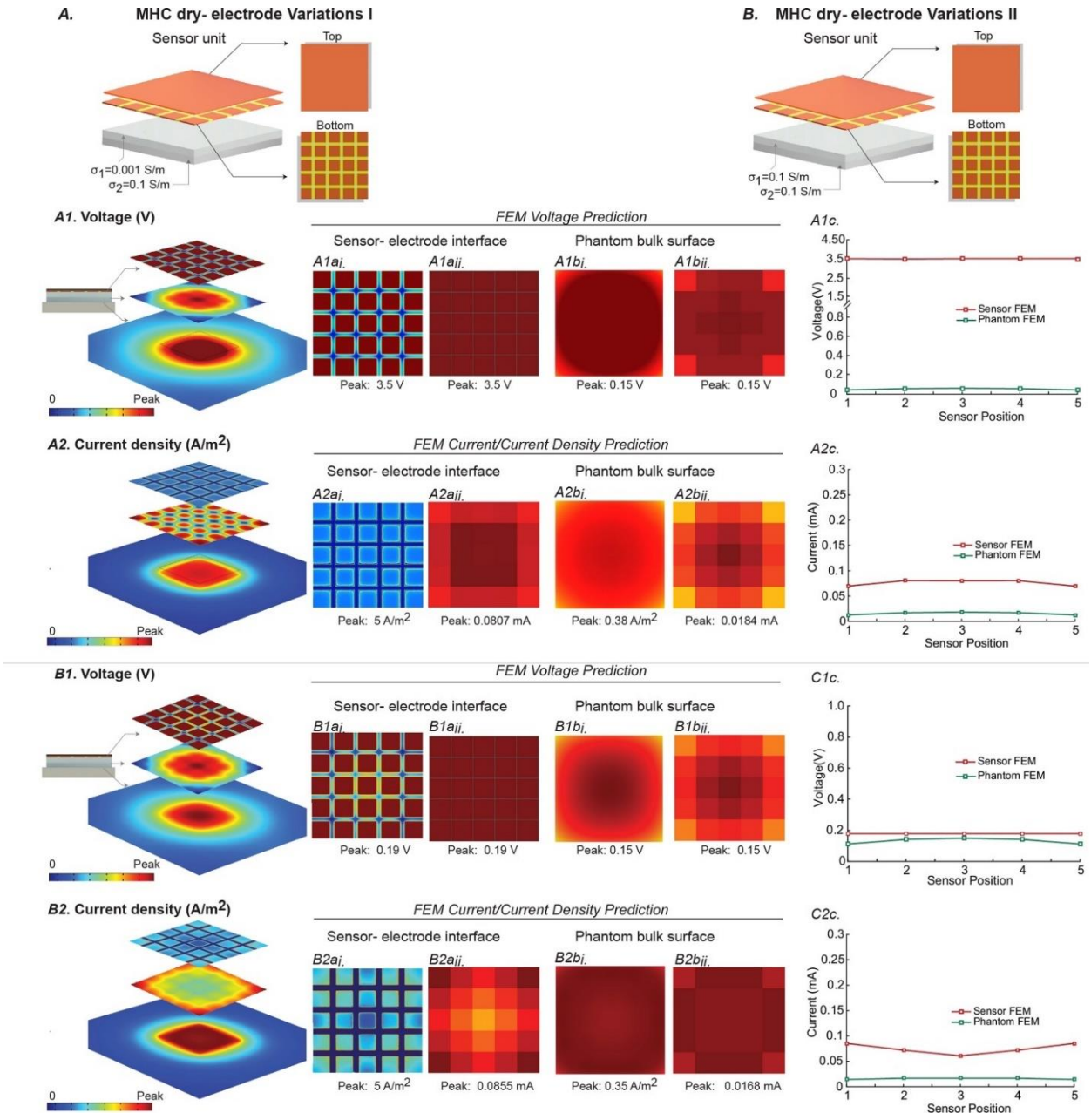

Figure 22. Performance of MHC dry electrode with variations in electrical conductivities of the dual layers. Voltage and current/current density distribution as predicted by FEM at the sensor-electrode interface and the phantom bulk surface are represented.(A) Illustration of voltage distribution at the sensor-electrode interface and phantom bulk surface when the conductivities of the dual layers are reversed (MHC dry-electrode Variation I: top layer:0.001 S/mand bottom layer:0.1 S/m). Stacked slice view of voltage distribution from dorsal to ventral end of the MHC Variation I electrode-phantom assembly (left panel).

FEM model predicted a comparable voltage at the sensor-electrode interface (A1ai, A1aii) and phantom bulk surface (A1bi, A1bii) as that of the actual MHC dry electrode. (A2) represents current density and current distribution as predicted by FEM simulation. The overall distribution of current density and current was analogous to the MHC dry-electrode (A2ai, A2aii, A2bi, A2bii, A2c). (B) Voltage and current density/current distribution with MHC dry-electrode Variation II (top layer and bottom layer:0.1 S/m). The left panel ofB1represents a distribution of voltage at the sensor-electrode interface and phantom bulk surface. FEM simulation predicted slightly lower peak voltage (0.19 V) at the sensor-electrode interface compared to the actual MHC dry-electrode (B1ai, B1aii), whereas peak voltage at the phantom bulk was comparable (B1bi, B1bii). Representation of current density distribution at different interfaces (B2). The simulation predicted comparable current density (B2ai) and current (B2aii) at the sensor-electrode interface, however, at the phantom bulk surface, current density (B2bi) and current (B2bii) was slightly lower than that of MHC dry electrode. (B2c) represents variation in current at the sensor-electrode interface and phantom bulk surface.

For MHC dry-electrode, the predicted peak voltage at the sensor- electrode interface was 3.2 V (Fig. 20B1ai, Fig. 20B1aii) and 0.16 V at the phantom bulk surface (Fig. 22B1bi, Fig. 22B1bii), higher than the conventional sponge-electrode. The experimental voltage measured at the phantom bulk surface during MHC dry-electrode stimulation was comparable to that of sponge-electrode (Fig. 20B1c and Fig. 20A1c). The FEM model predicted peak current density and current were 5 A/m^2 and 0.082 mA at the sensor-electrode interface and 0.41 A/m^2 and 0.0198 mA at the phantom bulk surface (Fig. 20B2ai and Fig. 20B2aii, and Fig. 20B2bi and Fig. 20B2bii) for the MHC dry-electrode. Overall current distribution at the phantom bulk surface was almost uniform, with peaks around the center (Fig. 20B2bi). Current distribution measured experimentally during MHC was comparable to that of conventional sponge-electrode (Max: 0.10 mA, Fig. 20B2c).

In MHC dry-electrode Variation I, the FEM predicted similar voltage and current density/current distribution as that of the original MHC dry-electrode (Fig. 19). However, results from MHC variation II were lower than that of the original configuration of dual hydrogel layers. In MHC variation II, the peak voltages at the sensor electrode interface and phantom bulk surface were 0.19 V and 0.15 V (Fig. 22B1ai, Fig. 22B1aii, and Fig. 22B1bi, Fig. 32B1bii), and the predicted peak current density and current at the sensor electrode interface and phantom bulk surface were 5 A/m^2 and 0.0855 mA, and 0.35 A/m^2 and 0.0168 mA respectively (Fig. 22B2ai, Fig. 22B2aii, and Fig. 22B2bi, Fig. 22B2bii).

2.4.4. Tolerability

A total of 120 treatment sessions were conducted, including the in vivo current mapping study. No serious adverse events were reported. Eight participants withdrew from the study: six participants withdrew due to scheduling issues (i.e. inability to meet scheduling criterion for a minimum of four sessions), one participant withdrew due to itching during a 2 mA MHC dry session (the only withdrawal during a session), and one participant withdrew without stating a reason. Thus, all but one withdrawal were between-sessions. In total, twenty subjects completed the entire study and group level analysis were conducted on only these 20 subjects. tDCS adverse events were assessed by a self-report questionnaire immediately post-stimulation period (session-wise data, Table 1).

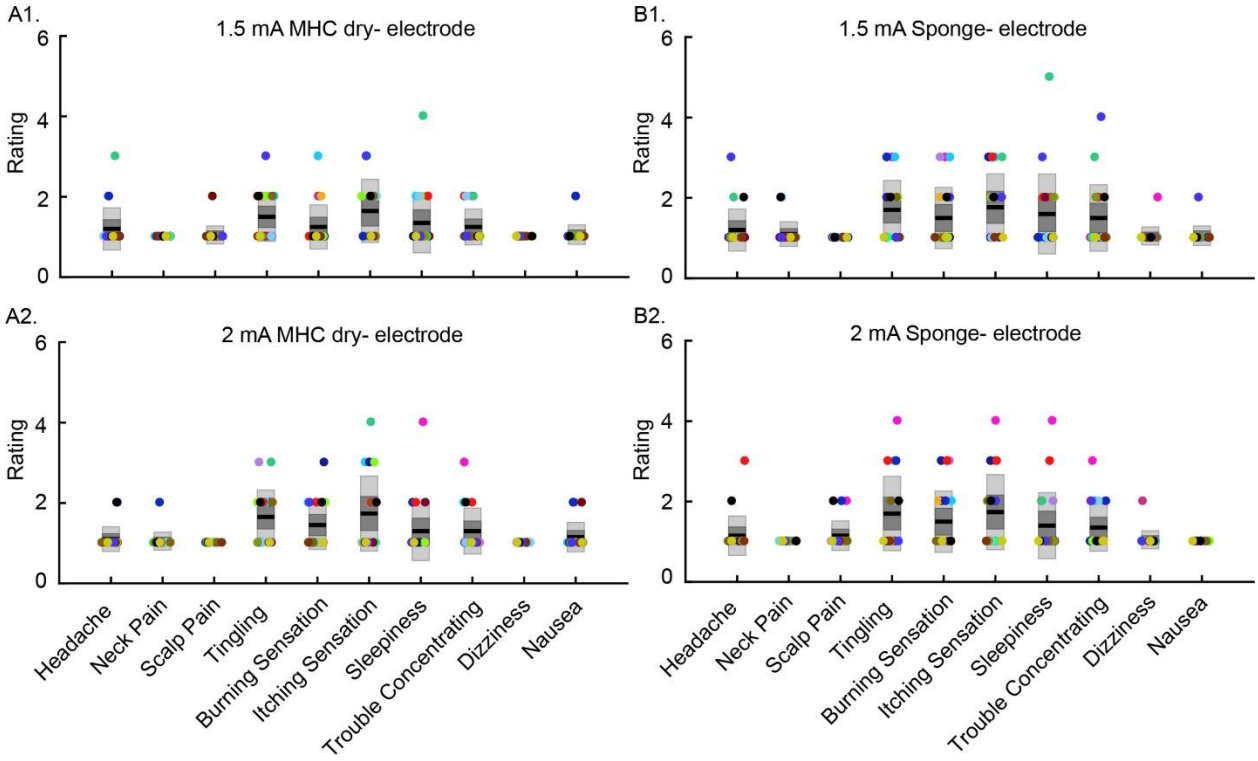

Figure 23. Representation of adverse events for both MHC dry-electrode and sponge-electrode across stimulation intensities (1.5 mA and 2 mA) on a scale of 1-5; 1: none, 5:max). Participants are color-coded. The highest incidence of adverse events across all treatment groups were skin tingling, burning, and itching sensations (A1, A2, B1, B2). There was no statistically significant difference ($P>0.05$) in adverse events between stimulation intensities, however between the electrode types, there was a significant difference ($P<0.05$): less adverse events reported in the MHC dry-electrode.

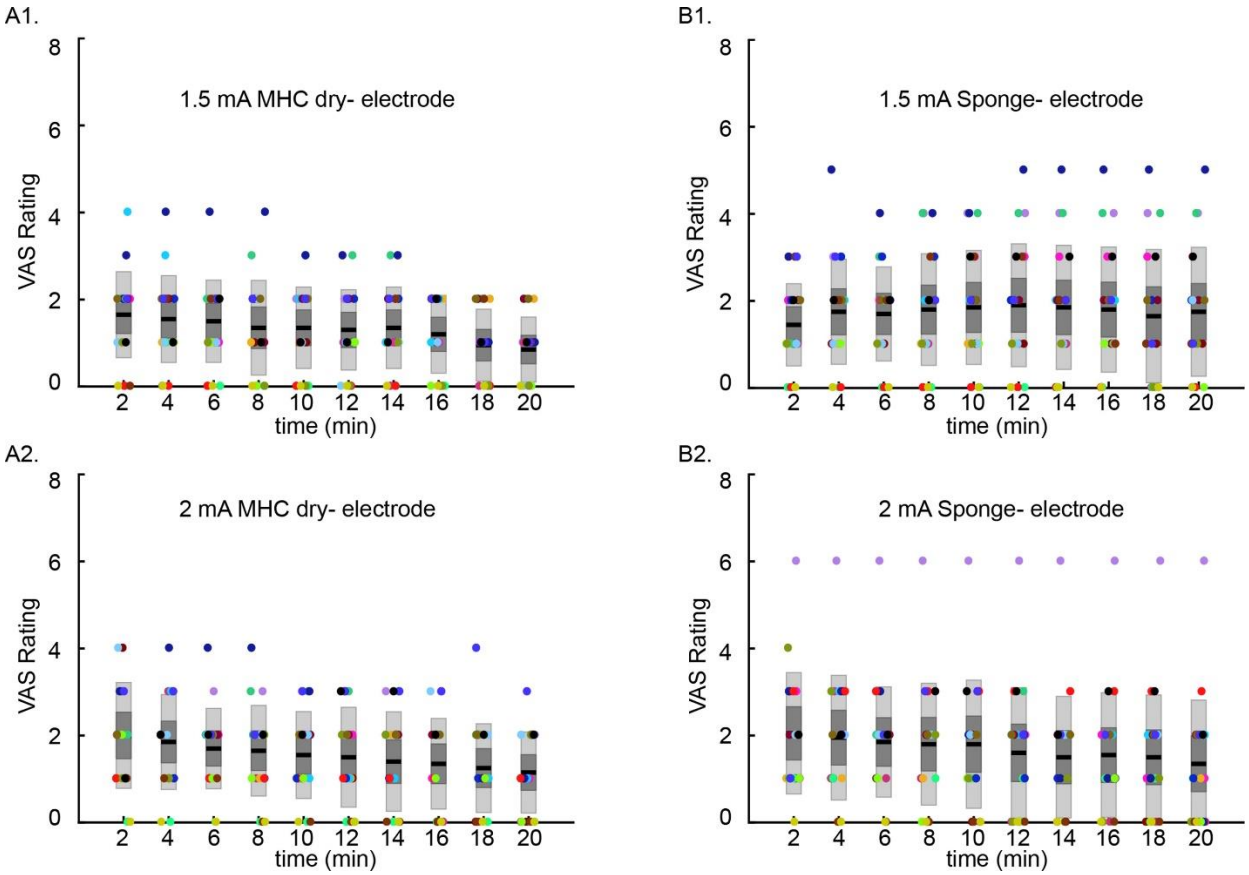

Figure 24. Adverse events reporting for MHC dry-electrode and sponge-electrode at different stimulation intensities for relationship to tDCS. There was no significant difference($P>0.05$) in adverse events between conventional sponge-electrode (B1, B2) and MHC dry-electrode (A1, A2), and the stimulation intensities (1.5 mA Vs 2 mA).

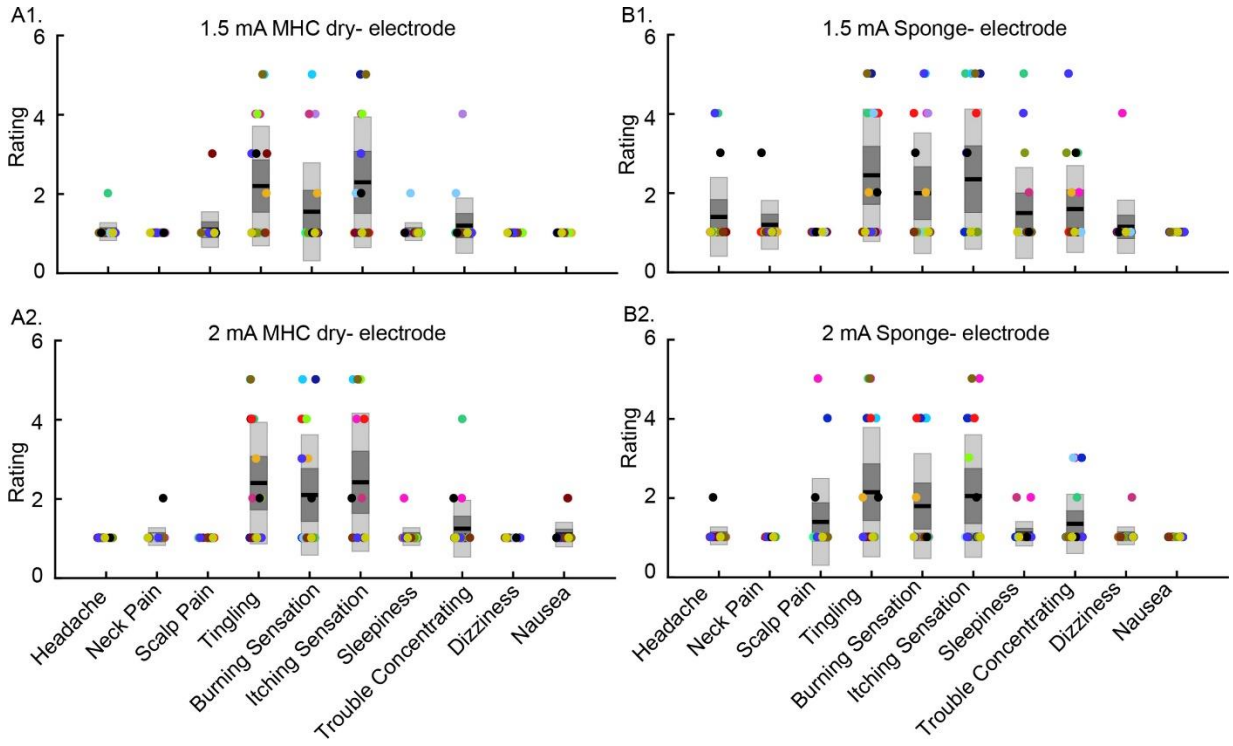

Figure 25. VAS rating at different stimulation intensities (1.5 mA and 2 mA) for a conventional sponge and MHC dry electrode. Participants (20) were color-coded as the cumulative adverse events and relationship to tDCS data, and the VAS pain score (1e10 scale; 1: no pain, 10: unbearable pain) was collected every 2 min during each stimulation sessions. There was no significant different ($P<0.05$) in the VAS rating across all four stimulation sessions.

The most common adverse events with the highest incidence across all treatment groups were skin tingling, burning, and itching sensations. The cumulative adverse events across stimulation intensities (1.5 mA (Mdn =1) Vs 2 mA (Mdn =1)) when analyzed using the Wilcoxon signed-rank test (non-parametric test) were not significantly different ($Z = -0.003$, $P = 0.997$), whereas across electrode types (MHC dry-electrode (Mdn =1) Vs sponge-electrode (Mdn =1)), the adverse events were higher for the sponge-electrode ($Z = -2.344$, $P = 0.019$) (Fig. 23). When analyzed the interaction between the electrode types and stimulation intensities in relationship to the tDCS, the adverse events were comparable ($Z = -1.760$, $P = 0.078$; $Z = -.439$, $P = 0.660$). The

median for stimulation intensities and the electrode types was 1 (Fig. 24). Since there was no significant time effect ($P > 0.05$) on the VAS data (VAS collected every 2 minutes during each stimulation session), the time data sets were collapsed together and analyzed for statistical significance. The VAS pain score was higher in the sponge-electrode (Mdn=2) than the MHC dry-electrode (Mdn=1.5) ($Z = 5.341$, $P = 1.41e-7$), whereas across the stimulation intensities (1.5 mA (Mdn = 2), 2 mA (Mdn = 2)), the VAS pain score was comparable ($Z = -0.567$, $P = 0.571$) (Fig. 25).

2.5. Discussion

We first defined a dry-electrode as 1) excluding any liquid of viscous electrolyte (as typical for conventional tDCS and HD-tDCS electrodes (Woods et al., 2016)) with the benefit of no accidental spread and no residue; 2) excluding any adhesive at the skin interface (common in TENS but rare for tDCS (Paneri et al., 2016)) either integrated into or around the electrolyte; and 3) excluding any electrode preparation steps, even just saturation, except connection to the stimulator (which is an implicit step for a swapping disposable electrodes). A Multilayer Hydrogel Composite (MHC) dry-electrode design which satisfied these basic criteria was developed and then the electrode performance was verified in terms of current delivery and tolerability. For the conditions tested here, the MHC-electrodes performed sufficiently based on the improved VAS and comparable adverse event reporting, when compared to the conventional sponge-electrodes.

Focused on tDCS technology, we did not test any additional stimulation waveforms in this study. But tDCS is considered demanding from an electrode design standpoint (Merrill et al., 2005) - for example, charge balanced pulses waveforms can be applied with conventional adhesive hydrogel electrodes while tDCS requires specialized electrodes (Paneri et al., 2016) - so our

success with tDCS is encouraging for additional waveforms. Still, only empirical testing can ultimately validate tolerability for each waveform and electrode design. In addition, we evaluated performance only below the hair line (SO positions) whereas tDCS is typically applied with at least one electrode above the headline (e.g. the common M1-SO montage). At a minimum, the MHC dry-electrodes may already be used below the hair line (e.g. SO) and a wet electrode above (e.g. M1). Noting the diffusivity of tDCS, other common montages, such as bifrontal positions (Brunoni et al., 2017; Sampaio-Junior et al., 2018), may be emulated by lowering the electrode below the hairline, without necessarily compromising brain current flow. Notwithstanding these questions, our results may encourage future work on the design and applications of dry-electrode stimulation.

Appendix 3: Adaptive current tDCS up to 4 mA

3.1. Outline

This Appendix describes the design and validation of electrodes and an adaptive controller to provide tDCS up to 4 mA. A version of this study has been published (Niranjan Khadka et al., 2019b). We concluded that provided specific electrodes and controllers, adaptive 4 mA tDCS is tolerated and effectively blinded, with acceptability likely higher in a clinical population and absence of regular querying. Indeed, presenting participants with overt controls increases rumination on sensation.

3.2. Introduction

With >1500 published reports in the past 5 years, transcranial direct current stimulation (tDCS) is an exhaustively investigated interventional neurotechnology (Woods et al., 2016), but using limited intensities. Circa 2000, canonical studies used 1 mA intensity (Nitsche and Paulus, 2000) and earlier clinical trials tested 2 mA (Brunoni et al., 2012). Over the next two decades and across a breadth of indications, only current of 1-2 mA intensities have been tested (Grossman et al., 2018; Loo et al., 2018) with limited exceptions. tDCS with 2.5 mA has been used in select clinical populations (Benabid et al., 1991; Loo et al., 2018). A case report of 3 mA over an extended period was considered safe (Andrade, 2013, p.). In 16 healthy participants 3 mA tDCS, with topical anesthetic cream, was tolerated and produced intensity-specific neuromodulation (Mosayebi Samani et al., 2019). A review of early evaluations of tDCS circa 1960 identified a single instance of 3 mA, with local anesthetic used (Esmaeilpour et al., 2017). High-definition tDCS (HD-tDCS) was tolerated at 3 mA (Reckow et al., 2018) in a sample of older adults. 3 mA split across two HD-tDCS targets (1.5 mA each) was tolerated (Hill et al., 2018). A single session

of 4 mA tDCS was evaluated safe and tolerated in 3 stroke patients (Chhatbar et al., 2017; Nitsche and Bikson, 2017). Brief 4 mA tDCS was applied to participants under general anesthesia with Deep Brain Stimulation (DBS) electrodes (Chhatbar et al., 2017). Twenty sessions of Adaptive 4 mA (using methods formulated here) was tolerated in 2 participants with major depression (Trapp et al., 2019).

Evidence from animal studies suggest that 4 mA does not approach injurious limits (Bikson et al., 2016; Jackson et al., 2017). The past decade has introduced advancements in tDCS electrode (Hahn et al., 2013; Khadka et al., 2018a; Niranjan Khadka et al., 2019d; Truong and Bikson, 2018) and stimulator technology (Hahn et al., 2013; Truong and Bikson, 2018)that may increase tolerability at higher currents. Despite extensive evidence that 1-2 mA tDCS relevant electric field modulate neuronal function (Jackson et al., 2016; Krause et al., 2017; Liu et al., 2018; Nitsche et al., 2005), benefits of moderately increasing current intensity have been debated (Vöröslakos et al., 2018).

We evaluated the total applied current and tolerability of three types of Adaptive 4 mA tDCS controllers; all types included adaptive ramps, impedance-based current mediation and a Relax-mode, but they differed in how Relax-mode was triggered: relying only on VAS pain score (condition 1: Adaptive 4 mA); relying on VAS pain score and participant activation of a Relax-button (condition 2: Adaptive 4 mA with Relax-button); relying on VAS pain score and participant activation of a Relax-button over the course of the session (condition 3: Adaptive 4 mA with historical-Relax-button). Total applied current and tolerability of the three adaptive conditions were also compared against 2 mA tDCS (condition 4) and sham tDCS (condition 5). tDCS was controlled by a customized tablet-based stimulator which, in all conditions, queried VAS pain and provided an Abort-button (activation will stop stimulation), and only in condition 2 and 3, a Relax-

button was provided (activation will transiently decrease based on a control algorithm). The ideal adaptive controller maximizes current delivery (up to 4 mA) while maintaining tolerability and avoiding dropouts.

In a randomized single-blind parallel-group design, 50 healthy adults received three daily 11-min (30 s ramp up + 10 min sustained period + 30 s ramp down) tDCS session of their assigned condition, while engaging in a distractor task. We report all tested conditions were well tolerated. While a priori providing participant with Relax-button may expect enhanced tolerability, we report the opposite (despite reduced current), presumably reflecting increased rumination of sensation. The tolerability of Adaptive 4 mA condition (without Relax-button) was not significantly different from 2 mA of Sham tDCS. These results do not bear on 4 mA tDCS without our controller or use of different electrodes. Noting we accessed a healthy population; our outcomes may be conservative for acceptability in clinical populations. These results support further investigation of Adaptive 4 mA with appropriate device design, electrodes, supervision, and a system for exploring still higher currents. Portions of these results were previously presented in abstract form (Borges et al., 2017; Niranjan Khadka et al., 2019a).

3.3. Materials and Methods

This study spans experimental measurement in participants, and an analysis of current, impedance, and self-reported tolerability and efficacy data.

3.3.1. Participants

The study was conducted in accordance to the protocols and procedures approved by the Institutional Review Board of the City College of New York, CUNY. Fifty healthy participants (37 males and 13 females; age 19-34 years; mean age 24.7± 4.9) were enrolled in this participant-

blind study. Participants with any evidence of skin disorders or sensitive skin (e.g. eczema, severe rashes), blisters, open wounds, burns including sun-burns, cuts or irritation (e.g. due to shaving), or other skin defects which compromise the integrity of the skin at or near stimulation locations were excluded from this study. All participants provided written informed consent to participate in the study. Participants were seated in an upright relaxed position throughout the stimulation.

3.3.2. Sensation and adverse events

Self-reporting questionnaires completed by the participants before and after each session (Table 1) assessed the extent of adverse events including headaches, nausea, neck pain, scalp pain, tingling, burning sensation, itching sensation, sleepiness, trouble concentrating, and dizziness on an intensity rating scale from 1- 4 (1 = absent, 2 = mild, 3 = moderate, and 4 = severe). In addition, participants quantified their experienced adverse events in relationship to tDCS on a scale from 1 – 5 (1 = none, 2 =remote, 3 = possible, 4 = probable, and 5 =definite). VAS (Visual analogue scale) pain score (scale: 0 - 10; 0: no pain, 10: intolerable pain) was collected every 2 min during the stimulation via a built-in VAS graphical user interface (GUI) of the tablet-based stimulator.

Condition	Adverse Events	Headache	Neck pain	Scalp pain	Tingling	Burning Sensation	Itching	Sleepiness	Trouble concentrating	Dizziness	Nausea
Adaptive 4 mA	Intensity (mean ± SD)	(1.13 ± 0.35)	(1.06 ± 0.26)	(1.20 ± 0.56)	(1.46 ± 0.64)	(1.53 ± 0.74)	(1.46 ± 0.64)	(1.20 ± 0.41)	(1.00 ± 0.00)	(1.00 ± 0.00)	(1.15 ± 0.36)
	Relation (mean ± SD)	(1.00 ± 0.00)	(1.00 ± 0.00)	(1.26 ± 1.03)	(1.80 ± 1.65)	(1.73 ± 1.53)	(1.46 ± 1.25)	(1.00 ± 0.00)	(1.00 ± 0.00)	(1.00 ± 0.00)	(1.10 ± 0.30)
Adaptive 4 mA with Relax-button	Intensity (mean ± SD)	(1.06 ± 0.26)	(1.06 ± 0.25)	(1.33 ± 0.48)	(1.00 ± 0.86)	(1.40 ± 0.63)	(1.93 ± 0.96)	(1.13 ± 0.35)	(1.06 ± 0.25)	(1.20 ± 0.56)	(1.00 ± 0.00)
	Relation (mean ± SD)	(1.26 ± 0.70)	(1.26 ± 0.70)	(1.73 ± 1.38)	(2.46 ± 1.76)	(2.00 ± 1.55)	(2.86 ± 1.95)	(1.00 ± 0.00)	(1.00 ± 0.00)	(1.13 ± 0.52)	(1.00 ± 0.00)
Adaptive 4 mA with historic-Relax-button	Intensity (mean ± SD)	(1.06 ± 0.26)	(1.13 ± 0.52)	(1.33 ± 0.62)	(1.67 ± 0.49)	(1.20 ± 0.41)	(2.13 ± 1.25)	(1.27 ± 0.46)	(1.20 ± 0.41)	(1.13 ± 0.35)	(1.00 ± 0.00)
	Relation (mean ± SD)	(1.06 ± 0.26)	(1.00 ± 0.00)	(1.60 ± 1.12)	(3.00 ± 1.69)	(1.33 ± 0.90)	(2.93 ± 1.83)	(1.13 ± 0.52)	(1.13 ± 0.52)	(1.40 ± 1.12)	(1.00 ± 0.00)
2 mA tDCS	Intensity (mean ± SD)	(1.20 ± 0.41)	(1.06 ± 0.26)	(1.06 ± 0.26)	(1.53 ± 0.74)	(1.46 ± 0.74)	(2.00 ± 0.75)	(1.33 ± 0.49)	(1.40 ± 0.63)	(1.06 ± 0.26)	(1.15 ± 0.36)
	Relation (mean ± SD)	(1.00 ± 0.00)	(1.00 ± 0.00)	(1.00 ± 0.00)	(1.13 ± 0.52)	(1.40 ± 0.82)	(1.86 ± 1.30)	(1.00 ± 0.00)	(1.13 ± 0.52)	(1.00 ± 0.00)	(1.10 ± 0.30)
Sham	Intensity (mean ± SD)	(1.13 ± 0.35)	(1.17 ± 0.36)	(1.13 ± 0.35)	(1.33 ± 0.62)	(1.13 ± 0.35)	(1.73 ± 0.70)	(1.10 ± 0.28)	(0.00 ± 0.00)	(1.06 ± 0.26)	(1.00 ± 0.00)
	Relation (mean ± SD)	(1.13 ± 0.99)	(1.00 ± 0.00)	(1.46 ±1.24)	(1.60 ± 1.29)	(1.53 ± 1.41)	(2.13 ± 1.59)	(1.00 ± 0.00)	(0.00 ± 0.00)	(1.06 ± 0.25)	(1.00 ± 0.00)

Table 2: Summary of participant reported adverse events as intensity and perceived relationship to tDCS.

3.3.3. Participant feedback for stimulation

The participants can provide feedback through the stimulation tablet GUI with two buttons: (1) The Relax-button which transiently decreases the current to minimize the participant's discomfort- available in condition 2 (Adaptive 4 mA with Relax-button) and condition 3 (Adaptive 4 mA with historical-Relax-button); (2) The Abort-button which linearly ramps down the tDCS current to 0 mA at the rate of 0.1 mA per 3 s till the session terminates, was available in all conditions. All participants were instructed that they could activate the Abort-button at any time during the stimulation if, they experienced any discomfort, or their VAS pain score was > 7, or they wished to stop stimulation for "any reason or no reason at all". In addition, participants in condition 2 (Adaptive 4 mA with Relax-button) and condition 3 (Adaptive 4 mA with historical-Relax-button) were instructed that the Relax-button could be activated in an event of VAS pain score > 5. Effectively, participants were permitted to activate the Relax-button as often as they wanted regardless of pain perception, which could result in an excessive Relax activation (see Results). Participants were also prompted every 2 min to score VAS pain. Finally, the Abort or the Relax-mode were automatically triggered, if the reported VAS pain score was 7 or higher (Abort), and 5 or higher (Relax-mode) respectively.

3.3.4. Adaptive 4 mA Controller

All conditions where the current target was 4 mA used an adaptive controller and logic (i.e. in none of the cases current simply ramped up linearly to 4 mA). The Adaptive 4 mA controller includes parallel functions (Fig. 26) of: 1) step-wise ramp up; 2) Impedance-based current

moderation; 3) Relax-mode current moderation; 4) Abort trigger. The overall rationale for this controller (testing it was the primary objective of this study) was to maximize current delivery while maintaining tolerability.

When stimulation is initiated, the incremental ramp up initiates with a linear ramp up to 2 mA over 30 s. Impedance-based current moderation not by the Relax-mode is active during this first 30 s. Current is increased from 2 to 4 mA in a step-wise fashion where current is sustained for 15 s and then ramped up in 0.5 mA increments over 15 s. With each increment taking 30 s, and 4 increments from 2 to 4 mA, the minimum time for current to attain 4 mA from 2 mA increment is 120 s. The minimum time to start stimulation at 4 mA is therefore 150 s.

The impedance-based current mediation is active during all times of stimulation. If impedance is > 20 k□ threshold during the ramp up to 2 mA, or > 20 k□ threshold during the ramp from 2 mA to 4 mA, or >10 k□ threshold at the 4 mA target, then current is reduced proportionally to the resistance increase above the threshold. If impedance decreases below this threshold, impedance-based mediation stops.

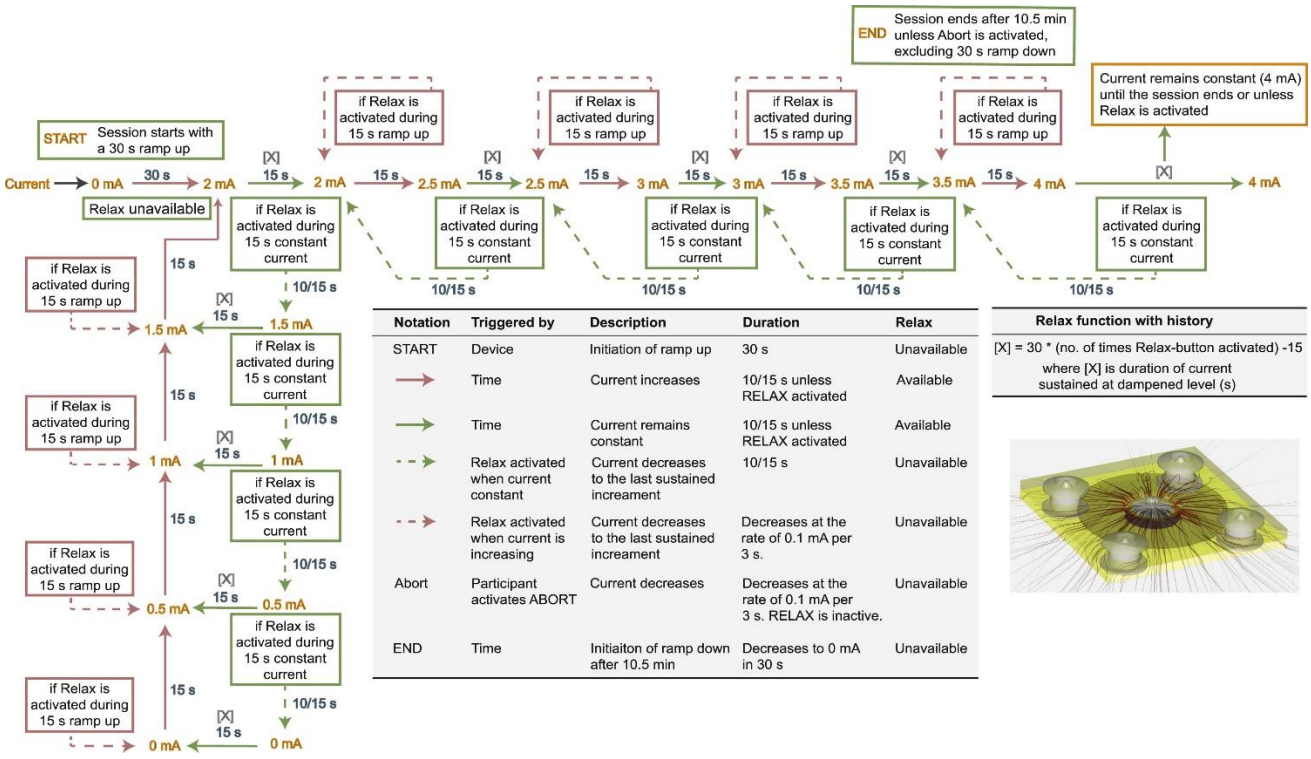

Notation	Triggered by	Description	Duration	Relax
START	Device	Initiation of ramp up	30 s	Unavailable
→	Time	Current increases	10/15 s unless RELAX activated	Available
→	Time	Current remains constant	10/15 s unless RELAX activated	Available
- - →	Relax activated when current constant	Current decreases to the last sustained increament	10/15 s	Unavailable
- - →	Relax activated when current is increasing	Current decreases to the last sustained increament	Decreases at the rate of 0.1 mA per 3 s.	Unavailable
Abort	Participant activates ABORT	Current decreases	Decreases at the rate of 0.1 mA per 3 s. RELAX is inactive.	Unavailable
END	Time	Initiaiton of ramp down after 10.5 min	Decreases to 0 mA in 30 s	Unavailable

Relax function with history
[X] = 30 * (no. of times Relax-button activated) -15 where [X] is duration of current sustained at dampened level (s)

Figure 26: 4 mA Adaptive Algorithm and Logic for Current Control. The current intensity transiently increases over time up to 4 mA with 15 s intervals of constant current phase followed by an increment of current intensity by 0.5 mA over a duration of 15 s. The Relax-button lowers the current for 10/15 s (depending upon the stimulation conditions) to the last sustained current intensity and then the current creeps back up after 15 s. The Abort-button terminates stimulation session and ramps down the current to 0 mA over a period of 30 s. The goal of the cyclical logic diagram is to obtain a well-tolerated optimal current intensity. (Inset) Optimized electrode with 5 rivets. FEM simulation of current streamlines showing current density is distributed.

The Relax-mode is triggered either automatically by a VAS pain score of > 5 or participant activation of the Relax-button, when available. In the simplest implementation, when triggered, the Relax-mode ramps down the current by a 0.5 mA to the last sustained increment current for 15 s (Condition 1, Adaptive 4 mA ; Condition 2, Adaptive 4 mA with Relax-button) or 10 s (Condition 3, Adaptive 4 mA with historical- Relax-button), sustains the reduced current for a

minimum of 15 s, and then ramps up the current back to the initial value over 15 s. Relax-mode can be triggered during the ramp up where it effectivity throttles, but does not stop the general increase. This mode can also be activated repeatedly except during the 15 s or 10 s ramp down and when otherwise disabled (during the first 30 s ramp up). Triggering a second Relax-mode while the current is ramping down from the first Relax-mode has no effect on the prior ramp down. In the adaptive 4 mA (where Relax-mode is only activated automatically) and adaptive 4 mA with Relax-button, the duration of reduced current is sustained for fixed 15 s, while in the adaptive 4 mA with historical- Relax-button, the duration of reduced current is sustained according to equation 1.

Duration of current sustained at dampened level (s)=30[no.of times Relax-button activated]*– 15 (1)

As aforementioned, VAS pain score > 7 or participant activation of Abort-button, when available, automatically triggered the Abort. Once triggered, current ramps down to zero current level and the sessions ends. Stimulation Conditions

Participants were randomly assigned to one of the five treatment conditions: Condition 1, Adaptive 4 mA stimulation; Condition 2, Adaptive 4 mA with Relax-button; Condition 3, Adaptive 4 mA with historical-Relax-button; Condition 4, 2 mA tDCS; Condition 5, Sham. A M1-SO montage was used with anode placed over the left primary motor cortex (C3: EEG 10-20) and cathode placed over the contralateral-supraorbital (Fp2: EEG 10-20) for all treatment conditions. Current was administered for 11 min (including 30 s of ramp up and down each and a 10 min sustained period) using a specialized device (Soterix Medical Inc., New York, USA; Ybrain Inc, Seongnam-si, Republic of Korea) of a tablet-based tDCS stimulator with GUI participant interface,

snap-headgear (which ensured placement; (Knotkova et al., 2019)), and single-use pre-saturated 5 x 5 cm snap electrodes EasyPad, Soterix Medical Inc., New York, USA).

The 11 min sessions were considered more than long enough to encompass period of impedance transients (Hahn et al., 2013; McFadden et al., 2011; Woods et al., 2016) and maximal self-report sensation (Greinacher et al., 2018). This study was not intended to resolve acute or lasting changes in brain function. A parallel-group design was used to avoid confounds from participants recognizing difference across conditions (e.g. being provided a Relax-button only in some conditions) and increase reliability or testing for changes across repeated sessions. Three repeated sessions, with at least one day interval, were considered sufficient to resolve any immediate (e.g. after one session) change in tolerability based on repetition (session number) across conditions. Scalp current and impedance were automatically queried in real-time upon the onset of stimulation by the smart stimulator and stored in cloud for later analysis.

a. Condition 1, Adaptive 4 mA: In this mode of stimulation, the current ramps up to 4 mA using an incremental ramp (Fig. 27A). The ramp up and sustained phase are limited based on impedance and VAS pain score (as needed) (Fig. 27B). The incremental ramp starts with a ramp up to 2 mA over 30 s during which Relax-mode is disabled, and then ramps up to 4 mA over a minimum (if Relax-mode is not triggered) of 120 s. The 2 to 4 mA ramp up is step-wise according to the adaptive controller logic (if Relax-mode is not activated): the current at 2 mA is sustained for 15 s and then linearly increases the current to 2.5 mA over 15 s, with this rule is repeated till the intended 4 mA current intensity is attained (Fig. 26). The adaptive 4 mA ramp up is thus a total of 150 s. In the participant GUI, the Abort-button is always available, but in this condition the Relax-button is not. Therefore, in the Adaptive 4 mA condition, the Relax-mode current mediation can only be triggered

automatically by a VAS pain score of > 5 (Fig. 27C). As in all conditions, Abort is automatically triggered by a VAS pain score > 7.

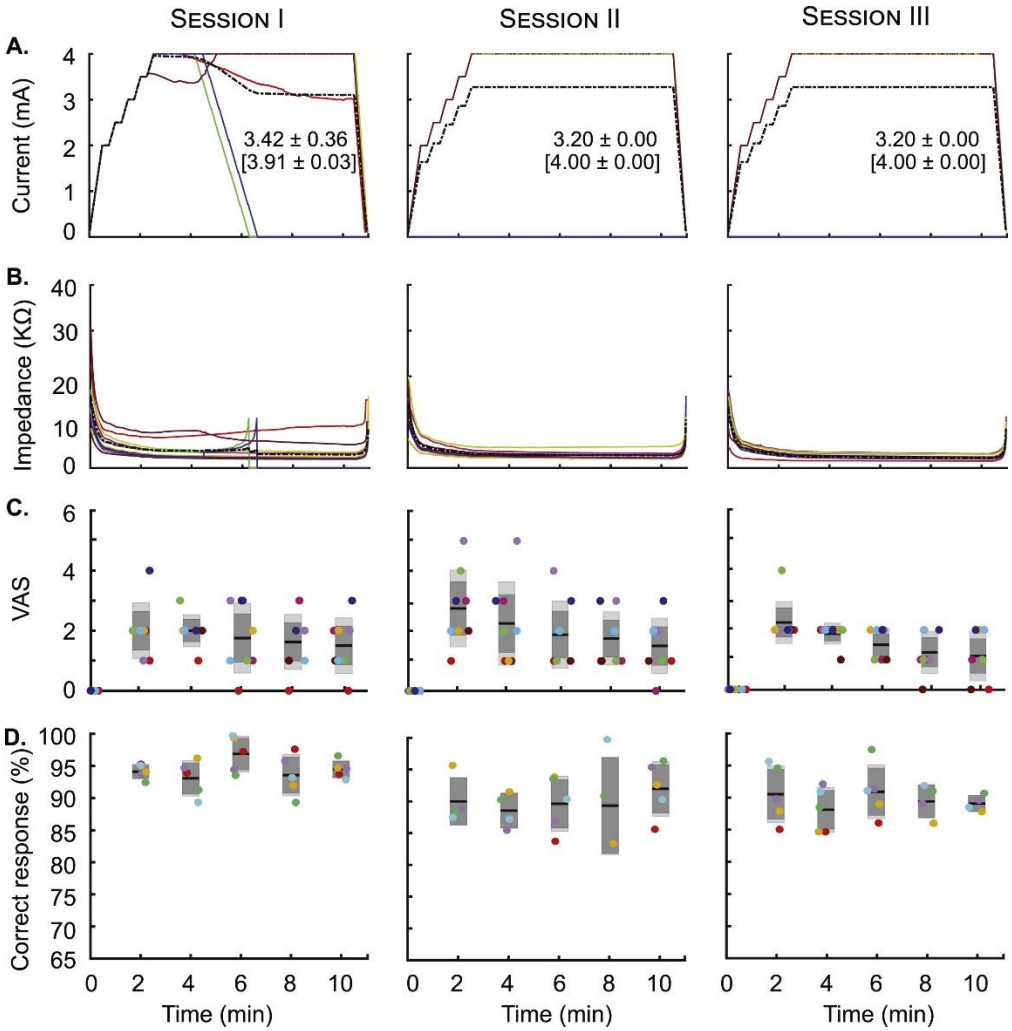

Figure 27: Current waveform, impedance, VAS pain score, and lexical decision task for Adaptive 4 mA condition. Participants per condition are color coded. Current ramps up and maintains to a 4 mA target with adaptive logic, (automatic only) VAS pain score-based Relax-mode activation, and impedance-based current moderation. (A) Current applied. There were 2 dropouts during session I (green and blue traces). Also, in session I there were 2 impedance-based current reduction (red and brown traces). Average traces (dashed line) and current values without the parenthesis represents condition including dropouts. Values within parenthesis represent average session current excluding dropouts. (B) Impedance. Average impedance across sessions

was < 10 kΩ. (C) Participant VAS pain score collected before and every 2 minutes during stimulation. Average VAS pain score across sessions was ≤ 3 with no instance of VAS pain score > 5. (D) Correct response range for the lexical decision task, scored every 2 minutes during stimulation, was 89-100 %.

b. Condition 2, Adaptive 4 mA with Relax-button: This mode is similar to Adaptive 4 mA with the addition of a Relax-button that participants can activate ad libitum, though in principle they are instructed to do so only under significant discomfort (VAS pain score > 5) (Fig. 28). After the 30 s ramp up to 2 mA, activating Relax-button triggers the transient Relax-mode current mediation. Relax-mode is also automatically activation by a VAS pain score > 5 (Fig. 28C). The Abort-button is available.

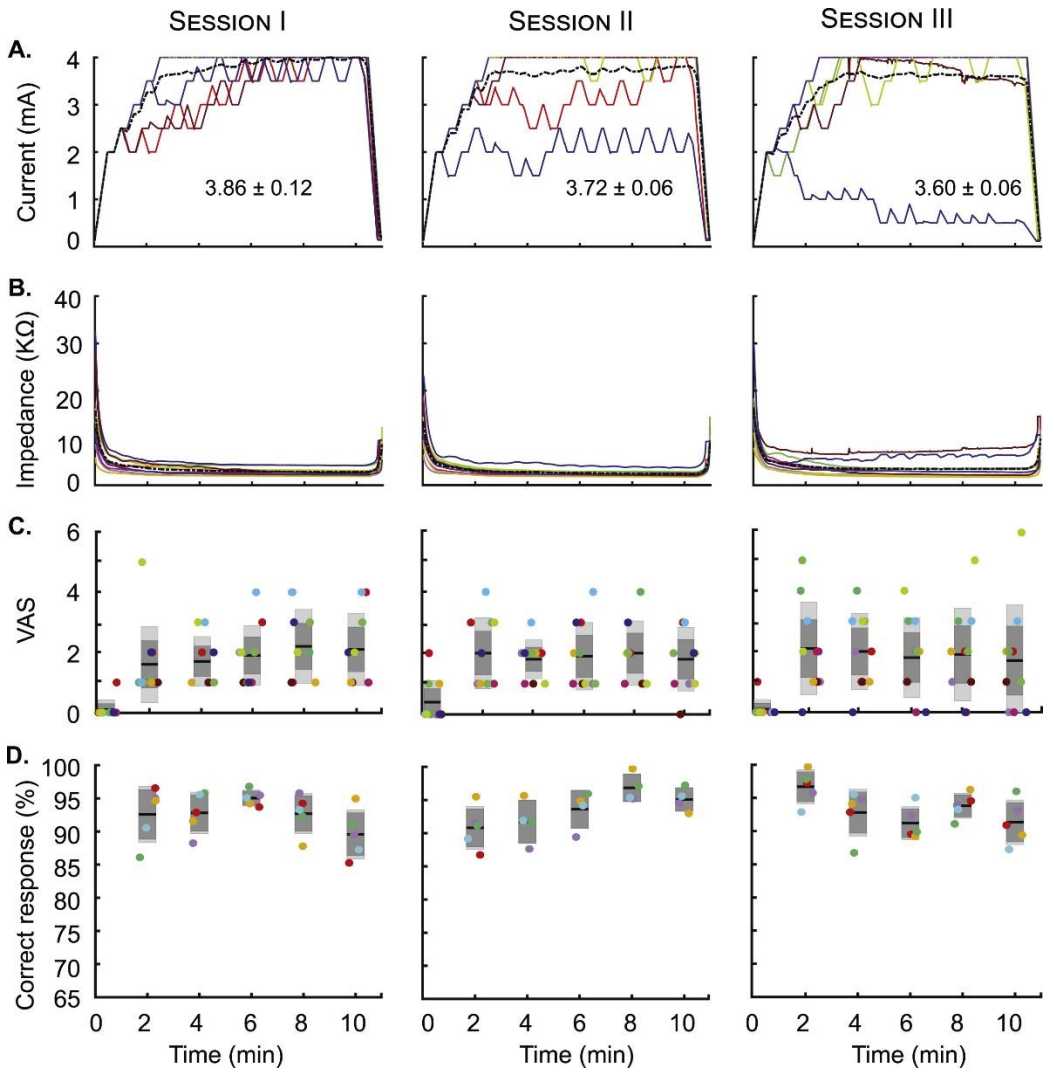

Figure 28: Current waveform, impedance, VAS, and percentage of correct response for the Adaptive 4 mA with Relax-button condition. Participants per condition are color coded. Current ramps up and maintains to a 4 mA target with adaptive logic, automatic (VAS pain score-based) and participant activated Relax-mode, and impedance-based current moderation. (A) Current applied. Reductions in current are associated with participant Relax-button activation used by a minority of participants (but repeatedly). A single instance of VAS pain score > 5 was reported at the end of session III. (B) Average impedance was < 10 kΩ for all participants across sessions. (C) Average VAS score collected before and every 2 minutes during stimulation, across sessions was

≤ 2. Once instance of VAS pain score > 5 at the end of session III (green dot). (D) Range of correct response of lexical decision task, scored every 2 minutes during stimulation was 86 -100 %.

c. Condition 3, Adaptive 4 mA with historical-Relax-button: This mode is similar to Adaptive 4 mA with Relax-button, however, after completion of a Relax-mode triggered ramp down (10 s), the current is sustained at this dampened level for a time that increases with the number of prior Relax-mode activation (equation 1) (Fig. 29). For example, activation of Relax-mode twice (by activating Relax-button or VAS pain score > 5) will sustain the reduced current for 45 s. The Abort-button is available.

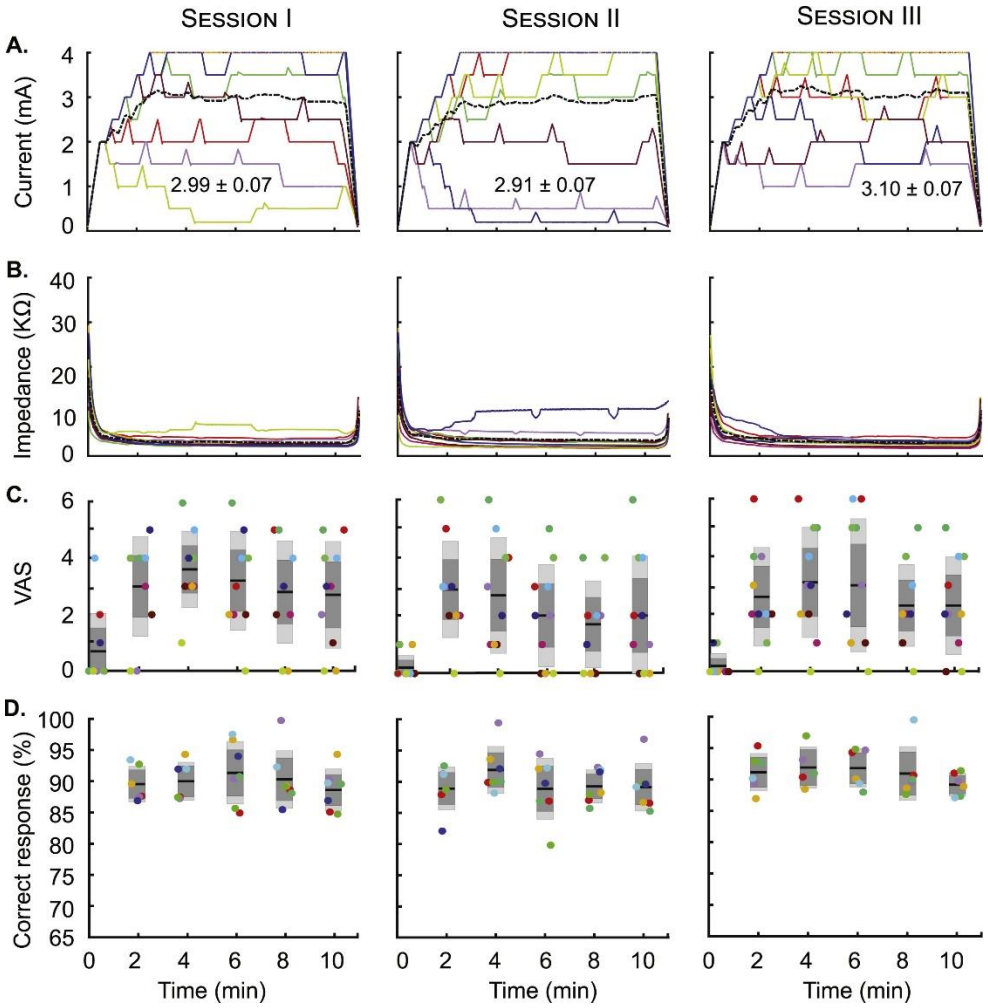

Figure 29: Current waveform, impedance, VAS, and lexical decision task for Adaptive 4 mA with historical-Relax-button condition. Participants per condition are color coded. Current ramps up and maintains up to a 4 mA target with adaptive logic, automatic (VAS pain score-based) and participant activated Relax-mode, and impedance-based current moderation. With increasing number of Relax-button activation, the duration of current moderation increases. (A) Current applied. Reductions in current are associated with participant activation of Relax-button and there were 9 instances of VAS pain score > 5 triggering an automatic Relax-mode. (B) Average impedance was < 10 kΩ. (C) Average VAS pain score, collected before and every 2 minutes during stimulation, across sessions was ~ 3. The highest VAS pain score was 6 reported by 4 participants (green, light blue, red, dark blue), a total of 9 instances. (D) Percentage of current response of the lexical decision task, scored every 2 minutes during stimulation, ranged from 80-100 %.

d. Condition 4, 2 mA tDCS: This mode is a conventional 2 mA tDCS mode of stimulation but with impedance-based current mediation (Fig. 29). Current ramps up linearly to 2 mA over 30 s, and is sustained for 10 min, before ramping down linearly over 30 s. The Abort-button is available.

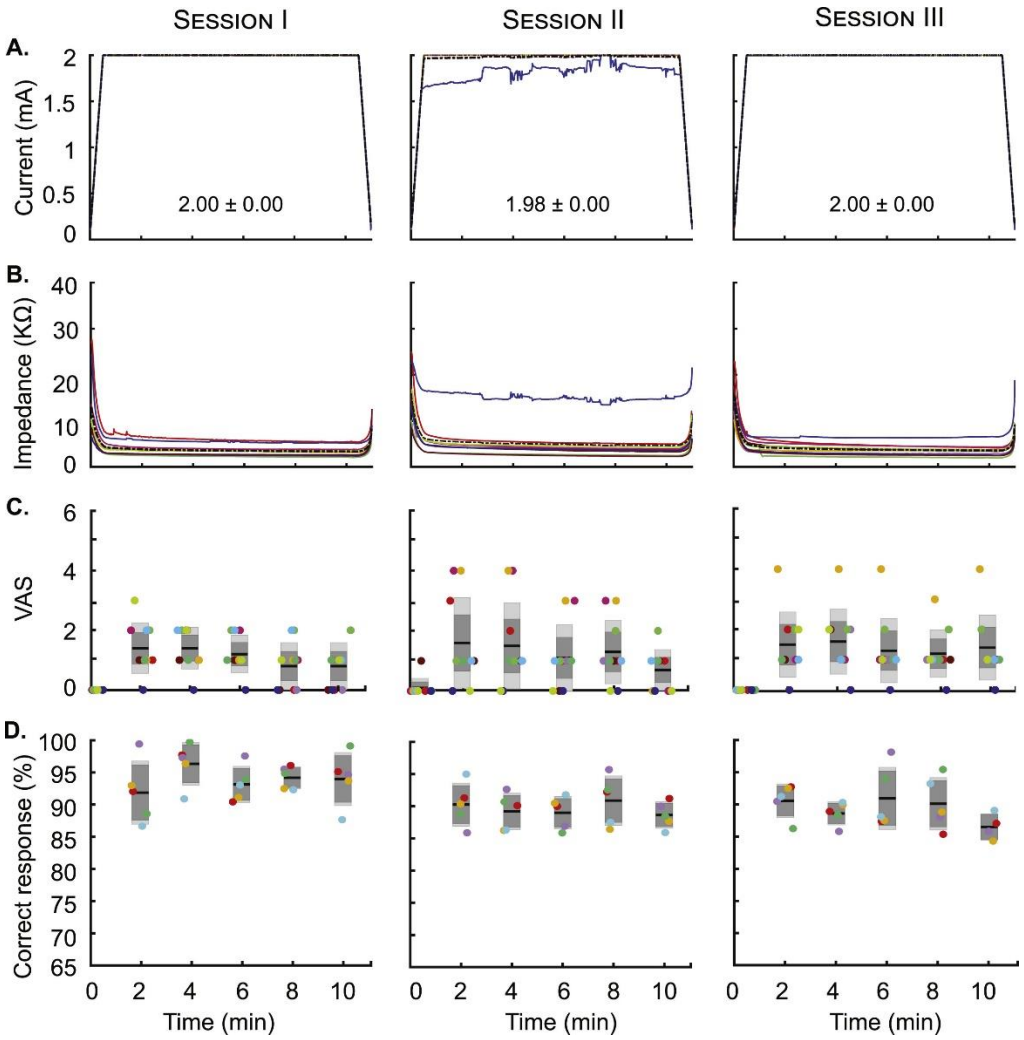

Figure 30: Current waveform, impedance, VAS, and lexical decision task for 2 mA stimulation condition. Participants per condition are color coded. Current ramps up and maintains to a 2 mA target with impedance-based current moderation (A) Current waveform. (B) Impedance. There was one session with impedance-based current reduction in session II (blue trace). (C) Average VAS pain score was < 2 across all sessions with no instance of VAS pain score > 4. (D) Range of correct response of the lexical decision was 85-100 %.

e. Condition 5, Sham stimulation: In this conventional mode of sham stimulation, current ramps up linearly to 2 mA over 30 s and then immediately ramps down over 30 s (Fig. 31). The Abort-button is available.

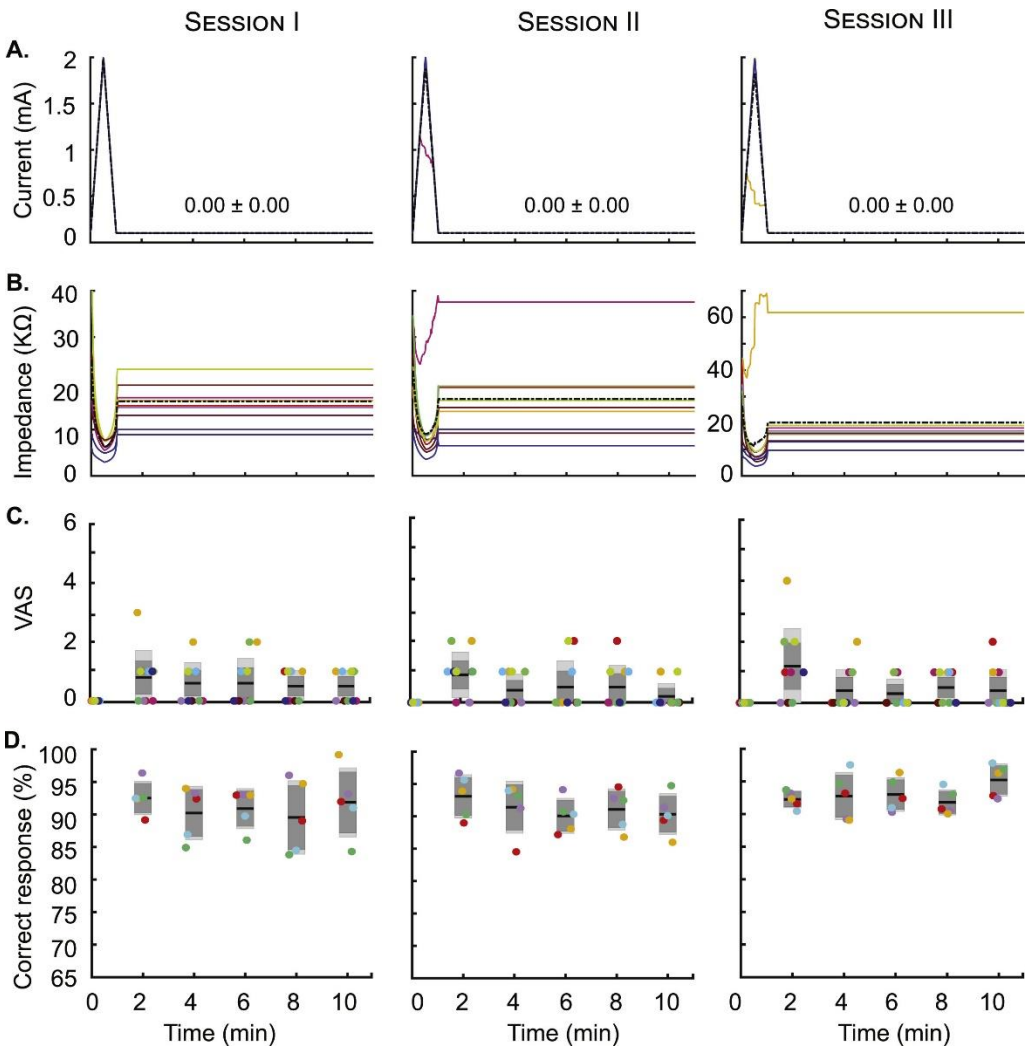

Figure 31: Current waveform, impedance, VAS pain score, and lexical decision task for Sham stimulation condition. Participants per condition are color coded. Current ramps up and down from a 2 mA target. (A) Current waveform. There was one abort each in session II and session III. (B) Impedance. Relatively higher impedances reflect depence on test current level. There was one impedance-based current reduction during the ramp up-down in session II. (C) Average VAS pain score, collected before and every 2 minutes during stimilation, was ≤ 1 across all sessions. (D) Range of correct response of the lexical decision, scored every 2 minutes during simulation, was 84-100 %.

3.3.5. Lexical decision task

During the stimulation session, the participants engaged in a lexical decision task (Branscheidt et al., 2018) as a distractor (Fig., 27D, 28D, 29D, 30D, 31D). On the computer screen separate from the tDCS device GUI, participants were presented with a mixture of words (e.g. canorous) and pseudowords (nonsense strings that represent the phonotactic rules of a language, like "trud" in English) and asked whether the presented stimulus was a word or not. The lexical decision task was paused every 2 min when participants were prompted to report the VAS pain score.

3.3.6. Statistical analysis

Normality test of VAS score and adverse events responses were tested using Shapiro-Wilk tests with Lilliefors significance correction. A corresponding parametric (ANOVA) or non-parametric (Kruskal-Wallis test) determined the significance of the data. When significant, post-hoc pairwise comparison was conducted using parametric Tukey's HSD test or non-parametric Dunn's test to find the difference between groups. A critical value (P) of < 0.05 was accepted as a significant difference between the groups. MATLAB function "rmoutliers" detected and removed outliers from the data based on mean (outlier defined as an element of a given dataset more than 3 standard deviations from the mean). Note that no outliers were detected for any primary outcome measures or for statistical test, but outliers were identified on lexical decision task (reflecting participants not engaging in the task) and were removed for graphing purposes.

3.4. Results

A total of 144 treatment sessions were completed. No serious adverse events were reported in the entire study. There were two aborts in the first session of the adaptive 4 mA waveform (no Relax-button) condition. In Sham stimulation (condition 5), there was one abort in session II and

one abort in session III. Per study design, participants who activate Abort-button withdrew from the rest of the sessions, regardless of their willingness to continue. Across all conditions and sessions, there were no instances of VAS pain score 7 (including in the participants who activated Abort-button), which would trigger an automatic Abort. Adverse events, VAS pain scores, lexical decision task performance, current, and impedance across every sessions of the study conditions were reported.

3.4.1. Current and Impedance

We analyzed the current intensities, both including and excluding the dropouts for the Adaptive 4 mA (no Relax-button) condition. Current intensities including the dropouts for the Adaptive 4 mA condition for sessions I, II, and III were 3.42 ± 0.36, 3.20 ± 0.00, and 3.20 ± 0.00, respectively (Fig. 27). Excluding the dropout, the current intensities for this session I, II, and III were 3.91 ± 0.03, 4.00 ± 0.00, and 4.00 ± 0.00, respectively. There were no instances of VAS pain score > 5 (which triggered an automatic Relax-mode) across sessions. There were 2 instances across sessions where impedance-based current mediation was active for at least 1 s (Fig. 28).

The current intensities (mean ± SD) for adaptive 4 mA with Relax-button were 3.86 ± 0.12, 3.72 ± 0.06, and 3.60 ± 0.06 for session I, II, and III, respectively. This reduction in current from the 4 mA target reflected Relax-button activation by a minority participant. These participants activated Relax-button repeatedly, while not reporting high VAS pain score. Across sessions, there was 1 instance of VAS pain score > 5. There was 1 instance across sessions where impedance-based current mediation was active for at least 1 s. No participant activated the Abort-button.

For Adaptive 4 mA with historical-Relax-button, the current intensities for session I, II, and III were 2.99 ± 0.07, 2.91 ± 0.07, and 3.10 ± 0.07, respectively. This reduction in target current

(4 mA) reflected Relax-button activation. There was no Abort-button activation and no instance of impedance-based current mediation across sessions. Across sessions, there were 9 total instances of VAS pain score > 5 (which triggered automatic Relax-mode).

For 2 mA stimulation, the current intensities for session I, II, and III were 2.00 ± 0.00, 1.98 ± 0.00, and 2.00 ± 0.00, respectively. The reduction in current for session II reflects 1 instance of impedance-based reduction. For 2 mA stimulation condition, there were no instance of VAS pain score > 5.

In Sham stimulation, there were no instance of VAS pain score > 5 (though as noted, 2 dropouts following Abort-button activation) and 2 instances across sessions in which impedance-based current mediation was active (always during the ramp up/down)

Average impedance in all study conditions except the sham condition was < 10 kΩ across sessions. For Sham stimulation, the average impedance excluding ramp down was > 20 kΩ across sessions, reflecting the nature of impedance measurement (not unusual conditions).

A two-way ANOVA tested the significant difference in the current intensities across different treatment groups. Including the dropouts (of the Adaptive 4 mA and Sham conditions), there was a statistically significant difference in group means among the study conditions, $F(4, 8) = 868.84$, $P < 0.05$. The mean current intensities across each study conditions were significantly different from all others (Tukey's HSD test; $P < 0.05$). In this analysis including the dropouts, Adaptive 4 mA with Relax-button condition has more current for each session (I: 3.86 ± 0.12; II: 3.72 ± 0.06; III: 3.60 ± 0.06) compared to other conditions. Interactions between the session number and study condition on current intensity was not significant, $F(2,8) = 1.5633$, $P > 0.05$. Excluding the drop-outs, the main effect of study conditions on mean current intensity was

significant (F (4,8) = 1126, P < 0.05). Mean current intensities across conditions were different from all others (P < 0.05). In this analysis excluding the dropouts, Adaptive 4 mA condition provided significantly more current in all three sessions (: 3.91 ± 0.06; II: 4.00 ± 0.00; III: 4.00 ± 0.00; P< 0.05) than Adaptive 4 mA with Relax-button condition. There was no significant interaction between the session number and the study condition (F (2,8) = 0.16, P > 0.05).

3.4.2. Adverse Events

Frequently reported adverse events were skin itching, tingling, and mild burning sensations (see supplemental Fig. 33 and 34). A non-parametric Kruskal-Wallis tested the significant difference in adverse events among the study conditions. There was no significant difference in the adverse events intensity among the five study conditions ($\chi 2 = 2.3$, df = 4, P > 0.05). However, across study conditions, adverse events intensity in relationship to tDCS was significantly different ($\chi 2 = 11.6$, df = 4, P < 0.05). Conventional 2 mA (mean rank = 21.0) and Adaptive 4 mA (mean rank = 25.65) conditions both had lower adverse events in relationship to tDCS (P < 0.05) than the Adaptive 4 mA with Relax-button (mean rank = 33.85) condition. Sham condition had lower adverse events in relationship to tDCS (P < 0.05) than adaptive 4 mA with historical-Relax-button and adaptive 4 mA with Relax-button conditions.

3.4.3. VAS pain score

The VAS pain score was statistically significant amongst the stimulation conditions ($\chi 2 = 49.71$, df = 4, P < 0.05, Kruskal-Wallis test; VAS mean rank: Sham (34.23); Adaptive 4 mA with historical-Relax-button (106.88); Adaptive 4 mA with Relax-button (92.52); 2 mA (64.68); Adaptive 4mA waveform (79.18)). VAS pain score for the Sham condition was significantly lower (P < 0.05) than the Adaptive 4 mA, Adaptive 4 mA with Relax-button and the Adaptive 4 mA with

historical-Relax-button. Conventional 2 mA tDCS had lower VAS pain score than Adaptive 4 mA with historical-Relax-button. There was no significant difference among the other remaining stimulation conditions ($P > 0.05$). Interactions between the session number and stimulation condition on VAS pain score was not significant ($\chi 2 = 0.4$, $df = 2$, $P > 0.05$) and didn't vary significantly across sessions for all stimulation conditions ($P > 0.05$).

3.4.4. Lexical Decision task

The subjective response of the lexical decision task for each study condition was reported as correct response percentage across sessions (min and max) as: Adaptive 4 mA (max: 100%; min: 89%), Adaptive 4 mA with Relax-button (max: 100%; min: 86%), Adaptive 4 mA with historical-Relax-button (max: 100%; min: 80%), 2 mA tDCS (max: 100%; min: 85%), Sham (max: 100%; min: 84%). The average correct response percentage was > 90 % across all stimulation conditions. Our study was not designed to resolve condition-specific effects on task; indeed, in some cases participants temporarily stopped engaging in the task (e.g. distraction, boredom) resulting in artifactual score reduction.

3.5. Discussion

Our results provide evidence in support for the tolerability of Adaptive 4 mA tDCS and so the feasibility of trials to test efficacy of higher dose tDCS. We do not identify a significant difference in subjective tolerability (VAS, adverse events) between Adaptive 4 mA, 2 mA, and Sham conditions. Tolerability across these conditions is also broadly consistent with prior reports using 2 mA (Antal et al., 2017; Fertonani et al., 2015; Kessler et al., 2012; Khadka et al., 2018a; Reckow et al., 2018). Our results should only be interpreted inclusive of our specific tDCS techniques including current escalation algorithm in 4 mA conditions (Fi. 24), impedance-based

current moderation and high-performance single-use electrodes across conditions, and other study design specifics discussed next.

Participants were informed that the purpose of this study was to evaluate their discomfort during the session and investigate the tolerability aspects of tDCS and were queried regularly on VAS pain score. This design, despite the distractor task, may have encouraged rumination on sensation thereby compromising self-reported tolerability. Indeed, in the two conditions where a Relax-button was offered to the participants (Adaptive 4 mA with Relax-button and Adaptive 4 mA with historical-Relax-button), tolerability was poorer compared to both Adaptive 4 mA and even conventional 2 mA. A clinical population may be more motivated and accepting (Aparício et al., 2016; Moffa et al., 2017) of mild adverse effects than our cohort of healthy young adults. Indeed, in a pilot clinical trial of Adaptive 4 mA, 20 sessions were all completed and tolerated (average VAS pains score of 1.1-1.6, max 3) in two participants with major depression (Trapp et al., 2019) – Relax-button (and Abort-button) were only in a physician directed controller, with no instance of request to activate by participants.

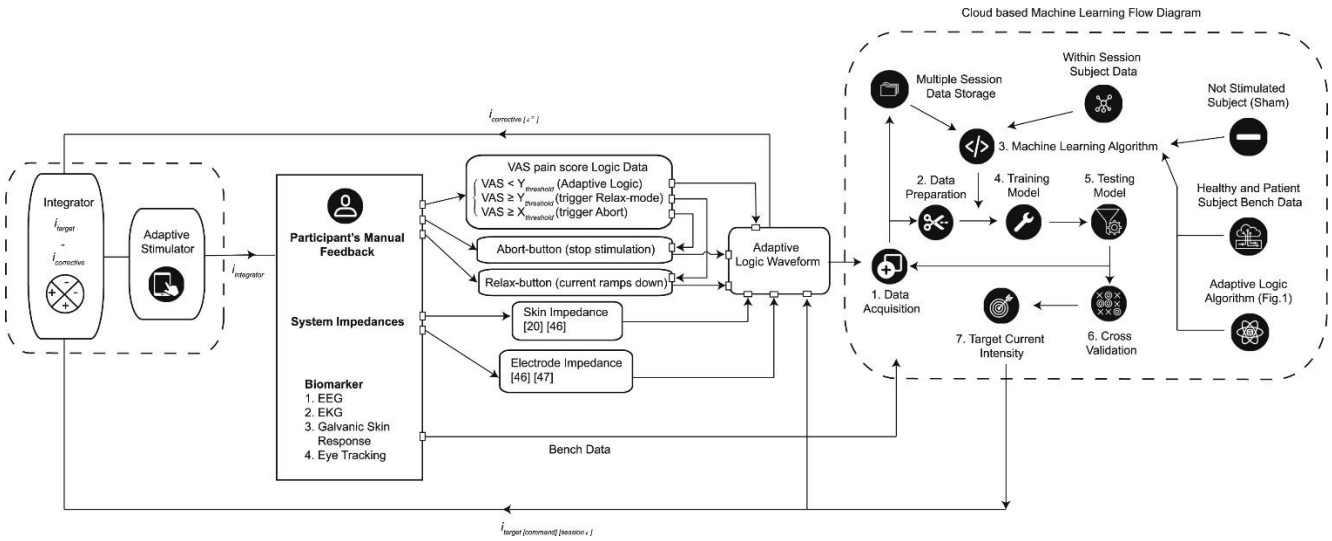

Figure 32. Concept for cloud based machine-learning Adaptive tDCS optimization. Optimized dosage and tolerability profile are maintained for efficacy of tDCS using an Adaptive Logic Waveform tailored from participant's manual feedbacks (VAS pain score, Abort-button, or Relax-button activation), automatic VAS pain score-based Relax-mode and Abort, system impedance (skin impedance (Hahn et al., 2013; Khadka et al., 2015a) and electrode impedance (Khadka et al., 2015b, 2015a), and biomarkers (EEG, EKG, galvanic skin response, eye tracking etc.). This waveform data is further processed via a cloud-based machine learning step to train, test, and validate the target current intensity for individualized tDCS. A smart cloud based current regulator device integrates the current output and other data collected from the participants.

We are not aware of prior tDCS studies with Abort or Relax buttons being overtly presented to participants in an integrated GUI device. All four study-dropouts followed activating Abort-button - two each in the Sham and Adaptive 4 mA conditions – never associated with especially high VAS pain score. Relax-mode activation was also not well correlated with VAS pain score and not reflecting instructions to activate Relax-button at VAS pain score > 5. Activation of Relax-button by some participants approached the maximum allowed iterations under Adaptive 4 mA with Relax-button (~10 times) and Adaptive 4 mA with historical-Relax-button (~4 times) suggesting continual Relax-button activation, even at current below 1 mA. Thus, when and how to include these features in Adaptive 4 mA trials is complicated.

We report no significant difference in VAS pain score or adverse events between Sham condition, 2 mA, and Adaptive 4 mA conditions. Given general discussions on the reliability of sham protocols in tDCS (Ezquerro et al., 2017; Fonteneau et al., 2019; Greinacher et al., 2018; Kessler et al., 2012; Palm et al., 2013; Turi et al., 2019), this warrants brief commentary. Foremost, the reliability of sham depends on tolerability of the active tDCS arm which is determined by electrode design and application protocols. Here, we used electrodes optimized for tDCS, that are

single-use and pre-prepared (saturated, no assembly) for consistency (Fig. 32). Second, the success of a sham arm in any given experiment is predicated on the overall study design (including how blinding success is defined) and not only perfectly replicating side-events. Indeed, since current evidently produces sensation, under sufficiently persnickety experimental design (including if we significantly increased participant number), participants will resolve differences between any doses.

The system developed and verified here, using Adaptive ramp, impedance-based current moderation, Relax-mode, and optimized electrodes may support testing of still higher current intensities, including in clinical populations. Providing participants control over the tDCS dose has implications for trial design - but dose titration, whether by clinician or patients, is universal across neuromodulation approaches (Perera et al., 2016; Riederer et al., 2015) with the exception of tDCS. Interestingly, our trial shows providing participants with such control does not necessarily enhance tolerability. The present study on tolerability is ambivalent to the benefits of higher currents (Esmaeilpour et al., 2018) but provides a system supporting dose-response studies that underpin intervention optimization, which have been curtailed to a limited range in tDCS.

Supplementary figures

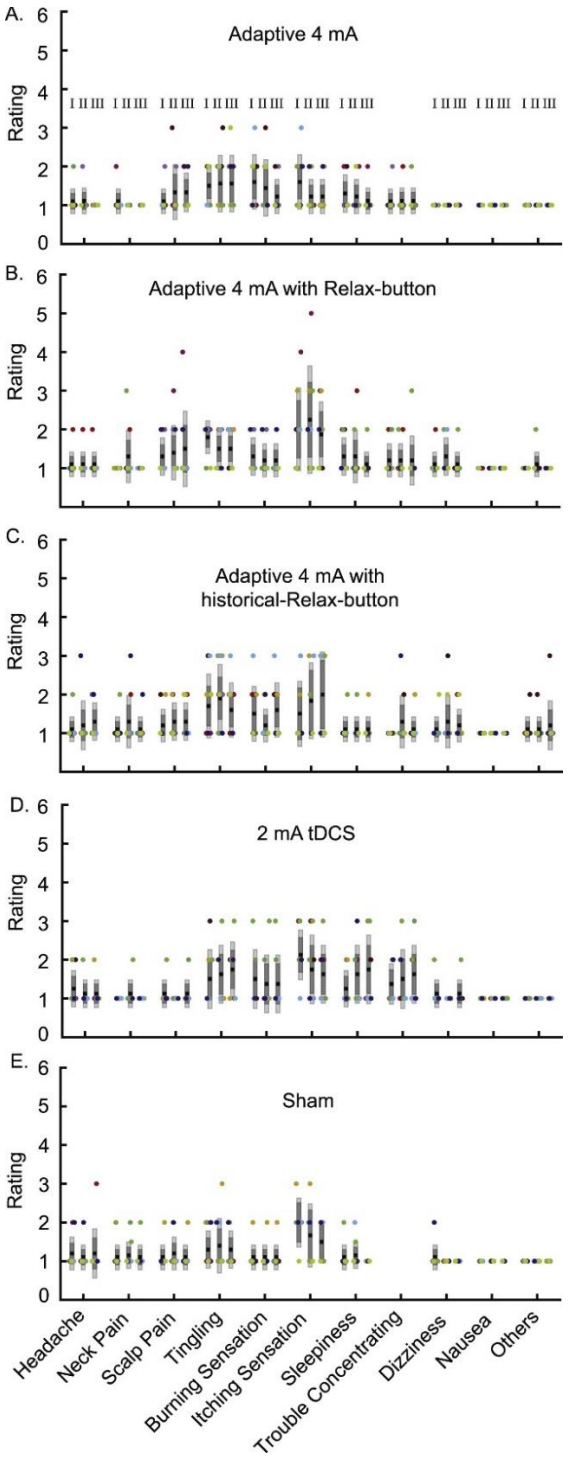

Figure 33: Adverse events for all stimulation conditions

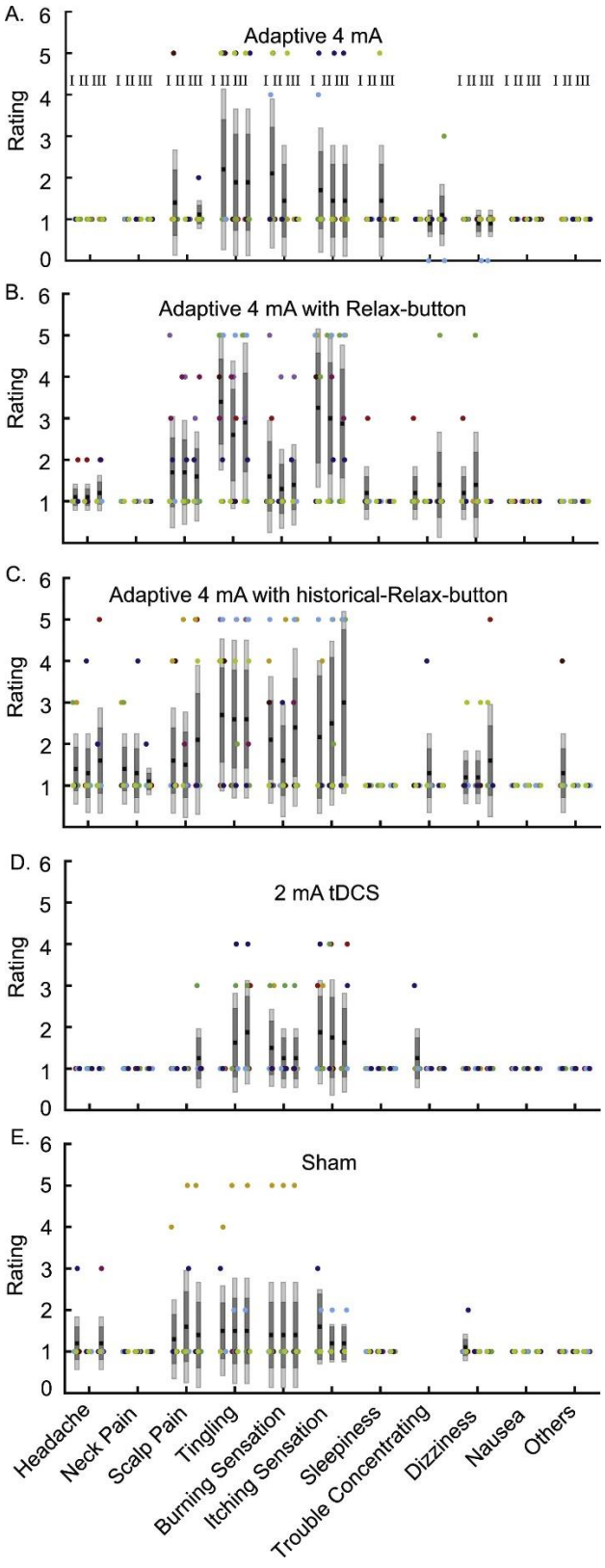

Figure 34. Adverse events for all stimulation conditions in relationship to tDCS.

Appendix 4: Principles of Within Electrode Current Steering (WECS)

4.1. Outline

This Appendix validates a novel method called Within Electrode Current Steering (WECS) to adjust current between electrodes not in contact with the tissue but rather embedded in an electrolyte on the body surface. A version of this study has been published (Khadka et al., 2015b). We demonstrated the principles of WECS using an exemplary electrode design typical for tDCS and extremes of current steering through within the electrode, without altering current distribution in brain target.

4.2. Background

Transcranial Direct Current Stimulation (tDCS) is a neuromodulation technique that involves non-invasive delivery of weak direct current (1-2 mA) to the brain. Conventionally, tDCS employs rectangular saline-soaked sponge pads (25-35 cm2) placed on the scalp, with an internal electrode connected to the current source. Impedance measurement across the current source output may fail to recognize non-uniform conditions at the skin interface such an uneven content or saturation. tDCS is well tolerated with minor adverse effects limited to transient skin irritation (Nitsche et al., 2003). Nonetheless, technology that enhances the sophistication of electrode design would further enhance tolerability and promote broad (e.g. home) use.

In order to enhance the reliability and tolerability of tDCS, we describe a novel method called Within Electrode Current Steering (WECS). This concept is distinct from (across electrode) current steering, as developed for implanted devices such as Deep Brain Stimulation (DBS), where

current is steered between electrodes that are each in contact with tissue, with the goal of changing desired brain regions that are activated (Butson and McIntyre, 2008). Within electrode current steering adjust current between electrodes not in contact with tissue but rather embedded in an electrolyte on the body surface. The goal here is not to alter brain current flow, but rather compensate for non-ideal conditions at the surface. This technology leverages our technique for independently isolating electrode impedance and over-potential during multi-channel stimulation (Khadka et al., 2015a).

With a novel approach, the objective of this first paper was to demonstrate the principles of WECS using an exemplary electrode design typical for tDCS (4 rivet-electrode sponge) and extremes of current steering (from uniform to single rivet). Through finite element modeling (FEM) of this illustrative case, we validate the underlying assumptions of WECS: steering current within electrodes but without altering current distribution in brain target. Having presented this novel idea through an exemplary case, this report supports future studies optimization of electrode design, automation of algorithms to control current (including using impedance measurement), and ultimately validation under experiment conditions.

4.3. Methods

4.3.1. Principles

WECS applies to non-invasive electrical stimulation with two or more electrodes (metal-rivets embedded in an electrolyte (saline or gel)) on the skin (Poreisz et al., 2007). Each electrode is independently powered by a current source. Success in implementation of WECS depends on geometry and material of each component of the assembly and an algorithm for current steering between electrodes. Here our goal is only to demonstrate the principle of such application through

a case design. Using a multi-scale model including realistic electrode and head geometry (Fig. 35A), we showed how current flow in the brain (target) is independent of current-steering at the electrode.

4.3.2. Electrode design

To illustrate implementation of WECS, we use a modified tDCS saline-saturated sponge (7x5x3cm, σ = 1.4S/m). The top face of the sponge is perforated with cylindrical Ag/AgCl electrodes (dout= 1.5cm, din= 0.61cm, extrusionouter =1cm, and extrusioninner = 0.50cm σ = 5.99E7S/m) which align with the top surface and protrude through half the sponge thickness (Fig. 35A). The electrodes are exposed on all surfaces and connect the lead (not shown) via male receptacles at the top. In principle, changing the diameter and distance between the electrodes, the distance between the electrodes and skin, or electrolyte conductivity will discriminate how current from the electrode reaches the skin (Kronberg and Bikson, 2012), but here our goal is to illustrate WECS principles in one fixed exemplary geometry. This electrode assembly is placed on the scalp (Fig. 35A), in our example over the motor region (M1). A return electrode is placed at over the contra-lateral orbit and is not of concern here.

4.3.3. Current steering

The electrode assembly receives a fixed total current of 1 mA (with -1 mA collected by the return electrode). The current is actively divided across the electrodes within the electrode assembly. Thus, under an "even" current split, 0.25 mA is delivered to each electrode. Under a "partially uneven" current split 0.5, 0.25, 0.25, and 0 mA current is delivered and under a "fully uneven" split 1.0 mA is delivered to one electrode and 0 mA current to the remaining electrodes.

4.3.4. Computational methods

WECS was modeled using a previously develop tDCS FEM workflow (Sadleir et al., 2010). A multidomain geometric mesh was generated of a head using a combination of 3D imaging data and computer aided design electrodes (Simpleware, Exeter, UK). The mesh was imported into a FEM solver (COMSOL, Burlington, MA), where conductivities (Kronberg and Bikson, 2012)were assigned to each tissue/material domain. Boundary conditions were applied (cathode ground, inward current density on rivets, insulated on other external surfaces), and the Laplace equation solved for Voltage (and in turn electric field and current density).

4.4. Results

To illustrate the principles of WECS, we considered a simplified electrode assembly with electrodes inside a saline saturated sponge, placed on the scalp (Fig. 35A), under two extremes of electrode current distribution conditions ("even" and "fully uneven") and one intermediary electrode current distribution ("partial uneven") (Fig. 35B). Streamline plots (Fig. 35C) of within sponge current flow demonstrate the distribution of current flow in each case from the electrodes to the skin surface. As expected, we found symmetry when steering current from fully uneven to even current application, but in each case current spreads across the electrode-assembly. At the electrode-assembly interface with the skin, the current density distribution varied only incrementally across conditions (e.g. less than would be expected with even minor changes in electrode assembly or skin properties (Kronberg and Bikson, 2012)) with no significant difference in peak current density (~2 A/m2; typically predicted around edges). Thus, with this electrode assembly design even if three of four electrodes failed, current steering to the one functional electrode would not significantly increase current density in the skin; hence, not effecting tolerability.

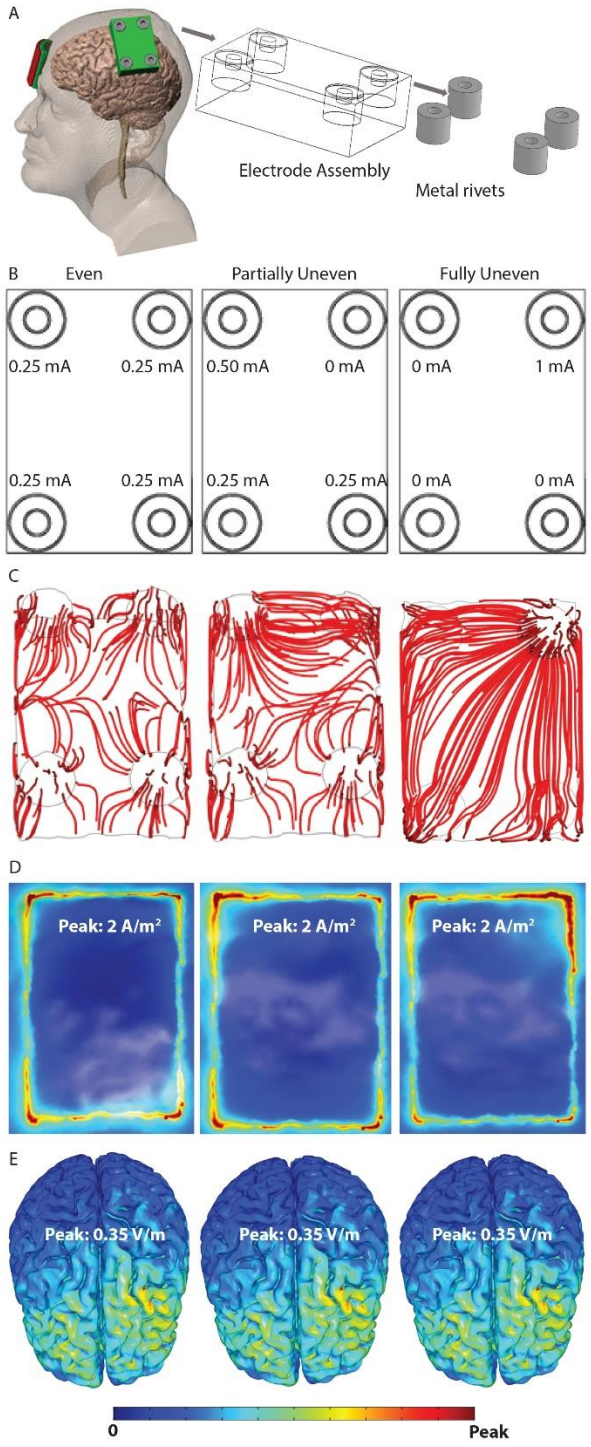

Figure 35: FEM analysis of electrode assembly to validate the underlying assumption of within electrode current steering. (A) Represents a montage with electrode assembly. (B) "Even", "Partially Uneven", and "Fully Uneven" current injection mode through metal rivets of an electrode assembly

keeping total current constant. (C) Illustrates streamline current flow from each metal rivets under all three current injection conditions. (D) Current density observed at the scalp electrode interface. (E) Presents an electric field distribution found in the brain target.

Furthermore, we predicted that the electric field at the brain under all three cases was essentially identical (Fig 35E). Therefore, using this electrode-assembly design, current can be steered across electrodes without effecting current distribution in the brain target. We note the goal of WECS in contrast to current-steering for implant, is not to alter current flow at the target (neuromodulation).

4.5. Discussion

Within Electrode Current Steering (WECS) is proposed here as a novel method to increase the tolerability of tDCS without altering underling neuromodulation. Thus, using an exemplary design, we illustrated how current flow in the brain can remain unaltered (Fig 35E) even as current is steered between electrodes inside the electrode-assembly. WECS can be generalized to other noninvasive electrical stimulation technique and potentially to invasive techniques where an artificial or natural electrolyte barrier exists between the electrode and the tissue. For invasive techniques, WECS may complement traditional current steering but be used to protect electrode and tissue from injury. Success of this approach depends on the appropriate design of the electrode assembly (Fig. 35A) and the algorithm used to steer current between electrodes – topics to be considered in future design efforts.

The essential principles in WECS design relate to producing functional equivalency between current arriving at each electrode as far as current entering the brain target. Specifically, regardless of how a total amount of current is distributed between electrodes, brain current flow

is unchanged. A further consideration is how current flow at the skin (scalp) is altered. On the one hand, current steering should avoid significant increases in current density at the skin, maintaining as uniform a current density at the skin as practical. On the other hand, when non-ideal conditions at the electrode or skin arise, including increasingly non-uniform current flow or electrode failure, current steering may be used to compensate. For example, if a given electrode fails and a high over-potential at the electrode is detected, current may be steered to other electrode to minimize electrochemical hazard (Poreisz et al., 2007)or if one region of the sponge becomes dry during use, current may be diverted to the most distant electrodes.

Inherent to the above concept is the ability to detect non-ideal conditions and program appropriate corrective measures. The simplest feedback is the voltage at each current source, which using signal processing and "test signals" (superimposed currents not used for neuromodulation) or a "sentinel electrode" (not used for DC) may be used to calculate single electrode impedance [3]. Additional information can be derived by using test signals to isolate the impedance of the sponge/electrolyte between the electrodes, generating a prediction for current density patterns that can be corrected.

Appendix 5: Temperature Increases by kilohertz frequency Spinal Cord Stimulation

5.1. Outline

This Appendix test the hypothesis that kilohertz frequency spinal cord stimulation (kHz-SCS) increases local tissue temperature by joule heat, which may influence the clinical outcomes. A version of this study has been published (Zannou* and Khadka* et al., 2019). We concluded that spinal tissue heating may impact short and long-term outcomes of kHz-SCS, and even as an adjunct mechanism, suggests distinct strategies for lead position and programming optimization.

5.2. Introduction

The emergence of kilohertz frequency (1-10 KHz) spinal cord stimulation (kHz-SCS)(Al-Kaisy et al., 2014; DiMarco and Kowalski, 2013; Fingas et al., 2007; Kinfe et al., 2016; Lempka et al., 2015; Russo and Van Buyten, 2015; Tiede et al., 2013) for the treatment of neuropathic pain has engendered studies on new mechanisms of actions (MoA) (Bicket et al., 2016; Lee et al., 2011; Lempka et al., 2015; Miller et al., 2016; Yearwood et al., 2010). Divergent clinical observations for conventional rate SCS and kHZ-SCS suggest difference in MoA which could in turn inform distinct programming optimization strategies. Notably, kHZ-SCS can provide an analgesic and side-effects profile distinct from conventional frequency (~100 Hz) SCS (Bicket et al., 2016; Kapural et al., 2016). For example, kHz-SCS does not produce the paresthesias associated with dorsal column activation in conventional SCS, and recent studies seemingly rule out direct activation of dorsal column fibers as the primary mechanism of action of kHz-SCS pain relief (Crosby et al., 2017; Song et al., 2014). Wash-in time for the therapeutic benefit of conventional

rate SCS is on the order of minutes, while responses to wash-in over a longer period (Al-Kaisy et al., 2014). Further indicating distinct MoA, kHz-SCS waveforms involve simultaneous decrease in pulse duration (well below membrane time constants) and increase in pulse frequency (beyond axon refractory periods) that challenge conventional models of stimulation (Linderoth and Foreman, 1999; Litvak et al., 2003).

Evidence against traditional neural MoA warrants investigation of other phenomena. We note that since the decrease in interpulse-interval (e.g. from 10 ms at 0.1 kHz to 0.1 ms at 10 kHz) is more drastic than the decrease in pulse duration (e.g. from 100 µS per phase at 0.1 kHz to 40 µS per phase at 10 kHz (Lempka et al., 2015; Yearwood et al., 2010), kHz stimulation is associated with higher duty cycle – and the RMS power of a rectangular waveform varies positively with the square root of its duty cycle. Through the principle of joule heating, the power of current flow from an implanted lead can produce temperature increases around the lead (Chang, 2003; Elwassif et al., 2012a; Kiyatkin et al., 2002; Labonte, 1994; LaManna et al., 1980a; Miller et al., 2016; Tungjitkusolmun et al., 2000). Thus, kHz stimulation deposits more power in the tissue than conventional spinal cord stimulation and is therefore more likely to significantly heat the tissue immediately surrounding the stimulation site. A temperature increase and resultant thermal conduction into the spinal cord can, in turn, affect neuronal function (Kiyatkin et al., 2002) (e.g., via alteration of ion channel or neurotransmitters dynamics) and related biological functions (e.g., via vasodilation (Tanaka et al., 2004), heat shock protein expression (Eng et al., 2014)) depending on the degree of change. Tissue heating further encourages the expression of anti-inflammatory agents, such as heat shock proteins (Wang et al., 2003), over a period of time consistent with the extended wash-in times of kHz-SCS treatment.

Any form of electrical stimulation produces passive heating and the extent of induced temperature increases are specific to both the stimulation and local tissue properties, with various stimulation and environmental parameters affecting the degree to which heating occurs(Chang, 2003; Kiyatkin et al., 2002; Masuda et al., 2011). Key stimulation parameters are the stimulation waveform (based on stimulator programming) and electrode montage (based on lead placement), which together with tissue anatomy and electrical conductivity determine joule heat deposition. An implanted stimulator is a constant energy source which will produce unlimited temperature increases without passive (e.g. heat conduction by CSF) or active (e.g. spinal tissue blood perfusion) heat dissipation by the tissue. As such, heating analysis depend on tissue properties such as thermal conductivity, metabolic rate, and blood perfusion; not only of the stimulation target but surrounding tissues. Indeed, we postulate that the local environment around SCS leads is especially conducive to temperature increases, namely the low conductivity of fat and enclosed anatomy of the vertebral canal. If heating due to these factors is sufficient during kHz frequency SCS to shape beneficial responses, then joule heating by SCS may be an adjuvant mechanism underlying therapy. However, the degree of heating during kHz-SCS, including as aggravated by increased power deposition due to pulse compression and/or the enclosed spinal environment, remains unexplored.

The objective of this study was to assess, for the first time, whether an increased duty-cycle (and so power) of High-Rate spinal cord stimulation will produce significant temperature increases in the spinal cord. Prior experimental and modeling studies of conventional non-invasive and invasive forms of brain stimulation has suggested minimal heating under normal device operation (less than 1^0C) (Maged M. Elwassif et al., 2006a; Elwassif et al., 2012a; Gahwiler et al., 1972; Khadka et al., 2018c; Kiyatkin and Sharma, 2009). This study predicts the degree of tissue

temperature rises driven by SCS joule heat, and characterizes the role of SCS waveform (including frequency, pulse width, and amplitude) and tissue properties. We measured temperature increases around an experimental SCS lead in a bath to verify a finite-element-model of SCS joule heat. We confirmed the dependence of temperature rise only on the power of the stimulation waveform, independent of other parameters. Finally, we predicted temperature increases during conventional and kHz- SCS at the dorsal spinal cord under passive and active bio-heat conditions in a geometric human spinal cord FEM model.

5.3. Method

5.3.1. Bath Phantom study

5.3.1.1. Saline Bath Phantom

Thermal and electrical conductivity measurements taken to verify the general heat transfer model were performed in a cylindrical glass container (diameter: 90 mm and height: 130 mm) with three varied NaCl concentrations (154 mmol/L, 34.22 mmol/L, and 3.42 mmol/L (approximating cerebrospinal fluid, meninges, and epidural space respectively). A thermal conductivity meter (Therm Test Inc., Canada) and an electrical conductivity meter (Jenco Instruments, Inc., San Diego, CA) measured the thermal and electrical properties of the saline solutions at 37 °C (core spinal cord temperature approximation). The measured corresponding conductivity values for each molar concentrations were: electrical conductivity (σ): 1.62 S/m, 0.47 S/m, and 0.047 S/m; and thermal conductivity (κ): 0.6268 W/(m.K), 0.6317 W/(m.K), and 0.6319 W/(m.K) respectively.

5.3.1.2. In vitro Stimulation

For the saline bath experiments, an experimental polyurethane SCS lead with 4 Platinum/Iridium electrode contacts (1.35 mm electrode diameter, 3 mm electrode length, 1 mm inter-electrode spacing) was placed at the center of the cylindrical container. The cylindrical container was then immersed in a temperature-controlled water bath (280 x 160 x 150 mm3) maintained at ~37 °C (Fig 1A) and baseline temperature was stabilized for > 60 minutes. Three different waveforms, namely sinusoidal, square, and a symmetric charge-balanced biphasic pulse waveforms mimicking the characteristics and parameters of clinical SCS waveforms (described by leading pulse duration, inter-pulse interval, recovery pulse duration), were generated using a function generator (AFG320, Tektronix, Beaverton, OR, USA). The generated waveforms were passed through a custom designed high-bandwidth linear current isolator to the experimental SCS lead. (Distal) Electrode contact 1(E1) and (proximal contact) 4 (E4) of the experimental SCS lead were energized for all saline bath experiments. Tested stimulation intensities were 1- 7 mA (peak) using rates of 0.1 KHz to 10 KHz. Only for phantom verification, biphasic rectangular waveform pulse widths of each phase (40 μs) and interphases (10 μs) were kept constant such that the duty cycle increased directly with stimulation frequency.

5.3.1.3. Temperature Measurement and Analysis

A fiber optic temperature probe (STS Probe Kit, LumaSense Technologies, Inc. CA, USA) sensed by a fiber optic thermometer (± 0.1 0C accuracy at calibration temperature, m600 FOT LAB KIT, LumaSense Technology, CA, USA) was positioned in the proximity of E4 to measure temperature increases during stimulation (Fig. 36A). We measured the peak temperature change in the bath radially from E4 (1 mm, 2 mm, 3 mm, and 4 mm) during stimulation as a function of peak stimulation amplitudes (1-7 mA), over a range of stimulation frequencies (0.1 KHz, 1 KHz, 5 KHz, 10 KHz, and 20 KHz) for sinusoidal, square, and SCS pulsed waveforms. Measured

temperature was digitized using TrueTemp data acquisition and graphing software (60 samples/measurement and 1 second measurement interval, LumaSense Technologies, Inc. CA, USA). Temperature was normalized with respect to the initial temperature (~370C), which was considered baseline.

5.3.2. Computational Models and Solution Method

5.3.2.1. Bioheat Model of Spinal Cord

Human spinal cord was simulated as a computer-aided design (CAD) derived model comprising seven compartments namely vertebrae (lower thoracic region, T8-T11), intervertebral disc, surrounding soft-tissues (minimally perfused), epidural fat, meninges, cerebrospinal fluid, and spinal cord (white matter and grey matter combined; Fig. 37). The dimensions of the individual tissues, modelled as isotropic homogenous volume conductors, were based on human cadaveric spinal cord from prior studies(Kameyama et al., 1996a). The diameter of spinal cord with dorsal roots was fixed (spinal cord, 6.4 mm; dorsal roots, 0.5 mm) and the thickness of the adjacent tissues were: CSF, 2.0 mm; meninges, 0.5 mm; and epidural fat 1.0 mm. We note that in situ, the diameter of the spinal cord varies along the vertebral column. Two SCS clinical leads were modelled and placed epidurally in a minimally staggered bilateral fashion (SCS Lead 1, 1 mm distal to the mediolateral midline at T8; SCS Lead 2, 0.5 mm away from SCS Lead 1 and proximal to the mediolateral midline at T9; Fig. 37A2). We energized only the first SCS lead; the second lead was passive, positioned to mimic a clinical placement, and used to assess the impact of the presence of a passive lead on heat dispersion (Valle-Giler and Sulaiman, 2014). The finite element method (FEM) model was solved using Pennes' bioheat equation governing joule heating during electrical stimulation (Laplace equation for electrostatics ($\nabla(\sigma\nabla V) = 0$) where V is potential and σ is

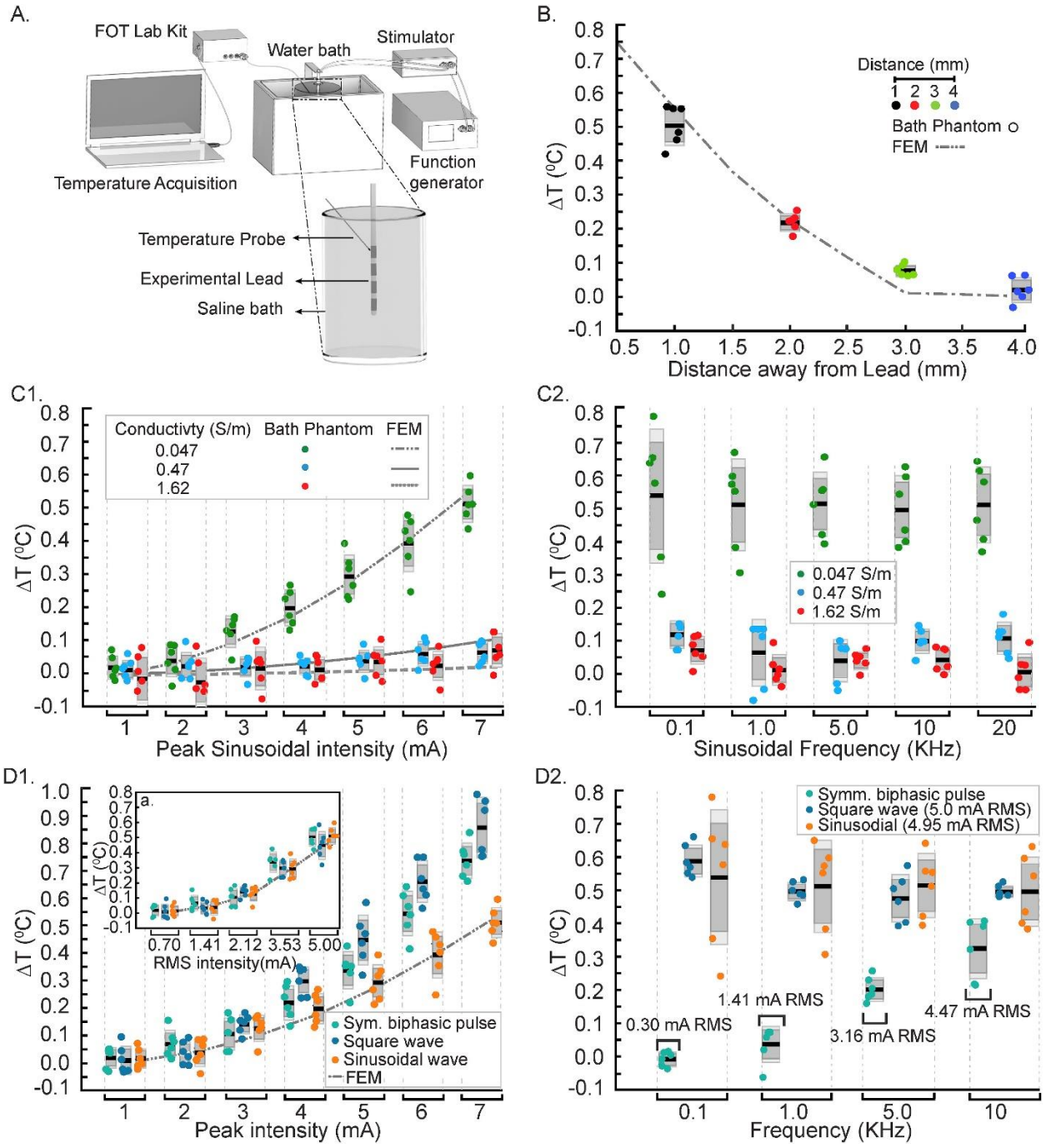

Figure 36: Measurement of temperature increases in phantom preparation across rates, waveforms (SCS, sinusoidal, square) and conductivities and verification of FEM SCS heat model. Dark grey box: standard error of the mean; Light grey box: standard deviation; black line: mean of the data, and the dots are the individual ΔT measurements. (A) Schematic of a salt bath experimental set up with an experimental SCS lead in a salt bath heated in a water bath, function generator driving custom isolator

energizing to the experimental SCS lead, and optical temperature probe mounted on a micro-manipulator. (B) ΔT measured at a radial direction away from the electrode contact (E4, positive polarity) when applying a 10 kHz Symmetric biphasic pulsed waveform at 5 mA peak in a low conductivity saline bath, and the corresponding FEM heat model. Spatial temperature field decreased with increasing radial distance as predicted with the highest temperature increases (mean ~ 0.5 0C) measured proximal to the lead (1 mm). (C1) For 10 kHz sinusoidal waveform, temperature increases as a function of peak stimulation intensity in varied saline bath conductivities: Green: 0.047 Sm−1; Blue: 0.47 S/m; Red: 1.62 S/m. Experimental (dots) and predicted (broken lines) ΔT significantly increased with stimulation intensity with higher sensitivity in lower conductivity saline baths. (C2) For 10 kHz sinusoidal waveform, ΔT measurement at varied stimulation frequencies (0.1, 1, 5, 10, 20 kHz) and conductivities. Temperature increases were independent of frequency and consistently higher for low saline conductivity ($p < 0.01$). (D1) ΔT across different waveforms and stimulation intensities (Main Panel: Peak; Inset: RMS matched) with frequency fixed at 10 KHz. (D2) ΔTs for the different waveforms across various frequencies at RMS stimulation intensities (Square, 5 mA; Sinusoidal, 4.95 mA; Symmetric biphasic pulsed, frequency-dependent RMS).

conductivity), metabolic heat generation rate (Q_{met} or MHG), and blood perfusion rate (ω_b or BPer) in the tissues as mentioned below:

$$\rho C_p \nabla T = \nabla.(\kappa \nabla T) - \rho_b C_b \omega_b (T - T_b) + Q_{met} + \sigma|\nabla V^2| \quad (1)$$

where ρ, C_p, T, σ, *and* κ represent tissue density, specific heat, temperature, electrical conductivity, and thermal conductivity, respectively. Biological properties of blood such as density (ρ_b), specific heat (C_b), and temperature (T_b) were assumed constant in all vascular spinal tissues (vertebrae, meninges, spinal cord) and the corresponding values were 1057 *kg /m*^{3}, 3600 *J / (kg. K)*, and 36.7 ^0C respectively. Blood perfusion rate (ω_b) values were tissue specific and were in the range of 0.0003-0.008 s^{-1} (Collins et al., 2004a; Xu et al., 1999a). In spinal tissues, metabolic activities due to local spinal cord metabolism and enhanced metabolism in response to SCS generates thermal

energy(Morrison and Nakamura, 2011)Blood circulation also plays a significant role in transporting thermal energy across the spinal tissues through convection (Hodson et al., 1989b). We considered the blood temperature in the spinal tissues to be 0.3 ^{0}C less than core spinal cord temperature (37 ^{0}C). We investigated how the interaction between metabolic heat generation and blood perfusion modulates kHz-SCS induced temperature increases. Prior to the application of kHz-SCS, the metabolic heat generation rate required to balance the initial spinal cord temperature was calculated using equation (2) (Hodson et al., 1989b; Wilson and Spence, 1988a) for the aforementioned perfusion rates as:

$$Q_{met} = \rho_b C_b \omega_b (T - Tb) \qquad (2)$$

where T and Tb are initial spinal cord and blood temperature. The calculated Metabolic Heat Generation (MHG) and the corresponding Blood Perfusion (BPer) values were given as; spinal cord and meninges ($Q_{met}, 9132\ Wm^{-3}$; $\omega_b, 0.008\ s^{-1}$), vertebrae ($Q_{met}, 342\ Wm^{-3}$; $\omega_b, 0.0003\ s^{-1}$), and minimally perfused soft-tissues ($Q_{met}, 457\ Wm^{-3}$; $\omega_b, 0.0004\ s^{-1}$). The balanced Q_{met} values approximated prior experimental measurements(Collins et al., 2004a; D. Fiala et al., 1999; Xu et al., 1999a). CSF convection is not incorporated but could be considered in future bio-heat models.

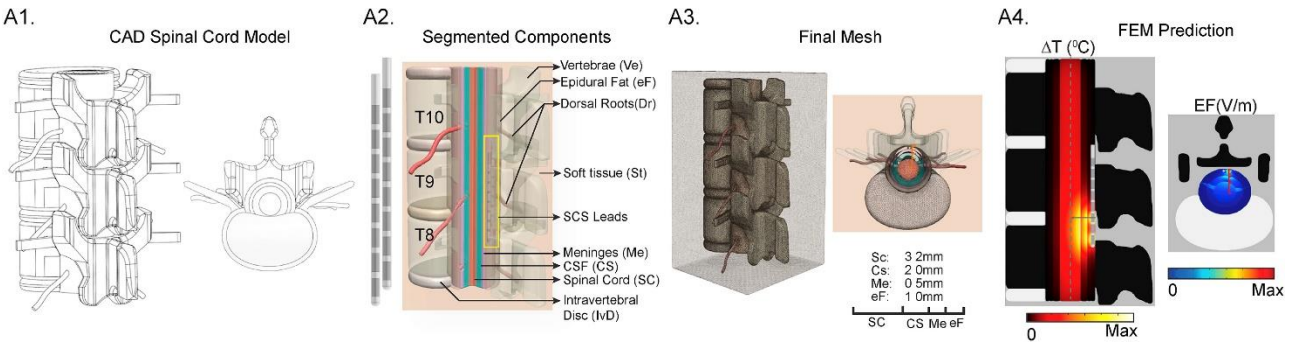

Figure 37: FEM SCS heat transfer model architecture and work flow. (A1) CAD derived spinal cord model with dimensions based on human cadaver study68. (A2) Geometry of sample clinical human SCS lead and a placement of the lead in a segmented spinal cord with dorsal roots and surrounding tissues. SCS lead was positioned into the epidural space between lower thoracic (T8-T10) vertebral region. Two leads were modelled as to mimic clinical intervention, positioned in a minimally staggered bilateral fashion. Epidural space was modelled with fatty tissues. (A3) Resulting volumetric mesh of spinal tissues. (A4) The numerical solution predicted ΔT (^0C) and EF (V/m) in the spinal tissues. Black line in the temperature profile plot and red line in the EF plot represent radial direction from the lead where temperature was sampled.

Mimicking clinical montages and waveforms, we energized electrode contacts E1 and E3 of the clinical SCS Lead 1 in a bipolar configuration (8 mm center-to-center electrode distance). Maximum temperature increases by conventional and kHz-SCS using rectangular waveforms for varied peak amplitudes (1, 2, 3, 3.5, 4, 5 mA), frequencies and pulse widths (50 *Hz* (200 µs), 100 *Hz* (200 µs), 1 *KHz* (40 µs and 100 µs), 5 *KHz* (40 µs), and 10 *KHz* (40 µs) were predicted and compared between active (bioheat) and passive heating cases at three different locations namely, at the distal edge E3 of the clinical SCS Lead 1 (~ 0.01 mm from the surface of the lead), at the proximal surface of the dorsal root to the SCS lead, and at the surface of spinal cord (~ 3.5 mm radial from the E3 electrode).

5.3.2.2. Boundary and initial condition

To model each stimulation waveform, we applied corresponding static RMS values (see phantom and model Results for justification). The accuracy of RMS intensities calculated analytically for a given intensity, frequency, and pulse width (see equation 3) were confirmed experimentally by stimulation across a resistive load (1 KΩ) with voltage acquisition using a digital mixed signal oscilloscope (MSO2024, Tektronix, OR, USA, ± (100 mv + 3 % of

threshold)), a DAQ (NI PCI 5922, National Instruments, TX, USA, ± 500 ppm (0.05 %) of input + 50 µV), and a digital multimeter (DMM 7510 7 $\frac{1}{2}$ Digit Graphical Sampling Multimeter, Tektronix, OR, USA, ± 60 ppm 0.0014% of input). The error in calculated versus measured RMS values was less than 5 %.

$$I_{RMS} = \sqrt{\frac{1}{T}\int_0^t I\,(t)_{peak}^2\,dt}$$

$$= I(t)_{peak}\sqrt{\frac{t}{T}}$$

$$= I_{Peak}\sqrt{D} \qquad (3)$$

where I_{Peak} is the peak bipolar stimulation intensity, I_{RMS} is the corresponding RMS value, T is the pulse duration, t is the pulse width, and D is the duty cycle.

A static inward normal current density ($J_{norm,\,RMS}$) corresponding to the stimulation current intensity ($I_{RMS,}$ Table 3) was injected through E1, and E3 was set as the return (producing a bipolar configuration). The electrical and thermal conductivities of the electrode contacts and the inter-electrode spacing were 4 x 10^6 *S/m* and 31 *W/(m.K)*, and σ=1 x 10^{-15} *S/m*; κ=0.0262 *W/(m.K)* respectively (Morrison and Nakamura, 2011).The outer boundaries of the spinal cord and the surrounding tissues were considered electrically insulated.

A. Passive heating

	10 KHz (40-10-40 μs)				5 KHz (40-10-40 μs)				1 KHz (40-100-40 μs)				1 KHz (100-100-100 μs)				100 Hz (200-100-200 μs)				50 Hz (200-100-200 μs)			
PCF	6.32				4.47				2.00				3.16				1.41				1.00			
I (mA)	ΔT (°C)				ΔT (°C)				ΔT (°C)				ΔT (°C)				ΔT (°C)				ΔT (°C)			
Peak	*RMS*	Lead	SC	Root	*RMS*	Lead	SC	Root	*RMS*	Lead	SC	Root	*RMS*	Lead	SC	Root	*RMS*	Lead	SC	Root	*RMS*	Lead	SC	Root
1.0	0.89	0.34	0.07	0.03	0.63	0.17	0.04	0.02	0.28	0.03	0.01	0.00	0.47	0.08	0.02	0.01	0.20	0.02	0.00	0.00	0.14	0.01	0.00	0.00
2.0	1.78	1.32	0.29	0.12	1.26	0.67	0.14	0.06	0.56	0.13	0.03	0.01	0.89	0.33	0.07	0.03	0.40	0.07	0.01	0.01	0.28	0.03	0.01	0.00
3.0	2.68	3.03	0.65	0.27	1.89	1.49	0.32	0.14	0.84	0.29	0.06	0.03	1.34	0.75	0.16	0.07	0.60	0.15	0.03	0.01	0.42	0.08	0.02	0.01
3.5	3.13	4.11	0.84	0.35	2.21	2.05	0.43	0.18	0.98	0.40	0.09	0.04	1.57	1.01	0.22	0.09	0.70	0.21	0.04	0.02	0.49	0.10	0.02	0.01
4.0	3.57	5.24	1.15	0.49	2.53	2.63	0.57	0.24	1.12	0.53	0.11	0.05	1.79	1.31	0.28	0.12	0.80	0.27	0.06	0.02	0.57	0.13	0.03	0.01
5.0	4.47	8.31	1.79	0.76	3.16	4.15	0.90	0.38	1.41	0.82	0.18	0.07	2.24	2.04	0.44	0.19	1.00	0.41	0.09	0.04	0.71	0.21	0.04	0.02

B. Active heating (Perfusion and MHR)

	10 KHz (40-10-40 μs)				5 KHz (40-10-40 μs)				1 KHz (40-100-40 μs)				1 KHz (100-100-100 μs)				100 Hz (200-100-200 μs)				50 Hz (200-100-200 μs)			
PCF	6.32				4.47				3.16				2.00				1.41				1.00			
I (mA)	ΔT (°C)				ΔT (°C)				ΔT (°C)				ΔT (°C)				ΔT (°C)				ΔT (°C)			
Peak	*RMS*	Lead	SC	Root	*RMS*	Lead	SC	Root	*RMS*	Lead	SC	Root	*RMS*	Lead	SC	Root	*RMS*	Lead	SC	Root	*RMS*	Lead	SC	Root
1.0	0.89	0.30	0.03	0.01	0.63	0.15	0.02	0.00	0.28	0.03	0.00	0.00	0.47	0.07	0.01	0.00	0.20	0.01	0.00	0.00	0.14	0.01	0.00	0.00
2.0	1.78	1.21	0.12	0.03	1.26	0.59	0.06	0.01	0.56	0.12	0.01	0.00	0.89	0.30	0.03	0.01	0.40	0.06	0.01	0.00	0.28	0.03	0.00	0.00
3.0	2.68	2.72	0.28	0.06	1.89	1.33	0.14	0.03	0.84	0.27	0.03	0.01	1.34	0.68	0.07	0.02	0.60	0.13	0.02	0.00	0.42	0.07	0.01	0.00
3.5	3.13	3.70	0.38	0.08	2.21	1.78	0.19	0.04	0.98	0.37	0.04	0.01	1.57	0.92	0.10	0.02	0.70	0.18	0.02	0.01	0.49	0.09	0.01	0.00
4.0	3.57	4.84	0.49	0.10	2.53	2.37	0.25	0.05	1.12	0.48	0.05	0.01	1.79	1.21	0.13	0.03	0.80	0.24	0.03	0.01	0.57	0.12	0.01	0.00
5.0	4.47	7.56	0.77	0.16	3.16	3.69	0.38	0.08	1.41	0.75	0.08	0.02	2.24	1.89	0.19	0.04	1.00	0.38	0.04	0.01	0.71	0.19	0.02	0.01

* Pulse Compression factor (PCF)

Table 3: FEM SCS Bio-heat model predicts temperature increases (ΔT) in fat around the Lead, the surface of spinal cord (SC), and the proximal origin of dorsal Root, as a function of stimulation waveform and intensity (I), for passive (A) and active (B) tissue models. For each waveform (top row) the corresponding Pulse Compression Factor (PCF) is indicated (see Methods). For each waveform and intensity simulation, the corresponding RMS is indicated. In addition to increments of 1 mA peak, 3.5 mA peak is also simulation (grey rows).

For the thermal boundary conditions, the temperature at the outer boundaries of the spinal column was fixed at core body temperature (37 ^{0}C)(D. Fiala et al., 1999; Xu et al., 1999a) with an assumption of no convective heat loss to the ambient temperature, no convective gradients across spinal surrounding tissues, and no SCS-induced heating at the model boundaries(Collins et al., 2004a). The initial temperature of the tissues was assumed to be 37^{0}C, and thermo-electrical

properties of biological tissues were based on average literature values(Gabriel et al., 1996b; IT'IS Foundation, 2015). Intravertebral disc (σ=0.830 *S/m*; *κ*=0.49 *W/ (m.K)* and csf (σ=1.65 *S/m*; *κ*=0.57 *W/ (m.K)* are avascular, and therefore have no BPer and MHG, whereas the other remaining tissues are vascularized and have BPer and MHG as listed: epidural fat (σ=0.25 *S/m*; *κ*=0.21 *W/ (m.K)*, ω_b= 0.0001 s^{-1}, Q_{met}= 58 Wm^{-3}) soft tissues (σ = 0.15 *S/m*; κ = 0.47 *W/ (m.K)*, ω_b= 0.0004 s^{-1}, Q_{met}= 457 Wm^{-3}), vertebrae (σ = 0.01 *S/m*; κ = 0.32 *W/(m.K)*, ω_b= 0.0003 s^{-1}, Q_{met}= 342 Wm^{-3}), meninges (σ = 0.368 *S/m*; κ = 0.44 *W/(m.K)*, ω_b= 0.008 s^{-1}, Q_{met}= 9132 Wm^{-3}), and spinal cord (σ = 0.126 *S/m*; κ = 0.51 *W/(m.K)*, ω_b= 0.008 s^{-1}, Q_{met}= 9132 Wm^{-3}). When indicated, these "standard" tissue values were manipulated by either 1) doubling or halving the electrical and/or thermal conductivities of a given compartment, or 2) by substituting properties across compartments.

5.3.2.3. Saline bath Phantom FEM

SCS saline bath phantom was modelled using equation (1) while eliminating the biological tissue parameters. The FEM Phantom model was parameterized based on the dimensions, conductivity, and initial temperature of the experimental set-up. As tested, we simulated one SCS experimental lead centrally placed in a saline bath phantom. For the electrical boundary conditions, a uniform RMS current density was applied at E4 (anode) and return at E1(cathode). The outer boundaries of the bath were considered electrically insulated. For thermal boundary conditions, the external boundary temperature and the initial temperature of the bath were fixed at 37 ^{0}C. To account for the voltage drop due to the electrode-saline interface(Cantrell et al., 2008; Merrill et al., 2005; Richardot and McAdams, 2002), a correction factor of 50% was applied in phantom stimulation(Elwassif et al., 2012b).

5.3.2.4. Model Construction and Computational Method

Human spinal cord and saline bath phantom models were CAD derived, assembled in SolidWorks 2016 (Dassault Systemes Americas Corp., Ma, USA), and imported using Simpleware ScanIP (Synopys Inc., CA, USA). The entire volume of the spinal tissue and the electrode assembly was 83.0 x 74 x 108 mm^3. Prior to the segmentation, tissues were resampled to have an isotropic resolution of 0.2 mm^3. Resampled images were segmented into seven tissues compartments along with the T8-T11 positioned SCS lead assembly using a combination of automatic and manual segmentation filters (Fig. 37A2). Using a voxel-based meshing algorithm of ScanIP, an adaptive tetrahedral mesh was generated. The final model size resulting from multiple mesh densities refinement contained approximately 4,600,000 tetrahedral elements for the full anatomy of spinal cord model and approximately 320,000 tetrahedral elements for the saline bath model (Fig. 37A3). The meshes were imported into COMSOL Multiphysics 5.1 (COMSOL Inc., MA, USA) to computationally solve the FEM model. The SCS model was solved for both passive heating (joule heating, without BPer and MHG) and active heating (bioheat, with BPer and MHG) conditions. The baseline temperature gradient for the active heating case was predicted by first solving the heat transfer model in the absence of electrical stimulation. In passive heating, the baseline temperature gradient was set to zero. The Saline bath model was solved only for passive heating condition. Both phantom and SCS models were solved under steady state assumption and corresponding temperature increases and field intensities were quantified. Heat flux and field intensity streamlines (seeded at selected tissue boundaries and proportional in diameter to the logarithm of corresponding magnitudes) were plotted to illustrate the overall distribution across tissues (Fig. 38).

5.3.3. Statistics and Analysis

Normality test on temperature increases were conducted using Lilliefors corrected K-S test statistical test. A two-way repeated measure analysis of variance (ANOVA) was used to assess the statistical differences in ΔT across different tested conditions (stimulation intensity, waveforms, frequencies, conductivities). A critical value (p) < 0.01 was accepted as a statistical difference between the groups. Further significance between groups were verified using Post hoc Scheffe's test (corrected multiple comparisons). The statistical relations between the experimental data the FEM data was evaluated through a simple linear regression MATLAB (R2016a, MathWorks, MA, USA).

The standard forms of *power law* tested super-linearity between the RMS and temperature increases, using a linear least squares fitting technique derived by Gauss and Legendre with a power function(Weisstein, n.d.) given as:

$$\Delta T = A * RMS^{\beta} \tag{4}$$

where 'β' is the power, and 'A' is the proportionality constant. The value of 'β 'determines the category of the relationship (β = 1, linear; β > 1, super-linear; β < 1, sublinear). Formulating the power function further on a log-log scale yield:

$$ln(\Delta T) = ln(A) + \beta * ln(RMS) \tag{5}$$

Equation (5) is a straight line with a slope 'β' and a y-intercept of $ln\ (A)$. Linear least square fit of the logarithmic data yields the correlation (r^2)(Weisstein, n.d.).

Pulse Compression Factor per stimulation intensity (PCF) captures the increase in RMS of a High-Rate waveform ($RMS_{High\text{-}Rate}$) compared to a conventional 1 mA peak 50 Hz 200 µs pulse-width waveform (RMS_{50}):

$$RMS_{High-Rate} = I_{peak} * PCF * RMS_{50} \quad (6)$$

$$PCF = 10 * \sqrt{Pw * f} \quad (7)$$

where 'Pw' and 'f 'are pulse width (sec) and frequency (Hz) for a given High-Rate waveform.

5.4. Results

5.4.1. Phantom Measurement and Model Verification

A specially designed chamber was used to quantify temperature increases around an experimental SCS lead in a saline bath using varied waveforms (Fig. 36A). A micro-manipulator mounted optical temperature probe mapped steady-state temperature increases during stimulation with varied waveforms. As predicted by the FEM, temperature increases when applying a 10 kHz symmetric biphasic pulsed waveform at 5 mA peak intensity in a low conductivity saline phantom was maximal near energized electrodes and decreased with radial distance (Fig. 36B). In separate experiments, salt bath conductivity was varied by saline concentration. The main effect of saline bath conductivity and stimulation intensities (1-7 mA peak sinusoidal) was significant (F (2, 105) = 218.95 $p < 0.01$ and F (6, 105) = 42.03, $p < 0.01$, a two-way ANOVA). The interaction between these factors on ΔT was also significant; (F (12, 105) = 19.88, $p < 0.01$). Temperature increases

were measured to be significantly greater in the lower saline bath conductivity (0.047 *S/m*) than in the other two saline bath conductivities (0.47 *S/m* and 1.62 *S/m;* Post-hoc Scheffe's test, Fig. 36C1). Across different saline conductivities at different sinusoidal frequencies, the measured temperature increases were significant; F (2,75) = 256.25, $p < 0.01$. ΔT was higher at lower conductivity saline bath (Fig. 36C2).

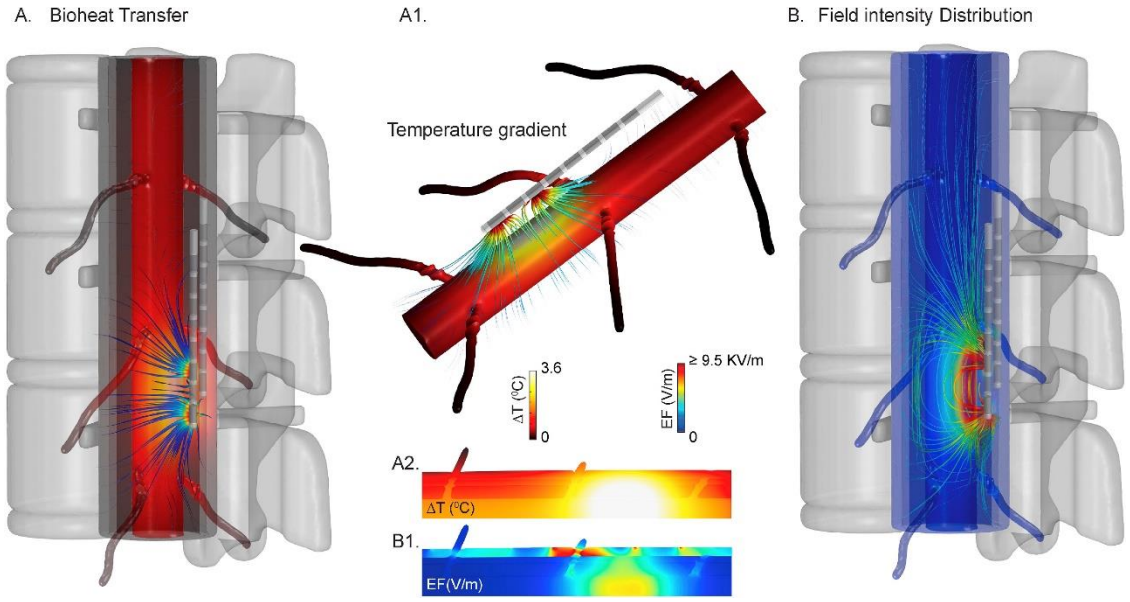

Figure 38: FEM Bioheat transfer model of Spinal Cord Stimulation predicts temperature changes and electric field intensities. (A) Temperature increases at the spinal cord modelled with dorsal roots, and surrounding tissues for a metabolic heat and blood perfusion modulated high rate spinal cord stimulation (kHZ-SCS). Temperature gradient streamlines originated from SCS leads to the spinal cord and dorsal roots are depicted. (A1) Accumulated heat (shown as heat flux streamlines) transported throughout spinal cord and dorsal roots during kHz-SCS. (A2, B2) illustrates predicted temperature and electric field (EF) spatial distribution on a spinal cord, dorsal roots, and other adjacent tissues. (B) Field intensity distribution across spinal cord and surrounding tissues. EF strength across each tissue are depicted by electric field streamlines seeded on every tissue boundary.

Temperature increased by up to ~1 ^{0} C with stimulation amplitude during stimulation using all 10 KHz waveforms (symmetric biphasic pulse, square, sinusoidal). In addition, when

considering only peak intensities, higher ΔT was observed during stimulation using pulsed and square waveforms versus the sinusoidal waveform ($F(2,105) = 41.14$, $p < 0.01$). However, this effect was found to be directly related to the RMS of the waveform (Fig. 36D1a) and not to the specific shape of the stimulation waveform ($F(2, 75) = 1.11$, $p > 0.01$).

In a separate series, temperature increases were measured across varied frequencies for all waveforms (symmetric biphasic pulse, square, sinusoidal) in a low conductivity saline bath with 5 mA peak current intensity (corresponding RMS: sinusoidal waveform, 4.95 mA; square waveform, 5 mA; in pulsed waveform, RMS varies with frequency (Fig. 36D2)). There was a main effect of stimulation waveforms on ΔT; $F(2, 60) = 133.44$, $p < 0.01$. Temperature increases (0 to ~ 0.4 ^{0}C) across frequencies for symmetric biphasic pulsed waveform were significant ($p < 0.01$); however, for true square and sinusoidal waveforms, ΔT did not increase significantly across frequencies ($p > 0.01$). Temperature rises appeared to reflect the increase in duty cycle and RMS only for the symmetric biphasic pulsed waveform. Conversely, significantly higher temperatures were measured overall at the 5 mA peak intensity for sinusoid and square waveform compared to the pulsed waveform- reflecting the 100% duty cycles and therefore higher RMS values of the sinusoid and square waveforms.

Computational FEM predictions of the phantom using the experimental lead and waveforms were correlated with experimental temperature increases measurement at varied saline conductivities (($R^2 = 0.24$, $F(1,40) = 12.20$, $p < 0.01$, 1.62 *S/m*; $R^2 = 0.26$, $F(1, 40) = 13.70$, $p < 0.01$, 0.47 *S/m*; $R^2 = 0.84$, $F(1,30) = 201.84$, $p < 0.01$, 0.0047 *S/m*) (Fig. 36C1). Computationally predicted and measured temperature increases were strongly correlated across different RMS stimulation intensities ($R^2 = 0.86$, $F(1, 27) = 167.39$, $p < 0.01$(Fig. 36D1a)). Accordingly, a strong

association between ΔTs were established along radial direction away from the experimental SCS lead; $R^2 = 0.96$, F (1, 21) = 495.59, $p < 0.01$ (Fig. 36B).

5.4.2. Computational Model of Heating by SCS: Influence of waveform with standard tissue parameters

Using a FEM bio-heat computational models of human spinal cord stimulation, tissue temperature increases were predicted under varied stimulation parameters (Table 3) for passive heating and active conditions initially using "standard" tissue parameters (see Methods). Six representative SCS waveforms were simulated, with selected frequency and duty cycle (corresponding Pulse Compression Factor noted in table; see Discussion), each with varied peak intensity from 1 to 5 mA (corresponding resultant RMS noted in table). For each waveform and intensity, we tabulate the maximum ΔT around the SCS clinical lead (E3 contact), at the proximal surface of the dorsal root to the SCS lead (~ 1 mm lateral to the stimulating lead), and at the surface of spinal cord (~ 3.5 mm radial to the stimulating lead).

From this analysis, several important predictions emerge. Heating under the standard active model (which includes blood perfusion (BPer) and metabolic heat generation (MHG)) was lower than the standard passive model (where BPer and MHG were absent). Maximum temperature increases were generated around the SCS clinical lead (the epidural fat). Temperature increases were relatively higher for waveforms with a higher Pulse Compression Factor. Both active and passive heating increased with stimulation RMS, and so with intensity or Pulse Compression Factor, in a super-linear manner (e.g. doubling stimulation intensity or Pulse Compression Factor doubles RMS and results in a > 2-fold increase in temperature (Fig. 39)). While relative temperature increases were more sensitive to intensity than Pulse Compression Factor, the highest

temperature increase were predicted under high Pulse Compression (e.g. the 10 *KHz* waveform). For example, using a conventional 50 Hz waveform (*PCF: 1.0*), temperature at the spinal cord (SC) increased < 0.05 ^{0}C even at 5 mA peak (*RMS: 0.71*) while using a 10 *KHz* waveform (*PCF: 6.32*) temperature at the spinal cord (SC) increased ~1 ^{0}C at 5 mA peak (*RMS: 4.47*).

Dependence of temperature increase on RMS (and so Intensity or Pulse Compression Factor) was modeled assuming a power law relationship, which results in a linear log-log dependence (see Methods). Surprisingly, and despite the complexity of the standard tissue model, this fit sufficiently, and reliability predicted temperature increases. Slope (β) approached 2 (i.e. temperature increasing with the square of RMS) - a super-linear (β >1) sensitivity of temperature to RMS. The proportionality constant (A) increased across fat (Lead), Spinal Cord, and Root compartments, all relativity higher in the passive (Fig. 39A1) verse active (Fig. 39B1) tissue model.

5.4.3. Computational Model of SCS: Parameter sensitivity analysis with fixed waveforms

Living tissue possess complex thermo-electrical properties(Weisstein, n.d.) and these properties are tissue specific. In the active model, we predicted the sensitivity of SCS temperature to tissue properties by halving or doubling the thermal and/or electrical conductivity (from the standard model; see Methods) of each tissue compartment. At 3.13 mA RMS (as for a 10 *KHz* SCS waveform with 3.5 mA peak), we considered a significant change in predicted temperature as > 0.03 ^{0}C and > 8 % from the standard model. No simulated changes in passive thermal and/or electrical conductivity at any tissue, except epidural fat (eF), produced a significant temperature change at the Lead, Spinal Cord, or Root. However, increases or decreases in epidural fat electrical conductivity significantly decreased or increased temperature across tissue compartments, respectively. The resulting predicted range of temperature increases using waveforms with 3.13

mA RMS were (Passive Model Range; Active Model Range): Lead (1.53 – 11.57 ^{0}C; 1.25 – 10.77 ^{0}C), Spinal Cord (0.42 - 1.72 ^{0}C; 0.18 – 0.72 ^{0}C), and Root (0.17 – 0.75 ^{0}C; 0.04 - 0.15 ^{0}C).

We considered the sensitivity and fit of the power-law function across tissue properties, specifically varying fat electrical (σ) and thermal (k) conductivity (doubling and halving). In all tissue conditions, the linearity of log-temperature verse log-RMS confirmed a power-law fit, with consistently super-linear sensitivity (β >1). Thus, for each tissue model, temperature could be predicted reliability by simply the corresponding power law function parameters, A and β (Fig. 39). In the passive model, β approached 2 across conditions. In the active model β could exceed 2, reflecting variance at low RMS, but not sensitivity at high RMS. The proportionality constant (A) varied more significantly across model parameters and tissue compartments, particularly near the Lead (Fig. 39A1, 39B1, 39B2).

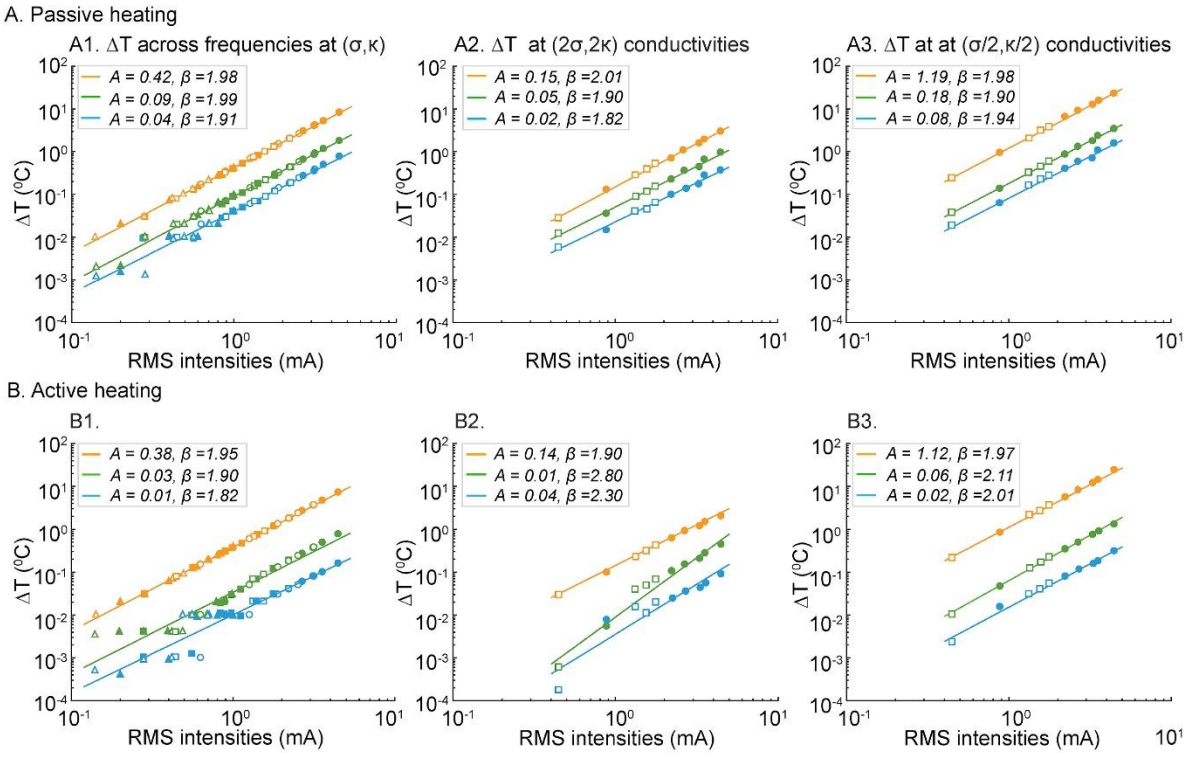

Power-law fit ($\Delta T = A * RMS^{\beta}$)

Frequency (KHz)
10 5 1 1* 0.1 0.05

Position
Lead
SC
Root

10 KHz (40-10-40 μs)
5 KHz (40-10-40 μs)
1 KHz (40-100-40 μs)
1* KHz (100-100-100 μs)
0.1 KHz (200-100-200 μs)
0.05 KHz (200-100-200 μs)

C. Passive heating

Conductivities	(A, β)		
	Lead	SC	Root
(σ,κ)	(0.42,1.98)	(0.09,1.99)	(0.04,1.91)
(σ,κ/2)	(0.60,1.99)	(0.09,1.95)	(0.04,1.90)
(σ,2κ)	(0.29,2.00)	(0.09,1.95)	(0.04,1.89)
(σ/2,κ)	(0.81,1.98)	(0.17,1.97)	(0.07,1.94)
(σ/2,κ/2)	(1.19,1.98)	(0.18,1.90)	(0.08,1.94)
(σ/2,2κ)	(0.58,1.99)	(0.15,1.98)	(0.07,1.94)
(2σ,κ)	(0.53,1.80)	(0.12,1.71)	(0.06,1.62)
(2σ,κ/2)	(0.31,1.99)	(0.06,1.92)	(0.03,1.84)
(2σ,2κ)	(0.15,2.01)	(0.05,1.90)	(0.02,1.82)

D. Active heating

Conductivities	(A, β)		
	Lead	SC	Root
(σ,κ)	(0.38,1.95)	(0.03,1.90)	(0.01,1.82)
(σ,κ/2)	(0.57,1.96)	(0.03,2.23)	(0.01,1.98)
(σ,2κ)	(0.27,1.94)	(0.03,2.28)	(0.01,2.07)
(σ/2,κ)	(0.74,1.97)	(0.06,2.11)	(0.02,1.99)
(σ/2,κ/2)	(1.12,1.97)	(0.06,2.11)	(0.02,2.01)
(σ/2,2κ)	(0.52,1.96)	(0.06,2.12)	(0.01,2.07)
(2σ,κ)	(0.20,1.92)	(0.01,2.76)	(0.01,2.20)
(2σ,κ/2)	(0.30,1.92)	(0.01,2.63)	(0.01,2.05)
(2σ,2κ)	(0.14,1.90)	(0.01,2.80)	(0.04,2.30

Figure 39: Power law-fit description of temperature increase with stimulation RMS in SCS model. Temperature changes (ΔT) at three locations (Lead, orange; Spinal Cord, green; and Root, light-blue) as a function of stimulation RMS, across passive or active tissue model with varied fat electrical and thermal conductivity, were predicted by the FEM SCS model (data points). For each tissue model and compartment, we determined a best power-law fit (see Methods), which is a line with proportionality constant A and slope β (lines) on a log-RMS verse log-Temperature plot. Data plots include standard passive (A1), standard active (B1) tissue models, high thermal and electrical fat conductivity (2σ, 2κ) passive (A2) and active (B2) models, and low thermal and electrical fat conductivity (σ/2, κ/2) passive (A3)

and active (B3). A and β across all 9 permutations of fat electrical (σ) and thermal (κ) conductivity are summarized for passive (C) and active (D) cases. RMS values plotted in A1 and A2 span stimulations frequencies of 0.05, 0.1, 1 (with low or high duty cycle), 5, and 10 KHz (waveforms indicated in legend and as used in Table 3). RMS values in A2, B2, A3 and B3 span 1, 5, and 10 KHz. A $\beta > 1$ indicates super-linear dependence of temperature rise on stimulation RMS; when $\beta = 2$ temperature increases with the square of RMS.

To evaluate the contribution of peripheral spinal tissues on the temperature increases, we considered series of idealized models staring with uniform epidural fat and then sequentially adding adjacent tissues, under both active and passive model conditions (Fig. 40). The order of simulated tissues and predicted maximum temperature increases at locations corresponding to Lead position ("Lead"), Spinal Cord surface ("SC"), and dorsal Root surface ("Root") are reported for both passive heating and active heating conditions (3.13 mA RMS at 10 *KHz*; Table 3). Maximum temperature increases and penetration (from the lead inward) is predicted in the uniform epidural fat model, with a relatively shallow electric field profile. The addition of Soft tissue (St), Vertebrae (Ve), and Intravertebral Disc (IvD) compartments and subsequent reduction of the size of the epidural fat layer(?) result in an incremental reduction in predicted temperatures increases – which is consistent with the notion that fat tissue properties are the most conducive to heating. The relative reduction in temperature between the active and passive models, as well as the reduction in electric field (which is always the same across active and passive models) emphasize these variables can change independently.

Further addition of Meninges (Me) to the model reduced predicted temperature rises notably in both relatively interior (Spinal Cord) and exterior (Lead, Root) regions - indicating that, compared to fat, the Meninges conduct heat away. The reduction in electric field at the Spinal Cord following addition of Meninges (from 165 V/m to 29.27 V/m) was comparable in scale to

the temperature decreases in the active model (from 1.22 ^{0}C to 0.25 ^{0}C) while in the passive model temperature was less sensitive (from 1.37 ^{0}C to 0.92 ^{0}C) – reflecting that the Meninges are vascularized in the active model. Further addition of CSF (CS) decreased predicted temperature rises at the SC and Root for the passive model, increased predicted temperature rises at the Lead for the passive model, and increased temperature in all compartments in the active model. The avascular nature of the CSF layer is overshadowed by its high electrical/thermal conductivity. Finally, addition of Spinal Cord (SC) restores the tissue parameters of standard model.

5.5 Discussion

Thermoregulation of CNS temperature is complex and depends on a high metabolic activity (LaManna et al., 1980b) and both passive (conduction) and active heat exchange (blood flow). Neurostimulation, such as SCS, can challenge this equilibrium in several ways by 1) altering neuronal and so metabolic activity (Elwassif et al., 2012b; Kim et al., 2007; Mrozek et al., 2012); with 2) changing the cellular microenvironment (Bikson et al., 2001; Kim et al., 2007); 3) changing vascular function as a result of both direct blood vessel stimulation(Mandel et al., 2013; Pulgar, 2015; Tanaka et al., 2004) and secondary to microenvironment changes; and 4) depositing of joule heat (Maged M. Elwassif et al., 2006b; Elwassif et al., 2012b). In the context of kHz-SCS, this study specifically addressed joule heat with the hypothesis that by increased power (pulse compression), kHz-SCS waveforms will superlinearly increase tissue temperature, potentially inducing downstream alterations in tissue function with therapeutic effects in chronic pain. Characteristic clinical responses to kHZ-SCS including as the lack of associated neural sequelae such as paresthesia and the frequency insensitivity of efficacy(Thomson et al., 2018) reconcile well with joule heating, while the delayed time course of effects (Al-Kaisy et al., 2015) may be

explain by temperature homeostatic responses or heat shock protein regulation of neuroinflammation.

5.5.1. Bioheat SCS Model

FEM bioheat models of phantom, verified experimentally, and of human spinal cord, subjected to a broad parametric sweep (> 100 simulations in this study), are suitable for assessing our hypothesis as they enable predictions as to whether or not SCS may produce temperature rises sufficient to produce biological effects.

Heating from chronic SCS represents an exogenous non-physiological challenge. We predicted temperature increases at the dorsal spinal cord of 0.18-1.72 °C and at the lead in epidural fat of 1.25 – 11.57°C under a typical kHz-SCS setting (10 *KHz*, pulse at 3.5 mA peak; corresponding to 3.13 mA RMS; Fig. 38, Table 3). This range depends on epidural fat electrical conductivity; the combination of high current density and low conductivity increases joule heating that is then conducted to other tissues.

The degree of heating is a super-linear function of stimulation RMS power (Fig. 36D2) such that kHz-SCS can produce significantly more temperature rise than conventional frequency SCS. Assuming $\beta \sim 2$ and integrating (7) with the power-law relationship (4) yields:

$$\Delta T = 0.02 * A * I_{peak}^2 * PCF^2 \quad (8)$$

where '*0.02'* is the square of RMS_{50} at 1 mA.

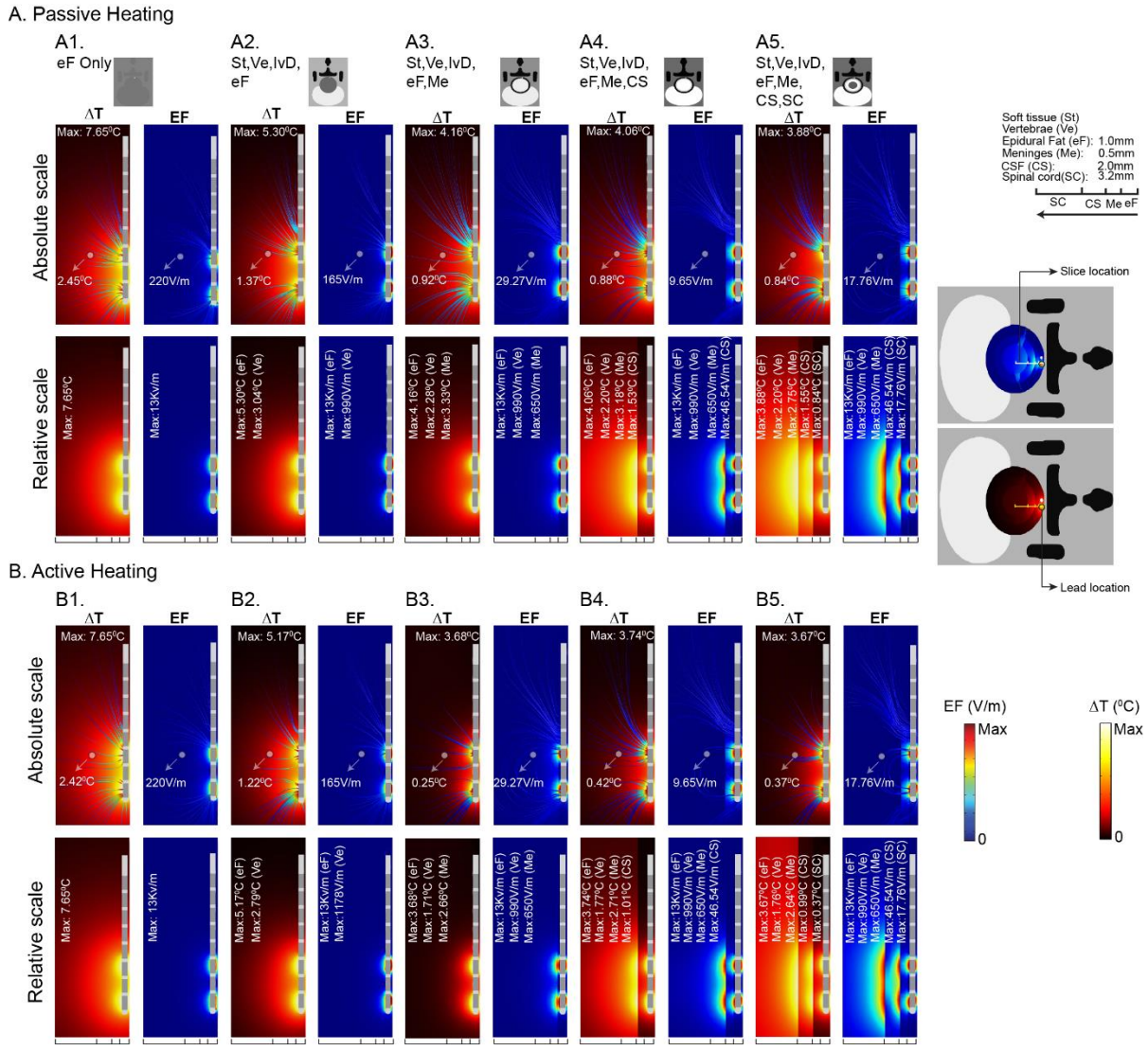

Figure 40: Tissue substitution analysis for passive and active heating conditions in SCS model. Predicted ΔT and EF were reported in both absolute scale (data sampled at a radial distance equal to the surface of spinal cord from the surface of epidural fact, represented by a gray dot) and relative scale (data sampled at a corresponding tissue surface for all tissue combination as illustrated in the figure) from parasagittal spinal tissue slice. On an absolute scale for both passive and active heating conditions, ΔT and EF decreased as more tissues were added around the epidural fat. With an entire tissue combination (A5, B5) on this scale, the ΔT and EF were 0.84 ^{0}C and 17.76 V/m in passive heating and 0.37 ^{0}C and 17.76 V/m in active heating. Similarly, on the relative scale for passive and active heating conditions, ΔT and EF decreased as more tissues were added. Maximum ΔT (7.65 ^{0}C) and EF (9.9 KV/m) were reported

around the lead with only epidural fat (A1, B1, relative scale). As more tissues were added, ΔT around the lead decreased to 3.88 ^{0}C in passive heating and 3.67 ^{0}C in active heating. Maximum predicted ΔT and EF at the spinal cord was 0.37 ^{0}C and 17.76 V/m with the entire tissue combination (A5, B5, relative scale).

A.Tissue Substitution and predicted ΔT

3.13 mA RMS, 10 KHz	Passive Heating			Active Heating		
	ΔT(°C)			ΔT(°C)		
Tissues	Lead	SC	Root	Lead	SC	Root
eF	7.39	2.45	0.99	7.32	2.42	1.00
eF, Ve, IvD	5.07	1.37	0.49	5.02	1.22	0.38
eF, Ve, IvD, Me	4.09	0.92	0.37	3.49	0.25	0.03
eF, Ve, IvD, Me, CS	4.13	0.88	0.36	3.59	0.42	0.13
eF, Ve, IvD, Me, CS, SC	4.11	0.84	0.35	3.60	0.37	0.08

Table 4: Tissue substitution order and resulting predicted temperature changes (ΔT) at the Lead, Spinal Cord, or Root tissue compartments. In this series only one waveform with 3.14 mA RMS was simulated. For each model the tissues modeled could include epidural fat (eF), vertebrae (Ve), intervertebral discs (IvD), meninges (Me), cerebral spinal fluid (CS), and spinal cord (CS).

Remarkably, at least across conditions considered here, temperature increases in any tissue inside the spinal canal were well fit using a power-law function (equation 8). With all lead position, electrode configuration, and passive and active tissue properties captured by a single proportionality constant (Fig. 39A). All waveform parameters collapse to Pulse Compression Factor, PCF (Equation 7). This heuristic finding has important potential consequences to SCS practice:

i. From a modeling standpoint, this finding could dramatically simplify future efforts to predict temperature changes as part of SCS therapy optimization and programming.

ii. Moreover, the super-linear sensitivity to PCF warrant attentions as incremental changes in waveform can spike tissue heating.

iii. From a mechanistic standpoint, if temperature increases underpin kHZ-SCS, then waveform power (as captured by PCF) is more important than any single waveform parameter (e.g. frequency, pulse width, shape) in generating effective therapy.

iv. However, a heating MoA does not indicate only waveform PCF predicts outcomes as other factors (e.g. electrode placement) influence the proportionality constant (A). Nor does this imply a fixed minimum for stimulation energy (charge, battery consumption) which depends on other factors such as device efficiency and impedance.

5.4.4. Physiological Implications

The nervous system, including the spinal cord, is sensitive to temperature changes. Temperature increases to ~44 °C (Mandel et al., 2013) result in brain damage in animal models after 60 minutes (Lawson et al., 2008; Morrison and Nakamura, 2011), with the temperature threshold for injury decreasing with increased exposure time. In animal models, significant changes in brain excitability have been noted with short-term increases of >2 °C (Harris et al., 1962a; Kim and Connors, 2012a; Matsumi et al., 1994a), with sensitivity to lower-temperature expected with long-term temperature increases. Brain temperature increases above 39 °C in ischemic brain injuries increases extracellular excitatory amino acids level, opening of blood-brain barrier, and elevated proteolysis of the neuronal cytoskeleton (LaManna et al., 1980b; Tasaki and Byrne, 1987). A sustained 1-2 °C rise in brain temperature after injury is potentially hazardous (Childs, 2008; Dietrich, 1992; Tasaki and Byrne, 1987). While there are *transient* changes in temperature during normal function (2-3 °C (Dietrich, 1992; LaManna et al., 1980b; Tasaki and Byrne, 1987; Wass et al., 1995)) a *sustained* temperature change may produce cumulative and profound changes in brain function. We predicted significant temperature changes in the spinal

cord that met or exceeded these thresholds, specifically using kHz frequency waveforms where Pulse Compression increases heat deposition. Our findings are a surprising and important first step toward determining a new heating mechanism for kHz-SCS as well as other relatively high power (kHz frequency) neuromodulation techniques (Patel et al., 2017; Wang et al., 2014).

Evidence for stimulation acutely changing neuronal firing and metabolism, perfusion (Elwassif et al., 2012b; LaManna et al., 1980b; Mrozek et al., 2012) and the extracellular environment(Kim et al., 2007) is specific (limited) to sub-kHz frequencies for SCS-relevant simulation amplitudes (Bikson et al., 2001; Pulgar, 2015; Tanaka et al., 2004); and so were not modeled here (Q_{met} and w_b were constant). Starting with kHz-stimulation joule heating, changes in brain function can derive from the acute changes in dynamics (e.g. ion channel gating, neurotransmitter clearance; (Bennetts et al., 2001; Chowdhury et al., 2014a)) or a homeostatic molecular response to chronic temperature changes (e.g. heat shock proteins). Slow temperature homeostatic changes provide a plausible explanation for the delayed onset of pain relief by kHz-SCS (Al-Kaisy et al., 2015; Thomson et al., 2018) and suggest specific molecular pathways (MoA) for pain relief including heat shock protein producing downregulation of neuroinflammation. For example, 72-kDa heat shock protein (Hsp70) inhibits activation of the pro-neuroinflammatory transcription factor, nuclear factor-kB in satellite glial cells (NF-kB) (Zheng et al., 2011). Knocking out NF-kB dependent satellite glial cell activation reduces expression of neuronal colony stimulating factor 1 (Csf1)(Lim et al., 2017), which can potentially reduce the inflammatory response and restore normal function of the spinal pain processing network. However, experimental measurement of expression factors associated such metabolic, genetic, and plastic changes that evolve with prolonged heating and the correlation of these changes with the function of the spinal pain processing network are required to validate this hypothesis.

Appendix 6: The Quasi-uniform assumption for Spinal Cord Stimulation translational research

6.1. Outline

This Appendix describes the quasi-uniform assumption which is a general theory that postulates local electric field predicts neuronal activation. A version of this study has been published (Niranjan Khadka et al., 2019c). We developed the computational current flow model of spinal cord stimulation (SCS) of humans and animal models to inform how the quasi-uniform assumption can support scaling neuromodulation dose between humans and translational animal.

6.2. Introduction

We extend the "quasi-uniform assumption" (Bikson et al., 2013) to apply it to animal models of spinal cord stimulation (SCS). For animal models of SCS to be meaningful, they must provide electrical stimulation in a way that approximates how the nervous system is activated during clinical therapy. Since the mechanisms of electrical stimulation are determined by which neuronal elements are excited (Ranck, 1975), SCS animal models would ideally use electrode montage (size, position) and current that stimulate the same distribution of neuronal elements as activated clinically. It is established that the spatial distribution of electric field across tissue (around neurons) determines which neuronal elements are excited (McIntyre and Grill, 1998; Rattay, 1999, 1986; Warman et al., 1992; Wongsarnpigoon and Grill, 2008), and so electrode montage and current in animal SCS models should create an electric field distribution approximating that produced clinically. However, this is impossible in practice, as animal anatomy is not proportionally scaled from humans. One can reproduce an electric field in one region of

interest (e.g. the dorsal column of one segment), but not the exquisitely detailed electric field changes over space - which will be species (even animal) and dose specific.

This challenge in approximating electric field spatial distribution is not specific to SCS, but applies to all translational models of brain stimulation leading to the formulation of the quasi-uniform assumption (Bikson et al., 2013). The quasi-uniform assumption should be understood as practical tool, not an ideal solution. The quasi-uniform assumption relies on two logical steps. First, the quasi-uniform assumption deviates from the dogma of relying on activating function (the electric field derivative) in predicting neuronal excitation (McIntyre and Grill, 1999; Rattay, 1999), and rather suggests that most CNS neuronal elements will be excited directly by the local electric field (Arlotti et al., 2012; Rahman et al., 2013; Rubinstein, 1993; Tranchina and Nicholson, 1986). In fact, experiments and activation-function-based modeling already demonstrate polarization sensitivity directly to local electric field magnitude for neuronal elements such as axons terminals (synapses), dendrites, and compact neurons (see Discussion). Second, as the electric field varies in a complex manner across tissue that is inconsistent across species (Hurlbert and Tator, 1994; Idlett et al., 2019; Swiontek et al., 1976; Xu et al., 2017), the quasi-uniform assumption indicates identifying one region of interest (a nominal target) and matching the electric field in just that region across animal and clinical cases. Ironically, the more one argues again the first aspect (that only exquisitely detailed modeling of electric field gradients along each neuron, compartment is sufficient), the more the second aspect becomes required - since electric field changes across an entire single neuron, much less a population of neurons, cannot be reproduced between human and animal.

The spatio-temporal distribution of electric fields in the body determines stimulation outcomes. Under quasi-static assumptions (Bossetti et al., 2008), the temporal waveform is easy

to replicate but the spatial distribution cannot be, where we can then find a basis in the quasi-uniform assumption.

There are three general approaches to scale stimulation dose in translational animal models. The first approach is to scale stimulation in the "dose space", namely to scale electrode size and/or current intensity by some arbitrary factor such as by animal size or physical space for the electrode. This approach is not principled (e.g. matching electrode current density between human and animal models does not produce equivalent outcomes; (Jackson et al., 2017)). The second approach is to use an acute physiological marker of nervous system activation (such as motor threshold; (Crosby et al., 2017, 2015a, 2015b; Guan et al., 2010; Koyama et al., 2018; Meuwissen et al., 2018; Prager, 2010; Sato et al., 2014; Schechtmann et al., 2008; Sdrulla et al., 2018; Song et al., 2013a, 2013b; Stiller et al., 1996; Yuan et al., 2014)) but using a stimulation waveform unlike that of interest for neuromodulation (e.g. using single pulse for motor threshold vs high rate pulse trains for neuromodulation). In this approach, the current is scaled based on this physiologic response, by the electrode montage is still ad hoc (e.g. what fits). Doing so ideally replicates in an animal model the neuronal elements (mechanism, and degree of activation) of a plausibly comparable acute physiological marker in human. However, the influence of stimulation other nervous system elements is not replicated, nor do the activated neuronal elements necessarily remain the same as waveform is changed. As a result, using an acute physiological maker to determine dose in animal is only valid as far as the acute physiological marker directly relates to the therapeutic mechanism.

The third approach to scale stimulation dose in translational animal models leverages computational models to predict electric fields (Bikson et al., 2015). In principle, this approach is based on long-standing principles that the electric field produced in the tissue along neuronal elements determines stimulation outcomes. But, our essential nuance to computational based

modeling, which is the quasi-uniform assumption, is the reliance of electric field magnitude on one region of interest. The generalization of electric field magnitude as a predictor of neuronal activation is addressed in the Discussion. However, our central point here is more practical: if one wants to rely on tissue electric field as a mean to justify scaling in an animal model, than reliance of electric field is not just useful but realistically inevitable, including in translational SCS studies (Idlett et al., 2019). To make this point, we apply it in high-resolution models of rodent, cat, and human. Previous studies have modeled SCS clinically (Hernández-Labrado et al., 2011; Howell et al., 2014; Huang et al., 2014; Lee et al., 2011; Lempka et al., 2015) and in specific animal models (Capogrosso et al., 2013a; Idlett et al., 2019; Xu et al., 2017)), and our approach here is not intended to be comprehensive (e.g. consider a wide range of electrode parameters) but rather reinforces these prior efforts in the context of the quasi-uniform assumption.

6.3. Materials and methods

We developed a computer-aided design (CAD) model of an exemplary brain slice chamber (din = 50 mm; dout = 60 mm; h = 40 mm), mimicking brain slice electric field stimulation (Bikson et al., 2004; Ghai et al., 2000; Gluckman et al., 1996) with two parallel conductive Ag/AgCl wire (d = 1mm; l = 60 mm), and SCS leads in SolidWorks (Dassault Systemes Corp., MA, USA).. For animal and human studies, we modelled two types of SCS leads namely a 4 Pt/Ir electrode contacts polyurethane SCS lead for animal study (rat: 1.35 mm electrode diameter, 3 mm electrode length, and 1 mm inter-electrode spacing; cat: 1.35 mm electrode diameter, 3 mm electrode length, and 1 mm inter-electrode spacing) and a 8 Pt/Ir electrode contacts SCS lead for human study (1.35 mm electrode diameter, 3 mm electrode length, and 1 mm inter-electrode spacing (Zannou et al., 2018)).

High resolution magnetic resonance imaging (MRI) scans of template healthy rat (0.1 mm), cat (0.1 mm), and human (0.8 mm) were segmented into tissue masks namely scalp, skull, csf, gray matter, white matter, cerebellum, hippocampus, thalamus, and air using Simpleware (Synopsys Inc., CA) by combining both automatic and manual morphological segmentation filters, and a volumetric FEM model was generated. SCS leads were then epidurally positioned over the targeted vertebrae level (lower cervical spine level and proximal to the mediolateral midline). We used voxel-based meshing algorithms which generated overly dense adaptive tetrahedral meshes of the brain slice chamber and the intricate animal models. The final mesh quality after multiple mesh refinements (within 1% error in voltage and current density at the spinal cord) was greater than 0.9 (COMSOL metric for mesh quality) indicating optimal elements in all models, and contained approximately 320000, 5950000, 22000000, 32200000 tetrahedral elements for slice chamber, rat, cat, and human model, respectively. The resulting volumetric meshes were later imported into COMSOL Multiphysics 5.1 (COMSOL Inc., MA, USA) to generate a finite element method (FEM) models. The models were computationally solved using Laplace equation for electric current physics ($\nabla(\sigma\nabla V)=0$), where V= potential and σ = conductivity) as field equation under stead-state assumption. Assigned material properties (electrical conductivities) for brain slice chamber, spinal tissues and electrode/lead were based on prior literature (Bikson et al., 2015; Song et al., 2015; Zannou et al., 2018).

In the brain slice chamber model, we simulated two parallel Ag/Agcl electrode placed laterally in a saline bath and applied normal current density equivalent to 1 mA ((J.n)* Areaanode = 1 mA) through one electrode (anode) while grounding the other electrode (cathode). The external boundaries of the brain slice chamber were electrically insulated (J.n = 0). In the rat, cat, and human SCS model, boundary conditions were applied in a bipolar configuration as: normal current

density at the exposed boundary of E4 (anode: 1 mA), ground at the exposed surface of E1 (cathode), insulation on all other external surfaces of the spinal cord and the peripheral tissues, and continuity for internal boundaries. We set the relative tolerance (convergence criteria) of each model to 1x 10-6 to get the most accurate solution while minimizing the errors. Corresponding voltage and electric fields were quantified from the simulations.

6.4. Results

Using exemplary computational models of the slice chamber with parallel electrodes and of rat, cat, and human with scaled cylindrical electrodes positioned epidurally over the targeted lower cervical vertebral column, the voltage and electric field intensity at the spinal cord and its peripheral tissues were predicted. Slice chamber FEM model predicted 0.22 V peak voltage and 0.01 V/mm electric field intensity. Predicted peak electric field around the lead (epidural space), csf, and spinal cord were 20, 7, and 1.02 V/mm, respectively for the rat model. For the cat model, predicted peak electric field intensity was 4.4, 0.14, and 0.06 V/mm at the epidural space, csf, and the spinal cord, respectively. Human SCS model predicted field intensities at the epidural space, csf and spinal cord of 15, 0.09, 0.06 V/mm respectively. Within the spinal cord, the electric field dropped to 50% of its peak intensity caudo-rostrally at 0.73 mm, 1.3 mm, and 1.5 mm and mediolaterally at 0.45 mm, 0.9 mm, and 0.85 mm distant from the peak intensity location for the rat, cat, and human respectively. The predicted electric field was only uniform in the slice chamber while, as expected, in the animal and human SCS the predicted electric field intensities were non-uniform - even on the scale of a single spinal neuron or axon (Hofstoetter et al., 2013; Holsheimer, 2002; Ladenbauer et al., 2010; Miranda et al., 2016; Rattay et al., 2000).

6.5. Discussion

The central proposition of this paper is that because it is not possible to reproduce the electric field distribution along diverse potential neuronal targets, the quasi-uniform assumption supports design and interpretation of animal models of SCS, (Fig. 39). A corollary of this proposition is the general applicability of considering the electric field magnitude as a meaningful predictor of neuronal activation. Each of these topics is considered separately below, but even to the extent detractors question the limits of the quasi-uniform assumption in general, then they acknowledge the limitations of translational animal models that necessitate this very assumption. The explicit goal of this paper is to explain the quasi-uniform assumption for translational animal research on spinal cord stimulation, with the broader and complex issue of general applicability addressed briefly (where an extended discussion beyond this paper scope). The computational models developed to illustrate the application of the quasi-uniform assumption largely confirm results from prior models (Holsheimer, 1998; Ladenbauer et al., 2010; Lempka et al., 2015; Miranda et al., 2016), and hardly capture the range of electrode configurations available; none-the-less they serve to show conventional notions of activating function are untenable in scaling dose between animal and human trials.

6.5.1. The quasi-uniform assumption in translational animal research

The quasi-uniform assumption (Bikson et al., 2015, 2013) is based on a proportional relationship between neuronal excitation and the local electric field magnitude (Arlotti et al., 2012; Rahman et al., 2013; Rubinstein, 1993; Tranchina and Nicholson, 1986). To the extent investigators aim to quantitively match tissue-level measures of electrical potency across human and animal models, the quasi-uniform assumption is required in translational animal studies of SCS. During SCS, the electric field varies in a complex manner across the spine (Fig. 41). It is not technically feasible in animal or brain slice studies to replicate the electric field in all regions of

the spinal cord – since doing so would require applying a stimulation dose in given animal model that reproduces the voltage distribution across an arbitrarily large number of neuronal elements exactly as produced in human stimulation (despite gross difference in anatomy and cellular morphology). Since this is practically impossible, the solution is to select a clinical region of interest (e.g. dorsal horn at one segment level), predict the clinical electric field in that region of the spine, and then to replicate that electric field in an analogous region of the animal model. In

selecting one electric field in a region of interest, the quasi-uniform assumption is applied. This approach was rigorously (implicitly) applied for an *ex vivo* mouse SCS model (Idlett et al., 2019).

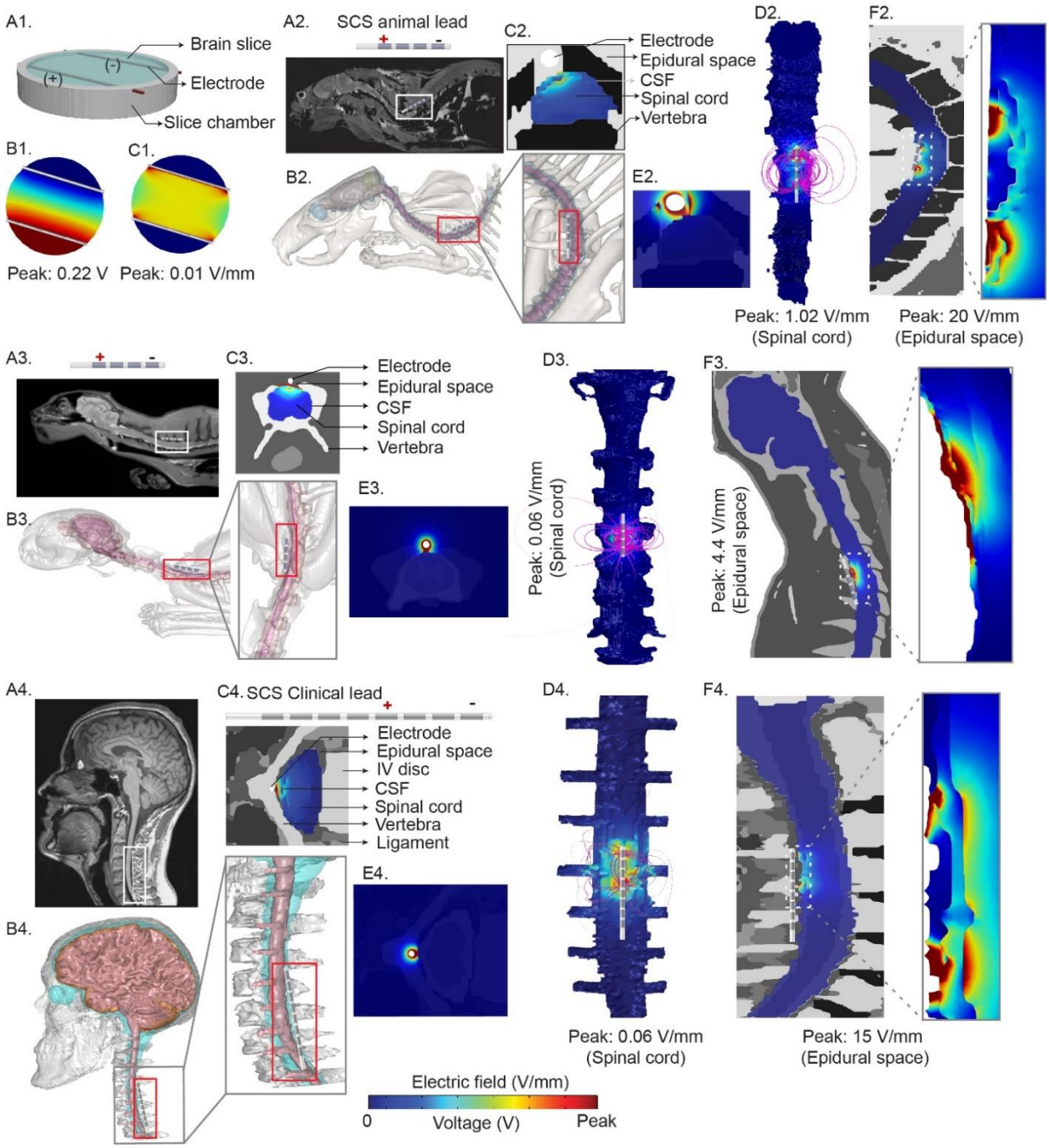

Figure 41: Evaluation of the quasi-uniform assumption for SCS including brain slice, rat, cat, human, and clinical current flow simulation. We developed computer-aided design (CAD) model of a slice

chamber, and a realistic MRI driven computational models of rat, cat, and human and predicted electric field and voltage across tissue. (A1) illustrates brain slice chamber with two parallel stimulating wires. (B1, C1) corresponding predicted peak voltage (0.22 V) and electric field intensity (0.01 V/mm) for the brain slice chamber in A1. (A2) MRI slice of a rat image with a SCS lead positioned epidurally along the lower cervical region. Segmented spinal cord tissues of the rat model (B2). (C2, D2) Cross-section view of predicted electric field and electric field streamlines plotted around the stimulating electrode contacts. (E2, F2) shows predicted peak electric field around the lead (epidural space: 20 V/mm) and the spinal cord (1.02 V/mm) respectively. (A3, B3, C3, D3, E3, F3) illustrates SCS lead positioning, segmentation, and electric field prediction in a cat FEM model. (A4) represents SCS lead positioning at the cervical vertebrae of a human FEM model. (B4) represents spinal cord tissue segmentation. (C4, E4) shows electric field distribution across spinal tissues. (D4) illustrates uniformly seeded electric field streamlines from the leads to the spinal cord (peak: 0.06 V/mm). (F4) represents predicted electric field in the epidural space (peak: 15 V/mm) and other peripheral spinal tissues. The key take-away of these predictions is not simply that peak electric field varies across species but that the spatial distribution of the electric field is complex and species specific, such that the electric field across species can only be matched in a selected ROI, not across all the spinal cord.

There are two general alternatives to leveraging the quasi-uniform assumption. The first alternative is to scale electrode size and/or current applied by a factor related to an arbitrary measure of animal size. For example, using a 50-fold smaller electrode and/or 50-fold less current. But such approaches are not expected to produce comparable neuromodulation and are only as principled as the arbitrary scaling factors. It is not prudent to apply "smaller" stimulation (a smaller electrode and reduced applied current) heuristically because the resulting electric field may not be clinically meaningful in humans. The second alternative is, using an arbitrary electrode geometry, to titrate current intensity to produce an overt physiological response in an animal model – for example a motor response. This approach is underpinned by the assumption that grossly

reproducing an overt physiological response that can be related to a clinical side-effect (e.g. motor twitch), will also reproduce a neuromodulation outcome in regard to a behavioral endpoint (e.g. reduction in pain) comparable to clinical SCS. This is only the case when the overt physiological outcome is the same pathway are the behavioral outcome or when the two are coincidentally related. Instead, one could identify the neuronal elements (e.g. dorsal column axon collaterals) that presumably underlie the desired behavioral outcome in humans (e.g. reduction in pain), and then provide stimulation in animal models to activate those same neuronal elements. This process therefore approximate tissue level influence which, for the reasons stated above, requires the quasi-uniform assumption.

The process of applying the quasi-uniform assumption is therefore: 1) identify the candidate neuronal element presumed responsible for the clinical outcome of interest; 2) using computational FEM model of current flow, simulate SCS dose in human (Fig. 41) to predict the peak electric field magnitude on those elements; 3) select a practical electrode geometry to be used in an animal model; 4) simulate the intensity applied to that electrode geometry to produce in the comparable neuronal element in the animal model as the electric field generated clinically (Fig. 41). For example, using the dorsal column as putative targets, for the specific electrode geometries considered in human and animal, we propose an intensity scaling factor of 17X and 1X to rat and cat. This workflow has limitations. Selecting which neuronal elements are relevant is an assumption, but a principled one that supports hypothesis testing. Special care is required in applying invasive micro-electrode stimulation in animal studies precisely because they produce highly non-uniform fields near the electrodes which may produce local activation unrelated to the neuronal elements of translational interest.

6.5.2. The quasi-uniform assumption as a general marker of neurostimulation

There is a long-standing theoretical consideration of the role of electric field change along neuronal compartments, rather than simply electric field magnitude, to predict neuronal activation (Basser and Roth, 2000; Brocker and Grill, 2013; Ranck, 1975; Reilly et al., 1985). These conclusions derive from considering of long, uniform, straight peripheral axons subject to stimulation with proximal micro-electrodes (Frijns et al., 1994; Rubinstein and Spelman, 1988). This formalism has been extended to more complex neuronal geometries and macro-electrode, including epidural spinal cord stimulation (Graham et al., 2019a; Holsheimer, 1998; Howell et al., 2014; Kent et al., 2014; N. Khadka et al., 2019; Lee et al., 2011). But it is well accepted that an axon termination or bend (Arlotti et al., 2012; Chakraborty et al., 2018; McNeal, 1976; Mourdoukoutas et al., 2018; Rubinstein, 1993; Tranchina and Nicholson, 1986), an axon traversing tissues of sufficient different resistivities (Capogrosso et al., 2013a; Danner et al., 2011; Ladenbauer et al., 2010; Miranda et al., 2007; Mourdoukoutas et al., 2018; F. Rattay et al., 2000; Struijk et al., 1993c), and overall compact neuronal structures (Aberra et al., 2018; Chan et al., 1988; Radman et al., 2009b, 2009a; Struijk et al., 1993c; Tranchina and Nicholson, 1986) will all effectively respond to the local electric field magnitude. Coburn (1985) notes "sharp turns in the path of the fiber itself can be equally influential [to extracellular potential changes] (Coburn, 1985)". Similarly noted is a characteristic feature of "dorsal column nerves fibers is the presence of myelinated collaterals perpendicular to the rostro-caudal fibers" such that activation by SCS is "significantly influenced by the presence of the collateral" (Struijk et al., 1992). Foundational texts on stimulation emphasize regions of curvature (e.g. bending of the spinal root) and changes in tissue environment (e.g. axons crossing from cerebrospinal fluid to white matter, or into the epidural space and vertebral bone) produce effective sensitivity to electric field magnitude (F. Rattay et al., 2000). The more detailed model precision, the more electric field magnitude

dependent effects emerge. Finally, it is not simply that terminal polarization, bends, and other changes in morphology or environment track electric field magnitude, but to the extent that these regions are then the most sensitive to stimulation, they will determine activation threshold for the entire neuron.

Indeed, detailed experimental analysis of central stimulation in animals supports electric field-based mechanism. This includes *in vivo* data evaluation that the threshold current as a function of distance from stimulation electrode, where increase in threshold with the square of distance is consistent with electric field-based stimulation (Nowak and Bullier, 1996). This distance-threshold relationship is remarkably accurate and reproduced across CNS structures (Armstrong et al., 1973; Hentall et al., 1984; Marcus et al., 1979; Nowak and Bullier, 1996; Stoney et al., 1968), including spinal cord (Gustafsson and Jankowska, 1976; Jankowska and Roberts, 1972; Joucla et al., 2012; Stoney et al., 1968). This relationship is so well established that it has been used for decades, to characterize the cellular targets of stimulation (e.g. the "k" value; (Armstrong et al., 1973; Hentall et al., 1984; Kubin and Davies, 1988; Marcus et al., 1979; Nowak and Bullier, 1996; Yeomans et al., 1986)). Additionally, decades of *in vitro* data applying uniform electric field (with zero electric field gradient) have characterized neuromodulation including oscillations, synaptic processing, and plasticity (Bikson et al., 2004; Kronberg et al., 2017). Trancutaneous spinal cord stimulation may also rely on locally uniform electric fields (Danner et al., 2011; Lesperance et al., 2018; Priori et al., 2014).

Model driven optimization for non-invasive electrical stimulation has almost universally relied (implicitly) on the quasi-uniform assumption, including models for transcranial Direct Current Stimulation (tDCS; (Abhishek Datta et al., 2009; Dmochowski et al., 2011)), transcranial Alternating Current Stimulation (tACS; (Rampersad et al., 2019; Reato et al., 2010)), and

Transcranial Magnetic Stimulation (TMS; (Gomez et al., 2018; Thielscher et al., 2011)), Electroconvulsive Therapy (ECT; (Bai et al., 2017, 2012; Lee et al., 2016)) – with few notable deviations (Miranda et al., 2007; Salvador et al., 2011). In modeling deep brain stimulation, the quasi-uniform assumption has been leveraged (Astrom et al., 2015; Chaturvedi et al., 2010; Cubo et al., 2019) in cases of constrained optimization methodology or to avoid computational complexity (e.g. software for clinical practice). In most computational model of Spinal Cord Stimulation, non-uniform electric field is coupled to neuron morphology (Holsheimer, 2002a; Lempka et al., 2019b), though optimization or validation of new SCS approaches can rely on (quasi-uniform) electric field distribution. (Anderson et al., 2019; Coburn, 1985; Hernández-Labrado et al., 2011; Huang et al., 2014)

6.5.3. Inevitability of the quasi-uniform in translational animal models

None of this discussion should be taken to diminish the value of detailed SCS modeling which has become increasingly complex from pioneering work by Holsheimer and colleagues (Holsheimer and Struijk, 1991; Holsheimer and Wesselink, 1997) and Coburn and colleagues (Coburn, 1985, 1980) to contemporary efforts (Durá et al., 2019; Lempka et al., 2015, 2019b; Min et al., 2014; Xu et al., 2017). When the functional models are used to prescribe optimal dose, it is an open question of how much does the detailed model verse (quasi-uniform) electric field-based analyses lead to distinct outcomes? With the latter lending themselves to closed-form (linear) optimization (Dmochowski et al., 2011) and fast (clinician toolbox) stimulation. Regardless, the scope of this paper is limited to consider the use of the quasi-uniform assumption in translational animal research. This, while the broader discussion about when polarization by electric field magnitude is relevant, we posit that the quasi-uniform assumption is not simply a principled, but an inevitable concept if tissue level electrical forces are to be rationally matched across specifics

using computational models. As discussed, modeling and experimental studies support that in a complex 'soup' morphology, electric field magnitude indeed predicts maximal polarization (e.g. Eλ; (Rattay, 1986)) including compact neuron polarization (Joucla and Yvert, 2009), axon terminations (synapse) and bends (e.g. at roots). In any case, it is practically impossible to replicate SCS electric field changes across even a single hypothetical spinal neuron between species – much less across the entire population of neurons – make the quasi-uniform assumption a technical necessity in those translational animal models that want to relate tissue level measures of stimulation intensity. Ultimately, the question of when and how electric field magnitude can be used as a surrogate for neuromodulation efficacy in SCS is a broad and ambitious question, and the argument of this paper is only to present the quasi-uniform assumption as one tool to support meaningful translational studies on SCS.

Appendix 7: Bio-Heat Model of Kilohertz-Frequency Deep Brain Stimulation Increases Brain Tissue Temperature

7.1. Outline

This Appendix test the hypothesis that 10 kHz-DBS modulates neuronal function through moderate local tissue heating, analogous to kilohertz spinal cord stimulation (10 kHz-SCS). A version of this study has been published (Khadka et al., 2020). In order to establish the role of tissue heating in 10 kHz-DBS (30 µs, 10 kHz, at intensities of 3-7 mA_{peak}), we characterize the range of temperature changes during clinical kHz-DBS protocols using computational study. We concluded that subject to validation with *in vivo* measurements, neuromodulation through a heating mechanism of action by 10 kHz-DBS can indicate novel therapeutic pathways and strategies for dose optimization.

7.2. Introduction

In the first study examining deep brain stimulation (DBS) at 10 kHz frequencies (10 kHz-DBS; also called ultra-high frequency DBS), we reported acute 10 kHz-DBS appears safe and may be effective in improving motor symptoms in patients with movement disorders (Harmsen et al., 2019). Furthermore, 10 kHz-DBS stimulation may have the potential to reduce stimulation-induced adverse effects, such as transient paresthesia and impaired speech, which are often encountered with DBS at conventional frequencies (Fagundes et al., 2016; McIntyre et al., 2015; Lozano et al., 2019). Selecting the optimal stimulation frequency for DBS can be challenging. Perceived loss of DBS efficacy at low kHz (< 5 kHz) derives from historical findings in limited parameter space (e.g. voltage-controlled, specific duty cycle)(Benabid et al., 1991), which was

supported by models of conventional mechanisms of action (Couto and Grill, 2016). Another factor that encourages the use of lower DBS frequencies is battery life (Ramasubbu et al., 2018); we note that increased power consumption is delivered into the electrode and subsequently into the surrounding deep brain tissue (Cubo et al., 2019).

The emergence of spinal cord stimulation (SCS) at 10 kHz (Al-Kaisy et al., 2014; Crosby et al., 2017; Kapural et al., 2016; Shechter et al., 2013; Song et al., 2014) has encouraged the exploration of novel neuromodulation mechanisms, including our hypothesis of tissue warming, based on the relatively high-power nature of clinical 10 kHz waveforms (Zannou et al., 2019b). Since heating of deep brain tissue will impact a myriad of neuronal functions linked to clinical efficacy (see Discussion), a pivotal step to establishing the role of moderate local heating in 10 kHz-DBS is predicting the degree of temperature increases. To this end, we expanded on our earlier phantom-verified bio-heat model of conventional rate DBS (Maged M. Elwassif et al., 2006a; Elwassif et al., 2012a), incorporating detailed MRI-derived representation of inhomogeneous local tissues, and emulating clinical 10 kHz-DBS protocols.

7.3. Methods

7.3.1. Bio-heat DBS model construction and solution method

High resolution magnetic resonance imaging (MRI) scans of standard human head (unsampled to 0.18 mm) were segmented (Simpleware, Synopsys Inc., CA, USA) into the following tissue masks : skin; skull; CSF; air; gray-matter; white-matter; cingulate gyrus; basal ganglia; corpus callosum; thalamus; subthalamic nucleus (STN); fornix, nucleus accumbens; hippocampus; amygdala; midbrain; mammillary bodies; pons; medulla oblongata; and insula. Computer-aided design (CAD) model of a clinical DBS lead (Medtronic 3387; 4 contact (0,1,2,

and 3) Pt/Ir DBS lead, contact length: 1.5 mm, inter-contact distance: 1.5 mm, diameter: 1.27 mm) was modelled (SolidWorks, Dassault Systemes Corp., MA, USA) and imported into the head model. A 0.5 mm thick encapsulation layer around the DBS lead with standard assigned conductivity (0.13 S/m) matched clinical impedance values (~1 kΩ) (Grill and Mortimer, 1994). The lead penetrated from the top of the skull at ~20 mm from the midline to the STN target at ~12 mm from the midline. Approximately 7 mm of the STN was contacted around the lead: contact 0 (deepest contact) was at the ventral border of the STN, contacts 1 and 2 were inside the STN, and contact 3 was at the dorsal border of the STN (Fig. 42). The volumetric conductor model was then meshed using a voxel-based meshing algorithm, and an adaptive tetrahedral mesh of the head was generated following multiple mesh densities refinements (within in 1% error in voltage and current density at the STN).

The stimulation (Laplace equation for electrostatics ($\nabla(\sigma\nabla V) = 0$ where V is potential and σ is conductivity) coupled Pennes' bioheat transfer equation (Equation 1) including joule heating, metabolic heat generation rate (Q_{met}), and blood perfusion rate (ω_b) in the brain tissues was solved.

$$\rho C_p \nabla T = \nabla.(\kappa\nabla T) - \rho_b C_b \omega_b (T - T_b) + Q_{met} + \sigma|\nabla V^2| \quad (1)$$

where ρ, C_p, T, σ, *and* κ represent tissue density, specific heat, temperature, electrical conductivity, and thermal conductivity respectively.

Blood density (ρ_b), specific heat (C_b), and temperature (T_b) were assumed constant in all vascularized brain tissues with corresponding values as 1045 kg/m^3, 3600 J/(kg. K), and 36.7 ^{0}C, respectively. Tissue specific perfusion rate (ω_b) ranged from 0.00063 - 0.0228 s^{-1} (Collins et al., 2004b; Xu et al., 1999b). Prior to the application of 10 kHz-DBS, the Q_{met} required to balance the

initial brain temperature was calculated using Equation 2 (Hodson et al., 1989a; Wilson and Spence, 1988b):

$$Q_{met} = \rho_b C_b \omega_b (T - T_b) \quad (2)$$

where T_b and T are initial blood and brain temperature.

The calculated Q_{met} values from Equation 2 for the corresponding ω_b values of the brain tissues were: grey matter ($\omega_b, 0.018\ s^{-1};\ Q_{met}, 15540\ Wm^{-3}$); white matter, corpus callosum, fornix, mammillary bodies ($\omega_b, 0.008\ s^{-1};\ Q_{met}, 4320\ Wm^{-3}$); hippocampus ($\omega_b, 0.00063\ s^{-1}; Q_{met}, 15540\ Wm^{-3}$); midbrain ($\omega_b, 0.028\ s^{-1};\ Q_{met}, 11370\ Wm^{-3}$); basal ganglia, thalamus, amygdala, cingulate, nucleus accumbens ($\omega_b, 0.02282\ s^{-1};\ Q_{met}, 15540\ Wm^{-3}$;); and, STN ($\omega_b, 0.02038\ s^{-1};\ Q_{met}, 13930\ Wm^{-3}$). Since CSF is avascular and enCAP is predominantly scar tissues, 0 values were assigned for Q_{met}, and ω_b were assigned. The balanced Q_{met} values approximated prior experimental measurements (Collins et al., 2004b; Dusan Fiala et al., 1999; Xu et al., 1999b).

Thermo-electric properties (σ, κ) of the biological tissues were based on the following aggregate literature values ("Dielectric Properties » IT'IS Foundation," n.d.; Gabriel et al., 1996a): CSF (1.65 S/m, 0.57 W/(m.K)); grey matter, STN, thalamus, amygdala, basal ganglia, nucleus accumbens, and cingulate gyrus (0.276 S/m, 0.55 W/(m.K)); midbrain (0.126 S/m, 0.51 W/(m.K)); white matter, mammillary bodies, and fornix (0.126 S/m, 0.48 W/(m.K)); hippocampus (0.126 S/m, 0.55 W/(m.K)); corpus callosum (0.060 S/m, 0.48 W/(m.K)); and, enCAP (0.13 S/m, 0.47 W/(m.K)). Electrical and thermal conductivities of the DBS contacts and insulating bands between contacts were (4E6 S/m, 31 W/(m.K)) and (0.0002 S/m, 0.026 W/(m.K)), respectively (Butson and

McIntyre, 2006). In some simulations the "standard" tissue conductivity parameters of enCAP and STN were manipulated by either doubling or halving.

Static RMS values were applied (Equation 3) for tested clinical kHz-DBS intensities (3-7 mA_{peak} at 30 µs and 10 kHz), and this approach was supported by prior phantom verification for conventional DBS (Elwassif et al., 2012a) and kHz-SCS (Khadka and Bikson, 2019; Zannou et al., 2019a).

$$I_{RMS} = I_{Peak}\sqrt{t * f} = I_{Peak}\sqrt{D} \quad (3)$$

where I_{RMS} is the corresponding RMS value of peak stimulation intensity (I_{peak}), t is the combined (anodic and cathodic phase) pulse width, f is the frequency, and D is the duty cycle.

Unless otherwise stated, contact 2 (C2) was energized in a monopolar electrode configuration as tested clinically (Harmsen et al., 2019). An inward normal current density ($J_{norm,\ RMS}$) was applied to the electrode with the bottom surface of the model grounded. For bipolar electrode configuration, contact 2 (C2) was energized (anode) while contact 1 (C1) was grounded (cathode). Remaining outer boundaries of the head were electrically insulated. The temperature of the outer boundaries of the model was set to core body temperature (37 ^{o}C) with no convection across outer head boundaries (M.M. Elwassif et al., 2006). The bio-heat 10 kHz-DBS model was then solved under the steady-state assumption and the corresponding temperature increases and field intensities were predicted. Temperature difference (ΔT) was calculated by subtracting tissue temperature increase by stimulation (joule heat) from tissue temperature increase without stimulation.

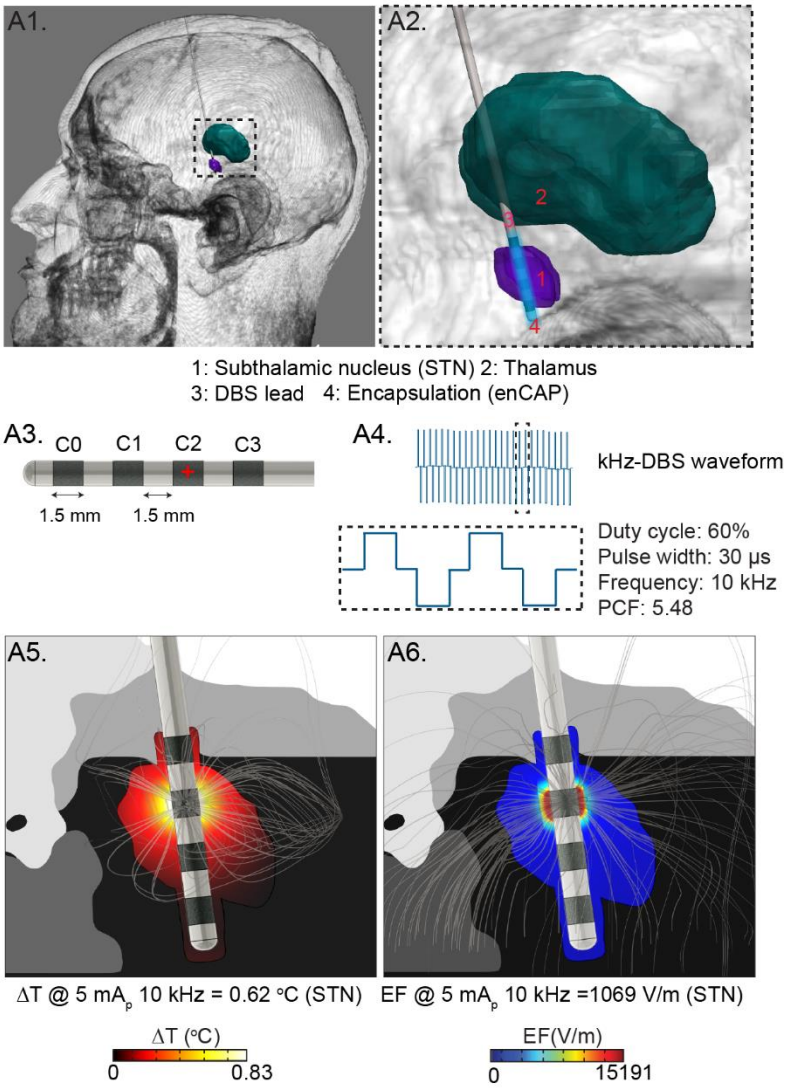

Figure 42: FEM bio-heat model predicts temperature increases during kHz-DBS. (A1) A high-resolution human head model with segmented brain tissues and a DBS lead. For the illustration purpose, only STN (purple) and thalamus (green) are shown. (A2) Inset details model anatomy, showing the STN (1), thalamus (2), DBS lead (3) at the STN target, and an encapsulation layer (4). (A3) Clinical DBS lead (Medtronic DBS 3387) with contact C2 energized in a monopolar electrode configuration. (A4) Clinical DBS waveform at 10 kHz with 30 µs pulse width per phase, resulting in a 5.48 Pulse Compression Factor (PCF) with 60 % duty (see 14 for details). Predicted temperature increases with heat flux streamlines

(A5) and electric field distribution with current streamlines (A6) across deep brain tissues at 5 mApeak (3.8 mA RMS).

7.3.2. Volume of tissue activated (VTA) and Volume of tissue heated (VTH)

An activating function based approach (second derivative of the electric potential) was implemented to estimate the volume of tissue activation (VTA) for conventional rate (130 Hz) DBS (Butson and McIntyre, 2006, 2005; Chaturvedi et al., 2010; Rattay, 1986). Specifically, the divergence of the gradient of the electric potential ($\nabla^2 V_e$) (generalization of the second derivative of the electric potential in 3D) was used to approximate the VTA (Astrom et al., 2015; Butson and McIntyre, 2006; Chaturvedi et al., 2010; Hemm et al., 2005; Horn et al., 2017). Activation threshold levels for different axon diameters (0.36 V/mm^2 corresponding to 2.5 µm or 0.82 V/mm^2 corresponding to 5 µm) at conventional rate DBS were implemented to define the VTA (Astrom et al., 2015). For volume of tissue heated (VTH) at 10 kHz-DBS, a ΔT threshold of 0.1 ^{0}C or 0.5 ^{0}C was considered. Both VTA and VTH were determined at 3, 5, and 7 mA peak with monopolar and bipolar stimulation (Fig. 44).

7.4. Results

We developed an MRI-derived finite element method (FEM) bio-heat computational model of 10 kHz-DBS, with tissue specific electrical and thermal (passive and blood flow) properties (Fig. 42). For each simulation, RMS current intensities that corresponded to clinically tested peak current intensities were applied to the model. Predicted peak temperature (ΔT) in the encapsulation layer (enCAP) and subthalamic nucleus (STN) increased supra-linearly as a function of stimulation intensity (standard tissue parameters, Fig. 43), reasonably fit by a power

law(Zannou et al., 2019b). Under standard tissue parameters, monopolar kHz-DBS at 2.3 mA_{RMS} (3 mA_{peak}) produces 0.13 ^{o}C temperature rise in the enCAP and 0.10 ^{o}C at the STN. At 3.8 mA_{RMS} (5 mA_{peak}) temperature increases by 0.83 ^{o}C in the enCAP and 0.62 ^{o}C at the STN. Finally, at 5.4 mA_{RMS} (7 mA_{p}) the temperature increases by 1.87 ^{o}C in the enCAP and 1.38 ^{o}C at the STN.

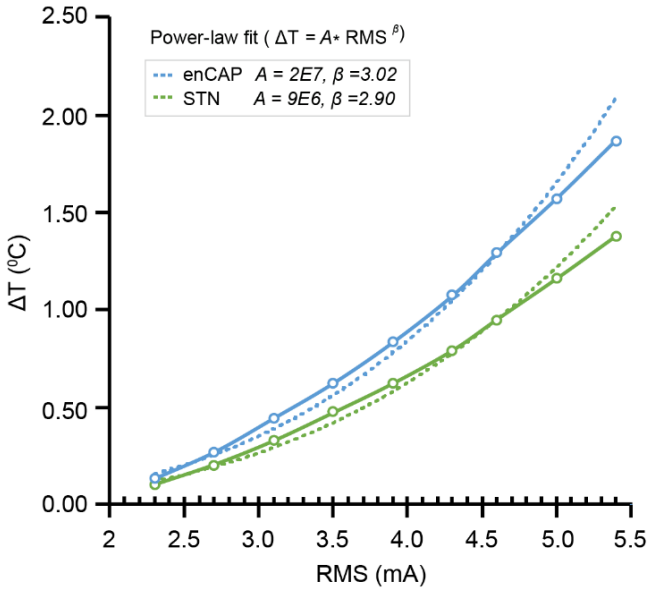

Figure 43: Stimulation intensity (RMS) versus temperature increases at encapsulation (enCAP) and subthalamic nucleus (STN). An MRI-derived FEM model of kHz-DBS predicts ΔT increases supra-linearly (β > 1) with kHz-DBS RMS intensities 14. Results were fit according to a power law.

For 10 kHz monopolar DBS with 3.8 mA_{RMS} (5 mA_{p}) intensity, we considered the sensitivity of heating to model tissue parameters, specifically doubling or halving the electrical and/or thermal conductivities of either the STN or enCAP (Table 5). Decreasing the electrical or thermal conductivity of either STN or enCAP always increased heating of both STN and enCAP. Heating of both the STN and enCAP was the most sensitive to reducing enCAP electrical conductivity (enCAP; σ/2, Ƙ)- namely, heating the 10 kHz-DBS increased the most with reducing enCAP conductivity compared to any other tissue parameter tested. STN heating was next more

sensitive to reducing STN thermal conductivity (STN; σ, Ƙ/2) while enCAP heating was next more sensitivity to reducing enCAP thermal conductivity (enCAP σ, Ƙ/2). Maximum temperature rises in both STN (1.35 ^{o}C) and enCAP (2.53 ^{o}C) were predicted for enCAP σ/2, Ƙ/2. Minimal temperature rises in both STN (0.02 ^{o}C) and enCAP (0.10 ^{o}C) were predicted for STN 2σ, 2Ƙ. In any combination tested, the ΔT was always higher in enCAP compared to the STN, except the (2σ, 2Ƙ) condition where heating in the STN was slightly greater than enCAP.

Activation thresholds corresponding to either 2.5 µm or 5 µm axon diameter stimulation at conventional rate DBS (130 Hz) defined the VTA. VTH thresholds of ΔT 0.1 ^{0}C and 0.5 ^{0}C were applied for 10 kHz-DBS. As a first approximation, under the assumptions simulated here, the volumes of VTA and VTH are comparable for the same dose. This may suggest that stimulation and heating have some additive effect in neural activation (neuromodulation). For a given current intensity and VTA/VTH threshold, both VTA and VTH roughly doubled for bipolar vs monopolar montages. Both VTA and VTH increased supralinearly with stimulation intensities (3,5,7 mA peak) and both bipolar and monopolar electrode configurations. For 7 mA (peak) bipolar and monopolar electrode configuration, the VTA and VTH spread beyond the STN. With monopolar 130 Hz DBS, the VTA were 14.15, 31.63, and 54.54 mm^3 at 0.36 V/mm^2 activation threshold, and 2.15, 5.83, and 10.81 mm^3 at 0.82 V/mm^2 activation threshold, for 3, 5, and 7 mA, respectively. The VTA for bipolar 130 Hz DBS at 3,5, and 7 mA intensities were 28.51, 58.21, and 90.94 mm^3 at 0.36 V/mm^2 threshold, and 4.53, 12.33, 22.28 mm^3 at 0.82 V/mm^2 threshold. When thresholding at 0.1 ^{0}C, the VTH for monopolar 10 kHz DBS were 2.61, 39.29, and 135.19 mm^3 and at a threshold 0.5 ^{0}C, the VTH were 0, 5.34, 23.55 mm^3 for 3, 5, and 7 mA peak, respectively. For a bipolar 10 kHz DBS, the VTH were 9.69, 135.66, and 298.23 mm^3 at 0.1 ^{0}C threshold, and 0, 20.62, and 82.99 mm^3 at 0.5 ^{0}C threshold for 3,5, and 7 mA peak respectively (Fig. 44).

7.5. Discussion

Our initial clinical findings on kHz-DBS are of interest because they open up a new therapeutic stimulation parameter space for future study and development (Harmsen et al., 2019). A heating mechanism of action (MoA) augments such considerations. For example, since heating depends only (and supra-linearly) on waveform RMS independent of other parameters, optimal electrode placement and lead resistance may differ following heating versus conventional MoA.

The biophysics of heating are analogous to experimentally-verified prior simulations of conventional rate DBS (Elwassif et al., 2012a; Maged M. Elwassif et al., 2006a) and kHz SCS (Khadka and Bikson, 2019; Zannou et al., 2019b, 2019a), however comparisons highlight the importance of stimulation dose (electrodes and waveform) as well as tissue anatomy and parameters. Compared to monopolar stimulation, energizing an adjacent contact in a bipolar electrode configuration may further increase temperature (Maged M. Elwassif et al., 2006a). This is compounded by reduced inter-electrode distances (e.g. Medtronic 3389 vs 3387 lead designs) (Maged M. Elwassif et al., 2006a). In kHz-SCS, the highly resistive epidural space plays a central role in temperature increases both at the lead and at the spinal cord (Zannou et al., 2019b). Here, the encapsulation layer plays a similar role in kHz DBS (Table 5)- namely, despite the difference in anatomy in both cases a high resistive tissue at the electrode surface increases joule heat deposition, which is then conducted to more distant tissue (Philpott et al., 2017).

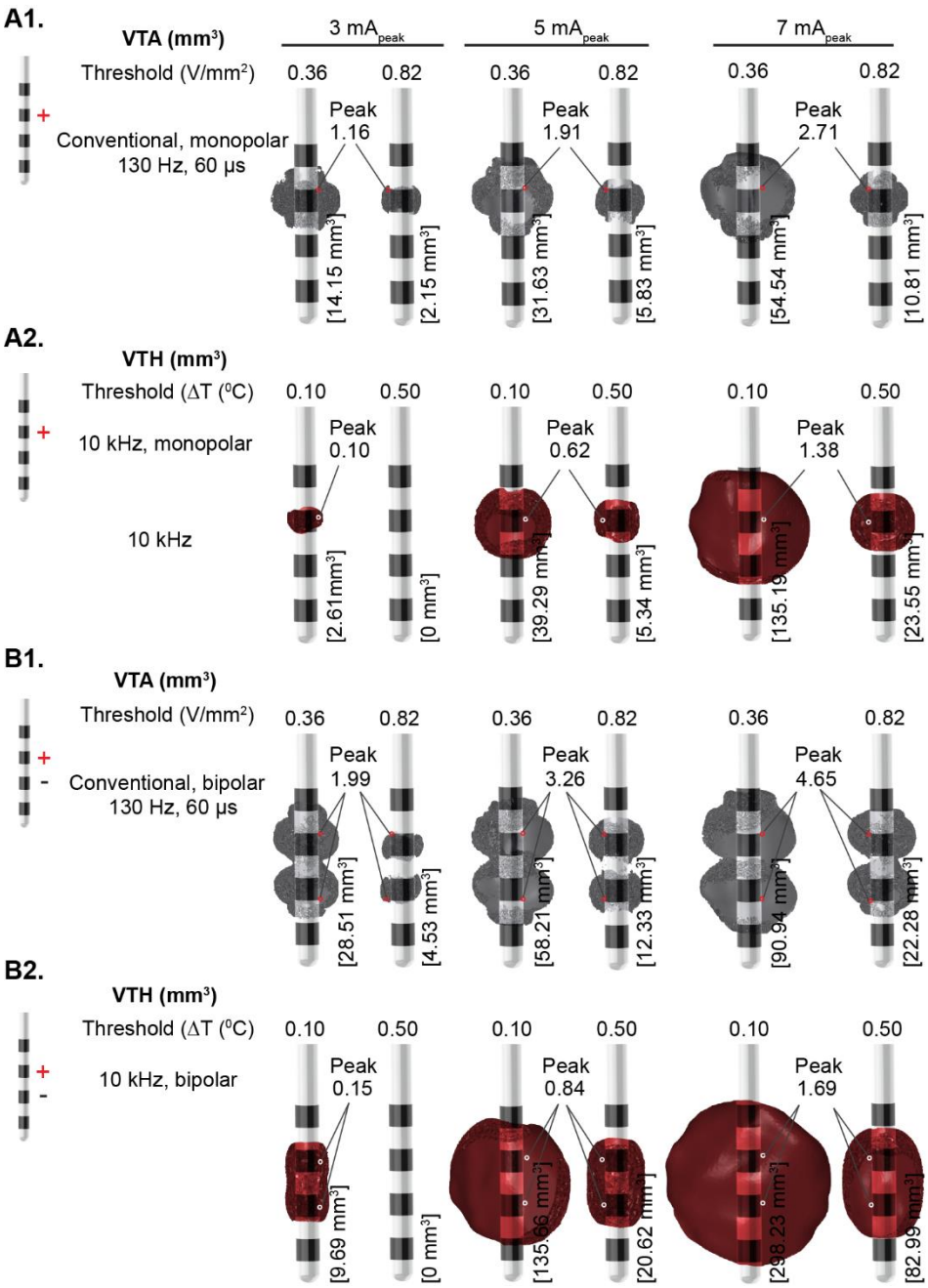

Figure 44: Activating function based VTA at conventional rate DBS (130 Hz at 60 µs), and VTH at 10 kHz-DBS with monopolar or bipolar electrode configuration at 3, 5, 7 mA peak with different thresholds. VTA and VTH both increase supralinearly with stimulation intensities and expand twice with bipolar montage vs monopolar montages.

enCAP conductivity sensitivities				STN conductivity sensitivities		
Conductivities	ΔT (^{0}C)		Resistance (Ω)	ΔT (^{0}C)		Resistance (Ω)
	enCAP	STN		enCAP	STN	
(σ, Ƙ)	0.83	0.62	747	0.83	0.62	747
(σ, Ƙ/2)	1.22	0.66	747	1.18	1.00	747
(σ, 2Ƙ)	0.60	0.55	747	0.61	0.36	747
(2σ, Ƙ)	0.36	0.28	520	0.77	0.55	660
(2σ, Ƙ/2)	0.56	0.30	520	1.09	0.91	660
(2σ, 2Ƙ)	0.23	0.24	520	0.10	0.02	660
(σ/2, Ƙ)	1.77	1.27	1175	0.95	0.72	885
(σ/2, Ƙ/2)	2.53	1.35	1175	1.34	1.15	885
(σ/2, 2Ƙ)	1.31	1.14	1175	0.70	0.44	885

Table 5: Conductivity sensitivities analysis at 3.8 mARMS (5 mAp) of the encapsulation layer (enCAP) and subthalamic nucleus (STN). Properties of the enCAP (left) or STN (right) were changed independently with resulting heating (ΔT) of both enCAP and STN reported. Tissue electrical conductivity (σ) and/or thermal conductivity (Ƙ) were doubled or halved. Total lead resistance (Ω) for each condition is also reported.

Notably, while increasing tissue resistivity increases heating for current-controlled stimulation, increasing tissue resistivity decreases heating for voltage-controlled stimulation (Maged M. Elwassif et al., 2006a). As such, the enCAP may increase heating under current-control while decreasing heating under voltage-control. All these device and tissue parameters interact; for example, voltage-controlled DBS at conventional rates with low impedance (minimal encapsulation layer) may also produce significant heating (Elwassif et al., 2012a; Maged M. Elwassif et al., 2006a). However, by virtue of a higher Pulse Compression Factor (PCF; (Zannou et al., 2019b)), kHz-DBS can achieve higher temperature. FDA guidelines for MRI-safety allow less than 2 ^{0}C over 1 hour of exposure at 1.5 T and 3.0 T frequencies (Health, 2019) with MRI compatible system resulting in 0.3 - 3.6 ^{0} C (Golestanirad et al., 2019; Kainz et al., 2002).

Functional tissue ablation specifically using DBS leads involves RMS intensities of 19 or more mA, produced peak heating of ~ 69.52 ^{0}C per our quadratic standard model. Generally, RF-ablation of deep brain aims for 42 - 49 ^{0}C, though interestingly transient increases to 45 ^{0}C can produce reversible functional lesions (Brodkey et al., 1964). Animal studies indicate reversible functional lesioning, for short exposures, at temperatures > 46 ^{0}C (Eve, 1900).

The precise degree of heating during kHz DBS will depend on lead design, electrode selection, waveform (RMS), and passive and active tissue properties (Table 5, Fig. 42, 44). Nevertheless, the DBS bioheat models developed here support predicting and optimizing heating across DBS approaches. This can be informed and contrasted to models of conventional-rate (e.g. 130 Hz) DBS. In general, for both VTA and VTH one can consider the brain area of modulation (perimeter of volume maps) and the nature of neuromodulation within the volume (threshold used for given volume map). Whereas for VTA this analysis addresses fiber activation of various types (predicted by activating function threshold) for VTH this analysis will depend on yet-unspecified neurophysiological process (predicted by temperature threshold). Both VTA and VTH increase supralinearly with intensities (Fig. 44; (Butson et al., 2007)) and expand ~2x with bipolar vs monopolar montages (Fig. 44; (Grant and Lowery, 2009; Walckiers et al., 2010)). Increases in tissue resistivity (for example enCAP or STN resistivities) increases both VTA and VTH under current-controlled stimulation, while decreasing both VTA and VTA under voltage-controlled stimulation (data not shown; (Butson et al., 2006)). Depending on dose, either VTH or VTA may expand beyond the (targeted) STN, with implications for efficacy or the therapeutic window (Fig. 44; (Frankemolle et al., 2010; McIntyre et al., 2004a, 2004b; McIntyre and Thakor, 2002)).

While the specific mechanisms of heating-based neuromodulation (at different VTH temperature thresholds) remains to be shown, the principle of heating-based neuromodulation is

established. All brain tissues are sensitive to temperature variations. Neuronal excitability, neurotransmitter function and plasticity, underlying metabolic functions, and connectivity and synchronization, are all modulated by heating (Kim and Connors, 2012b; Harris et al., 1962b; Matsumi et al., 1994b; Chowdhury et al., 2014b; Graham et al., 2008). Indeed there is a long standing record of neuromodulation techniques that are associated with heating and reversible changes in brain excitability including transcranial focused ultrasound (Darrow et al., 2019) and infrared stimulation (Duke et al., 2013). A heating DBS MoA suggests multiple plausible therapeutic pathways. Validating temperature increases with *in vivo* measures and characterizing such novel therapeutic cascades would suggest new avenues for DBS neuromodulation. Optimization approaches may approximate or differ from those based on conventional mechanisms (VTA vs VTH) (Alonso et al., 2016; Chaturvedi et al., 2010; R. Cubo et al., 2016), including the role of impedance in voltage vs current control (Lempka et al., 2010), impact of smaller electrodes as used in directional needs (Anderson et al., 2018; Rubén Cubo et al., 2016; Dembek et al., 2017; Pollo et al., 2014), and waveforms not dependent on pulse characteristics (Foutz and McIntyre, 2010). Computational models are both subject to experimental verification and underpin animal and human trials on mechanism of action (Grill, 2018; Howell et al., 2019; Kim et al., 2015; Lozano et al., 2019; Oza et al., 2018; Ramirez-Zamora et al., 2019; Wei and Grill, 2009), such that the novel theoretical framework developed here informs new avenues of DBS research and optimization. Tissue heating during kHz DBS would interact with any coincident theoretical mechanisms of action (e.g. electro-permeation of the BBB (Lopez-Quintero et al., 2010), conduction block (Couto and Grill, 2016)).

Appendix 8: Realistic Anatomically Detailed Open-Source Spinal Cord Stimulation (RADO-SCS) Model

8.1. Outline

This Appendix describes an open-source spinal cord model with both unprecedented resolution (precision) and transparency (reproducibility). A version of this study has been published (Khadka et al., 2020). The resulting model calculations of the electric fields generated in the white-matter and gray matter, and the axonal activation thresholds are broadly consistent with prior simulations. Freely-available online, the RADO-SCS will be updated continuously with version control.

8.2. Introduction

8.2.1. Broad impact of an open-source high-resolution computational SCS model

Computational models predict current flow patterns and neuronal activation during neuromodulation techniques, such as spinal cord stimulation (SCS) (Niranjan Khadka et al., 2019c; Khadka and Bikson, 2019; Lempka et al., 2015; Zannou et al., 2019b, 2019a). These models are key tools in designing, optimizing, and understanding SCS as they relate the controllable stimulation dose (i.e. electrode placement and waveform (Peterchev et al., 2012)) with the intended resulting activation of the spinal cord and nerves (Anderson et al., 2019; Zhang et al., 2014). Computational SCS models thus broadly inform modern clinical SCS practices, ongoing research into mechanisms of actions, and design of new interventions (Capogrosso et al., 2013b;

Holsheimer, 2002b, 1998; Holsheimer and Wesselink, 1997; Jensen and Brownstone, 2019; Lee et al., 2011; Struijk et al., 1993a; Zannou et al., 2019a, 2019b).

Since the early 1980's, models of SCS have been continuously refined and applied (Anaya et al., 2020; Anderson et al., 2019; Arle et al., 2016; Coburn, 1980; Coburn and Sin, 1985; Durá et al., 2019; Fernandes et al., 2019, 2018; Fiocchi et al., 2016; Hernández-Labrado et al., 2011; Holsheimer, 2002b; Howell et al., 2014; Huang et al., 2014; Kent et al., 2014; Ladenbauer et al., 2010; Lee et al., 2011; Lempka et al., 2015; Miranda et al., 2016; Struijk et al., 1993a, 1993b, 1991; Veizi et al., 2017; Wesselink et al., 1998; Zannou et al., 2019b) (see Table 6). Development of models of increasing complexity offered mirrored general enhancements in numerical modeling techniques (finite element analysis), with proprietary efforts by numerous groups, each subject to multiple version iterations. Without open-source model-geometry and a standard modeling pipeline, exact replication is difficult. Indeed, the more advanced (detailed) a model, the more intractable the model is to reproduce without source code. Moreover, even recent models can lack details of major anatomical structures of the spine.

Here, we develop the first open-source and the most precise structural model for SCS simulation, called the Realistic Anatomically Detailed Open-source Spinal Cord Stimulation (RADO-SCS) model. The RADO-SCS pipeline uses computer aided design (CAD) derived files of spinal tissues, along with available devices renders, meshes, finite element method (FEM) results, and axonal activation simulations. One exemplary SCS clinical lead was modeled and placed epidurally. However, users can redesign and position SCS leads based on any device and intervention specifics. Under a Creative Commons Attribution 4.0 International (CC BY 4.0) license, an open-source tissue anatomical mask and device model STL files of RADO-SCS 3.0 (current version) are available for free download from Zenodo.org

(https://doi.org/10.5281/zenodo.3715368). Any model related inquiries or an additional model files download request are addressed through https://www.neuralengr.org/spinal-cord-stimulation. RADO-SCS supports simulation of any SCS dose (technology) and will be subjected to ongoing updates with version control in Zenodo.org.

RADO-SCS supports stimulation of any SCS dose (technology) and will be subject to ongoing updates with version control. The more precise and complex a computational model, the more critical it is to share code for reproducibility and to prevent a need to redo the resource-intensive creation effort. Use of RADO-SCS thus provides users with 1) a transparent and reproducible platform to base any claims; 2) evolving state-of-the-art precision to the best model quality; and 3) cost and time savings. RADO-SCS is a unique tool for supporting computer-driven device design, dose optimization, and an efficient clinical trial design.

8.3. Methods

8.3.1. State-of-the-art RADO SCS model

Adding more details, increasing resolution and anatomical precision to earlier model versions (N. Khadka et al., 2019; Zannou et al., 2019a, 2019b), we developed the first RADO-SCS model, including additional spinal tissue compartments that were not previously developed/modelled. Adding these extra tissues will likely influence the current flow pattern from the SCS lead to the spinal cord or to another possible region of interest. We derived the dimensions and boundaries of tissue compartments of the RADO-SCS model from human cadaver studies, specifically from the lower thoracic spinal cord as discussed in our prior studies (Geddes and Baker, n.d.; Kameyama et al., 1996b; Zannou et al., 2019a, 2019b). In addition, we constructed some features, such as Lissauer's tract, thoracic aorta, sympathetic chains, dorsal and ventral roots,

and rootlets based on physiological trajectory data (Bozkurt et al., 2012). The RADO-SCS model consists of major spinal canal and peripheral tissue compartments with basic, moderate, and enhanced anatomical precision: vertebrae (moderate precision), intervertebral (IV) discs (moderate precision), epidural space (moderate precision), epidural space vasculature (basic precision), dura mater (moderate precision), dural sac (basic precision), intraforaminal tissue (basic precision), CSF (moderate precision), white-matter (enhanced precision), spinal cord vasculature (basic precision), Lissauer's tract (enhanced precision), gray matter (enhanced precision), dorsal and ventral root, rootlets (moderate precision), dorsal root ganglion (DRG) (moderate precision), sympathetic chain (trunk and ganglion) (basic precision), thoracic aorta and its branching (basic precision), peripheral vasculatures (basic precision), and soft tissues (basic precision) (Fig. 45).

Specifically, we modelled and positioned three vertebrae and IV discs to mimic the T9-T11 lower thoracic spine with an anatomical curvature and tissue specific flexion. We modelled four DRG lateral to the vertebrae (each side) in the rostro-caudal direction. The dorsal and ventral root converged together just beyond the DRG, while moving away from the cord to form a spinal nerve within the intervertebral foramen. These nerves and roots were surrounded by meninges and CSF. The dorsal and ventral rootlets emerged from the dorsal and ventral horn of the spinal cord. We constructed eight dorsal and eight ventral rootlets at each spinal level. We constructed the thoracic aorta (which supplies arterial

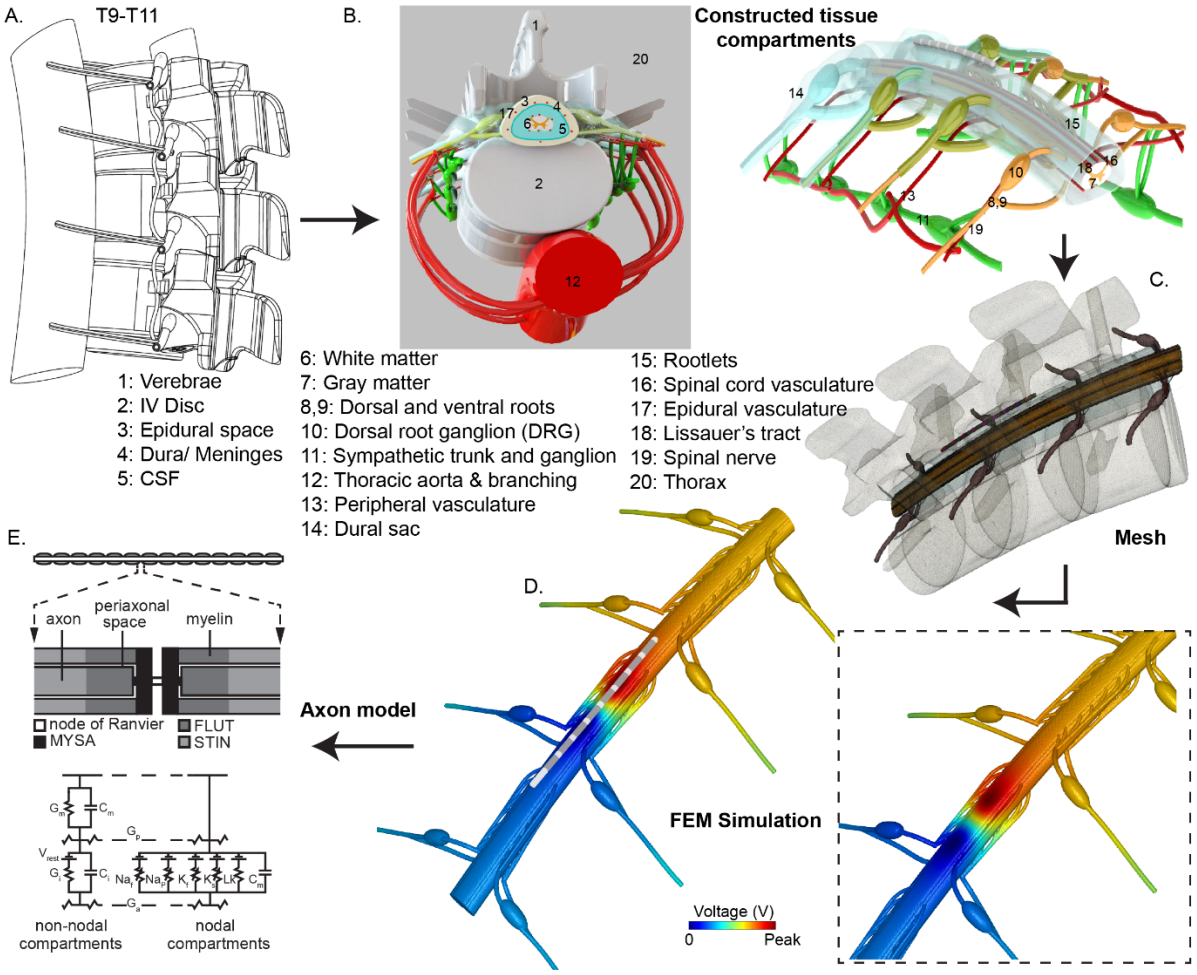

Figure 45: Computational FEM modelling and multi-compartment axon model pipeline of the RADO SCS model. (A) An outline of the T9-T11 spinal cord CAD geometry. (B) Constructed tissue compartments of the detailed SCS model. (C) Final mesh with adequate mesh quality. (D) FEM calculation of the extracellular voltage distribution generated at the surface of the spinal cord during SCS. (E) Multi-compartment sensory axon model used to estimate the activation thresholds for different fiber diameters using the voltage distributions calculated with the FEM (panel modified from (McIntyre and Grill, 2002)).

blood to the spinal cord) and its anastomotic network of radicular arteries that run along the dorsal and ventral roots of the spinal nerves. The radicular arteries further branched at the spinal cord. We constructed two sympathetic chains (trunk and ganglion) and we connected the nerve from each sympathetic trunk to the spinal nerve. Next, we constructed the dural sac/covering, a

membranous sheath that is part of the subarachnoid space, contains CSF, and surrounds the spinal cord. The outermost layer of the spinal tissue was an epidural space, which lies between dura mater and the vertebral wall and is a major spinal tissue compartment that predominately contains fat. We modelled miniature blood vessels within the epidural space. Next, we constructed dura which is the outermost layer of the meninges. Inside the dura was a layer of conductive CSF, which mimics the subarachnoid space that exists between the arachnoid and the pia mater. The inner most constructed tissue compartments were white-matter and gray-matter domains representing the spinal cord. We also included Lissauer's tract, a white-matter pathway near the dorsal horn and lateral aspect of the dorsal columns. We then placed the T9-T11 thoracic spinal column inside a thorax/soft tissues. Finally, we modeled an eight-contact clinical SCS lead (diameter: 1.25 mm, electrode contact length: 3 mm, inter-electrode insulation gap: 1 mm) (Fig. 46) and placed it 1 mm distal to the mediolateral dorsal column midline at the T10 spinal level.

8.3.2. Computational FEM model solution method

To generate a FEM and correct for some tissue-specific anatomical anomalies (for e.g., overlapping, extrusion, smoothing) using morphological image processing filters, we imported the assembled SolidWorks (Dassault Systemes Corp., MA, USA) CAD model files along with the SCS leads into Simpleware (Synopsys Inc., CA, USA). We generated an adaptive tetrahedral mesh using built-in voxel-based meshing algorithms in Simpleware. We refined the mesh density until additional model refinement produced less than 1% difference the voltage and current density at the spinal cord. The resulting model consisted of approximately 150 million tetrahedral elements. To generate a FEM solution, we then imported the volumetric mesh into COMSOL Multiphysics 5.1 (COMSOL Inc., MA, USA). For each model domain, we assigned the following electrical conductivities based on prior literature: vertebrae (0.04 S/m), intervertebral disc (0.60 S/m),

epidural space (0.04 S/m), epidural space vasculature (0.66 S/m), dura mater (0.037 S/m), dural sac (0.037 S/m), intraforaminal tissue (0.004 S/m), CSF (1.7 S/m), white-matter (isotropic: 0.1432 S/m or anisotropic: 0.083 S/m (transverse) and 0.6 S/m (longitudinal)), spinal cord vasculature (0.66 S/m), lissauer's tract (0.276 S/m or 0.083 S/m (transverse) and 0.6 S/m (longitudinal)), gray matter (0.276 S/m), dorsal and ventral root and rootlets (0.1432 S/m), DRG (0.1432 S/m), sympathetic chain (trunk and ganglion) (0.1432 S/m), thoracic aorta and its branching (0.66 S/m), peripheral vasculatures (0.66 S/m), soft tissues (0.004 S/m), metal electrodes (4 x 106 S/m), and lead insulation (2 x 10^{-5} S/m) (Chaturvedi et al., 2010; Niranjan Khadka et al., 2019; Zannou et al., 2019a, 2019b). We applied boundary conditions to represent bipolar SCS, with a 1 A load condition applied at electrode contact 3 (E3) while grounding electrode contact 5 (E5). We assigned insulating boundary conditions on all external model boundaries and continuity for the internal boundaries. We also assigned floating boundary conditions to the remaining inactive electrodes in the model that assumed an equipotential surface with zero net current. To determine the voltage distributions throughout the model, we then solved the Laplace equation ($\nabla(\sigma\nabla V) = 0$, where V is potential and σ is electrical conductivity) under a steady-state assumption. To improve solution accuracy, we set the relative tolerance to 1 x 10^{-6}. Finally, we then exported the three-dimensional (3D) extracellular voltage distributions calculated from the FEM and applied these voltage distributions to the axon models described below.

8.3.3. Multicompartment cable model of sensory Axons

We developed computer models of sensory axons within the dorsal columns of the spinal cord based on a previously-published model of a mammalian sensory axon for specific fiber diameters that were parametrized to reproduce action potential shape, conduction velocity, and strength-duration relationship for sensory axons (Fig. 45E) (Gaines et al., 2018; Graham et al.,

2019b; Howells et al., 2012; McIntyre and Grill, 2002). Each sensory Aβ axon model was a double-cable model consisting of nodes of Ranvier separated by three distinct myelin segments: the myelin attachment segment (MYSA), paranodal main segment (FLUT), and the internode regions (STIN).

We distributed the sensory axon models throughout the white matter of the spinal cord using Lloyd's Algorithm (Lloyd, 1982). The specific fiber sizes considered in our model matched the diameters explicitly parameterized in a previous study (McIntyre and Grill, 2002). We calculated the density of fibers in the model using histological measurements of fibers in the most superficial 300 μm of the dorsal columns (Feirabend et al., 2002). To reduce computational demand, we reduced the total number of fibers solved for this project to 1 % of anatomic density.

To determine the activation thresholds for each individual fiber, we applied the extracellular voltages calculated in the FEM to our axon models using the software package, NEURON (Hines and Carnevale, 1997), within Python programming environment. We modeled the time-dependent output generated by an implantable pulse generator during current-controlled stimulation. To calculate the appropriate spatiotemporal voltage distributions, we then scaled the time-dependent voltage output by the spatial FEM voltage solution (Lempka et al., 2019a, 2019c; Lempka and Patil, 2018). Using custom made scripts, we applied these extracellular voltages onto the model axons with the extracellular mechanism in NEURON and used a bisection algorithm (error < 1%) to calculate the activation threshold for each axon. In our simulations, we applied a stimulus train consisting of pulses applied at a rate of 50 Hz, pulse width of 300 μs, and a passive discharge phase of 6 ms in duration. We included a total of three pulses in our simulations. To determine the pulse amplitude required to produce tonic firing for each axon, we defined the activation threshold as the lowest pulse amplitude required to generate action potentials for both of the final two pulses of our three-pulse stimulus train. For our sensory axon model, axons that

generate action potentials during the final two stimulus pulses will typically continue to generate action potentials at a one-to-one ratio with each stimulus pulse for pulse trains of longer durations.

8.3.4. General modeling workflow of RADO-SCS

Users can download all STL files of the detailed spinal tissues and prepositioned SCS lead, along with detailed documentation and version control, using the weblink provided above. Depending upon the user needs, users can either use all model files (i.e. segmented tissues) or exclude a selection from their model. Users can either customize the model by adding their own electrode/lead or reposition the included lead by using commercial or freely-available CAD software, such as Solidworks (Dassault Systemes Corp., MA, USA), Autodesk (Autodesk, Inc., CA, USA), FreeCAD (https://www.freecadweb.org), etc. The final model file can then be meshed using commercial software, such as Simpleware (Synopsys Inc., CA, USA), or other open-source packages, such as Gmsh (http://gmsh.info/), to generate a volumetric FEM mesh. The mesh can then be imported and solved using a commercial FEM solver, such as COMSOL Multiphysics (COMSOL Inc., MA, USA), or open-source packages, such as SimScale (https://www.simscale.com/). The users can then compute the extracellular voltage predicted by the FEM model and couple it with multi-compartment axon models (see [55] for details on how cable models of mammalian nerve fibers are developed) using NEURON (open-source), Python (open-source), or MATLAB (MathWorks, MA, USA) programming environments to estimate different fiber type activation thresholds.

8.4. Results

The RADO-SCS model included a total of 245 STL files (including tissues and leads). We further merged alike STL into a single mask using image processing that resulted in 19 tissue

masks (millimeter and sub-millimeter dimensions) and 4 lead masks (2 lead types with 2 masks for each contacts and insulating gap). The resulting volumetric mesh generated after multiple mesh refinements included >150 million tetrahedral elements requiring 13 hours of meshing time on the dedicated supercomputer cluster configured for finite element analysis. Numerically solving the RADO-SCS FEM required an additional 48 hours of computing time on the dedicated supercomputer cluster. We then applied the extracellular voltages calculated from the FEM to a population of 2039 model axons located within the DCs of the spinal cord. Developing the axonal models and interpolating the extracellular voltages took an additional four hours of computing time. The average computing time required to calculate the activation threshold for an individual axon model was typically under one hour, giving a total run time for all fibers of approximately 1672 computational-hours, corresponding to 22 hours of real time in cluster computing.

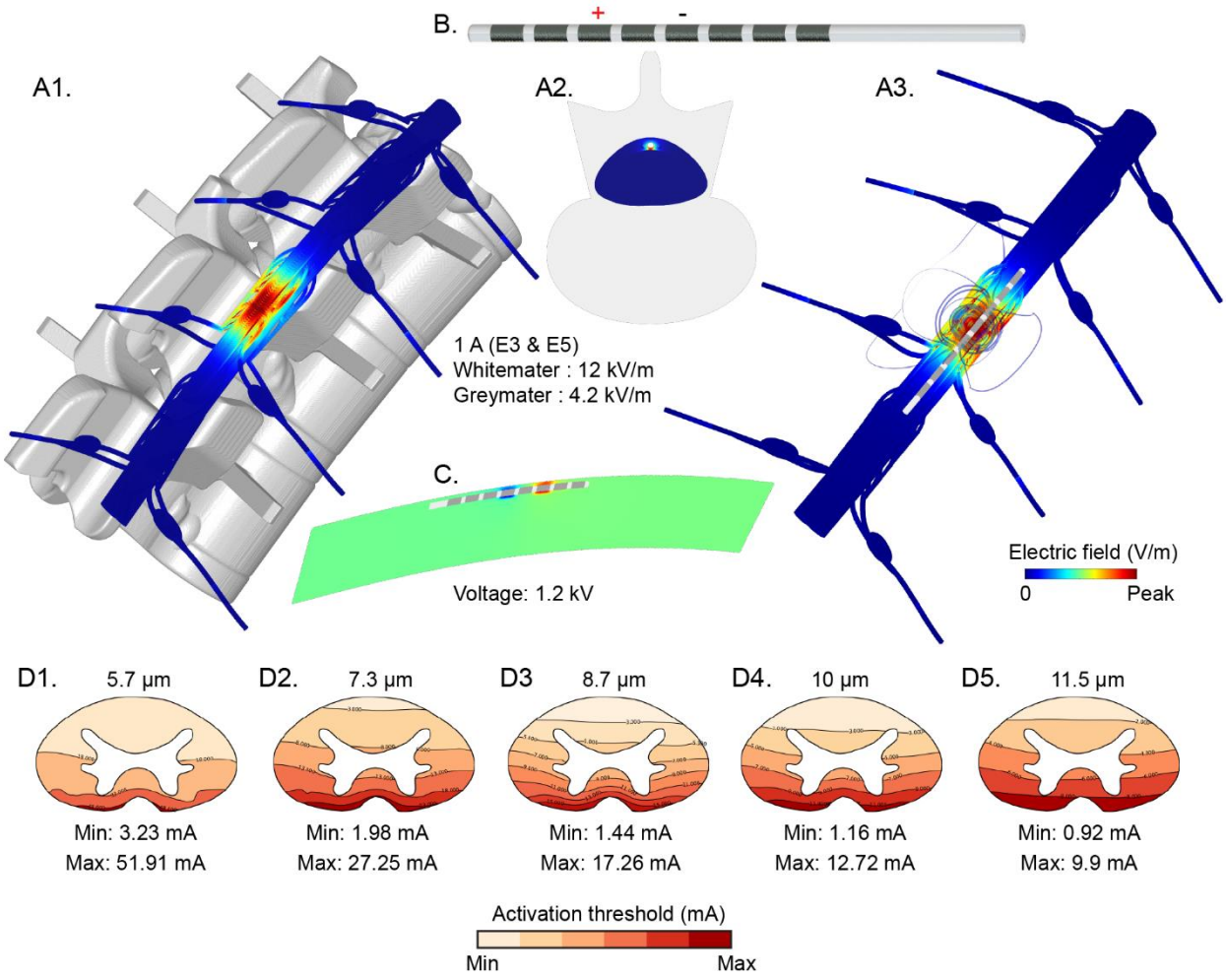

Figure 46: Predicted voltage distribution and electric field from the FEM and fiber activation thresholds. (A1, A2, A3) Predicted peak electric field at 1 A stimulation was 12 kV/m (white matter) and 4.2 kV/m (gray matter), respectively. (B) Illustration of the SCS lead used in the model and the stimulation configuration used in the exemplary model analysis. (C) Predicted peak voltage (1.2 kV) at the surface of the spinal cord. (D1, D2, D3, D4, D5) activation threshold for different fiber diameters. For 5.7, 7.3, 8.7, 10.0, and 11.5 µm fiber diameters, the maximum activation thresholds were 51.9, 21.3, 17.3, 12.7, and 9.9 mA, respectively.

We used an example situation of bipolar stimulation for an exemplary SCS lead positioned epidurally at the targeted lower vertebral spinal levels of the RADO-SCS model and we calculated the voltage and electric field distributions in different tissue compartments. Peak electric fields

predicted in the white matter and gray matter were 12 kV/m and 4.2 kV/m for 1A stimulation current, respectively. Peak voltage at the surface of the spinal cord was 1.2 kV (Fig. 46). The predicted electric field intensities were not uniform in the spinal tissues.

The activation thresholds throughout the white matter are shown in Fig. 46. As expected, the largest diameter fibers (11.5 μm) had the lowest activation thresholds, and the most dorsal fibers were activated at thresholds below 1 mA. As the diameter of the fibers decreased, the activation thresholds increased. The smallest diameter fibers (5.7 μm) in the model had a minimum activation threshold of 3.23 mA.

8.5. Discussion

8.5.1. Application of state-of-the-art RADO-SCS model

SCS volume conductor models are used for systematic optimization of the design and clinical implementation of SCS technologies, with ongoing efforts to enhance model precision and accuracy. Here, our goal was to develop an open-source high-resolution and anatomically-detailed SCS model and disseminate it to the scientific community. Currently, there is limited access to open-source platforms for SCS modeling, and available models have simple geometries and do not incorporate important tissue compartments. Thus, there is a need to develop and disseminate a high-resolution open-source SCS model. Using our modelling proficiencies, high-end computer resources, and an extensive literature search on anatomical details of spinal cord and peripheral tissues, we developed the first high-resolution open-source SCS model. This model is not only sophisticated in terms of details and architecture, but it also has good precision to predict meaningful current flow. All structural files are freely available to download under the Creative Commons Attribution-Noncommercial International License. In addition, any direct questions

regarding the downloadable files or modeling workflow can be directed to the online forum available in the model weblink. Questions will be addressed promptly by the corresponding authors via email. Any new updates will be periodically added to the source webpage and the model will be periodically checked for any issues.

On one hand, if a user elects to exclude significant details in the RADO-SCS model (e.g. select to use only bone, fat, CSF, and spinal cord masks), the outcome is still a transparent and reproducible structural anatomical pipeline. Whereas on the other hand, the RADO-SCS with its complete complement of tissues provides the opportunity for SCS stimulations with state-of-the-art precision, albeit requiring significant computational resources. The exemplary simulations that we conducted in this study are intended only to illustrate a successful workflow. It is an open question which model details (e.g. vasculature) will significantly impact simulation results, and the answer to this question will moreover depend on the application considered (e.g. electrode placement) and the hypothesized mechanisms of action. Nevertheless, such questions cannot be answered without comparing a precise SCS model with simplified counterparts. In this sense, the RADO-SCS model not only supports models with state-of-the-art precision, but analysis of which model details are While all modeling pipelines reference data from anatomical scans, “image (MRI) derived models” segment tissue overlaid on medical imaging scans from an individual (Lempka et al., 2019c; Zannou et al., 2019a). MRI-derived models have been increasingly adopted in situations where clinically available scans support individualized models (Fernandes et al., 2018; Fiocchi et al., 2016; Parazzini et al., 2014). When models involve incorporation of anatomical details that are not captured within the images (e.g. submillimeter tissue features from imaging scans with only millimeter resolution), then such structures must be rendered by referencing a range of data across techniques and subjects, including cadaver studies. When a

majority of modeled tissues are thus rendered, the value of a strictly MRI-derived model (based on an individual scans) becomes unclear. An advantage of fully CAD-derived models is that each tissue is generated based on prescribed geometric features and thus supports reproducibility, systematic alteration, and ongoing refinement.

8.5.2. Anatomical details of prior SCS models and a need for state-of-the-art open-source SCS model

Finite element analysis has been widely implemented in 2D and 3D spinal cord current flow models. Although a multitude of computational SCS models of rodent and non-human primates has been developed and implemented for motor control following spinal cord injury (Capogrosso et al., 2018, 2013b; Greiner and Capogrosso, 2019), here we specifically focused on human SCS modelling studies (minimally invasive or non-invasive) for pain management. We categorized prior SCS models based on tissue compartments (considered vs. not considered/absent) and anatomical precision (limited, basic precision, moderate precision, and enhanced precision) (see Table 6 for details about these comparison terminologies).

References	RADO-SCS	Anaya, 2019	Zannou, 2019	Graham, 2019
Model derivation	CAD derived	CAD derived	CAD derived	CAD derived
Spine level	T8-T11	Lower thoracic	T8-T11	L5
Tissue compartments				
Vertebrae	✔, MP	✔, MP	✔, MP	✔, BP
IV Disc	✔, MP	✔, MP	✔, MP	✖
Epidural space (predominantly fat)	✔, MP	✔, BP	✔, BP	✖
Dura mater/ Meninges/Dural sac	✔, MP	✔, BP	✔, BP	✔, BP
Cerebrospinal fluid (CSF)	✔, MP	✔, BP	✔, BP	✖
Spinal Cord	✔, EP	✔, EP	✔, BP	✖
White-matter	✔, EP	✔, EP	✖	✖
Gray-matter	✔, EP	✔, EP	✖	✖
Lissauer's tract	✔, EP	✖	✖	✖
Roots	✔, MP	✖	✔, BP	✔, BP
Ventral root	✔, MP	✖	✖	✖
Dorsal root	✔, MP	✖	✖	✔, BP
Dorsal root ganglion (DRG)	✔, MP	✖	✖	✔, BP
Dorsal and Ventral rootlets	✔, MP	✔, MP (Dorsal only)	✔, BP	✖
Intraforaminal tissue	✔, BP	✖	✖	✔, BP
Sympathetic chain (trunk, ganglion)	✔, BP	✖	✖	✖
Thoracic aorta and sub-vasculature	✔, BP	✖	✔, BP	✖
Epidural space vasculature	✔, BP	✖	✖	✖
White-matter vasculature	✔, BP	✖	✖	✖
Peripheral spinal tissues/thorax	✔, BP	✔, BP	✔, BP	✔, BP

Compartments: ✖, Not considered/Absent; ✔, Considered; , Unclear.
Anatomical details: **LT**, Limited; **MP**, Moderate precision; **BP**, Basic precision; **EP**, Enhanced precision.

Table (Continued).

Anderson, 2019	Lempka, 2019	Durá, 2019	Fernandes, 2018, 2019	Wagner, 2018,	Kent, 2018	Arle, 2016, 2013
CAD derived	CAD derived	CAD derived	MRI derived	CAD derived	CAD derived	CAD derived
T8-T10	Lower thoracic	T10	Whole Spine	L1-S2	θ	θ; T8-T9 (2013)
✖	✔, MP	✔, BP	✔, EP	θ	✔, LT	✔, BP; ✖ (2013)
✖	✖	✖	✔, EP	θ	✖	✖
✔, BP	✔, BP	✔, BP	θ	✔, MP	✖	✔, BP
✔, BP	✔, BP	✔, BP	✔, EP	θ	✖	✔, BP
✔, BP	✔, MP	✔, BP	✔, EP	✔, MP	✖	✔, BP
✔, BP	✔, MP	✔, MP	✔, EP	✔, MP	✖	✔, BP
✔, BP	✔, MP	✔, MP	✔, EP	✔, MP	✖	✔, BP
✔, BP	✔, MP	✔, MP	✔, EP	✔, MP	✖	✔, BP
✖	✖	✖	✖	✖	✖	✖
✖	✔(Modeled as a cable)	✔, LT	✔, BP	✔, MP	✖	✔, BP; ✖ (2013)
✖	✖	✖	✔, BP	✔, MP	✖	✖
✖	✔ (DR fibers)	✔, (DR fibers)	✔, BP	✔, MP	✔, BP	✔, BP
✖	✖	✖	✖	✖	✔, BP	✖
✖	✖	✖	✖	✔, MP	✖	✖
✖	✖	✖	✖	✖	✔, LT	✖
✖	✖	✖	✖	✖	✖	✖
✖	✖	✖	✖	✖	✖	✖
✖	✖	✖	✖	✖	✖	✖
✖	✖	✖	✖	✖	✖	✖
✖	✔, BP	✖	✔, EP	θ	✖	✔, BP

Table (Continued).

Lempka, 2015	Huang, 2014	Kent, 2014	Howell, 2014	Fiocchi S, 2016; Parazzini, 2014	Laird, 2013	H-Lábrádo, 2011
CAD derived	CAD derived	CAD derived	CAD derived	MRI dervied	CAD derived	CAD derived
Lower thoracic	thoracic	T7-T10	T3-L2	Whole Spine	T10	C2-T1
✔, BP	✔, BP	✔, BP	✔, MP	✔, EP	✔, LT	✔, BP
✖	✖	✖	✔, MP	✔, EP	✖	✔, BP
✔, BP	✔, BP	✔, BP	✔, MP	θ	✔, LT	✔, BP
✔, BP	✔, BP	✖	✔, MP	✖	✖	✔, BP
✔, BP	✔, BP	✔, BP	✔, MP	✔, EP	✔, LT	✔, BP
✔, EP	✔, BP	✔, BP	✔, MP	✔, EP (Single compartment)	✔, LT	✔, BP
✔, EP	✔, BP	✔, BP	✔, MP	✖	✔, LT	✔, BP
✔, EP	✔, BP	✔, BP	✔, MP	✖	✔, LT	✔, BP
✖	✖	✖	✖	✖	✖	✖
✔, BP	✖	✖	✔ (Modeled as a cable)	✖	✔(Modeled as a cable)	✖
✖	✖	✖	✖	✖	θ	✖
✔, BP	✖	✖	✔ (DR fibers)	✖	θ	✖
✖	✖	✖	✖	✖	✖	✖
✖	✖	✖	✖	✖	✖	✖
✖	✖	✖	✖	✖	✖	✖
✖	✖	✖	✖	✖	✖	✖
✖	✖	✖	✖		✖	✖
✖	✖	✖	✖	✖	✖	✖
✖	✖	✖	✖	✖	✖	✖
✔, BP	✖	✖	✔, BP	✔, EP	✖	✔, BP

Table (Continued).

Veizi, 2017; Lee, 2011	Howard, 2011	Danner, 2011; Ladenbauer, 2010	Manola, 2007, 2004	Holsheimer, 2002	Rattay, 2000
CAD derived	CAD derived	CAD derived	CAD derived	CAD derived	CAD derived
T1- T12 & lower-lumbar and sacral	θ	T11- T12, L1-L4	θ	θ	T11-T12, L1-L2
✔, BP	✔, LT	✔, MP	✔, BP	✔, BP	✔, BP
✖	✖	✔, BP	✖	✖	✖
✔, BP	✔, LT	✔, BP	✔, BP	✔, BP	✔, BP
✔, BP	✖	✖	✔, BP	✖	✔, BP
✔, BP	✔, LT	✔, BP	✔, BP	✔, BP	✔, BP
✔, EP	✔, LT	✔, BP	✔, BP	✔, BP	✔, MP
✔, EP	✔, LT	✔, BP	✔, BP	✔, BP	✔, MP
✔, EP	✔, LT	✔, BP	✔, BP	✔, BP	✔, MP
✖	✖	✖	✖	✖	✖
✔ (Modeled as a cable)	✖	✔ (Modeled as a cable)	✔ (Modeled as a cable)	✔ (Modeled as a cable)	✔ (Modeled as a cable)
✖	✖	✔ (VR fiber)	✖	✖	✖
✔ (DR fibers)	✖	✔ (DR fiber)	✔ (DR fibers)	✔ (DR fibers)	✔ (DR fibers)
✖	✖	✖	✖	✖	✖
✖	✖	✖	✖	✖	✖
✖	✖	✖	✖	✖	✖
✖	✖	✖	✖	✖	✖
✖	✖	✖	✖	✖	✖
✖	✖	✖	✖	✖	✖
✖	✖	✖	✖	✖	✖
✔, BP	✖	✔, BP	✔, BP	✔, BP	✔, BP

Table (Continued).

Wesselink, 1998, 1999; Holsheimer, 1995; Struijk, 1993a, 1993b	Struijk, 1991, 1992	Coburn and Sin, 1985	Sin and Coburn, 1983	Coburn, 1980
CAD derived	CAD derived	CAD derived	CAD derived	CAD derived
C4-C6, T4-T7, T10-T11	C5, C6	θ	θ	Thoracic
✔, BP	✖	✔, BP	✔, LT	✔, LT
✖	✖	✖	✖	✖
✔, BP	✔, BP	✔, BP	✔, LT	✔, LT
✔, BP	✖	✖	✖	✖
✔, BP	✔, BP	✔, BP	✔, LT	✔, LT
✔, BP	✔, BP	✔, BP	✔, LT	✔, LT
✔, BP	✔, BP	✔, BP	✔, LT	✔, LT
✔, BP	✔, BP	✔, BP	✔, LT	✔, LT
✖	✖	✖	✖	✖
✔ (Modeled as a cable)	✖	✔, BP	✖	✔, LT
✖	✖	✔, BP	✖	✔, LT
✔ (DR fibers)	✖	✔, BP	✖	✔, LT
✖	✖	✖	✖	✖
✖	✖	✖	✖	✖
✖	✖	✖	✖	✖
✖	✖	✖	✖	✖
✖	✖	✖	✖	✖
✖	✖	✖	✖	✖
✖	✖	✖	✖	✖
✔, BP	✔, BP	✔, BP	✔, LT	✔, LT

Table 6: Comparison of the RADO SCS model with other existing SCS models based on model derivation (CAD vs. MRI), constructed tissue compartments (unclear, considered, and not considered/absent), and precision in anatomical details (limited, basic, moderate, and enhanced). Limited refers to SCS models with minimal anatomical precision in constructed tissue compartments. Basic precision SCS models have regular shapes (e.g., cylindrical, triangular, rectangular prisms, wedges, bricks, or cubes) as tissue compartments, no flexion in geometry, and uniform dimension across spine levels. Moderate precision SCS models include tissue compartments with minimal resolution or have regular geometric shapes with some flexion and uniform dimension across spine level. Enhanced precision refers to SCS models with tissue compartments with realistic geometry, additional anatomical details (flexion, bifurcation, union), high resolution, and spine level specific dimensions.

In the early 1980's, Coburn developed the first 2D FEM model representing non-homogeneous human spinal cord tissues for invasive SCS. The model comprised of major spinal tissue domains, such as thoracic vertebrae, epidural fat, CSF, spinal roots, white matter, and gray

matter with limited precision (Coburn, 1980). In 1983, Sin and Coburn developed a simplified version of the original Coburn 2D SCS model, excluding spinal roots (limited precision) (Sin and Coburn, 1983). Coburn and colleagues in 1985, and Struijk and colleagues in 1991 and 1992 developed 3D FEM models of SCS including major tissues of the spinal canal with basic precision and coarse meshing. In both models, dura was absent, with only Coburn's model including a basic spinal root (Coburn, 1985; Coburn and Sin, 1985; Struijk et al., 1992, 1991). Struijk and colleagues in 1993a and 1993b, Holsheimer and colleagues in 1995 and 1997, and Wesselink and colleagues in 1998 and 1999 developed a 3D SCS model including the mid cervical (C4-C6), mid thoracic (T4-T7), and low thoracic (T10-T11) vertebral spine level with major spinal canal tissue compartments, including dura mater and surrounding tissue layers (thorax), all tissue compartments with basic precision (Holsheimer et al., 1995, p. 195; Holsheimer and Wesselink, 1997; Struijk et al., 1993a, 1993b; Wesselink et al., 1999, 1998). These models simulated either dorsal root (DR) fibers and/or dorsal column (DC) fibers using multicompartment cable models. Wesselink et al. included white matter anisotropy and encapsulation layer between the electrode and dura (Holsheimer and Wesselink, 1997; Wesselink et al., 1998).

In 2000, Rattay and colleagues developed a T11-L2 SCS model with basic precision in vertebrae, epidural space, dura, CSF, rootlets trajectory, and thorax, whereas the spinal cord (including gray matter and white matter) had moderate precision in anatomical details. They simulated DR fiber activation using a multicompartment cable model (F Rattay et al., 2000). In 2002, Holsheimer used a simplified 3D SCS model that lacked a dura mater compartment (basic precision) to discuss which nerve fibers along the spinal cord were activated by SCS intensities within the therapeutic range (Holsheimer, 2002b). Manola and colleagues in 2005 and 2007 used a basic precision 3D SCS model that included vertebrae, epidural fat, dura, CSF, gray-matter,

white-matter, and general thorax in the FEM. They used cable models to simulate DR and DC fiber activation (Manola et al., 2007; Manola and Holsheimer, 2004). A more sophisticated CAD-derived SCS model was developed in 2010 by Ladenbauer and colleagues and Danner and colleagues in 2011 for non-invasive and invasive SCS with a vertebral column of moderate precision (Danner et al., 2011; Ladenbauer et al., 2010). This model represented spinal tissue compartments at basic anatomical precision, with uniform dimensions across spine levels. The model also did not include a dura mater in the FEM. The dorsal and ventral root fiber activation were further analyzed using cable models (Ladenbauer et al., 2010). In 2011, Howard and colleagues developed a simplified 2D SCS model with no dura mater and limited precision in the modelled tissue compartments (Howard et al., 2011). Lee and colleagues in 2011 and Veizi and colleagues in 2017 developed a 3D FEM SCS model of a low thoracic and a sacral level spinal-Lempka et al, 2015 developed a 3D SCS model (lower thoracic spinal cord) of kilohertz frequency SCS with white matter and gray matter with enhanced precision and other tissue compartments with basic anatomical precision (Veizi et al., 2017). Arle and colleagues in 2014 and 2016 used an FEM derived from the Wesselink (Wesselink et al., 1999) and Holsheimer groups' SCS model (Greiner and Capogrosso, 2019; Ladenbauer et al., 2010) (basic anatomical precision) (Danner et al., 2011; Fernandes et al., 2019). In their 2014 SCS model, vertebrae and spinal roots were missing (Danner et al., 2011). Fernandes et al., 2018 and 2019 utilized a MRI-derived human model based on the Virtual Population Family (Laird and Parker, 2013) comprising thirteen tissue compartments; namely skin, fat (including subcutaneous adipose tissue), muscle, bone, heart, lungs, viscera, vertebrae, IV disc, dura mater, CSF, brainstem, and spinal cord (gray matter and white matter). The model had enhanced anatomical precision on peripheral spinal tissues/thorax,

vertebrae, IV disc, CSF, dura mater, and spinal cord, but basic precision in the roots. It was unclear whether the epidural space (fat) was included in the model.

Durá et al., 2019 developed a simplified 3D SCS model at the T10 spine level with basic anatomical precision in vertebrae, epidural fat, dura mater, CSF, while both white-matter and gray-matter had moderate anatomical precision. DR fiber geometry included in the FEM had limited anatomical precision (Durá et al., 2019). In 2018, Kent and colleagues developed a 3D dorsal root ganglion (DRG) model with basic anatomical precision of the dorsal root and the DRG, and limited precision in epidural tissues and vertebrae (Kent et al., 2018). Wagner and colleagues in 2018 constructed a moderate precision SCS model of L1-S2 spine level including epidural fat, CSF, gray-matter, white mater, spinal roots (dorsal and ventral), and rootlets. However, it was unclear whether vertebrae, discs, dura, and thorax were included in the model (Wagner et al., 2018). Lempka and colleagues in 2019 constructed a patient-specific FEM SCS model with spinal cord, CSF, epidural fat, and a simplified spine domain. All segmented tissue compartments had moderate anatomical precision. They also modeled DC and DR fibers using multicompartment cable models (Lempka et al., 2019c, 2019a).

In 2019, Anderson and colleagues developed a simple 3D SCS model with basic anatomical precision of major spinal canal tissue compartments (white matter, gray matter, CSF, dura, and extradural tissue layer) (Anderson et al., 2019). A human L5 DRG model with basic anatomical precision was developed by Graham et al. in 2019 where they represented general thorax, bone, intraforaminal tissue, dural covering, and DRG using simplified shapes (Graham et al., 2019b). Bikson's group in 2019 developed a simplified T8-T10 SCS model comprising vertebrae (moderate precision), IV disc (moderate precision), epidural space/fat (basic precision), meninges/dura mater (basic precision), CSF (basic precision), spinal cord (basic precision), spinal

roots (basic precision), rootlets (basic precision), thoracic aorta and sub-vasculature (basic precision), and soft tissues/thorax (basic precision) (N. Khadka et al., 2019; Zannou et al., 2019a, 2019b). In the same year, Lempka's group developed an updated 3D SCS model of the lower thoracic spine level consisting gray matter and white matter of the spinal cord (enhanced anatomical precision), dorsal rootlets (moderate precision), CSF (basic precision), dura mater (basic precision), epidural fat (basic precision), vertebrae (moderate precision), and discs (moderate precision) (Anaya et al., 2020). This model had additional details and precision in some tissue compartments compared to their 2015 SCS model, but some major spinal tissue compartments were not included in the model, the dimensions of the tissue compartments were uniform across spinal levels, and the surrounding tissue/thorax had simplified geometry.

Prior SCS studies clearly demonstrate that computational models represent a valuable tool to study the potential mechanisms of action of SCS and to optimize the design and implementation of SCS technologies. However, it is imperative that these computational models include the appropriate level of details to accurately predict the neural response to SCS and to correlate model predictions with clinical outcomes. Various simplifications to the model design may affect model-based predictions of the neural response to SCS. Therefore, we believe that there is a need for an anatomically-detailed high-resolution spinal cord model that captures major spinal tissue compartments in order to support enhanced prediction of SCS current flow. Here, the RADO-SCS is a state-of-the-art open-source contribution.

Conclusions and Future Work

A. Summary of Results

The purpose of this dissertation work was to answer three fundamental questions related to tDCS: 1) Does tDCS-induced skin reddening profile match model predicted current density profile? (Aim 1); 2) Is there any skin heating during tDCS and if skin heating is due to joule heat? (Aim 2); 3) Can a realistic skin model with complex multi-layers and ultrastructures explain the current flow pattern through the skin and their role in tDCS-induced skin reddening and skin heating? (Aim 3). In the Aim 1, we concluded that skin reddening profile is not a uniform and it does not match the local current density predicted by the model. In the Aim 2, we concluded that tDCS produced minimal skin heating, but the temperature was below exposed skin level (not injurious), and the multi-layer skin model predicted higher temperature increase due to joule heat compared to prior homogeneous skin model. In the Aim 3, we concluded that realistic skin tissue layers and ultrastructures fundamentally change current flow depending upon the parameters and the model with these details match experimental observations of reddening.

B. General Considerations

1. *Alignment of model with experimental results*

i. Skin reddening (Erythema)

In the Aim 1, the local current density predicted by the homogenous FEM model did not match the skin experimental reddening profile (main hypothesis was rejected). We then proposed an alternative hypothesis that experimental skin current density is indeed (relatively) uniform, and the homogenous model prediction is therefore incorrect. Prior simplistic (e.g. homogenous or two-

layer) models lack relevant details of skin structures and thus did not align with the experimental findings such as skin reddening. In order to address this possibility, in the Aim 3, we modeled the skin with multi-layers (epidermis, dermis, and fat), with or without additional ultra-structures (hair follicles, sweat glands, and blood vessels).

- The addition of multi-layers (considering a range of conductivity parameters) without ultra-structures resulted in the prediction of higher current density around the electrode perimeter, both in the epidermis and dermis skin layers.
- The addition of sweat glands only (hair follicles and blood vessels absent) into the multi-layer skin model resulted in the predictions of peak current density around the sweat glands in both the epidermis and dermis layers. These current density hotspots were consistent (uniform) across the sweat glands, both near and far from the electrode edges.
- Further addition of only blood vessels (hair follicles and sweat glands absent) into the multi-layer skin model resulted in the prediction of higher current density around the electrode edges in the epidermis and upper dermis. However, at the lower dermis and fat, the current density was consistent (uniform) across blood vessels under the electrode, both near and far from the electrode edges.

Therefore, there are two ultrastructure details that can be incorporated into the multi-layer skin model to produce prediction of current flow patterns that are consistent with the experimental observations of skin reddening. The first is an addition of sweat glands which removes current concentration at the electrode edges. The second is an addition of blood vessels which shows that current density across the modeled vasculature is uniform under the electrode. The Aim 3 considers a range of model details and parameters, and we cannot conclude at this time what the "ideal" model parameters should be. However, we know that multiple-skin layers and ultrastructures are

certainly present in the real skin and incorporating these details into the model fundamentally impacts the predictions - and that a model with these details match experimental observations of reddening.

ii. Skin temperature

- In the Aim 2, a post-hoc analysis on temperature measurement across the multiple sensors (perimeter sensors vs center sensors) indicated no significant difference in temperature change across the sensors (i.e. to the resolution of the measurement, the skin under the electrode perimeter did not heat more than the skin under the center of the electrode).These measurements were collected across different time points with no difference between center and perimeter at any time point.
- In the Aim 2, the multi-layer skin model without ultra-structures predicted a moderate annulus of heating at the perimeter compared to the middle, near the start time of stimulation (0.35 ^{o}C difference between the perimeter and the middle for active stimulation at t =5 min), but not near the end time of stimulation (< 0.01 ^{o}C difference between the perimeter and the middle for active stimulation at t = 20 min) (Fig. 7D2). However, the difference in between the center and perimeter were also observed in the non-stimulation case suggesting that they reflect the application of the sponge pad. The model thus matches experimental distribution near the end of stimulation (~t = 20 min) but not near the start time of stimulation (~t =5 min).
- Since adding sweat glands and blood vessels into the multi-layer skin model eliminated or reduced current concentration at the edges, we expect that a bioheat model of such a detailed skin would increase the uniformity of temperature predicted at the surface of skin across the early and late times of stimulation - consistent with the experimental

measurement of skin temperature across all the time points. However, the temperature non-uniformity predicted simply as a result of the sponge pad presence (which was not observed experimentally) would still be present.

- In addition, the multi-layer skin model predicted 0.38 ^{o}C temperature increase due to joule heat (the difference between peak temperature in the active case compared to no-stimulation at t=20 min) which is less than the experimental measurement of ~1.3 ^{o}C. Possibly, the addition of model ultrastructures (e.g. sweat glands, blood vessels) may increase joule heat by producing local hot-spots of current. Additionally, we did not model stimulation-induced blood flow, which would further increase skin temperature in the active case (since core temperature is above the skin temperature). Indeed, the observation of redness under the electrode (Aim 1) directly points to the contribution from increased blood flow. We believe that stimulation induced blood flow (which is apparently uniform under the electrode, see above) is the most likely missing factor to reconcile the modeled and experimental measures of temperature rise (both peak and spatial profile).

Additional opportunities to relate the model predictions with experimental results are noted below.

2. *Role of joule heat in skin heating*

The phantom is a homogeneous volume which mimics how skin is typically modeled. It is not feasible to build a skin phantom that reproduces skin multi-layers (note the thickness of epidermis (0.1 mm) and ultra-structures. The phantom conductivity (0.465 S/m) was selected to match the average skin conductivity across the layers, and this value was used in prior simplistic bio-heat model (Datta et al., 2009). We also applied a thin layer of electrolyte paste to facilitate the electrode phantom contact, which was not modeled. The phantom indicated negligible

temperature increase (0.1 ^{o}C at t=20 min) due to the joule heat. The modeling of the phantom served to verify the simple model assumptions.

- As noted, prior homogeneous skin models predict negligible temperature and may not reflect accurate skin heating, including due to the joule heat. Therefore, there is a need for a detailed skin model that reliably predicts temperature increase due to the joule heat.
- We developed a multi-layer skin model (epidermis, dermis, and fat) incorporating blood perfusion and metabolism. The perfusion and metabolism in this model were selected based on literature, however they do not influence skin heating in response to stimulation as simulated (since they are not responsive to current). Compared to the phantom model, the multi-layer skin model predicted higher temperature increase. This increase was a result of joule heating through higher resistivities (electrical and thermal) of the skin tissue layers. This increase was closer to, but still less than the experimental measures, with the remaining difference attributable to other factors missing in the model (see above).

3. *Higher current and temperature increase*

- More current flow will inevitably produce more joule heating. Temperature increase at higher current (> 2 mA) is not explored in the main dissertation Aims. However, our pilot skin temperature measurement using 4 mA suggested that temperature can increase up to 2 ^{o}C, and this increase is still below exposed skin level (sponge cooling temperature was ~ 2.3 ^{o}C). Therefore, we expect that even at moderately higher current, temperature at the surface of the skin will not reach injurious levels and possibly not reach directly perceptible levels (compared to the exposed skin temperature).

- The model can be used to predict temperature rise under any current intensity. However, such a model would need to be appropriately parameterized. As discussed above and below, we feel that the current model iteration does not fully capture experimental observations, but we do suggest specific improvements in the model that may reconcile model predictions with the existing experiments for 2 mA.We expect the use of high current is then ultimately limited by pain and heat-sensitive nerve activation (rather than actual heating). In theory, an advanced and accurate skin model can help design electrodes and waveforms that limit these cutaneous sensations.

4. *Inflammatory response during tDCS*

- Guarienti et al., 2015 used ketoprofen 2% (a nonsteroidal anti-inflammatory agent) to effectively minimize tDCS-induced erythema for blinding improvement. Ketoprofen did not impact self-reported adverse events such as tingling or burning sensation. In the same study, application of lidocaine (an anesthetic agent) did not reduce erythema, but also (surprisingly) did not significantly impact self-reported adverse events. Guarienti et al. assessed only the frequency (e.g. likelihood) of adverse events, not their intensity.
- There is a limited data on the role of inflammatory response during tDCS. Data from Guarienti et al. is consistent with the skin redness increasing in active tDCS condition (Aim 1) and also with an associated activation of blood flow (see above) that is suppressed by an anti-inflammatory agent.

5. Temporal response of temperature

- In the period after DC stimulation was turned off (post-stimulation, Fig. 7D1), there was no experimental evidence of further skin temperature increase. Temperature also did not

recover to baseline in the 5 minutes after stimulation, which can be explained by the heat capacity of the skin.

- In the phantom, there was no statistically significant effect of time in temperature increase for any condition (anode, cathode, or control). There was also no evidence of further stimulation-induced phantom temperature increases after stimulation (post-stimulation, Fig. 7C1).

6. Use of forearm vs forehead for stimulation

We believe that the forearm is a reasonable approximation of the forehead. The forearm has been previously used in tDCS electrode development and tolerability testing, and is considered reliable to predict the same effects on the head (Minhas et al., 2011). Moreover, we have also conducted preliminary temperature measurement at the forehead in the Appendix 2, and observed similar temperature increase as in the forearm stimulation.

7. Values for blood perfusion

In the Aim 2, the blood perfusion values for skin model were selected based on the established literature values. However, a sensitivity analysis of perfusion values on any skin temperature increase was not conducted in this Aim because the values of perfusion (and metabolism) did not impact the predicted change in the temperature during tDCS (as we did not model vascular flare response, and blood perfusion would not impact joule heat; see above).

8. Hairline and skin reddening

We used M1-SO montage to apply tDCS (anode positioned over the right forehead) and analyzed skin reddening only under the anode. In theory, skin reddening patterns in the hairline may not be consistent with the reddening in the hairless skin because the hair follicles influence

current flow pattern (Aim 3). However, both hairless skin and skin with hair have other skin ultrastructures, notably blood vessels and sweat glands. In the Aim 3, we predict the presence of blood vessels and sweat glands fundamentally impacts current flow patterns (distribution and hot spots). We did not directly compare the skin model with blood vessels, sweat glands, and hair follicles against the skin model with blood vessels, sweat glands, but no hair follicles. If the difference between these two models are not significant, it would suggest that the skin effects are not different at or below the hairline. We are not aware of any consistent experimental reports of the difference in adverse events between above vs below hairline electrode placements. A lack of experimental difference between above vs below hairline electrode placements would be consistent with a model showing minimal impact of hair follicles.

9. *Direct comparison of measured temperature and predicted temperature*

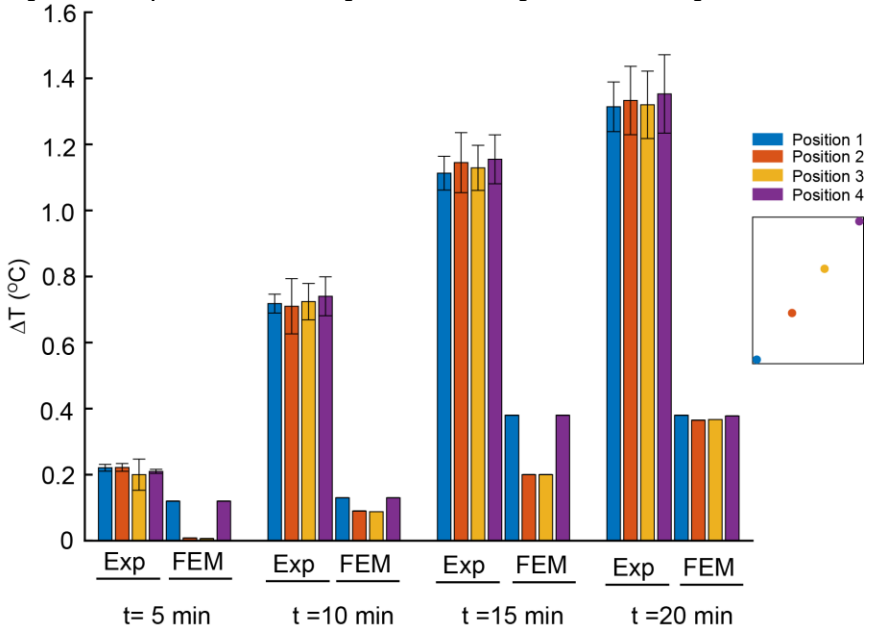

Figure 47: Comparison between experimental temperature increase and predicted temperature increase during 2 mA tDCS at four different location under the sponge pad for four different time points. The sampling locations are color coded and are sampled from edge-to-edge diagonally. In the case of the experiment, they represent locations for the four thermocouple sensors. Experimental

data shows temperature measurement for ten subjects (mean ± SEM). Across the sampling locations, the temperature change is higher in the experiment than the model. Predicted temperature (FEM) is using a multi-layer skin model without ultrastructures. ΔT is relative to control (no-stimulation).

A post-hoc multiple comparison following Kruskal-Wallis test on the temperature measurement across different locations at each time point (t =5 min, 10 min, 15 min, and 20 min) indicated that there was no significant difference in temperature change ($P > 0.01$) across the locations (i.e. to the resolution of the measurement, the skin under the electrode perimeter did not heat more than the skin under the center of the electrode).

The multi-layer skin model without ultra-structures predicted a non-uniform temperature change across different locations for t =5 min, 10 min, and 15 min. However, near the end time of stimulation (t= 20 min), there was less than 0.01 ^{O}C temperature change across different locations, suggesting that model match experimental distribution of temperature near the end of stimulation (t= 20 min) but not near the start time of stimulation (~ t= 5 min).

The multi-layer skin model predicted ~ 0.38 ^{O}C temperature increase due to joule heat (the difference between peak temperature in the active case compared to no-stimulation (t=20 min) which is less than the experimental measurement of ~1.3 ^{O}C (t=20 min)).

Since adding sweat glands and blood vessels into the multi-layer skin model eliminated or reduced current concentration at the edges, we expect that a bioheat model of such a detailed skin would increase uniformity of temperature predicted at the surface of skin across the early and late times of stimulation - consistent with the experimental measurement of skin across all time points.

C. Future Direction

To this end, we developed few novel hypothesis, principles, and technology which can be successfully leveraged to future device design. Current density measurement under the electrode will help to relate the current density profile of the experiment and the model. Also, skin reddening spatial profile can be related with the current density profile. Experimental measurement of the current density will validate the accuracy of the realistic skin model. The temperature simulation in the Aim 2 can be further studied using the high-resolution skin model from the Aim 3. The multi-layer skin model from the Aim 2 does not have skin-ultrastructure and it predicted 0.38 ^{O}C temperature increase due to joule heat, which is less than the experimental measurement. However, adding sweat glands and blood vessels into the multi-layer skin model may significantly increase joule heat, increasing alignment of the model prediction with the experiment. Also, adding sweat glands and blood vessels into the multi-layer skin model (Aim 3) reduced current concentration at the edges, we expect a bioheat model of this detailed skin would predict a uniform temperature at the surface of skin- consistent with the experiment.

Furthermore, the method/technology developed in the Appendix 1 can be implemented into multi-channel electrical stimulation to monitor individual electrode impedance during tDCS. Within electrode current steering (WECS) technology principle proposed in the Appendix 4 can be used to design a novel electrode for tDCS which also uses technology designed in the Appendix 1. The performance of this novel electrode needs to be tested. High-resolution analytically realistic and detailed skin model developed in the Aim 3 is not only itself a novel model, but it is also a power tool which can be explicitly used for electrode design and rapid prototype testing. Although we have not modelled the blood vessels correctly in this skin model, adding blood vessel wall and lumen will make this model the state-of-the-art tool. From this model, we understood the role of

blood vessels in current dispersion to deeper tissues. This idea can be applied in transcranial current flow modeling (adding vasculature in the model) to understand the neurovascular neuromodulation. In the Aim 2, we used intermediate skin model to simulate bio-heat with perfusion and metabolism. Using the advanced skin model from the Aim 3 will help to understand the role of vasculature in skin temperature increase as well. In the Appendix 2, we tested the performance of novel dry electrode for tDCS, the role of electrode material (used in dry electrode) in cutaneous current flow can be assessed using the skin model from the Aim 3. In the Appendix 3, we developed a novel adaptive controller for administering tDCS up to 4 mA. This controller can be further optimized using machine learning to update the adaptive current by incorporating system impedance (skin impedance, electrode impedance) and data from biomarkers (EEG). In the Appendix 5, we proposed a novel tissue-heating related neuromodulation hypothesis for kHz frequency spinal cord stimulation. This hypothesis needs to be tested via *in vitro* experiments and *in vivo* measurements in human/animal study. In the Appendix 7, we modeled brain tissue temperature increases during kHz-frequency Deep Brain Stimulation to support the hypothesis presented in Appendix 5 regarding kHz frequency stimulation. This hypothesis also needs to be tested empirically. Finally, in the Appendix 8, we developed the first realistic open-source spinal cord model (RADO-SCS) for SCS, DRG, or transspinal electrical stimulation. This model is CAD derived and which can be replaced the CAD files with realistic MRI derived vertebrae, IV discs, and vasculature in future version control of this model.

References

Aberra, A.S., Peterchev, A.V., Grill, W.M., 2018. Biophysically realistic neuron models for simulation of cortical stimulation. J Neural Eng 15, 066023. https://doi.org/10.1088/1741-2552/aadbb1

Abram, S.E., Asiddao, C.B., Reynolds, A.C., 1980. Increased skin temperature during transcutaneous electrical stimulation. Anesth. Analg. 59, 22–25.

Al-Kaisy, A., Palmisani, S., Smith, T., Harris, S., Pang, D., 2015. The use of 10-kilohertz spinal cord stimulation in a cohort of patients with chronic neuropathic limb pain refractory to medical management. Neuromodulation 18, 18–23; discussion 23. https://doi.org/10.1111/ner.12237

Al-Kaisy, A., Van Buyten, J.-P., Smet, I., Palmisani, S., Pang, D., Smith, T., 2014. Sustained effectiveness of 10 kHz high-frequency spinal cord stimulation for patients with chronic, low back pain: 24-month results of a prospective multicenter study. Pain Med 15, 347–354. https://doi.org/10.1111/pme.12294

Alonso, F., Latorre, M.A., Göransson, N., Zsigmond, P., Wårdell, K., 2016. Investigation into Deep Brain Stimulation Lead Designs: A Patient-Specific Simulation Study. Brain Sciences 6, 39. https://doi.org/10.3390/brainsci6030039

Ambrus, G.G., Antal, A., Paulus, W., 2011. Comparing cutaneous perception induced by electrical stimulation using rectangular and round shaped electrodes. Clin Neurophysiol 122, 803–807. https://doi.org/10.1016/j.clinph.2010.08.023

Anaya, C.J., Zander, H.J., Graham, R.D., Sankarasubramanian, V., Lempka, S.F., 2020. Evoked Potentials Recorded From the Spinal Cord During Neurostimulation for Pain: A Computational Modeling Study. Neuromodulation: Technology at the Neural Interface 23, 64–73. https://doi.org/10.1111/ner.12965

Anderson, D.J., Kipke, D.R., Nagel, S.J., Lempka, S.F., Machado, A.G., Holland, M.T., Gillies, G.T., Howard, M.A., Wilson, S., 2019. Intradural Spinal Cord Stimulation: Performance Modeling of a New Modality. Front Neurosci 13, 253. https://doi.org/10.3389/fnins.2019.00253

Anderson, D.N., Osting, B., Vorwerk, J., Dorval, A.D., Butson, C.R., 2018. Optimized programming algorithm for cylindrical and directional deep brain stimulation electrodes. J Neural Eng 15, 026005. https://doi.org/10.1088/1741-2552/aaa14b

Andrade, C., 2013. Once- to twice-daily, 3-year domiciliary maintenance transcranial direct current stimulation for severe, disabling, clozapine-refractory continuous auditory hallucinations in schizophrenia. J ECT 29, 239–242. https://doi.org/10.1097/YCT.0b013e3182843866

Antal, A., Alekseichuk, I., Bikson, M., Brockmöller, J., Brunoni, A.R., Chen, R., Cohen, L.G., Dowthwaite, G., Ellrich, J., Flöel, A., Fregni, F., George, M.S., Hamilton, R., Haueisen, J., Herrmann, C.S., Hummel, F.C., Lefaucheur, J.P., Liebetanz, D., Loo, C.K., McCaig, C.D., Miniussi, C., Miranda, P.C., Moliadze, V., Nitsche, M.A., Nowak, R., Padberg, F., Pascual-Leone, A., Poppendieck, W., Priori, A., Rossi, S., Rossini, P.M., Rothwell, J., Rueger, M.A., Ruffini, G., Schellhorn, K., Siebner, H.R., Ugawa, Y., Wexler, A., Ziemann, U., Hallett, M., Paulus, W., 2017. Low intensity transcranial electric stimulation: Safety, ethical, legal regulatory and application guidelines. Clin Neurophysiol 128, 1774–1809. https://doi.org/10.1016/j.clinph.2017.06.001

Antal, A., Boros, K., Poreisz, C., Chaieb, L., Terney, D., Paulus, W., 2008. Comparatively weak after-effects of transcranial alternating current stimulation (tACS) on cortical excitability in humans. Brain Stimul 1, 97–105. https://doi.org/10.1016/j.brs.2007.10.001

Aparício, L.V.M., Guarienti, F., Razza, L.B., Carvalho, A.F., Fregni, F., Brunoni, A.R., 2016. A Systematic Review on the Acceptability and Tolerability of Transcranial Direct Current Stimulation Treatment in Neuropsychiatry Trials. Brain Stimul 9, 671–681. https://doi.org/10.1016/j.brs.2016.05.004

Arle, J.E., Mei, L., Carlson, K.W., Shils, J.L., 2016. High-Frequency Stimulation of Dorsal Column Axons: Potential Underlying Mechanism of Paresthesia-Free Neuropathic Pain Relief. Neuromodulation: Technology at the Neural Interface 19, 385–397. https://doi.org/10.1111/ner.12436

Arlotti, M., Rahman, A., Minhas, P., Bikson, M., 2012. Axon terminal polarization induced by weak uniform DC electric fields: a modeling study. Conf Proc IEEE Eng Med Biol Soc 2012, 4575–4578. https://doi.org/10.1109/EMBC.2012.6346985

Armstrong, D.M., Harvey, R.J., Schild, R.F., 1973. The spatial organisation of climbing fibre branching in the cat cerebellum. Exp Brain Res 18, 40–58.

Astrom, M., Diczfalusy, E., Martens, H., Wardell, K., 2015. Relationship between neural activation and electric field distribution during deep brain stimulation. IEEE Trans Biomed Eng 62, 664–672. https://doi.org/10.1109/TBME.2014.2363494

Bai, S., Gálvez, V., Dokos, S., Martin, D., Bikson, M., Loo, C., 2017. Computational models of Bitemporal, Bifrontal and Right Unilateral ECT predict differential stimulation of brain regions associated with efficacy and cognitive side effects. Eur. Psychiatry 41, 21–29. https://doi.org/10.1016/j.eurpsy.2016.09.005

Bai, S., Loo, C., Al Abed, A., Dokos, S., 2012. A computational model of direct brain excitation induced by electroconvulsive therapy: comparison among three conventional electrode placements. Brain Stimul 5, 408–421. https://doi.org/10.1016/j.brs.2011.07.004

Balogun, J.A., Tang, S., He, Y., Hsieh, J.M., Katz, J.S., 1996. Effects of high-voltage galvanic stimulation of ST36 and ST37 acupuncture points on peripheral blood flow and skin temperature. Disabil Rehabil 18, 523–528.

Basser, P.J., Roth, B.J., 2000. New currents in electrical stimulation of excitable tissues. Annu Rev Biomed Eng 2, 377–397. https://doi.org/10.1146/annurev.bioeng.2.1.377

Benabid, A.L., Pollak, P., Gervason, C., Hoffmann, D., Gao, D.M., Hommel, M., Perret, J.E., de Rougemont, J., 1991. Long-term suppression of tremor by chronic stimulation of the ventral intermediate thalamic nucleus. Lancet 337, 403–406. https://doi.org/10.1016/0140-6736(91)91175-t

Bennett, D., 2011. NaCl doping and the conductivity of agar phantoms. Materials Science and Engineering: C 31, 494–498. https://doi.org/10.1016/j.msec.2010.08.018

Bennetts, B., Roberts, M.L., Bretag, A.H., Rychkov, G.Y., 2001. Temperature dependence of human muscle ClC-1 chloride channel. J. Physiol. (Lond.) 535, 83–93.

Bicket, M.C., Dunn, R.Y., Ahmed, S.U., 2016. High-Frequency Spinal Cord Stimulation for Chronic Pain: Pre-Clinical Overview and Systematic Review of Controlled Trials. Pain Med 17, 2326–2336. https://doi.org/10.1093/pm/pnw156

Bikson, M., Brunoni, A.R., Charvet, L.E., Clark, V.P., Cohen, L.G., Deng, Z.-D., Dmochowski, J., Edwards, D.J., Frohlich, F., Kappenman, E.S., Lim, K.O., Loo, C., Mantovani, A., McMullen, D.P., Parra, L.C., Pearson, M., Richardson, J.D., Rumsey, J.M., Sehatpour, P., Sommers, D., Unal, G., Wassermann, E.M., Woods, A.J., Lisanby, S.H., 2018. Rigor

and reproducibility in research with transcranial electrical stimulation: An NIMH-sponsored workshop. Brain Stimul 11, 465–480. https://doi.org/10.1016/j.brs.2017.12.008
Bikson, M., Datta, A., Elwassif, M., 2009. Establishing safety limits for transcranial direct current stimulation. Clin Neurophysiol 120, 1033–1034. https://doi.org/10.1016/j.clinph.2009.03.018
Bikson, M., Dmochowski, J., Rahman, A., 2013. The "quasi-uniform" assumption in animal and computational models of non-invasive electrical stimulation. Brain Stimul 6, 704–705. https://doi.org/10.1016/j.brs.2012.11.005
Bikson, M., Grossman, P., Thomas, C., Zannou, A.L., Jiang, J., Adnan, T., Mourdoukoutas, A.P., Kronberg, G., Truong, D., Boggio, P., Brunoni, A.R., Charvet, L., Fregni, F., Fritsch, B., Gillick, B., Hamilton, R.H., Hampstead, B.M., Jankord, R., Kirton, A., Knotkova, H., Liebetanz, D., Liu, A., Loo, C., Nitsche, M.A., Reis, J., Richardson, J.D., Rotenberg, A., Turkeltaub, P.E., Woods, A.J., 2016. Safety of Transcranial Direct Current Stimulation: Evidence Based Update 2016. Brain Stimul 9, 641–661. https://doi.org/10.1016/j.brs.2016.06.004
Bikson, M., Inoue, M., Akiyama, H., Deans, J.K., Fox, J.E., Miyakawa, H., Jefferys, J.G.R., 2004. Effects of uniform extracellular DC electric fields on excitability in rat hippocampal slices in vitro. J. Physiol. (Lond.) 557, 175–190. https://doi.org/10.1113/jphysiol.2003.055772
Bikson, M., Lian, J., Hahn, P.J., Stacey, W.C., Sciortino, C., Durand, D.M., 2001. Suppression of epileptiform activity by high frequency sinusoidal fields in rat hippocampal slices. J. Physiol. (Lond.) 531, 181–191.
Bikson, M., Truong, D.Q., Mourdoukoutas, A.P., Aboseria, M., Khadka, N., Adair, D., Rahman, A., 2015. Modeling sequence and quasi-uniform assumption in computational neurostimulation. Prog. Brain Res. 222, 1–23. https://doi.org/10.1016/bs.pbr.2015.08.005
Bioimpedance and Bioelectricity Basics - 3rd Edition [WWW Document], n.d. URL https://www.elsevier.com/books/bioimpedance-and-bioelectricity-basics/grimnes/978-0-12-411470-8 (accessed 3.9.20).
Björklund, S., Engblom, J., Thuresson, K., Sparr, E., 2013. Glycerol and urea can be used to increase skin permeability in reduced hydration conditions. Eur J Pharm Sci 50, 638–645. https://doi.org/10.1016/j.ejps.2013.04.022
Bohm, E., 1978. Transcutaneous electrical nerve stimulation in chronic pain after peripheral nerve injury. Acta Neurochir (Wien) 40, 277–283.
Borges, H., Khadka, N., Boateng, A., Paneri, B., Nassis, E., Shin, Y., Choi, H., Kim, S., Lee, K., Bikson, M., 2017. Tolerability of up to 4 mA tDCS using adaptive stimulation. Brain Stimulation 10, e31–e32. https://doi.org/10.1016/j.brs.2017.04.044
Bossetti, C.A., Birdno, M.J., Grill, W.M., 2008. Analysis of the quasi-static approximation for calculating potentials generated by neural stimulation. J Neural Eng 5, 44–53. https://doi.org/10.1088/1741-2560/5/1/005
Bozkurt, M., Canbay, S., Neves, G.F., Aktüre, E., Fidan, E., Salamat, M.S., Başkaya, M.K., 2012. Microsurgical anatomy of the dorsal thoracic rootlets and dorsal root entry zones. Acta Neurochir (Wien) 154, 1235–1239. https://doi.org/10.1007/s00701-012-1395-0
Branscheidt, M., Hoppe, J., Zwitserlood, P., Liuzzi, G., 2018. tDCS over the motor cortex improves lexical retrieval of action words in poststroke aphasia. J. Neurophysiol. 119, 621–630. https://doi.org/10.1152/jn.00285.2017

Brocker, D.T., Grill, W.M., 2013. Chapter 1 - Principles of electrical stimulation of neural tissue, in: Lozano, A.M., Hallett, M. (Eds.), Handbook of Clinical Neurology, Brain Stimulation. Elsevier, pp. 3–18. https://doi.org/10.1016/B978-0-444-53497-2.00001-2

Brodkey, J.S., Miyazaki, Y., Ervin, F.R., Mark, V.H., 1964. Reversible Heat Lesions with Radiofrequency Current: A Method of Stereotactic Localization. Journal of Neurosurgery 21, 49–53. https://doi.org/10.3171/jns.1964.21.1.0049

Brunoni, A.R., Amadera, J., Berbel, B., Volz, M.S., Rizzerio, B.G., Fregni, F., 2011. A systematic review on reporting and assessment of adverse effects associated with transcranial direct current stimulation. Int. J. Neuropsychopharmacol. 14, 1133–1145. https://doi.org/10.1017/S1461145710001690

Brunoni, A.R., Moffa, A.H., Sampaio-Junior, B., Borrione, L., Moreno, M.L., Fernandes, R.A., Veronezi, B.P., Nogueira, B.S., Aparicio, L.V.M., Razza, L.B., Chamorro, R., Tort, L.C., Fraguas, R., Lotufo, P.A., Gattaz, W.F., Fregni, F., Benseñor, I.M., ELECT-TDCS Investigators, 2017. Trial of Electrical Direct-Current Therapy versus Escitalopram for Depression. N. Engl. J. Med. 376, 2523–2533. https://doi.org/10.1056/NEJMoa1612999

Brunoni, A.R., Nitsche, M.A., Bolognini, N., Bikson, M., Wagner, T., Merabet, L., Edwards, D.J., Valero-Cabre, A., Rotenberg, A., Pascual-Leone, A., Ferrucci, R., Priori, A., Boggio, P.S., Fregni, F., 2012. Clinical research with transcranial direct current stimulation (tDCS): Challenges and future directions. Brain Stimulation 5, 175–195. https://doi.org/10.1016/j.brs.2011.03.002

Butson, C.R., Cooper, S.E., Henderson, J.M., McIntyre, C.C., 2007. Patient-specific analysis of the volume of tissue activated during deep brain stimulation. NeuroImage 34, 661–670. https://doi.org/10.1016/j.neuroimage.2006.09.034

Butson, C.R., Maks, C.B., McIntyre, C.C., 2006. Sources and effects of electrode impedance during deep brain stimulation. Clinical Neurophysiology 117, 447–454. https://doi.org/10.1016/j.clinph.2005.10.007

Butson, C.R., McIntyre, C.C., 2008. Current steering to control the volume of tissue activated during deep brain stimulation. Brain Stimulation 1, 7–15. https://doi.org/10.1016/j.brs.2007.08.004

Butson, C.R., McIntyre, C.C., 2006. Role of electrode design on the volume of tissue activated during deep brain stimulation. J Neural Eng 3, 1–8. https://doi.org/10.1088/1741-2560/3/1/001

Butson, C.R., McIntyre, C.C., 2005. Role of electrode design on the volume of tissue activated during deep brain stimulation. J. Neural Eng. 3, 1–8. https://doi.org/10.1088/1741-2560/3/1/001

Cantrell, D.R., Inayat, S., Taflove, A., Ruoff, R.S., Troy, J.B., 2008. Incorporation of the electrode–electrolyte interface into finite-element models of metal microelectrodes. J. Neural Eng. 5, 54. https://doi.org/10.1088/1741-2560/5/1/006

Capogrosso, M., Wagner, F.B., Gandar, J., Moraud, E.M., Wenger, N., Milekovic, T., Shkorbatova, P., Pavlova, N., Musienko, P., Bezard, E., Bloch, J., Courtine, G., 2018. Configuration of electrical spinal cord stimulation through real-time processing of gait kinematics. Nature Protocols 13, 2031–2061. https://doi.org/10.1038/s41596-018-0030-9

Capogrosso, M., Wenger, N., Raspopovic, S., Musienko, P., Beauparlant, J., Luciani, L.B., Courtine, G., Micera, S., 2013a. A Computational Model for Epidural Electrical Stimulation of Spinal Sensorimotor Circuits. J. Neurosci. 33, 19326–19340. https://doi.org/10.1523/JNEUROSCI.1688-13.2013

Capogrosso, M., Wenger, N., Raspopovic, S., Musienko, P., Beauparlant, J., Luciani, L.B., Courtine, G., Micera, S., 2013b. A Computational Model for Epidural Electrical Stimulation of Spinal Sensorimotor Circuits. J. Neurosci. 33, 19326–19340. https://doi.org/10.1523/JNEUROSCI.1688-13.2013

Çetingül, M.P., Herman, C., 2010. A heat transfer model of skin tissue for the detection of lesions: sensitivity analysis. Phys. Med. Biol. 55, 5933. https://doi.org/10.1088/0031-9155/55/19/020

Chakraborty, D., Truong, D.Q., Bikson, M., Kaphzan, H., 2018. Neuromodulation of Axon Terminals. Cereb. Cortex 28, 2786–2794. https://doi.org/10.1093/cercor/bhx158

Chan, C.Y., Hounsgaard, J., Nicholson, C., 1988. Effects of electric fields on transmembrane potential and excitability of turtle cerebellar Purkinje cells in vitro. J. Physiol. (Lond.) 402, 751–771. https://doi.org/10.1113/jphysiol.1988.sp017232

Chang, I., 2003. Finite element analysis of hepatic radiofrequency ablation probes using temperature-dependent electrical conductivity. Biomed Eng Online 2, 12. https://doi.org/10.1186/1475-925x-2-12

Charvet, L., Shaw, M., Dobbs, B., Frontario, A., Sherman, K., Bikson, M., Datta, A., Krupp, L., Zeinapour, E., Kasschau, M., 2017. Remotely Supervised Transcranial Direct Current Stimulation Increases the Benefit of At-Home Cognitive Training in Multiple Sclerosis. Neuromodulation: Technology at the Neural Interface. https://doi.org/10.1111/ner.12583

Chaturvedi, A., Butson, C.R., Lempka, S.F., Cooper, S.E., McIntyre, C.C., 2010. Patient-specific models of deep brain stimulation: influence of field model complexity on neural activation predictions. Brain Stimul 3, 65–67. https://doi.org/10.1016/j.brs.2010.01.003

Chhatbar, P.Y., Chen, R., Deardorff, R., Dellenbach, B., Kautz, S.A., George, M.S., Feng, W., 2017. Safety and tolerability of transcranial direct current stimulation to stroke patients - A phase I current escalation study. Brain Stimul 10, 553–559. https://doi.org/10.1016/j.brs.2017.02.007

Childs, C., 2008. Human brain temperature: regulation, measurement and relationship with cerebral trauma: part 1. Br J Neurosurg 22, 486–496. https://doi.org/10.1080/02688690802245541

Chowdhury, S., Jarecki, B.W., Chanda, B., 2014a. A molecular framework for temperature-dependent gating of ion channels. Cell 158, 1148–1158. https://doi.org/10.1016/j.cell.2014.07.026

Chowdhury, S., Jarecki, B.W., Chanda, B., 2014b. A molecular framework for temperature-dependent gating of ion channels. Cell 158, 1148–1158. https://doi.org/10.1016/j.cell.2014.07.026

Coburn, B., 1985. A theoretical study of epidural electrical stimulation of the spinal cord--Part II: Effects on long myelinated fibers. IEEE Trans Biomed Eng 32, 978–986. https://doi.org/10.1109/TBME.1985.325649

Coburn, B., 1980. Electrical stimulation of the spinal cord: two-dimensional finite element analysis with particular reference to epidural electrodes. Med Biol Eng Comput 18, 573–584. https://doi.org/10.1007/bf02443129

Coburn, B., Sin, W.K., 1985. A theoretical study of epidural electrical stimulation of the spinal cord--Part I: Finite element analysis of stimulus fields. IEEE Trans Biomed Eng 32, 971–977. https://doi.org/10.1109/tbme.1985.325648

Collins, C.M., Smith, M.B., Turner, R., 2004a. Model of local temperature changes in brain upon functional activation. J. Appl. Physiol. 97, 2051–2055. https://doi.org/10.1152/japplphysiol.00626.2004
Collins, C.M., Smith, M.B., Turner, R., 2004b. Model of local temperature changes in brain upon functional activation. J. Appl. Physiol. 97, 2051–2055. https://doi.org/10.1152/japplphysiol.00626.2004
Couto, J., Grill, W.M., 2016. Kilohertz Frequency Deep Brain Stimulation Is Ineffective at Regularizing the Firing of Model Thalamic Neurons. Front. Comput. Neurosci. 10. https://doi.org/10.3389/fncom.2016.00022
Cramp, Gilsenan, Lowe, Walsh, 2000. The effect of high- and low-frequency transcutaneous electrical nerve stimulation upon cutaneous blood flow and skin temperature in healthy subjects. Clinical Physiology 20, 150–157. https://doi.org/10.1046/j.1365-2281.2000.00240.x
Crosby, N.D., Goodman Keiser, M.D., Smith, J.R., Zeeman, M.E., Winkelstein, B.A., 2015a. Stimulation parameters define the effectiveness of burst spinal cord stimulation in a rat model of neuropathic pain. Neuromodulation 18, 1–8; discussion 8. https://doi.org/10.1111/ner.12221
Crosby, N.D., Janik, J.J., Grill, W.M., 2017. Modulation of activity and conduction in single dorsal column axons by kilohertz-frequency spinal cord stimulation. J. Neurophysiol. 117, 136–147. https://doi.org/10.1152/jn.00701.2016
Crosby, N.D., Weisshaar, C.L., Smith, J.R., Zeeman, M.E., Goodman-Keiser, M.D., Winkelstein, B.A., 2015b. Burst and Tonic Spinal Cord Stimulation Differentially Activate GABAergic Mechanisms to Attenuate Pain in a Rat Model of Cervical Radiculopathy. IEEE Trans Biomed Eng 62, 1604–1613. https://doi.org/10.1109/TBME.2015.2399374
Cubo, Rubén, Åström, M., Medvedev, A., 2016. Optimization of lead design and electrode configuration in Deep Brain Stimulation. International Journal On Advances in Life Sciences 8, 76–86.
Cubo, R., Fahlström, M., Jiltsova, E., Andersson, H., Medvedev, A., 2019. Calculating deep brain stimulation amplitudes and power consumption by constrained optimization. Journal of Neural Engineering 16, 016020. https://doi.org/10.1088/1741-2552/aaeeb7
Cubo, R., Medvedev, A., Åström, M., 2016. Model-Based Optimization of Individualized Deep Brain Stimulation Therapy. IEEE Design Test 33, 74–81. https://doi.org/10.1109/MDAT.2015.2480705
Danner, S.M., Hofstoetter, U.S., Ladenbauer, J., Rattay, F., Minassian, K., 2011. Can the human lumbar posterior columns be stimulated by transcutaneous spinal cord stimulation? A modeling study. Artif Organs 35, 257–262. https://doi.org/10.1111/j.1525-1594.2011.01213.x
Darrow, D.P., O'Brien, P., Richner, T.J., Netoff, T.I., Ebbini, E.S., 2019. Reversible neuroinhibition by focused ultrasound is mediated by a thermal mechanism. Brain Stimul 12, 1439–1447. https://doi.org/10.1016/j.brs.2019.07.015
DaSilva, A.F., Volz, M.S., Bikson, M., Fregni, F., 2011. Electrode Positioning and Montage in Transcranial Direct Current Stimulation. J Vis Exp. https://doi.org/10.3791/2744
Datta, Abhishek, Bansal, V., Diaz, J., Patel, J., Reato, D., Bikson, M., 2009. Gyri-precise head model of transcranial direct current stimulation: improved spatial focality using a ring

electrode versus conventional rectangular pad. Brain Stimul 2, 201–207, 207.e1. https://doi.org/10.1016/j.brs.2009.03.005
Datta, A., Elwassif, M., Bikson, M., 2009. Bio-heat transfer model of transcranial DC stimulation: Comparison of conventional pad versus ring electrode, in: Annual International Conference of the IEEE Engineering in Medicine and Biology Society, 2009. EMBC 2009. Presented at the Annual International Conference of the IEEE Engineering in Medicine and Biology Society, 2009. EMBC 2009, pp. 670–673. https://doi.org/10.1109/IEMBS.2009.5333673
Dean, D.A., Ramanathan, T., Machado, D., Sundararajan, R., 2008. Electrical Impedance Spectroscopy Study of Biological Tissues. J Electrostat 66, 165–177. https://doi.org/10.1016/j.elstat.2007.11.005
Dembek, T.A., Reker, P., Visser-Vandewalle, V., Wirths, J., Treuer, H., Klehr, M., Roediger, J., Dafsari, H.S., Barbe, M.T., Timmermann, L., 2017. Directional DBS increases side-effect thresholds-A prospective, double-blind trial. Mov. Disord. 32, 1380–1388. https://doi.org/10.1002/mds.27093
Dielectric Properties » IT'IS Foundation [WWW Document], n.d. URL https://itis.swiss/virtual-population/tissue-properties/database/dielectric-properties/ (accessed 8.30.19).
Dietrich, W.D., 1992. The importance of brain temperature in cerebral injury. J. Neurotrauma 9 Suppl 2, S475-485.
DiMarco, A.F., Kowalski, K.E., 2013. Activation of inspiratory muscles via spinal cord stimulation. Respir Physiol Neurobiol 189, 438–449. https://doi.org/10.1016/j.resp.2013.06.001
Dmochowski, J.P., Datta, A., Bikson, M., Su, Y., Parra, L.C., 2011. Optimized multi-electrode stimulation increases focality and intensity at target. J Neural Eng 8, 046011. https://doi.org/10.1088/1741-2560/8/4/046011
Dobbs, B., Pawlak, N., Biagioni, M., Agarwal, S., Shaw, M., Pilloni, G., Bikson, M., Datta, A., Charvet, L., 2018. Generalizing remotely supervised transcranial direct current stimulation (tDCS): feasibility and benefit in Parkinson's disease. J Neuroeng Rehabil 15. https://doi.org/10.1186/s12984-018-0457-9
Duck, F.A., 1990. Physical Properties of Tissue: A Comprehensive Reference Book. Academic Press.
Duke, A.R., Jenkins, M.W., Lu, H., McManus, J.M., Chiel, H.J., Jansen, E.D., 2013. Transient and selective suppression of neural activity with infrared light. Sci Rep 3. https://doi.org/10.1038/srep02600
Dundas, J.E., Thickbroom, G.W., Mastaglia, F.L., 2007a. Perception of comfort during transcranial DC stimulation: Effect of NaCl solution concentration applied to sponge electrodes. Clinical Neurophysiology 118, 1166–1170. https://doi.org/10.1016/j.clinph.2007.01.010
Dundas, J.E., Thickbroom, G.W., Mastaglia, F.L., 2007b. Perception of comfort during transcranial DC stimulation: Effect of NaCl solution concentration applied to sponge electrodes. Clinical Neurophysiology 118, 1166–1170. https://doi.org/10.1016/j.clinph.2007.01.010
Durá, J.L., Solanes, C., De Andrés, J., Saiz, J., 2019. Computational Study of the Effect of Electrode Polarity on Neural Activation Related to Paresthesia Coverage in Spinal Cord Stimulation Therapy. Neuromodulation 22, 269–279. https://doi.org/10.1111/ner.12909

Durand, S., Fromy, B., Bouyé, P., Saumet, J.L., Abraham, P., 2002. Vasodilatation in response to repeated anodal current application in the human skin relies on aspirin-sensitive mechanisms. The Journal of Physiology 540, 261–269. https://doi.org/10.1113/jphysiol.2001.013364

Dusch, M., Schley, M., Obreja, O., Forsch, E., Schmelz, M., Rukwied, R., 2009. Comparison of electrically induced flare response patterns in human and pig skin. Inflamm. Res. 58, 639–648. https://doi.org/10.1007/s00011-009-0029-3

Dusch, M., Schley, M., Rukwied, R., Schmelz, M., 2007. Rapid flare development evoked by current frequency-dependent stimulation analyzed by full-field laser perfusion imaging. Neuroreport 18, 1101–1105. https://doi.org/10.1097/WNR.0b013e3281e72cff

Edelberg, Robert., 1977. RELATION OF ELECTRICAL PROPERTIES OF SKIN TO STRUCTURE AND PHYSIOLOGIC STATE. Journal of Investigative Dermatology 69, 324–327. https://doi.org/10.1111/1523-1747.ep12507771

Elwassif, M.M., Datta, A., Rahman, A., Bikson, M., 2012a. Temperature control at DBS electrodes using a heat sink: experimentally validated FEM model of DBS lead architecture. J. Neural Eng. 9, 046009. https://doi.org/10.1088/1741-2560/9/4/046009

Elwassif, M.M., Datta, A., Rahman, A., Bikson, M., 2012b. Temperature control at DBS electrodes using a heat sink: experimentally validated FEM model of DBS lead architecture. J Neural Eng 9, 046009. https://doi.org/10.1088/1741-2560/9/4/046009

Elwassif, Maged M., Kong, Q., Vazquez, M., Bikson, M., 2006a. Bio-heat transfer model of deep brain stimulation-induced temperature changes. J. Neural Eng. 3, 306–315. https://doi.org/10.1088/1741-2560/3/4/008

Elwassif, Maged M., Kong, Q., Vazquez, M., Bikson, M., 2006b. Bio-heat transfer model of deep brain stimulation induced temperature changes. Conf Proc IEEE Eng Med Biol Soc 1, 3580–3583. https://doi.org/10.1109/IEMBS.2006.259425

Elwassif, M.M., Kong, Q., Vazquez, M., Bikson, M., 2006. Bio-Heat Transfer Model of Deep Brain Stimulation Induced Temperature changes, in: 28th Annual International Conference of the IEEE Engineering in Medicine and Biology Society, 2006. EMBS '06. Presented at the 28th Annual International Conference of the IEEE Engineering in Medicine and Biology Society, 2006. EMBS '06, pp. 3580–3583. https://doi.org/10.1109/IEMBS.2006.259425

Eng, J.W.-L., Reed, C.B., Kokolus, K.M., Repasky, E.A., 2014. Housing Temperature Influences the Pattern of Heat Shock Protein Induction in Mice following Mild Whole Body Hyperthermia. Int J Hyperthermia 30, 540–546. https://doi.org/10.3109/02656736.2014.981300

Esmaeilpour, Z., Marangolo, P., Hampstead, B.M., Bestmann, S., Galletta, E., Knotkova, H., Bikson, M., 2018. Incomplete evidence that increasing current intensity of tDCS boosts outcomes. Brain Stimul 11, 310–321. https://doi.org/10.1016/j.brs.2017.12.002

Esmaeilpour, Z., Schestatsky, P., Bikson, M., Brunoni, A.R., Pellegrinelli, A., Piovesan, F.X., Santos, M.M.S.A., Menezes, R.B., Fregni, F., 2017. Notes on Human Trials of Transcranial Direct Current Stimulation between 1960 and 1998. Front Hum Neurosci 11, 71. https://doi.org/10.3389/fnhum.2017.00071

Eve, F.C., 1900. The effect of temperature on the functional activity of the upper cervical ganglion. J Physiol 26, 119–124.

Ezquerro, F., Moffa, A.H., Bikson, M., Khadka, N., Aparicio, L.V.M., de Sampaio-Junior, B., Fregni, F., Bensenor, I.M., Lotufo, P.A., Pereira, A.C., Brunoni, A.R., 2017. The

Influence of Skin Redness on Blinding in Transcranial Direct Current Stimulation Studies: A Crossover Trial. Neuromodulation: Technology at the Neural Interface 20, 248–255. https://doi.org/10.1111/ner.12527
Fagundes, V. de C., Rieder, C.R.M., da Cruz, A.N., Beber, B.C., Portuguez, M.W., 2016. Deep Brain Stimulation Frequency of the Subthalamic Nucleus Affects Phonemic and Action Fluency in Parkinson's Disease. Parkinsons Dis 2016. https://doi.org/10.1155/2016/6760243
Feirabend, H.K.P., Choufoer, H., Ploeger, S., Holsheimer, J., van Gool, J.D., 2002. Morphometry of human superficial dorsal and dorsolateral column fibres: significance to spinal cord stimulation. Brain 125, 1137–1149. https://doi.org/10.1093/brain/awf111
Fernandes, S.R., Pereira, M., Salvador, R., Miranda, P.C., de Carvalho, M., 2019. Cervical trans-spinal direct current stimulation: a modelling-experimental approach. Journal of NeuroEngineering and Rehabilitation 16. https://doi.org/10.1186/s12984-019-0589-6
Fernandes, S.R., Salvador, R., Wenger, C., Carvalho, M. de, Miranda, P.C., 2018. Transcutaneous spinal direct current stimulation of the lumbar and sacral spinal cord: a modelling study. J. Neural Eng. 15, 036008. https://doi.org/10.1088/1741-2552/aaac38
Ferree, T.C., Luu, P., Russell, G.S., Tucker, D.M., 2001. Scalp electrode impedance, infection risk, and EEG data quality. Clinical Neurophysiology 112, 536–544. https://doi.org/10.1016/S1388-2457(00)00533-2
Fertonani, A., Ferrari, C., Miniussi, C., 2015. What do you feel if I apply transcranial electric stimulation? Safety, sensations and secondary induced effects. Clin Neurophysiol 126, 2181–2188. https://doi.org/10.1016/j.clinph.2015.03.015
Fiala, D., Lomas, K.J., Stohrer, M., 1999. A computer model of human thermoregulation for a wide range of environmental conditions: the passive system. J. Appl. Physiol. 87, 1957–1972.
Fiala, Dusan, Lomas, K.J., Stohrer, M., 1999. A computer model of human thermoregulation for a wide range of environmental conditions: the passive system. Journal of Applied Physiology 87, 1957–1972. https://doi.org/10.1152/jappl.1999.87.5.1957
Fingas, M., Clark, D.L., Colbourne, F., 2007. The effects of selective brain hypothermia on intracerebral hemorrhage in rats. Exp. Neurol. 208, 277–284. https://doi.org/10.1016/j.expneurol.2007.08.018
Fiocchi, S., Ravazzani, P., Priori, A., Parazzini, M., 2016. Cerebellar and Spinal Direct Current Stimulation in Children: Computational Modeling of the Induced Electric Field. Front. Hum. Neurosci. 10. https://doi.org/10.3389/fnhum.2016.00522
Fonteneau, C., Mondino, M., Arns, M., Baeken, C., Bikson, M., Brunoni, A.R., Burke, M.J., Neuvonen, T., Padberg, F., Pascual-Leone, A., Poulet, E., Ruffini, G., Santarnecchi, E., Sauvaget, A., Schellhorn, K., Suaud-Chagny, M.-F., Palm, U., Brunelin, J., 2019. Sham tDCS: A hidden source of variability? Reflections for further blinded, controlled trials. Brain Stimul 12, 668–673. https://doi.org/10.1016/j.brs.2018.12.977
Foutz, T., McIntyre, C., 2010. Evaluation of novel stimulus waveforms for deep brain stimulation. J Neural Eng 7, 066008. https://doi.org/10.1088/1741-2560/7/6/066008
Frankemolle, A.M.M., Wu, J., Noecker, A.M., Voelcker-Rehage, C., Ho, J.C., Vitek, J.L., McIntyre, C.C., Alberts, J.L., 2010. Reversing cognitive-motor impairments in Parkinson's disease patients using a computational modelling approach to deep brain stimulation programming. Brain 133, 746–761. https://doi.org/10.1093/brain/awp315

Frijns, J.H., Mooij, J., ten Kate, J.H., 1994. A quantitative approach to modeling mammalian myelinated nerve fibers for electrical prosthesis design. IEEE Trans Biomed Eng 41, 556–566. https://doi.org/10.1109/10.293243

Gabriel, S., Lau, R.W., Gabriel, C., 1996a. The dielectric properties of biological tissues: III. Parametric models for the dielectric spectrum of tissues. Phys. Med. Biol. 41, 2271. https://doi.org/10.1088/0031-9155/41/11/003

Gabriel, S., Lau, R.W., Gabriel, C., 1996b. The dielectric properties of biological tissues: II. Measurements in the frequency range 10 Hz to 20 GHz. Phys Med Biol 41, 2251–2269.

Gaggero, P.O., Adler, A., Brunner, J., Seitz, P., 2012. Electrical impedance tomography system based on active electrodes. Physiol. Meas. 33, 831–847. https://doi.org/10.1088/0967-3334/33/5/831

Gahwiler, B.H., Mamoon, A.M., Schlapfer, W.T., Tobias, C.A., 1972. Effects of temperature on spontaneous bioelectric activity of cultured nerve cells. Brain Res. 40, 527–533. https://doi.org/10.1016/0006-8993(72)90157-6

Gaines, J.L., Finn, K.E., Slopsema, J.P., Heyboer, L.A., Polasek, K.H., 2018. A model of motor and sensory axon activation in the median nerve using surface electrical stimulation. J Comput Neurosci 45, 29–43. https://doi.org/10.1007/s10827-018-0689-5

Geddes, L.A., Baker, L.E., n.d. The specific resistance of biological material—A compendium of data for the biomedical engineer and physiologist. Medical & Biological Engineering 5, 271–293.

Gholami-Boroujeny, S., Mekonnen, A., Batkin, I., Bolic, M., 2015. Theoretical Analysis of the Effect of Temperature on Current Delivery to the Brain During tDCS. Brain Stimul 8, 509–514. https://doi.org/10.1016/j.brs.2014.12.006

Gilad, O., Horesh, L., Holder, D.S., 2007. Design of electrodes and current limits for low frequency electrical impedance tomography of the brain. Med Bio Eng Comput 45, 621–633. https://doi.org/10.1007/s11517-007-0209-7

Golestanirad, L., Kirsch, J., Bonmassar, G., Downs, S., Elahi, B., Martin, A., Iacono, M.-I., Angelone, L.M., Keil, B., Wald, L.L., Pilitsis, J., 2019. RF-induced heating in tissue near bilateral DBS implants during MRI at 1.5 T and 3T: The role of surgical lead management. NeuroImage 184, 566–576. https://doi.org/10.1016/j.neuroimage.2018.09.034

Gomez, L.J., Goetz, S.M., Peterchev, A.V., 2018. Design of transcranial magnetic stimulation coils with optimal trade-off between depth, focality, and energy. J Neural Eng 15, 046033. https://doi.org/10.1088/1741-2552/aac967

Gomez-Tames, J., Sugiyama, Y., Laakso, I., Tanaka, S., Koyama, S., Sadato, N., Akimasa Hirata, 2016. Effect of microscopic modeling of skin in electrical and thermal analysis of transcranial direct current stimulation. Phys. Med. Biol. 61, 8825. https://doi.org/10.1088/1361-6560/61/24/8825

Graham, B.A., Brichta, A.M., Callister, R.J., 2008. Recording temperature affects the excitability of mouse superficial dorsal horn neurons, in vitro. J. Neurophysiol. 99, 2048–2059. https://doi.org/10.1152/jn.01176.2007

Graham, R.D., Bruns, T.M., Duan, B., Lempka, S.F., 2019a. Dorsal root ganglion stimulation for chronic pain modulates Aβ-fiber activity but not C-fiber activity: a computational modeling study. Clinical Neurophysiology. https://doi.org/10.1016/j.clinph.2019.02.016

Graham, R.D., Bruns, T.M., Duan, B., Lempka, S.F., 2019b. Dorsal root ganglion stimulation for chronic pain modulates Aβ-fiber activity but not C-fiber activity: A computational

modeling study. Clin Neurophysiol 130, 941–951. https://doi.org/10.1016/j.clinph.2019.02.016
Grant, P.F., Lowery, M.M., 2009. Electric field distribution in a finite-volume head model of deep brain stimulation. Medical Engineering & Physics 31, 1095–1103. https://doi.org/10.1016/j.medengphy.2009.07.006
Greinacher, R., Buhôt, L., Möller, L., Learmonth, G., 2018. The Time Course of Ineffective Sham Blinding During 1mA tDCS. bioRxiv 462424. https://doi.org/10.1101/462424
Greiner, N., Capogrosso, M., 2019. Anatomically Realistic Computational Model to Assess the Specificity of Epidural Electrical Stimulation of the Cervical Spinal Cord, in: Masia, L., Micera, S., Akay, M., Pons, J.L. (Eds.), Converging Clinical and Engineering Research on Neurorehabilitation III, Biosystems & Biorobotics. Springer International Publishing, pp. 44–48.
Grill, W.M., 2018. Temporal Pattern of Electrical Stimulation is a New Dimension of Therapeutic Innovation. Curr Opin Biomed Eng 8, 1–6. https://doi.org/10.1016/j.cobme.2018.08.007
Grill, W.M., Mortimer, J.T., 1994. Electrical properties of implant encapsulation tissue. Ann Biomed Eng 22, 23–33.
Grimnes, S., 1983. Dielectric breakdown of human skinin vivo. Med. Biol. Eng. Comput. 21, 379–381. https://doi.org/10.1007/BF02478510
Grimnes, S., Jabbari, A., Martinsen, Ø.G., Tronstad, C., 2011. Electrodermal activity by DC potential and AC conductance measured simultaneously at the same skin site. Skin Res Technol 17, 26–34. https://doi.org/10.1111/j.1600-0846.2010.00459.x
Grossman, P., Alekseichuk, I., Lara de, G., Paneri, K., Kunz, P., Turi, Z., Bikson, M., Paulus, W., Antal, A., 2018. transcranial Direct Current Stimulation Studies Open Database (tDCS-OD). bioRxiv. https://doi.org/10.1101/369215
Grychtol, B., Adler, A., 2013. FEM electrode refinement for electrical impedance tomography, in: 2013 35th Annual International Conference of the IEEE Engineering in Medicine and Biology Society (EMBC). Presented at the 2013 35th Annual International Conference of the IEEE Engineering in Medicine and Biology Society (EMBC), IEEE, Osaka, pp. 6429–6432. https://doi.org/10.1109/EMBC.2013.6611026
Guan, Y., Wacnik, P.W., Yang, F., Carteret, A.F., Chung, C.-Y., Meyer, R.A., Raja, S.N., 2010. Spinal Cord Stimulation-induced AnalgesiaElectrical Stimulation of Dorsal Column and Dorsal Roots Attenuates Dorsal Horn Neuronal Excitability in Neuropathic Rats. Anesthes 113, 1392–1405. https://doi.org/10.1097/ALN.0b013e3181fcd95c
Guarienti, F., Caumo, W., Shiozawa, P., Cordeiro, Q., Boggio, P.S., Benseñor, I.M., Lotufo, P.A., Bikson, M., Brunoni, A.R., 2015. Reducing transcranial direct current stimulation-induced erythema with skin pretreatment: considerations for sham-controlled clinical trials. Neuromodulation 18, 261–265. https://doi.org/10.1111/ner.12230
Guarienti, F., Caumo, W., Shiozawa, P., Cordeiro, Q., Boggio, P.S., Benseñor, I.M., Lotufo, P.A., Bikson, M., Brunoni, A.R., 2014. Reducing Transcranial Direct Current Stimulation-Induced Erythema With Skin Pretreatment: Considerations for Sham-Controlled Clinical Trials. Neuromodulation : journal of the International Neuromodulation Society. https://doi.org/10.1111/ner.12230
Guleyupoglu, B., Febles, N., Minhas, P., Hahn, C., Bikson, M., 2014. Reduced discomfort during high-definition transcutaneous stimulation using 6% benzocaine. Frontiers in neuroengineering 7, 28. https://doi.org/10.3389/fneng.2014.00028

Gustafsson, B., Jankowska, E., 1976. Direct and indirect activation of nerve cells by electrical pulses applied extracellularly. J. Physiol. (Lond.) 258, 33–61. https://doi.org/10.1113/jphysiol.1976.sp011405
Hahn, C., Rice, J., Macuff, S., Minhas, P., Rahman, A., Bikson, M., 2013. Methods for extra-low voltage transcranial direct current stimulation: current and time dependent impedance decreases. Clin Neurophysiol 124, 551–556. https://doi.org/10.1016/j.clinph.2012.07.028
Harmsen, I.E., Lee, D.J., Dallapiazza, R.F., De Vloo, P., Chen, R., Fasano, A., Kalia, S.K., Hodaie, M., Lozano, A.M., 2019. Ultra-high-frequency deep brain stimulation at 10,000 Hz improves motor function. Mov. Disord. 34, 146–148. https://doi.org/10.1002/mds.27550
Harris, A.B., Erickson, L., Kendig, J.H., Mingrino, S., Goldring, S., 1962a. Observations on selective brain heating in dogs. J. Neurosurg. 19, 514–521. https://doi.org/10.3171/jns.1962.19.6.0514
Harris, A.B., Erickson, L., Kendig, J.H., Mingrino, S., Goldring, S., 1962b. Observations on selective brain heating in dogs. J. Neurosurg. 19, 514–521. https://doi.org/10.3171/jns.1962.19.6.0514
Health, C. for D. and R., 2019. Assessment of Radiofrequency-Induced Heating in the Magnetic Resonance (MR) Environment for Multi-Configuration Passive Medical Devices [WWW Document]. U.S. Food and Drug Administration. URL http://www.fda.gov/regulatory-information/search-fda-guidance-documents/assessment-radiofrequency-induced-heating-magnetic-resonance-mr-environment-multi-configuration (accessed 12.17.19).
Hemm, S., Mennessier, G., Vayssière, N., Cif, L., Coubes, P., 2005. Co-registration of stereotactic MRI and isofieldlines during deep brain stimulation. Brain Research Bulletin, Proceedings of the 14th and 15th Meetings of the European Network for CNS Transplantation and Repair (NECTAR) 68, 59–61. https://doi.org/10.1016/j.brainresbull.2005.08.024
Hentall, I.D., Zorman, G., Kansky, S., Fields, H.L., 1984. Relations among threshold, spike height, electrode distance, and conduction velocity in electrical stimulation of certain medullospinal neurons. J. Neurophysiol. 51, 968–977. https://doi.org/10.1152/jn.1984.51.5.968
Hernández-Labrado, G.R., Polo, J.L., López-Dolado, E., Collazos-Castro, J.E., 2011. Spinal cord direct current stimulation: finite element analysis of the electric field and current density. Med Biol Eng Comput 49, 417–429. https://doi.org/10.1007/s11517-011-0756-9
Hill, A.T., Rogasch, N.C., Fitzgerald, P.B., Hoy, K.E., 2018. Effects of single versus dual-site High-Definition transcranial direct current stimulation (HD-tDCS) on cortical reactivity and working memory performance in healthy subjects. Brain Stimul 11, 1033–1043. https://doi.org/10.1016/j.brs.2018.06.005
Hines, M.L., Carnevale, N.T., 1997. The NEURON Simulation Environment. Neural Computation 9, 1179–1209. https://doi.org/10.1162/neco.1997.9.6.1179
Hodson, D.A., Barbenel, J.C., Eason, G., 1989a. Modelling transient heat transfer through the skin and a contact material. Phys. Med. Biol. 34, 1493. https://doi.org/10.1088/0031-9155/34/10/011
Hodson, D.A., Barbenel, J.C., Eason, G., 1989b. Modelling transient heat transfer through the skin and a contact material. Phys Med Biol 34, 1493–1507.

Holsheimer, J., 2002a. Which Neuronal Elements are Activated Directly by Spinal Cord Stimulation. Neuromodulation: Technology at the Neural Interface 5, 25–31. https://doi.org/10.1046/j.1525-1403.2002._2005.x
Holsheimer, J., 2002b. Which Neuronal Elements are Activated Directly by Spinal Cord Stimulation. Neuromodulation 5, 25–31. https://doi.org/10.1046/j.1525-1403.2002._2005.x
Holsheimer, J., 1998. Computer modelling of spinal cord stimulation and its contribution to therapeutic efficacy. Spinal Cord 36, 531–540.
Holsheimer, J., Barolat, G., Struijk, J.J., He, J., 1995. Significance of the Spinal Cord Position in Spinal Cord Stimulation, in: Advances in Stereotactic and Functional Neurosurgery 11, Acta Neurochirurgica Supplementum. Springer, Vienna, pp. 119–124. https://doi.org/10.1007/978-3-7091-9419-5_26
Holsheimer, J., Struijk, J.J., 1991. How do geometric factors influence epidural spinal cord stimulation? A quantitative analysis by computer modeling. Stereotact Funct Neurosurg 56, 234–249. https://doi.org/10.1159/000099410
Holsheimer, J., Wesselink, W.A., 1997. Optimum electrode geometry for spinal cord stimulation: The narrow bipole and tripole. Med. Biol. Eng. Comput. 35, 493–497. https://doi.org/10.1007/BF02525529
Horn, A., Reich, M., Vorwerk, J., Li, N., Wenzel, G., Fang, Q., Schmitz-Hübsch, T., Nickl, R., Kupsch, A., Volkmann, J., Kühn, A.A., Fox, M.D., 2017. Connectivity Predicts deep brain stimulation outcome in Parkinson disease. Annals of Neurology 82, 67–78. https://doi.org/10.1002/ana.24974
Howell, B., Choi, K.S., Gunalan, K., Rajendra, J., Mayberg, H.S., McIntyre, C.C., 2019. Quantifying the axonal pathways directly stimulated in therapeutic subcallosal cingulate deep brain stimulation. Hum Brain Mapp 40, 889–903. https://doi.org/10.1002/hbm.24419
Howell, B., Lad, S.P., Grill, W.M., 2014. Evaluation of Intradural Stimulation Efficiency and Selectivity in a Computational Model of Spinal Cord Stimulation. PLOS ONE 9, e114938. https://doi.org/10.1371/journal.pone.0114938
Howells, J., Trevillion, L., Bostock, H., Burke, D., 2012. The voltage dependence of Ih in human myelinated axons. J Physiol 590, 1625–1640. https://doi.org/10.1113/jphysiol.2011.225573
Hsieh, T.-H., Dhamne, S.C., Chen, J.-J.J., Carpenter, L.L., Anastasio, E.M., Pascual-Leone, A., Rotenberg, A., 2012. Minimal heating of aneurysm clips during repetitive transcranial magnetic stimulation. Clin Neurophysiol 123, 1471–1473. https://doi.org/10.1016/j.clinph.2011.10.048
Hua, P., Woo, E.J., Webster, J.G., Tompkins, W.J., 1993. Finite element modeling of electrode-skin contact impedance in electrical impedance tomography. IEEE Transactions on Biomedical Engineering 40, 335–343. https://doi.org/10.1109/10.222326
Huang, Q., Oya, H., Flouty, O.E., Reddy, C.G., Howard, M.A., Gillies, G.T., Utz, M., 2014. Comparison of spinal cord stimulation profiles from intra- and extradural electrode arrangements by finite element modelling. Med Biol Eng Comput 52, 531–538. https://doi.org/10.1007/s11517-014-1157-7
Hurlbert, R.J., Tator, C.H., 1994. Characterization of longitudinal field gradients from electrical stimulation in the normal and injured rodent spinal cord. Neurosurgery 34, 471–482; discussion 482-483. https://doi.org/10.1227/00006123-199403000-00013

Hussain, A.A., Themstrup, L., Mogensen, M., Jemec, G.B.E., 2017. Optical Coherence Tomography Imaging of the Skin, in: Humbert, P., Fanian, F., Maibach, H.I., Agache, P. (Eds.), Agache's Measuring the Skin: Non-Invasive Investigations, Physiology, Normal Constants. Springer International Publishing, Cham, pp. 493–502. https://doi.org/10.1007/978-3-319-32383-1_53

Idlett, S.L., Halder, M., Zhang, T., Quevedo, J.N., Brill, N., Gu, W., Moffitt, M.A., Hochman, S., 2019. Assessment of axonal recruitment using model-guided preclinical spinal cord stimulation in the ex vivo adult mouse spinal cord. J. Neurophysiol. https://doi.org/10.1152/jn.00538.2018

IT'IS Foundation, 2015. Tissue Properties Database V3.0. https://doi.org/10.13099/VIP21000-03-0

Jackson, M.P., Bikson, M., Liebetanz, D., Nitsche, M., 2017. How to consider animal data in tDCS safety standards. Brain Stimul 10, 1141–1142. https://doi.org/10.1016/j.brs.2017.08.004

Jackson, M.P., Rahman, A., Lafon, B., Kronberg, G., Ling, D., Parra, L.C., Bikson, M., 2016. Animal models of transcranial direct current stimulation: Methods and mechanisms. Clin Neurophysiol 127, 3425–3454. https://doi.org/10.1016/j.clinph.2016.08.016

Jankowska, E., Roberts, W.J., 1972. An electrophysiological demonstration of the axonal projections of single spinal interneurones in the cat. J Physiol 222, 597–622.

Jensen, M.P., Brownstone, R.M., 2019. Mechanisms of spinal cord stimulation for the treatment of pain: Still in the dark after 50 years. Eur J Pain 23, 652–659. https://doi.org/10.1002/ejp.1336

Joucla, S., Branchereau, P., Cattaert, D., Yvert, B., 2012. Extracellular neural microstimulation may activate much larger regions than expected by simulations: a combined experimental and modeling study. PLoS ONE 7, e41324. https://doi.org/10.1371/journal.pone.0041324

Joucla, S., Yvert, B., 2009. The "mirror" estimate: an intuitive predictor of membrane polarization during extracellular stimulation. Biophys. J. 96, 3495–3508. https://doi.org/10.1016/j.bpj.2008.12.3961

Kainz, W., Neubauer, G., Überbacher, R., Alesch, F., Chan, D.D., 2002. Temperature measurement on neurological pulse generators during MR scans. Biomed Eng Online 1, 2. https://doi.org/10.1186/1475-925X-1-2

Kalia, Y.N., Guy, R.H., 1995. The Electrical Characteristics of Human Skin in Vivo. Pharm Res 12, 1605–1613. https://doi.org/10.1023/A:1016228730522

Kameyama, T., Hashizume, Y., Sobue, G., 1996a. Morphologic features of the normal human cadaveric spinal cord. Spine 21, 1285–1290.

Kameyama, T., Hashizume, Y., Sobue, G., 1996b. Morphologic features of the normal human cadaveric spinal cord. Spine 21, 1285–1290.

Kappenman, E.S., Luck, S., 2010. The effects of electrode impedance on data quality and statistical significance in ERP recordings - Kappenman - 2010 - Psychophysiology - Wiley Online Library [WWW Document]. URL https://onlinelibrary.wiley.com/doi/epdf/10.1111/j.1469-8986.2010.01009.x (accessed 3.9.20).

Kapural, L., Yu, C., Doust, M.W., Gliner, B.E., Vallejo, R., Sitzman, B.T., Amirdelfan, K., Morgan, D.M., Yearwood, T.L., Bundschu, R., Yang, T., Benyamin, R., Burgher, A.H., 2016. Comparison of 10-kHz High-Frequency and Traditional Low-Frequency Spinal Cord Stimulation for the Treatment of Chronic Back and Leg Pain: 24-Month Results

From a Multicenter, Randomized, Controlled Pivotal Trial. Neurosurgery 79, 667–677. https://doi.org/10.1227/NEU.0000000000001418
Kempe, R., Huang, Y., Parra, L.C., 2014. Simulating pad-electrodes with high-definition arrays in transcranial electric stimulation. J Neural Eng 11, 026003. https://doi.org/10.1088/1741-2560/11/2/026003
Kent, A.R., Min, X., Hogan, Q.H., Kramer, J.M., 2018. Mechanisms of Dorsal Root Ganglion Stimulation in Pain Suppression: A Computational Modeling Analysis. Neuromodulation: Technology at the Neural Interface 21, 234–246. https://doi.org/10.1111/ner.12754
Kent, A.R., Min, X., Rosenberg, S.P., Fayram, T.A., 2014. Computational modeling analysis of a spinal cord stimulation paddle lead reveals broad, gapless dermatomal coverage, in: 2014 36th Annual International Conference of the IEEE Engineering in Medicine and Biology Society. Presented at the 2014 36th Annual International Conference of the IEEE Engineering in Medicine and Biology Society, pp. 6254–6257. https://doi.org/10.1109/EMBC.2014.6945058
Kessler, S.K., Minhas, P., Woods, A.J., Rosen, A., Gorman, C., Bikson, M., 2013. Dosage Considerations for Transcranial Direct Current Stimulation in Children: A Computational Modeling Study. PLOS ONE 8, e76112. https://doi.org/10.1371/journal.pone.0076112
Kessler, S.K., Turkeltaub, P.E., Benson, J.G., Hamilton, R.H., 2012. Differences in the experience of active and sham transcranial direct current stimulation. Brain Stimul 5, 155–162. https://doi.org/10.1016/j.brs.2011.02.007
Khadka, N., Bikson, M., 2019. Response to the Letter to the Editor by Caraway et al. on "Tissue Temperature Increases by a 10 kHz Spinal Cord Stimulation System: Phantom and Bioheat Model." Neuromodulation: Technology at the Neural Interface 22, 988–988. https://doi.org/10.1111/ner.13079
Khadka, Niranjan, Borges, H., Kauffman, T., Pascal, A., Paneri, B., Nassis, E., Shin, Y., Choi, H., Kim, S., Lee, K., Bikson, M., 2019a. Abstract #109: Tolerability of an Adaptive-tDCS upto 4 mA using subject assessment and machine-learning to optimize dose. Brain Stimulation: Basic, Translational, and Clinical Research in Neuromodulation 12, e37–e38. https://doi.org/10.1016/j.brs.2018.12.116
Khadka, Niranjan, Borges, H., Paneri, B., Kaufman, T., Nassis, E., Zannou, A.L., Shin, Y., Choi, H., Kim, S., Lee, K., Bikson, M., 2019b. Adaptive current tDCS up to 4 mA. Brain Stimulation. https://doi.org/10.1016/j.brs.2019.07.027
Khadka, N., Borges, H., Zannou, A.L., Jang, J., Kim, B., Lee, K., Bikson, M., 2018a. Dry tDCS: Tolerability of a novel multilayer hydrogel composite non-adhesive electrode for transcranial direct current stimulation. Brain Stimul 11, 1044–1053. https://doi.org/10.1016/j.brs.2018.07.049
Khadka, N., Harmsen, I.E., Lozano, A.M., Bikson, M., n.d. Bio-Heat Model of Kilohertz-Frequency Deep Brain Stimulation Increases Brain Tissue Temperature. Neuromodulation: Technology at the Neural Interface n/a. https://doi.org/10.1111/ner.13120
Khadka, N., Liu, X., Zander, H., Swami, J., Rogers, E., Lempka, S., Bikson, M., 2020. Realistic anatomically detailed open-source spinal cord stimulation (RADO-SCS) model. J. Neural Eng. https://doi.org/10.1088/1741-2552/ab8344

Khadka, N., Rahman, A., Sarantos, C., Truong, D.Q., Bikson, M., 2015a. Methods for Specific Electrode Resistance Measurement During Transcranial Direct Current Stimulation. Brain Stimulation 8, 150–159. https://doi.org/10.1016/j.brs.2014.10.004

Khadka, N., Seibt, O., Patel, V., Thomas, C., Mokrejs, A., Guleyupoglu, B., Truong, D.Q., Bikson, M., 2017. Factors Influencing Current Flow Through the Skin during Transcranial Electrical Stimulation: Role of Waveform, Tissue Properties, and Macro-Pores. Brain Stimulation: Basic, Translational, and Clinical Research in Neuromodulation 10, e16. https://doi.org/10.1016/j.brs.2016.11.071

Khadka, N., Truong, D.Q., Bikson, M., 2015b. Principles of Within Electrode Current Steering. J. Med. Devices 9, 020947-020947–2. https://doi.org/10.1115/1.4030126

Khadka, Niranjan, Truong, D.Q., Williams, P., Martin, J.H., Bikson, M., 2019c. The Quasi-uniform assumption for Spinal Cord Stimulation translational research. Journal of Neuroscience Methods 328, 108446. https://doi.org/10.1016/j.jneumeth.2019.108446

Khadka, Niranjan, Woods, A.J., Bikson, M., 2019d. Transcranial Direct Current Stimulation Electrodes, in: Knotkova, H., Nitsche, M.A., Bikson, M., Woods, A.J. (Eds.), Practical Guide to Transcranial Direct Current Stimulation: Principles, Procedures and Applications. Springer International Publishing, Cham, pp. 263–291. https://doi.org/10.1007/978-3-319-95948-1_10

Khadka, N., Zannou, A., Truong, D., Zhang, T., Esteller, R., Hersey, B., Bikson, M., 2019. Generation 2 kilohertz spinal cord stimulation (kHz-SCS) bioheat multi-physics model. Brain Stimulation: Basic, Translational, and Clinical Research in Neuromodulation 12, 566. https://doi.org/10.1016/j.brs.2018.12.876

Khadka, N., Zannou, A.L., Zunara, F., Truong, D.Q., Dmochowski, J., Bikson, M., 2018b. Minimal Heating at the Skin Surface During Transcranial Direct Current Stimulation. Neuromodulation: Technology at the Neural Interface 21, 334–339. https://doi.org/10.1111/ner.12554

Khadka, N., Zannou, A.L., Zunara, F., Truong, D.Q., Dmochowski, J., Bikson, M., 2018c. Minimal Heating at the Skin Surface During Transcranial Direct Current Stimulation. Neuromodulation 21, 334–339. https://doi.org/10.1111/ner.12554

Khan, S., Borsic, A., Manwaring, P., Hartov, A., Halter, R., 2013. FPGA Based High Speed Data Acquisition System for Electrical Impedance Tomography. J Phys Conf Ser 434, 012081. https://doi.org/10.1088/1742-6596/434/1/012081

Khanam, P.N., Ponnamma, D., AL-Madeed, M.A., 2015. Electrical Properties of Graphene Polymer Nanocomposites, in: Sadasivuni, K.K., Ponnamma, D., Kim, J., Thomas, S. (Eds.), Graphene-Based Polymer Nanocomposites in Electronics, Springer Series on Polymer and Composite Materials. Springer International Publishing, pp. 25–47. https://doi.org/10.1007/978-3-319-13875-6_2

Kim, D., Jeong, J., Jeong, S., Kim, S., Jun, S.C., Chung, E., 2015. Validation of Computational Studies for Electrical Brain Stimulation With Phantom Head Experiments. Brain Stimul 8, 914–925. https://doi.org/10.1016/j.brs.2015.06.009

Kim, J.A., Connors, B.W., 2012a. High temperatures alter physiological properties of pyramidal cells and inhibitory interneurons in hippocampus. Front Cell Neurosci 6, 27. https://doi.org/10.3389/fncel.2012.00027

Kim, J.A., Connors, B.W., 2012b. High temperatures alter physiological properties of pyramidal cells and inhibitory interneurons in hippocampus. Front Cell Neurosci 6, 27. https://doi.org/10.3389/fncel.2012.00027

Kim, S., Tathireddy, P., Normann, R.A., Solzbacher, F., 2007. In vitro and in vivo study of temperature increases in the brain due to a neural implant, in: 2007 3rd International IEEE/EMBS Conference on Neural Engineering. Presented at the 2007 3rd International IEEE/EMBS Conference on Neural Engineering, pp. 163–166. https://doi.org/10.1109/CNE.2007.369637

Kinfe, T.M., Pintea, B., Link, C., Roeske, S., Güresir, E., Güresir, Á., Vatter, H., 2016. High Frequency (10 kHz) or Burst Spinal Cord Stimulation in Failed Back Surgery Syndrome Patients With Predominant Back Pain: Preliminary Data From a Prospective Observational Study. Neuromodulation: Technology at the Neural Interface 19, 268–275. https://doi.org/10.1111/ner.12379

Kiyatkin, E.A., Brown, P.L., Wise, R.A., 2002. Brain temperature fluctuation: a reflection of functional neural activation. Eur. J. Neurosci. 16, 164–168. https://doi.org/10.1046/j.1460-9568.2002.02066.x

Kiyatkin, E.A., Sharma, H.S., 2009. Permeability of the blood-brain barrier depends on brain temperature. Neuroscience 161, 926–939. https://doi.org/10.1016/j.neuroscience.2009.04.004

Knotkova, H., Riggs, A., Berisha, D., Borges, H., Bernstein, H., Patel, V., Truong, D.Q., Unal, G., Arce, D., Datta, A., Bikson, M., 2019. Automatic M1-SO Montage Headgear for Transcranial Direct Current Stimulation (TDCS) Suitable for Home and High-Throughput In-Clinic Applications. Neuromodulation 22, 904–910. https://doi.org/10.1111/ner.12786

Kolarsick, P.A.J., Kolarsick, M.A., Goodwin, C., 2011. Anatomy and Physiology of the Skin. Journal of the Dermatology Nurses' Association 3, 203. https://doi.org/10.1097/JDN.0b013e3182274a98

Koyama, S., Xia, J., Leblanc, B.W., Gu, J.W., Saab, C.Y., 2018. Sub-paresthesia spinal cord stimulation reverses thermal hyperalgesia and modulates low frequency EEG in a rat model of neuropathic pain. Scientific Reports 8, 7181. https://doi.org/10.1038/s41598-018-25420-w

Krasteva, V.T., Papazov, S.P., 2002. Estimation of current density distribution under electrodes for external defibrillation. Biomed Eng Online 1, 7. https://doi.org/10.1186/1475-925X-1-7

Krause, M.R., Zanos, T.P., Csorba, B.A., Pilly, P.K., Choe, J., Phillips, M.E., Datta, A., Pack, C.C., 2017. Transcranial Direct Current Stimulation Facilitates Associative Learning and Alters Functional Connectivity in the Primate Brain. Curr. Biol. 27, 3086-3096.e3. https://doi.org/10.1016/j.cub.2017.09.020

Kronberg, G., Bikson, M., 2012. Electrode assembly design for transcranial Direct Current Stimulation: a FEM modeling study. Conf Proc IEEE Eng Med Biol Soc 2012, 891–895. https://doi.org/10.1109/EMBC.2012.6346075

Kronberg, G., Bridi, M., Abel, T., Bikson, M., Parra, L.C., 2017. Direct Current Stimulation Modulates LTP and LTD: Activity Dependence and Dendritic Effects. Brain Stimul 10, 51–58. https://doi.org/10.1016/j.brs.2016.10.001

Kubin, L., Davies, R.O., 1988. Sites of termination and relay of pulmonary rapidly adapting receptors as studied by spike-triggered averaging. Brain Res. 443, 215–221.

Labonte, S., 1994. Numerical model for radio-frequency ablation of the endocardium and its experimental validation. IEEE Transactions on Biomedical Engineering 41, 108–115. https://doi.org/10.1109/10.284921

Ladenbauer, J., Minassian, K., Hofstoetter, U.S., Dimitrijevic, M.R., Rattay, F., 2010. Stimulation of the human lumbar spinal cord with implanted and surface electrodes: a computer simulation study. IEEE Trans Neural Syst Rehabil Eng 18, 637–645. https://doi.org/10.1109/TNSRE.2010.2054112

Lagopoulos, J., Degabriele, R., 2008. Feeling the heat: the electrode–skin interface during DCS. Acta Neuropsychiatrica 20, 98–100. https://doi.org/10.1111/j.1601-5215.2008.00274.x

Laird, J.H., Parker, J.L., 2013. A model of evoked potentials in spinal cord stimulation, in: 2013 35th Annual International Conference of the IEEE Engineering in Medicine and Biology Society (EMBC). Presented at the 2013 35th Annual International Conference of the IEEE Engineering in Medicine and Biology Society (EMBC), pp. 6555–6558. https://doi.org/10.1109/EMBC.2013.6611057

LaManna, J.C., Rosenthal, M., Novack, R., Moffett, D.F., Jöbsis, F.F., 1980a. Temperature coefficients for the oxidative metabolic responses to electrical stimulation in cerebral cortex. J. Neurochem. 34, 203–209. https://doi.org/10.1111/j.1471-4159.1980.tb04641.x

LaManna, J.C., Rosenthal, M., Novack, R., Moffett, D.F., Jöbsis, F.F., 1980b. Temperature coefficients for the oxidative metabolic responses to electrical stimulation in cerebral cortex. J. Neurochem. 34, 203–209.

Lawson, J.J., McIlwrath, S.L., Woodbury, C.J., Davis, B.M., Koerber, H.R., 2008. TRPV1 Unlike TRPV2 Is Restricted to a Subset of Mechanically Insensitive Cutaneous Nociceptors Responding to Heat. The Journal of Pain 9, 298–308. https://doi.org/10.1016/j.jpain.2007.12.001

Lee, D., Hershey, B., Bradley, K., Yearwood, T., 2011. Predicted effects of pulse width programming in spinal cord stimulation: a mathematical modeling study. Med Biol Eng Comput 49, 765. https://doi.org/10.1007/s11517-011-0780-9

Lee, W.H., Lisanby, S.H., Laine, A.F., Peterchev, A.V., 2016. Comparison of electric field strength and spatial distribution of electroconvulsive therapy and magnetic seizure therapy in a realistic human head model. Eur Psychiatry 36, 55–64. https://doi.org/10.1016/j.eurpsy.2016.03.003

Leite, J., Gonçalves, Ó.F., Pereira, P., Khadka, N., Bikson, M., Fregni, F., Carvalho, S., 2018. The differential effects of unihemispheric and bihemispheric tDCS over the inferior frontal gyrus on proactive control. Neurosci Res 130, 39–46. https://doi.org/10.1016/j.neures.2017.08.005

Lempka, S.F., Johnson, M.D., Miocinovic, S., Vitek, J.L., McIntyre, C.C., 2010. Current-controlled deep brain stimulation reduces in vivo voltage fluctuations observed during voltage-controlled stimulation. Clin Neurophysiol 121, 2128–2133. https://doi.org/10.1016/j.clinph.2010.04.026

Lempka, S.F., McIntyre, C.C., Kilgore, K.L., Machado, A.G., 2015. Computational Analysis of Kilohertz Frequency Spinal Cord Stimulation for Chronic Pain Management. Anesthesiology 122, 1362–1376. https://doi.org/10.1097/ALN.0000000000000649

Lempka, S.F., Patil, P.G., 2018. Innovations in spinal cord stimulation for pain. Curr Opin Biomed Eng 8, 51–60. https://doi.org/10.1016/j.cobme.2018.10.005

Lempka, S.F., Zander, H., Anaya, C.J., Wyant, A., Ozinga, J.G., Machado, A.G., 2019a. Model-Based Analysis of Spinal Cord Stimulation for Chronic Pain, in: Masia, L., Micera, S., Akay, M., Pons, J.L. (Eds.), Converging Clinical and Engineering Research on Neurorehabilitation III, Biosystems & Biorobotics. Springer International Publishing, pp. 39–43.

Lempka, S.F., Zander, H.J., Anaya, C.J., Wyant, A., Ozinga, J.G., Machado, A.G., 2019b. Patient-Specific Analysis of Neural Activation During Spinal Cord Stimulation for Pain. Neuromodulation. https://doi.org/10.1111/ner.13037

Lempka, S.F., Zander, H.J., Anaya, C.J., Wyant, A., Ozinga, J.G., Machado, A.G., 2019c. Patient-Specific Analysis of Neural Activation During Spinal Cord Stimulation for Pain. Neuromodulation. https://doi.org/10.1111/ner.13037

Lesperance, L.S., Lankarany, M., Zhang, T.C., Esteller, R., Ratté, S., Prescott, S.A., 2018. Artifactual hyperpolarization during extracellular electrical stimulation: Proposed mechanism of high-rate neuromodulation disproved. Brain Stimul 11, 582–591. https://doi.org/10.1016/j.brs.2017.12.004

Lim, H., Lee, H., Noh, K., Lee, S.J., 2017. IKK/NF-κB-dependent satellite glia activation induces spinal cord microglia activation and neuropathic pain after nerve injury. Pain 158, 1666–1677. https://doi.org/10.1097/j.pain.0000000000000959

Linderoth, B., Foreman, R.D., 1999. Physiology of Spinal Cord Stimulation: Review and Update. Neuromudulation: Technology at the Neural Interface 2, 150–164. https://doi.org/10.1046/j.1525-1403.1999.00150.x

Litvak, L.M., Smith, Z.M., Delgutte, B., Eddington, D.K., 2003. Desynchronization of electrically evoked auditory-nerve activity by high-frequency pulse trains of long duration. J Acoust Soc Am 114, 2066–2078. https://doi.org/10.1121/1.1612492

Liu, A., Vöröslakos, M., Kronberg, G., Henin, S., Krause, M.R., Huang, Y., Opitz, A., Mehta, A., Pack, C.C., Krekelberg, B., Berényi, A., Parra, L.C., Melloni, L., Devinsky, O., Buzsáki, G., 2018. Immediate neurophysiological effects of transcranial electrical stimulation. Nat Commun 9, 5092. https://doi.org/10.1038/s41467-018-07233-7

Loo, C.K., Husain, M.M., McDonald, W.M., Aaronson, S., O'Reardon, J.P., Alonzo, A., Weickert, C.S., Martin, D.M., McClintock, S.M., Mohan, A., Lisanby, S.H., International Consortium of Research in tDCS (ICRT), 2018. International randomized-controlled trial of transcranial Direct Current Stimulation in depression. Brain Stimul 11, 125–133. https://doi.org/10.1016/j.brs.2017.10.011

Lopez-Quintero, S.V., Datta, A., Amaya, R., Elwassif, M., Bikson, M., Tarbell, J.M., 2010. DBS-relevant electric fields increase hydraulic conductivity of in vitro endothelial monolayers. J Neural Eng 7, 16005. https://doi.org/10.1088/1741-2560/7/1/016005

Lozano, A.M., Lipsman, N., Bergman, H., Brown, P., Chabardes, S., Chang, J.W., Matthews, K., McIntyre, C.C., Schlaepfer, T.E., Schulder, M., Temel, Y., Volkmann, J., Krauss, J.K., 2019. Deep brain stimulation: current challenges and future directions. Nat Rev Neurol 15, 148–160. https://doi.org/10.1038/s41582-018-0128-2

Luna, J.L.V., Krenn, M., Ramírez, J.A.C., Mayr, W., 2015. Dynamic Impedance Model of the Skin-Electrode Interface for Transcutaneous Electrical Stimulation. PLOS ONE 10, e0125609. https://doi.org/10.1371/journal.pone.0125609

Lykken, D.T., 1970. Square-Wave Analysis of Skin Impedance. Psychophysiology 7, 262–275. https://doi.org/10.1111/j.1469-8986.1970.tb02232.x

Mandel, Y., Manivanh, R., Dalal, R., Huie, P., Wang, J., Brinton, M., Palanker, D., 2013. Vasoconstriction by Electrical Stimulation: New Approach to Control of Non-Compressible Hemorrhage. Sci Rep 3. https://doi.org/10.1038/srep02111

Manola, L., Holsheimer, J., 2004. Technical Performance of Percutaneous and Laminectomy Leads Analyzed by Modeling. Neuromodulation: Technology at the Neural Interface 7, 231–241. https://doi.org/10.1111/j.1094-7159.2004.04207.x

Manola, L., Holsheimer, J., Veltink, P.H., Bradley, K., Peterson, D., 2007. Theoretical Investigation Into Longitudinal Cathodal Field Steering in Spinal Cord Stimulation. Neuromodulation: Technology at the Neural Interface 10, 120–132. https://doi.org/10.1111/j.1525-1403.2007.00100.x

Marcus, S., Zarzecki, P., Asanuma, H., 1979. An estimate of effective spread of stimulating current. Exp Brain Res 34, 68–72.

Martinsen, O.G., Grimnes, S., Sveen, O., 1997. Dielectric properties of some keratinised tissues. Part 1: Stratum corneum and nail in situ. Med Biol Eng Comput 35, 172–176.

Mason, J.L., MacKay, N.A.M., 1976. Pain Sensations Associated with Electrocutaneous Stimulation. IEEE Transactions on Biomedical Engineering BME-23, 405–409. https://doi.org/10.1109/TBME.1976.324652

Masuda, H., Hirata, A., Kawai, H., Wake, K., Watanabe, S., Arima, T., Poulletier de Gannes, F., Lagroye, I., Veyret, B., 2011. Local exposure of the rat cortex to radiofrequency electromagnetic fields increases local cerebral blood flow along with temperature. J. Appl. Physiol. 110, 142–148. https://doi.org/10.1152/japplphysiol.01035.2010

Matsumi, N., Matsumoto, K., Mishima, N., Moriyama, E., Furuta, T., Nishimoto, A., Taguchi, K., 1994a. Thermal damage threshold of brain tissue--histological study of heated normal monkey brains. Neurol. Med. Chir. (Tokyo) 34, 209–215.

Matsumi, N., Matsumoto, K., Mishima, N., Moriyama, E., Furuta, T., Nishimoto, A., Taguchi, K., 1994b. Thermal damage threshold of brain tissue--histological study of heated normal monkey brains. Neurol. Med. Chir. (Tokyo) 34, 209–215. https://doi.org/10.2176/nmc.34.209

Matsumoto, H., Ugawa, Y., 2017. Adverse events of tDCS and tACS: A review. Clin Neurophysiol Pract 2, 19–25. https://doi.org/10.1016/j.cnp.2016.12.003

McFadden, J.L., Borckardt, J.J., George, M.S., Beam, W., 2011. Reducing Procedural Pain and Discomfort Associated with Transcranial Direct Current Stimulation. Brain Stimul 4, 38–42. https://doi.org/10.1016/j.brs.2010.05.002

McIntyre, C.C., Chaturvedi, A., Shamir, R.R., Lempka, S.F., 2015. Engineering the Next Generation of Clinical Deep Brain Stimulation Technology. Brain Stimulation 8, 21–26. https://doi.org/10.1016/j.brs.2014.07.039

McIntyre, C.C., Grill, W.M., 2002. Extracellular stimulation of central neurons: influence of stimulus waveform and frequency on neuronal output. J. Neurophysiol. 88, 1592–1604. https://doi.org/10.1152/jn.2002.88.4.1592

McIntyre, C.C., Grill, W.M., 1999. Excitation of central nervous system neurons by nonuniform electric fields. Biophys. J. 76, 878–888. https://doi.org/10.1016/S0006-3495(99)77251-6

McIntyre, C.C., Grill, W.M., 1998. Sensitivity analysis of a model of mammalian neural membrane. Biol Cybern 79, 29–37. https://doi.org/10.1007/s004220050455

McIntyre, C.C., Savasta, M., Kerkerian-Le Goff, L., Vitek, J.L., 2004a. Uncovering the mechanism(s) of action of deep brain stimulation: activation, inhibition, or both. Clin Neurophysiol 115, 1239–1248. https://doi.org/10.1016/j.clinph.2003.12.024

McIntyre, C.C., Savasta, M., Walter, B.L., Vitek, J.L., 2004b. How does deep brain stimulation work? Present understanding and future questions. J Clin Neurophysiol 21, 40–50. https://doi.org/10.1097/00004691-200401000-00006

McIntyre, C.C., Thakor, N.V., 2002. Uncovering the mechanisms of deep brain stimulation for Parkinson's disease through functional imaging, neural recording, and neural modeling. Crit Rev Biomed Eng 30, 249–281. https://doi.org/10.1615/critrevbiomedeng.v30.i456.20

McNeal, D.R., 1976. Analysis of a model for excitation of myelinated nerve. IEEE Trans Biomed Eng 23, 329–337.
Merrill, D.R., Bikson, M., Jefferys, J.G.R., 2005. Electrical stimulation of excitable tissue: design of efficacious and safe protocols. Journal of Neuroscience Methods 141, 171–198. https://doi.org/10.1016/j.jneumeth.2004.10.020
Meuwissen, K.P.V., Gu, J.W., Zhang, T.C., Joosten, E.A.J., 2018. Conventional-SCS vs. Burst-SCS and the Behavioral Effect on Mechanical Hypersensitivity in a Rat Model of Chronic Neuropathic Pain: Effect of Amplitude. Neuromodulation: Technology at the Neural Interface 21, 19–30. https://doi.org/10.1111/ner.12731
Michael, A.C., Borland, L.M. (Eds.), 2007. Electrochemical Methods for Neuroscience, Frontiers in Neuroengineering. CRC Press/Taylor & Francis, Boca Raton (FL).
Miller, J.P., Eldabe, S., Buchser, E., Johanek, L.M., Guan, Y., Linderoth, B., 2016. Parameters of Spinal Cord Stimulation and Their Role in Electrical Charge Delivery: A Review. Neuromodulation 19, 373–384. https://doi.org/10.1111/ner.12438
Min, X., Kent, A.R., Rosenberg, S.P., Fayram, T.A., 2014. Modeling dermatome selectivity of single-and multiple-current source spinal cord stimulation systems. Conf Proc IEEE Eng Med Biol Soc 2014, 6246–6249. https://doi.org/10.1109/EMBC.2014.6945056
Minhas, P., Bansal, V., Patel, J., Ho, J.S., Diaz, J., Datta, A., Bikson, M., 2010. Electrodes for high-definition transcutaneous DC stimulation for applications in drug-delivery and electrotherapy, including tDCS. J Neurosci Methods 190, 188–197. https://doi.org/10.1016/j.jneumeth.2010.05.007
Minhas, P., Datta, A., Bikson, M., 2011. Cutaneous perception during tDCS: Role of electrode shape and sponge salinity. Clin Neurophysiol 122, 637–638. https://doi.org/10.1016/j.clinph.2010.09.023
Miranda, P.C., Correia, L., Salvador, R., Basser, P.J., 2007. Tissue heterogeneity as a mechanism for localized neural stimulation by applied electric fields. Phys Med Biol 52, 5603–5617. https://doi.org/10.1088/0031-9155/52/18/009
Miranda, P.C., Faria, P., Hallett, M., 2009. What does the ratio of injected current to electrode area tell us about current density in the brain during tDCS? Clin Neurophysiol 120, 1183–1187. https://doi.org/10.1016/j.clinph.2009.03.023
Miranda, P.C., Lomarev, M., Hallett, M., 2006. Modeling the current distribution during transcranial direct current stimulation. Clinical Neurophysiology 117, 1623–1629. https://doi.org/10.1016/j.clinph.2006.04.009
Miranda, P.C., Salvador, R., Wenger, C., Fernandes, S.R., 2016. Computational models of non-invasive brain and spinal cord stimulation, in: 2016 38th Annual International Conference of the IEEE Engineering in Medicine and Biology Society (EMBC). Presented at the 2016 38th Annual International Conference of the IEEE Engineering in Medicine and Biology Society (EMBC), pp. 6457–6460. https://doi.org/10.1109/EMBC.2016.7592207
Moffa, A.H., Brunoni, A.R., Fregni, F., Palm, U., Padberg, F., Blumberger, D.M., Daskalakis, Z.J., Bennabi, D., Haffen, E., Alonzo, A., Loo, C.K., 2017. Safety and acceptability of transcranial direct current stimulation for the acute treatment of major depressive episodes: Analysis of individual patient data. J Affect Disord 221, 1–5. https://doi.org/10.1016/j.jad.2017.06.021
Mogensen, M., Thrane, L., Joergensen, T.M., Andersen, P.E., Jemec, G.B.E., 2009. Optical coherence tomography for imaging of skin and skin diseases. Semin Cutan Med Surg 28, 196–202. https://doi.org/10.1016/j.sder.2009.07.002

Morrison, S.F., Nakamura, K., 2011. Central neural pathways for thermoregulation. Front Biosci (Landmark Ed) 16, 74–104.
Mosayebi Samani, M., Agboada, D., Jamil, A., Kuo, M.-F., Nitsche, M.A., 2019. Titrating the neuroplastic effects of cathodal transcranial direct current stimulation (tDCS) over the primary motor cortex. Cortex 119, 350–361. https://doi.org/10.1016/j.cortex.2019.04.016
Mourdoukoutas, A.P., Truong, D.Q., Adair, D.K., Simon, B.J., Bikson, M., 2018. High-Resolution Multi-Scale Computational Model for Non-Invasive Cervical Vagus Nerve Stimulation. Neuromodulation 21, 261–268. https://doi.org/10.1111/ner.12706
Mrozek, S., Vardon, F., Geeraerts, T., 2012. Brain Temperature: Physiology and Pathophysiology after Brain Injury [WWW Document]. Anesthesiology Research and Practice. https://doi.org/10.1155/2012/989487
Mueller, E.E., Loeffel, R., Mead, S., 1953. Skin Impedance in Relation to Pain Threshold Testing by Electrical Means. Journal of Applied Physiology 5, 746–752. https://doi.org/10.1152/jappl.1953.5.12.746
Nitsche, M.A., Bikson, M., 2017. Extending the parameter range for tDCS: Safety and tolerability of 4 mA stimulation. Brain Stimul 10, 541–542. https://doi.org/10.1016/j.brs.2017.03.002
Nitsche, M.A., Cohen, L.G., Wassermann, E.M., Priori, A., Lang, N., Antal, A., Paulus, W., Hummel, F., Boggio, P.S., Fregni, F., Pascual-Leone, A., 2008. Transcranial direct current stimulation: State of the art 2008. Brain Stimul 1, 206–223. https://doi.org/10.1016/j.brs.2008.06.004
Nitsche, M.A., Liebetanz, D., Lang, N., Antal, A., Tergau, F., Paulus, W., 2003. Safety criteria for transcranial direct current stimulation (tDCS) in humans. Clin Neurophysiol 114, 2220–2222; author reply 2222-2223. https://doi.org/10.1016/s1388-2457(03)00235-9
Nitsche, M.A., Paulus, W., 2000. Excitability changes induced in the human motor cortex by weak transcranial direct current stimulation. J. Physiol. (Lond.) 527 Pt 3, 633–639.
Nitsche, M.A., Seeber, A., Frommann, K., Klein, C.C., Rochford, C., Nitsche, M.S., Fricke, K., Liebetanz, D., Lang, N., Antal, A., Paulus, W., Tergau, F., 2005. Modulating parameters of excitability during and after transcranial direct current stimulation of the human motor cortex. J. Physiol. (Lond.) 568, 291–303. https://doi.org/10.1113/jphysiol.2005.092429
Nowak, L.G., Bullier, J., 1996. Spread of stimulating current in the cortical grey matter of rat visual cortex studied on a new in vitro slice preparation. J. Neurosci. Methods 67, 237–248.
O'Connell, N.E., Cossar, J., Marston, L., Wand, B.M., Bunce, D., Moseley, G.L., De Souza, L.H., 2012. Rethinking Clinical Trials of Transcranial Direct Current Stimulation: Participant and Assessor Blinding Is Inadequate at Intensities of 2mA. PLoS ONE 7, e47514. https://doi.org/10.1371/journal.pone.0047514
Olsen, J., Themstrup, L., Jemec, G.B.E., 2015. Optical coherence tomography in dermatology. G Ital Dermatol Venereol 150, 603–615.
Opitz, A., Paulus, W., Will, S., Antunes, A., Thielscher, A., 2015. Determinants of the electric field during transcranial direct current stimulation. Neuroimage 109, 140–150. https://doi.org/10.1016/j.neuroimage.2015.01.033
Orlov, N.D., O'Daly, O., Tracy, D.K., Daniju, Y., Hodsoll, J., Valdearenas, L., Rothwell, J., Shergill, S.S., 2017. Stimulating thought: a functional MRI study of transcranial direct current stimulation in schizophrenia. Brain 140, 2490–2497. https://doi.org/10.1093/brain/awx170

Oza, C.S., Brocker, D.T., Behrend, C.E., Grill, W.M., 2018. Patterned low-frequency deep brain stimulation induces motor deficits and modulates cortex-basal ganglia neural activity in healthy rats. J. Neurophysiol. 120, 2410–2422. https://doi.org/10.1152/jn.00929.2017

Palm, U., Keeser, D., Schiller, C., Fintescu, Z., Reisinger, E., Padberg, F., Nitsche, M., 2008. Skin lesions after treatment with transcranial direct current stimulation (tDCS). Brain Stimulation 1, 386–387. https://doi.org/10.1016/j.brs.2008.04.003

Palm, U., Reisinger, E., Keeser, D., Kuo, M.-F., Pogarell, O., Leicht, G., Mulert, C., Nitsche, M.A., Padberg, F., 2013. Evaluation of sham transcranial direct current stimulation for randomized, placebo-controlled clinical trials. Brain Stimul 6, 690–695. https://doi.org/10.1016/j.brs.2013.01.005

Paneri, B., Adair, D., Thomas, C., Khadka, N., Patel, V., Tyler, W.J., Parra, L., Bikson, M., 2016. Tolerability of Repeated Application of Transcranial Electrical Stimulation with Limited Outputs to Healthy Subjects. Brain Stimul 9, 740–754. https://doi.org/10.1016/j.brs.2016.05.008

Panescu, D., Cohen, K.P., Webster, J.G., Stratbucker, R.A., 1993. The mosaic electrical characteristics of the skin. IEEE Trans Biomed Eng 40, 434–439. https://doi.org/10.1109/10.243418

Panescu, D., Webster, J.G., Stratbucker, R.A., 1994. A nonlinear finite element model of the electrode-electrolyte-skin system. IEEE Transactions on Biomedical Engineering 41, 681–687. https://doi.org/10.1109/10.301735

Parazzini, M., Fiocchi, S., Liorni, I., Rossi, E., Cogiamanian, F., Vergari, M., Priori, A., Ravazzani, P., 2014. Modeling the current density generated by transcutaneous spinal direct current stimulation (tsDCS). Clinical Neurophysiology 125, 2260–2270. https://doi.org/10.1016/j.clinph.2014.02.027

Patel, Y.A., Saxena, T., Bellamkonda, R.V., Butera, R.J., 2017. Kilohertz frequency nerve block enhances anti-inflammatory effects of vagus nerve stimulation. Scientific Reports 7, srep39810. https://doi.org/10.1038/srep39810

Pavšelj, N., Préat, V., Miklavčič, D., 2007. A Numerical Model of Skin In Vivo Experiments. Ann Biomed Eng 35, 2138–2144. https://doi.org/10.1007/s10439-007-9378-7

Perera, T., George, M.S., Grammer, G., Janicak, P.G., Pascual-Leone, A., Wirecki, T.S., 2016. The Clinical TMS Society Consensus Review and Treatment Recommendations for TMS Therapy for Major Depressive Disorder. Brain Stimulation 9, 336–346. https://doi.org/10.1016/j.brs.2016.03.010

Peterchev, A.V., Wagner, T.A., Miranda, P.C., Nitsche, M.A., Paulus, W., Lisanby, S.H., Pascual-Leone, A., Bikson, M., 2012. Fundamentals of transcranial electric and magnetic stimulation dose: Definition, selection, and reporting practices. Brain Stimulation 5, 435–453. https://doi.org/10.1016/j.brs.2011.10.001

Pettersen, F.-J., Høgetveit, J.O., 2011. From 3D tissue data to impedance using Simpleware ScanFE+IP and COMSOL Multiphysics – a tutorial. Journal of Electrical Bioimpedance 2, 13–32. https://doi.org/10.5617/jeb.173

Philpott, J.M., Zemlin, C.W., Damiano, R., 2017. Chapter 4 - The Art and Science of Making Effective Maze Ablation Lines, in: Philpott, J.M., Zemlin, C.W., Damiano, R. (Eds.), Surgical Treatment of Atrial Fibrillation. Academic Press, pp. 63–96. https://doi.org/10.1016/B978-0-12-804671-5.00004-4

Piérard-Franchimont, C., Hermanns-Lê, T., Piérard, and G.E., 2016. Skin Capacitance Mapping of Eccrine Sweat Gland Activity during Pregnancy. The Open Access Journal of Science and Technology 4. https://doi.org/10.11131/2016/101187

Pierard-Franchimont, C., Pierard, G., 2015. Sweat Gland Awakening on Physical Training: A Skin Capacitance Mapping Observation. Clinical Research in Dermatology : Open Access 2.

Pollo, C., Kaelin-Lang, A., Oertel, M.F., Stieglitz, L., Taub, E., Fuhr, P., Lozano, A.M., Raabe, A., Schüpbach, M., 2014. Directional deep brain stimulation: an intraoperative double-blind pilot study. Brain 137, 2015–2026. https://doi.org/10.1093/brain/awu102

Poreisz, C., Boros, K., Antal, A., Paulus, W., 2007. Safety aspects of transcranial direct current stimulation concerning healthy subjects and patients. Brain Res. Bull. 72, 208–214. https://doi.org/10.1016/j.brainresbull.2007.01.004

Prager, J.P., 2010. What does the mechanism of spinal cord stimulation tell us about complex regional pain syndrome? Pain Med 11, 1278–1283. https://doi.org/10.1111/j.1526-4637.2010.00915.x

Priori, A., Ciocca, M., Parazzini, M., Vergari, M., Ferrucci, R., 2014. Transcranial cerebellar direct current stimulation and transcutaneous spinal cord direct current stimulation as innovative tools for neuroscientists. J Physiol 592, 3345–3369. https://doi.org/10.1113/jphysiol.2013.270280

Pulgar, V.M., 2015. Direct electric stimulation to increase cerebrovascular function. Front Syst Neurosci 9. https://doi.org/10.3389/fnsys.2015.00054

Radman, T., Datta, A., Ramos, R.L., Brumberg, J.C., Bikson, M., 2009a. One-dimensional representation of a neuron in a uniform electric field. Conf Proc IEEE Eng Med Biol Soc 2009, 6481–6484. https://doi.org/10.1109/IEMBS.2009.5333586

Radman, T., Ramos, R.L., Brumberg, J.C., Bikson, M., 2009b. Role of cortical cell type and morphology in subthreshold and suprathreshold uniform electric field stimulation in vitro. Brain Stimul 2, 215–228, 228.e1–3. https://doi.org/10.1016/j.brs.2009.03.007

Rahman, A., Reato, D., Arlotti, M., Gasca, F., Datta, A., Parra, L.C., Bikson, M., 2013. Cellular effects of acute direct current stimulation: somatic and synaptic terminal effects. J. Physiol. (Lond.) 591, 2563–2578. https://doi.org/10.1113/jphysiol.2012.247171

Raimundo, R.J.S., Uribe, C.E., Brasil-Neto, J.P., 2012. Lack of clinically detectable acute changes on autonomic or thermoregulatory functions in healthy subjects after transcranial direct current stimulation (tDCS). Brain Stimul 5, 196–200. https://doi.org/10.1016/j.brs.2011.03.009

Ramasubbu, R., Lang, S., Kiss, Z.H.T., 2018. Dosing of Electrical Parameters in Deep Brain Stimulation (DBS) for Intractable Depression: A Review of Clinical Studies. Front Psychiatry 9, 302. https://doi.org/10.3389/fpsyt.2018.00302

Ramirez-Zamora, A., Giordano, J., Boyden, E.S., Gradinaru, V., Gunduz, A., Starr, P.A., Sheth, S.A., McIntyre, C.C., Fox, M.D., Vitek, J., Vedam-Mai, V., Akbar, U., Almeida, L., Bronte-Stewart, H.M., Mayberg, H.S., Pouratian, N., Gittis, A.H., Singer, A.C., Creed, M.C., Lazaro-Munoz, G., Richardson, M., Rossi, M.A., Cendejas-Zaragoza, L., D'Haese, P.-F., Chiong, W., Gilron, R., Chizeck, H., Ko, A., Baker, K.B., Wagenaar, J., Harel, N., Deeb, W., Foote, K.D., Okun, M.S., 2019. Proceedings of the Sixth Deep Brain Stimulation Think Tank Modulation of Brain Networks and Application of Advanced Neuroimaging, Neurophysiology, and Optogenetics. Front Neurosci 13, 936. https://doi.org/10.3389/fnins.2019.00936

Rampersad, S., Roig-Solvas, B., Yarossi, M., Kulkarni, P.P., Santarnecchi, E., Dorval, A.D., Brooks, D.H., 2019. Prospects for transcranial temporal interference stimulation in humans: A computational study. Neuroimage 116124. https://doi.org/10.1016/j.neuroimage.2019.116124

Ranck, J.B., 1975. Which elements are excited in electrical stimulation of mammalian central nervous system: a review. Brain Res. 98, 417–440.

Rattay, F., 1999. The basic mechanism for the electrical stimulation of the nervous system. Neuroscience 89, 335–346.

Rattay, F., 1986. Analysis of models for external stimulation of axons. IEEE Trans Biomed Eng 33, 974–977. https://doi.org/10.1109/TBME.1986.325670

Rattay, F, Minassian, K., Dimitrijevic, M., 2000. Epidural electrical stimulation of posterior structures of the human lumbosacral cord: 2. quantitative analysis by computer modeling. Spinal Cord 38, 473–489. https://doi.org/10.1038/sj.sc.3101039

Rattay, F., Minassian, K., Dimitrijevic, M.R., 2000. Epidural electrical stimulation of posterior structures of the human lumbosacral cord: 2. quantitative analysis by computer modeling. Spinal Cord 38, 473–489.

Reato, D., Rahman, A., Bikson, M., Parra, L.C., 2010. Low-intensity electrical stimulation affects network dynamics by modulating population rate and spike timing. J. Neurosci. 30, 15067–15079. https://doi.org/10.1523/JNEUROSCI.2059-10.2010

Reckow, J., Rahman-Filipiak, A., Garcia, S., Schlaefflin, S., Calhoun, O., DaSilva, A.F., Bikson, M., Hampstead, B.M., 2018. Tolerability and blinding of 4x1 high-definition transcranial direct current stimulation (HD-tDCS) at two and three milliamps. Brain Stimul 11, 991–997. https://doi.org/10.1016/j.brs.2018.04.022

Reilly, J.P., Freeman, V.T., Larkin, W.D., 1985. Sensory effects of transient electrical stimulation--evaluation with a neuroelectric model. IEEE Trans Biomed Eng 32, 1001–1011. https://doi.org/10.1109/TBME.1985.325509

Richardot, A., McAdams, E.T., 2002. Harmonic analysis of low-frequency bioelectrode behavior. IEEE Transactions on Medical Imaging 21, 604–612. https://doi.org/10.1109/TMI.2002.800576

Riederer, F., Penning, S., Schoenen, J., 2015. Transcutaneous Supraorbital Nerve Stimulation (t-SNS) with the Cefaly® Device for Migraine Prevention: A Review of the Available Data. Pain Ther 4, 135–147. https://doi.org/10.1007/s40122-015-0039-5

Rubinstein, J.T., 1993. Axon termination conditions for electrical stimulation. IEEE Trans Biomed Eng 40, 654–663. https://doi.org/10.1109/10.237695

Rubinstein, J.T., Spelman, F.A., 1988. Analytical theory for extracellular electrical stimulation of nerve with focal electrodes. I. Passive unmyelinated axon. Biophys. J. 54, 975–981. https://doi.org/10.1016/S0006-3495(88)83035-2

Russo, M., Van Buyten, J.-P., 2015. 10-kHz High-Frequency SCS Therapy: A Clinical Summary. Pain Med 16, 934–942. https://doi.org/10.1111/pme.12617

Sadleir, R.J., Vannorsdall, T.D., Schretlen, D.J., Gordon, B., 2010. Transcranial direct current stimulation (tDCS) in a realistic head model. Neuroimage 51, 1310–1318. https://doi.org/10.1016/j.neuroimage.2010.03.052

Salvador, R., Silva, S., Basser, P.J., Miranda, P.C., 2011. Determining which mechanisms lead to activation in the motor cortex: a modeling study of transcranial magnetic stimulation using realistic stimulus waveforms and sulcal geometry. Clin Neurophysiol 122, 748–758. https://doi.org/10.1016/j.clinph.2010.09.022

Sampaio-Junior, B., Tortella, G., Borrione, L., Moffa, A.H., Machado-Vieira, R., Cretaz, E., Fernandes da Silva, A., Fraguas, R., Aparício, L.V., Klein, I., Lafer, B., Goerigk, S., Benseñor, I.M., Lotufo, P.A., Gattaz, W.F., Brunoni, A.R., 2018. Efficacy and Safety of Transcranial Direct Current Stimulation as an Add-on Treatment for Bipolar Depression: A Randomized Clinical Trial. JAMA Psychiatry 75, 158–166. https://doi.org/10.1001/jamapsychiatry.2017.4040

Sato, K.L., Johanek, L.M., Sanada, L.S., Sluka, K.A., 2014. Spinal cord stimulation reduces mechanical hyperalgesia and glial cell activation in animals with neuropathic pain. Anesth. Analg. 118, 464–472. https://doi.org/10.1213/ANE.0000000000000047

Saturnino, G.B., Antunes, A., Thielscher, A., 2015. On the importance of electrode parameters for shaping electric field patterns generated by tDCS. NeuroImage 120, 25–35. https://doi.org/10.1016/j.neuroimage.2015.06.067

Schechtmann, G., Song, Z., Ultenius, C., Meyerson, B.A., Linderoth, B., 2008. Cholinergic mechanisms involved in the pain relieving effect of spinal cord stimulation in a model of neuropathy. PAIN 139, 136–145. https://doi.org/10.1016/j.pain.2008.03.023

Schwan, H.P., 1966. Alternating current electrode polarization. Biophysik 3, 181–201. https://doi.org/10.1007/BF01191612

Scudds, R.J., Helewa, A., Scudds, R.A., 1995. The effects of transcutaneous electrical nerve stimulation on skin temperature in asymptomatic subjects. Phys Ther 75, 621–628.

Sdrulla, A.D., Guan, Y., Raja, S.N., 2018. Spinal Cord Stimulation: Clinical Efficacy and Potential Mechanisms. Pain Pract 18, 1048–1067. https://doi.org/10.1111/papr.12692

Sha, N., Kenney, L.P.J., Heller, B.W., Barker, A.T., Howard, D., Moatamedi, M., 2008. A Finite Element Model to Identify Electrode Influence on Current Distribution in the Skin. Artificial Organs 32, 639–643. https://doi.org/10.1111/j.1525-1594.2008.00615.x

Shechter, R., Yang, F., Xu, Q., Cheong, Y.-K., He, S.-Q., Sdrulla, A., Carteret, A.F., Wacnik, P.W., Dong, X., Meyer, R.A., Raja, S.N., Guan, Y., 2013. Conventional and Kilohertz-frequency Spinal Cord Stimulation Produces Intensity- and Frequency-dependent Inhibition of Mechanical Hypersensitivity in a Rat Model of Neuropathic Pain. Anesthes 119, 422–432. https://doi.org/10.1097/ALN.0b013e31829bd9e2

Shiozawa, P., da Silva, M.E., Raza, R., Uchida, R.R., Cordeiro, Q., Fregni, F., Brunoni, A.R., 2013. Safety of repeated transcranial direct current stimulation in impaired skin: a case report. J ECT 29, 147–148. https://doi.org/10.1097/YCT.0b013e318279c1a1

Sin, W.K., Coburn, B., 1983. Electrical stimulation of the spinal cord: a further analysis relating to anatomical factors and tissue properties. Med. Biol. Eng. Comput. 21, 264–269. https://doi.org/10.1007/BF02478492

Smith, DuncanR., 1993. Agarose Gel Electrophoresis, in: Murphy, D., Carter, DavidA. (Eds.), Transgenesis Techniques, Methods in Molecular Biology™. Humana Press, pp. 433–438. https://doi.org/10.1385/0-89603-245-0:433

Song, Z., Ansah, O.B., Meyerson, B.A., Pertovaara, A., Linderoth, B., 2013a. The rostroventromedial medulla is engaged in the effects of spinal cord stimulation in a rodent model of neuropathic pain. Neuroscience 247, 134–144. https://doi.org/10.1016/j.neuroscience.2013.05.027

Song, Z., Ansah, O.B., Meyerson, B.A., Pertovaara, A., Linderoth, B., 2013b. Exploration of supraspinal mechanisms in effects of spinal cord stimulation: role of the locus coeruleus. Neuroscience 253, 426–434. https://doi.org/10.1016/j.neuroscience.2013.09.006

Song, Z., Viisanen, H., Meyerson, B.A., Pertovaara, A., Linderoth, B., 2014. Efficacy of Kilohertz-Frequency and Conventional Spinal Cord Stimulation in Rat Models of Different Pain Conditions. Neuromodulation: Technology at the Neural Interface 17, 226–235. https://doi.org/10.1111/ner.12161

Stiller, C.O., Cui, J.G., O'Connor, W.T., Brodin, E., Meyerson, B.A., Linderoth, B., 1996. Release of gamma-aminobutyric acid in the dorsal horn and suppression of tactile allodynia by spinal cord stimulation in mononeuropathic rats. Neurosurgery 39, 367–374; discussion 374-375. https://doi.org/10.1097/00006123-199608000-00026

Stoney, S.D., Thompson, W.D., Asanuma, H., 1968. Excitation of pyramidal tract cells by intracortical microstimulation: effective extent of stimulating current. J. Neurophysiol. 31, 659–669. https://doi.org/10.1152/jn.1968.31.5.659

Struijk, J.J., Holsheimer, J., Barolat, G., He, J., Boom, H.B.K., 1993a. Paresthesia thresholds in spinal cord stimulation: a comparison of theoretical results with clinical data. IEEE Transactions on Rehabilitation Engineering 1, 101–108. https://doi.org/10.1109/86.242424

Struijk, J.J., Holsheimer, J., Boom, H.B., 1993b. Excitation of dorsal root fibers in spinal cord stimulation: a theoretical study. IEEE Trans Biomed Eng 40, 632–639. https://doi.org/10.1109/10.237693

Struijk, J.J., Holsheimer, J., Boom, H.B.K., 1993c. Excitation of dorsal root fibers in spinal cord stimulation: a theoretical study. IEEE Transactions on Biomedical Engineering 40, 632–639. https://doi.org/10.1109/10.237693

Struijk, J.J., Holsheimer, J., van der Heide, G.G., Boom, H.B., 1992. Recruitment of dorsal column fibers in spinal cord stimulation: influence of collateral branching. IEEE Trans Biomed Eng 39, 903–912. https://doi.org/10.1109/10.256423

Struijk, J.J., Holsheimer, J., van Veen, B.K., Boom, H.B., 1991. Epidural spinal cord stimulation: calculation of field potentials with special reference to dorsal column nerve fibers. IEEE Trans Biomed Eng 38, 104–110. https://doi.org/10.1109/10.68217

Suchi, T., 1955. Experiments on electrical resistance of the human epidermis. Jpn. J. Physiol. 5, 75–80.

Swiontek, T.J., Sances, A., Larson, S.J., Ackmann, J.J., Cusick, J.F., Meyer, G.A., Millar, E.A., 1976. Spinal cord implant studies. IEEE Trans Biomed Eng 23, 307–312. https://doi.org/10.1109/tbme.1976.324590

Systems, C. on C.C., Devices (1973 : Monterey, C., Geldard, F.A., 1974. Conference on cutaneous communication systems and devices. Sponsored jointly by the Advanced Research Projects Agency of the U.S. Dept. of Defense and the office of Naval Research and held at the Royal Inn, Monterey California, on April 17-18, 1973. [s.l.] : Psychonomic Society.

Tanaka, S., Komori, N., Barron, K.W., Chandler, M.J., Linderoth, B., Foreman, R.D., 2004. Mechanisms of sustained cutaneous vasodilation induced by spinal cord stimulation. Auton Neurosci 114, 55–60. https://doi.org/10.1016/j.autneu.2004.07.004

Tasaki, I., Byrne, P.M., 1987. Heat production associated with synaptic transmission in the bullfrog spinal cord. Brain Res. 407, 386–389.

Thielscher, A., Opitz, A., Windhoff, M., 2011. Impact of the gyral geometry on the electric field induced by transcranial magnetic stimulation. NeuroImage 54, 234–243. https://doi.org/10.1016/j.neuroimage.2010.07.061

Thomson, S.J., Tavakkolizadeh, M., Love-Jones, S., Patel, N.K., Gu, J.W., Bains, A., Doan, Q., Moffitt, M., 2018. Effects of Rate on Analgesia in Kilohertz Frequency Spinal Cord Stimulation: Results of the PROCO Randomized Controlled Trial. Neuromodulation 21, 67–76. https://doi.org/10.1111/ner.12746

Tiede, J., Brown, L., Gekht, G., Vallejo, R., Yearwood, T., Morgan, D., 2013. Novel spinal cord stimulation parameters in patients with predominant back pain. Neuromodulation 16, 370–375. https://doi.org/10.1111/ner.12032

Tonezzer, T., Caffaro, L.A.M., Menon, K.R.S., Brandini da Silva, F.C., Moran de Brito, C.M., Sarri, A.J., Casarotto, R.A., 2017. Effects of transcutaneous electrical nerve stimulation on chemotherapy-induced peripheral neuropathy symptoms (CIPN): a preliminary case-control study. J Phys Ther Sci 29, 685–692. https://doi.org/10.1589/jpts.29.685

Tortella, G., 2015. Transcranial direct current stimulation in psychiatric disorders. World Journal of Psychiatry 5, 88. https://doi.org/10.5498/wjp.v5.i1.88

Torvi, D.A., Dale, J.D., 1994. A finite element model of skin subjected to a flash fire. J Biomech Eng 116, 250–255.

Tranchina, D., Nicholson, C., 1986. A model for the polarization of neurons by extrinsically applied electric fields. Biophys. J. 50, 1139–1156. https://doi.org/10.1016/S0006-3495(86)83558-5

Trapp, N.T., Xiong, W., Gott, B.M., Espejo, G.D., Bikson, M., Conway, C.R., 2019. Proceedings #51: 4 mA Adaptive Transcranial Direct Current Stimulation for Treatment-Resistant Depression: Early Demonstration of Feasibility with a 20-Session Course. Brain Stimulation: Basic, Translational, and Clinical Research in Neuromodulation 12, e124–e125. https://doi.org/10.1016/j.brs.2018.12.220

Tregear, R.T., 1966. Physical Functions of Skin. Academic Press.

Truong, D.Q., Bikson, M., 2018. Physics of Transcranial Direct Current Stimulation Devices and Their History. J ECT 34, 137–143. https://doi.org/10.1097/YCT.0000000000000531

Truong, D.Q., Magerowski, G., Blackburn, G.L., Bikson, M., Alonso-Alonso, M., 2013. Computational modeling of transcranial direct current stimulation (tDCS) in obesity: Impact of head fat and dose guidelines. Neuroimage Clin 2, 759–766. https://doi.org/10.1016/j.nicl.2013.05.011

Tungjitkusolmun, S., Woo, E.J., Cao, H., Tsai, J.Z., Vorperian, V.R., Webster, J.G., 2000. Finite element analyses of uniform current density electrodes for radio-frequency cardiac ablation. IEEE Trans Biomed Eng 47, 32–40. https://doi.org/10.1109/10.817617

Turi, Z., Ambrus, G.G., Ho, K.-A., Sengupta, T., Paulus, W., Antal, A., 2014. When size matters: large electrodes induce greater stimulation-related cutaneous discomfort than smaller electrodes at equivalent current density. Brain Stimul 7, 460–467. https://doi.org/10.1016/j.brs.2014.01.059

Turi, Z., Csifcsák, G., Boayue, N.M., Aslaksen, P., Antal, A., Paulus, W., Groot, J., Hawkins, G.E., Forstmann, B., Opitz, A., Thielscher, A., Mittner, M., 2019. Blinding is compromised for transcranial direct current stimulation at 1 mA for 20 min in young healthy adults. Eur. J. Neurosci. https://doi.org/10.1111/ejn.14403

Valle-Giler, E.P., Sulaiman, W.A.R., 2014. Midline minimally invasive placement of spinal cord stimulators: a technical note. Ochsner J 14, 51–56.

Veizi, E., Hayek, S.M., North, J., Brent Chafin, T., Yearwood, T.L., Raso, L., Frey, R., Cairns, K., Berg, A., Brendel, J., Haider, N., McCarty, M., Vucetic, H., Sherman, A., Chen, L., Mekel-Bobrov, N., 2017. Spinal Cord Stimulation (SCS) with Anatomically Guided (3D)

Neural Targeting Shows Superior Chronic Axial Low Back Pain Relief Compared to Traditional SCS-LUMINA Study. Pain Med 18, 1534–1548. https://doi.org/10.1093/pm/pnw286

Vöröslakos, M., Takeuchi, Y., Brinyiczki, K., Zombori, T., Oliva, A., Fernández-Ruiz, A., Kozák, G., Kincses, Z.T., Iványi, B., Buzsáki, G., Berényi, A., 2018. Direct effects of transcranial electric stimulation on brain circuits in rats and humans. Nat Commun 9, 483. https://doi.org/10.1038/s41467-018-02928-3

Wagner, F.B., Mignardot, J.-B., Le Goff-Mignardot, C.G., Demesmaeker, R., Komi, S., Capogrosso, M., Rowald, A., Seáñez, I., Caban, M., Pirondini, E., Vat, M., McCracken, L.A., Heimgartner, R., Fodor, I., Watrin, A., Seguin, P., Paoles, E., Van Den Keybus, K., Eberle, G., Schurch, B., Pralong, E., Becce, F., Prior, J., Buse, N., Buschman, R., Neufeld, E., Kuster, N., Carda, S., von Zitzewitz, J., Delattre, V., Denison, T., Lambert, H., Minassian, K., Bloch, J., Courtine, G., 2018. Targeted neurotechnology restores walking in humans with spinal cord injury. Nature 563, 65–71. https://doi.org/10.1038/s41586-018-0649-2

Wagner, T., Fregni, F., Fecteau, S., Grodzinsky, A., Zahn, M., Pascual-Leone, A., 2007. Transcranial direct current stimulation: A computer-based human model study. NeuroImage 35, 1113–1124. https://doi.org/10.1016/j.neuroimage.2007.01.027

Wake, K., Sasaki, K., Watanabe, S., 2016. Conductivities of epidermis, dermis, and subcutaneous tissue at intermediate frequencies. Phys. Med. Biol. 61, 4376–4389. https://doi.org/10.1088/0031-9155/61/12/4376

Walckiers, G., Fuchs, B., Thiran, J.-P., Mosig, J.R., Pollo, C., 2010. Influence of the implanted pulse generator as reference electrode in finite element model of monopolar deep brain stimulation. J. Neurosci. Methods 186, 90–96. https://doi.org/10.1016/j.jneumeth.2009.10.012

Wang, H., Wang, B., Normoyle, K.P., Jackson, K., Spitler, K., Sharrock, M.F., Miller, C.M., Best, C., Llano, D., Du, R., 2014. Brain temperature and its fundamental properties: a review for clinical neuroscientists. Front Neurosci 8. https://doi.org/10.3389/fnins.2014.00307

Wang, J., Wei, Y., Wen, J., Li, X., 2015. Skin burn after single session of transcranial direct current stimulation (tDCS). Brain Stimul 8, 165–166. https://doi.org/10.1016/j.brs.2014.10.015

Wang, S., Diller, K.R., Aggarwal, S.J., 2003. Kinetics study of endogenous heat shock protein 70 expression. J Biomech Eng 125, 794–797. https://doi.org/10.1115/1.1632522

Warman, E.N., Grill, W.M., Durand, D., 1992. Modeling the effects of electric fields on nerve fibers: determination of excitation thresholds. IEEE Trans Biomed Eng 39, 1244–1254.

Wass, C.T., Lanier, W.L., Hofer, R.E., Scheithauer, B.W., Andrews, A.G., 1995. Temperature Changes of greater or equal to 1 degree Celsius Alter Functional Neurologic Outcome and Histopathology in a Canine Model of Complete Cerebral Ischemia. Anesthes 83, 325-335.

Wei, X.F., Grill, W.M., 2009. Impedance characteristics of deep brain stimulation electrodes in vitro and in vivo. J Neural Eng 6, 046008. https://doi.org/10.1088/1741-2560/6/4/046008

Weisstein, E.W., n.d. Least Squares Fitting--Power Law [WWW Document]. URL http://mathworld.wolfram.com/LeastSquaresFittingPowerLaw.html (accessed 8.1.18).

Welzel, J., 2001. Optical coherence tomography in dermatology: a review. Skin Research and Technology 7, 1–9. https://doi.org/10.1034/j.1600-0846.2001.007001001.x

Werner, J., Buse, M., 1988. Temperature profiles with respect to inhomogeneity and geometry of the human body. Journal of Applied Physiology 65, 1110–1118. https://doi.org/10.1152/jappl.1988.65.3.1110
Wesselink, W.A., Holsheimer, J., Boom, H.B.K., 1999. A model of the electrical behaviour of myelinated sensory nerve fibres based on human data. Med. Biol. Eng. Comput. 37, 228–235. https://doi.org/10.1007/BF02513291
Wesselink, W.A., Holsheimer, J., Boom, H.B.K., 1998. Analysis of current density and related parameters in spinal cord stimulation. IEEE Transactions on Rehabilitation Engineering 6, 200–207. https://doi.org/10.1109/86.681186
Wilson, S.B., Spence, V.A., 1988a. A tissue heat transfer model for relating dynamic skin temperature changes to physiological parameters. Phys Med Biol 33, 895–912.
Wilson, S.B., Spence, V.A., 1988b. A tissue heat transfer model for relating dynamic skin temperature changes to physiological parameters. Phys Med Biol 33, 895–912.
Wongsarnpigoon, A., Grill, W.M., 2008. Computational modeling of epidural cortical stimulation. J Neural Eng 5, 443–454. https://doi.org/10.1088/1741-2560/5/4/009
Woods, A.J., Antal, A., Bikson, M., Boggio, P.S., Brunoni, A.R., Celnik, P., Cohen, L.G., Fregni, F., Herrmann, C.S., Kappenman, E.S., Knotkova, H., Liebetanz, D., Miniussi, C., Miranda, P.C., Paulus, W., Priori, A., Reato, D., Stagg, C., Wenderoth, N., Nitsche, M.A., 2016. A technical guide to tDCS, and related non-invasive brain stimulation tools. Clin Neurophysiol 127, 1031–1048. https://doi.org/10.1016/j.clinph.2015.11.012
Woods, A.J., Bryant, V., Sacchetti, D., Gervits, F., Hamilton, R., 2015. Effects of Electrode Drift in Transcranial Direct Current Stimulation. Brain Stimul 8, 515–519. https://doi.org/10.1016/j.brs.2014.12.007
Xu, Q., Kong, L., Zhou, H., He, J., 2017. Epidural Stimulation of Rat Spinal Cord at Lumbosacral Segment Using a Surface Electrode: A Computer Simulation Study. IEEE Trans Neural Syst Rehabil Eng 25, 1763–1772. https://doi.org/10.1109/TNSRE.2016.2625312
Xu, X., Tikuisis, P., Giesbrecht, G., 1999a. A mathematical model for human brain cooling during cold-water near-drowning. J. Appl. Physiol. 86, 265–272.
Xu, X., Tikuisis, P., Giesbrecht, G., 1999b. A mathematical model for human brain cooling during cold-water near-drowning. J. Appl. Physiol. 86, 265–272.
Yamamoto, T., Yamamoto, Y., 1981. Non-linear electrical properties of skin in the low frequency range. Med. Biol. Eng. Comput. 19, 302. https://doi.org/10.1007/BF02442549
Yamamoto, T., Yamamoto, Y., 1976. Electrical properties of the epidermal stratum corneum. Med. & biol. Engng. 14, 151–158. https://doi.org/10.1007/BF02478741
Yearwood, T., Hershey, B., Bradley, K., Lee, D., 2010. Pulse width programming in spinal cord stimulation: a clinical study. Pain physician 13, 321–335.
Yeomans, J., Prior, P., Bateman, F., 1986. Current-distance relations of axons mediating circling elicited by midbrain stimulation. Brain Research 372, 95–106. https://doi.org/10.1016/0006-8993(86)91462-9
Yousef, H., Sharma, S., 2018. Anatomy, Skin (Integument), Epidermis, in: StatPearls. StatPearls Publishing, Treasure Island (FL).
Yuan, B., Liu, D., Liu, X., 2014. Spinal cord stimulation exerts analgesia effects in chronic constriction injury rats via suppression of the TLR4/NF-κB pathway. Neurosci. Lett. 581, 63–68. https://doi.org/10.1016/j.neulet.2014.08.023

Zannou, A.L., Khadka, N., FallahRad, M., Truong, D.Q., Kopell, B.H., Bikson, M., 2019a. Tissue Temperature Increases by a 10 kHz Spinal Cord Stimulation System: Phantom and Bioheat Model. Neuromodulation. https://doi.org/10.1111/ner.12980

Zannou, A.L., Khadka, N., Truong, D.Q., Zhang, T., Esteller, R., Hershey, B., Bikson, M., 2019b. Temperature increases by kilohertz frequency spinal cord stimulation. Brain Stimul 12, 62–72. https://doi.org/10.1016/j.brs.2018.10.007

Zhang, T.C., Janik, J.J., Grill, W.M., 2014. Mechanisms and models of spinal cord stimulation for the treatment of neuropathic pain. Brain Res. 1569, 19–31. https://doi.org/10.1016/j.brainres.2014.04.039

Zheng, X., Alsop, D.C., Schlaug, G., 2011. Effects of transcranial direct current stimulation (tDCS) on human regional cerebral blood flow. Neuroimage 58, 26–33. https://doi.org/10.1016/j.neuroimage.2011.06.018

Author biography

Niranjan Khadka was born in Kathmandu, Nepal, in 1987. He received his BS and MPhil degree in biomedical engineering from the City College of New York, CUNY in 2014 and 2018, respectively. He worked as a researcher in the same institution for almost 10 years. During these years, Niranjan authored 34 articles (journal article and book chapters), 20 abstracts, and 3 patents. He received the PhD in biomedical engineering from the City College of New York in 2020, under the guidance of Dr. Marom Bikson. Niranjan received several scholarships and accolades, including the Wallace H. Coulter Award for Outstanding Graduate Researcher in 2017. His invention named "Design of wireless intraoperative pulse oximeter with reticulated head" was selected as "Top 10 medical device with commercial potential" in 2015. He earned honors in Electronics and Circuits coursed offered by MIT in 2012. Niranjan received travel grants in few brain stimulation conferences including North American Neuromodulation Society (NANS) and Brain stimulation conference for novel therapeutic stimulation approaches and open-source SCS model.

Publications:

1. **Khadka, N.**, Rahman, A., Sarantos, C., Truong, D.Q., Bikson, M., 2015a. Methods for Specific Electrode Resistance Measurement During Transcranial Direct Current Stimulation. Brain Stimulation 8, 150–159. https://doi.org/10.1016/j.brs.2014.10.004
2. **Khadka, N.**, Truong, D.Q., Bikson, M., 2015b. Principles of Within Electrode Current Steering. J. Med. Devices 9, 020947-020947–2. https://doi.org/10.1115/1.4030126
3. **Khadka, N.**, Borges, H., Zannou, A.L., Jang, J., Kim, B., Lee, K., Bikson, M., 2018a. Dry tDCS: Tolerability of a novel multilayer hydrogel composite non-adhesive electrode for transcranial direct current stimulation. Brain Stimul 11, 1044–1053. https://doi.org/10.1016/j.brs.2018.07.049
4. **Khadka, N.**, Borges, H., Paneri, B., Kaufman, T., Nassis, E., Zannou, A.L., Shin, Y., Choi, H., Kim, S., Lee, K., Bikson, M., 2019b. Adaptive current tDCS up to 4 mA. Brain Stimulation. https://doi.org/10.1016/j.brs.2019.07.027
5. Zannou, A.L.*, **Khadka, N.***, Truong, D.Q., Zhang, T., Esteller, R., Hershey, B., Bikson, M., 2019b. Temperature increases by kilohertz frequency spinal cord stimulation. Brain

Stimul 12, 62–72. https://doi.org/10.1016/j.brs.2018.10.007
6. **Khadka, N.**, Woods, A.J., Bikson, M., 2019e. Transcranial Direct Current Stimulation Electrodes, in: Knotkova, H., Nitsche, M.A., Bikson, M., Woods, A.J. (Eds.), Practical Guide to Transcranial Direct Current Stimulation: Principles, Procedures and Applications. Springer International Publishing, Cham, pp. 263–291. https://doi.org/10.1007/978-3-319-95948-1_10
7. **Khadka, N.**, Harmsen, I.E., Lozano, A.M., Bikson, M., 2019. Bio-Heat Model of Kilohertz-Frequency Deep Brain Stimulation Increases Brain Tissue Temperature. Neuromodulation: Technology at the Neural Interface. https://doi.org/10.1111/ner.13120
8. **Khadka, N**, Truong, D.Q., Williams, P., Martin, J.H., Bikson, M., 2019d. The Quasi-uniform assumption for Spinal Cord Stimulation translational research. Journal of Neuroscience Methods 328, 108446. https://doi.org/10.1016/j.jneumeth.2019.108446
9. **Khadka, N.**, Bikson, M., 2019. Response to the Letter to the Editor by Caraway et al. on "Tissue Temperature Increases by a 10 kHz Spinal Cord Stimulation System: Phantom and Bioheat Model." Neuromodulation: Technology at the Neural Interface 22, 988–988. https://doi.org/10.1111/ner.13079
10. **Khadka, N.**, Liu, X., Zander, H., Swami, J., Rogers, E., Lempka, S., Bikson, M., 2020. Realistic anatomically detailed open-source spinal cord stimulation (RADO-SCS) model. J. Neural Eng. https://doi.org/10.1088/1741-2552/ab8344
11. **Khadka, N.**, Borges, H., Kauffman, T., Pascal, A., Paneri, B., Nassis, E., Shin, Y., Choi, H., Kim, S., Lee, K., Bikson, M., 2019a. Abstract #109: Tolerability of an Adaptive-tDCS upto 4 mA using subject assessment and machine-learning to optimize dose. Brain Stimulation: Basic, Translational, and Clinical Research in Neuromodulation 12, e37–e38. https://doi.org/10.1016/j.brs.2018.12.116
12. **Khadka, N.**, Seibt, O., Patel, V., Thomas, C., Mokrejs, A., Guleyupoglu, B., Truong, D.Q., Bikson, M., 2017. Factors Influencing Current Flow Through the Skin during Transcranial Electrical Stimulation: Role of Waveform, Tissue Properties, and Macro-Pores. Brain Stimulation: Basic, Translational, and Clinical Research in Neuromodulation 10, e16. https://doi.org/10.1016/j.brs.2016.11.071
13. **Khadka, N.**, Zannou, A., Truong, D., Zhang, T., Esteller, R., Hersey, B., Bikson, M., 2019. Generation 2 kilohertz spinal cord stimulation (kHz-SCS) bioheat multi-physics model. Brain Stimulation: Basic, Translational, and Clinical Research in Neuromodulation 12, 566. https://doi.org/10.1016/j.brs.2018.12.876
14. **Khadka, N.**, Zannou, A.L., Zunara, F., Truong, D.Q., Dmochowski, J., Bikson, M., 2018b. Minimal Heating at the Skin Surface During Transcranial Direct Current Stimulation. Neuromodulation: Technology at the Neural Interface 21, 334–339. https://doi.org/10.1111/ner.12554
15. Alam, M., Truong, D.Q., **Khadka, N.**, Bikson, M., 2016. Spatial and polarity precision of concentric high-definition transcranial direct current stimulation (HD-tDCS). Phys. Med. Biol. 61, 4506. https://doi.org/10.1088/0031-9155/61/12/4506
16. Bikson, M., Datta, A., **Khadka, N.**, 2016a. Electrode Assemblies for Delivering Therapeutic Electrostimulation. US20160129237 A1.
17. Bikson, M., Parra, L.C., Datta, A., **Khadka, N.**, Macuff, S.A., 2016b. System and method for conducting multi-electrode electrical stimulation. US9339642 B1.
18. Bikson, M., Truong, D.Q., Mourdoukoutas, A.P., Aboseria, M., **Khadka, N.**, Adair, D., Rahman, A., 2015a. Modeling sequence and quasi-uniform assumption in computational

neurostimulation. Prog. Brain Res. 222, 1–23. https://doi.org/10.1016/bs.pbr.2015.08.005
19. Borges, H., **Khadka, N.**, Boateng, A., Paneri, B., Nassis, E., Shin, Y., Choi, H., Kim, S., Lee, K., Bikson, M., 2017. Tolerability of up to 4 mA tDCS using adaptive stimulation. Brain Stimulation 10, e31–e32. https://doi.org/10.1016/j.brs.2017.04.044
20. Chen, C.-F., Bikson, M., Chou, L.-W., Shan, C., **Khadka, N.**, Chen, W.-S., Fregni, F., 2017. Higher-order power harmonics of pulsed electrical stimulation modulates corticospinal contribution of peripheral nerve stimulation. Sci Rep 7, 43619. https://doi.org/10.1038/srep43619
21. Edemann-Callesen, H., Habelt, B., Wieske, F., Jackson, M., **Khadka, N.**, Mattei, D., Bernhardt, N., Heinz, A., Liebetanz, D., Bikson, M., Padberg, F., Hadar, R., Nitsche, M.A., Winter, C., 2018. Non-invasive modulation reduces repetitive behavior in a rat model through the sensorimotor cortico-striatal circuit. Translational Psychiatry 8, 11. https://doi.org/10.1038/s41398-017-0059-5
22. Esmaeilpour, Z., Milosevic, M., Azevedo, K., **Khadka, N.**, Navarro, J., Brunoni, A., Popovic, M.R., Bikson, M., Fonoff, E.T., 2017. Intracranial voltage recording during transcranial direct current stimulation (tDCS) in human subjects with validation of a standard model. Brain Stimulation 10, e72–e75. https://doi.org/10.1016/j.brs.2017.04.114
23. Ezquerro, F., Moffa, A.H., Bikson, M., **Khadka, N.**, Aparicio, L.V.M., de Sampaio-Junior, B., Fregni, F., Bensenor, I.M., Lotufo, P.A., Pereira, A.C., Brunoni, A.R., 2017. The Influence of Skin Redness on Blinding in Transcranial Direct Current Stimulation Studies: A Crossover Trial. Neuromodulation: Technology at the Neural Interface 20, 248–255. https://doi.org/10.1111/ner.12527
24. FallahRad, M., Zannou, A.L., **Khadka, N.**, Prescott, S.A., Ratté, S., Zhang, T., Esteller, R., Hershey, B., Bikson, M., 2019. Electrophysiology equipment for reliable study of kHz electrical stimulation. J. Physiol. (Lond.) 597, 2131–2137. https://doi.org/10.1113/JP277654
25. Leite, J., Gonçalves, Ó.F., Pereira, P., **Khadka, N.**, Bikson, M., Fregni, F., Carvalho, S., 2018. The differential effects of unihemispheric and bihemispheric tDCS over the inferior frontal gyrus on proactive control. Neurosci Res 130, 39–46. https://doi.org/10.1016/j.neures.2017.08.005
26. Paneri, B., Adair, D., Thomas, C., **Khadka, N.**, Patel, V., Tyler, W.J., Parra, L., Bikson, M., 2016. Tolerability of Repeated Application of Transcranial Electrical Stimulation with Limited Outputs to Healthy Subjects. Brain Stimul 9, 740–754. https://doi.org/10.1016/j.brs.2016.05.008
27. Paneri, B., **Khadka, N.**, Patel, V., Thomas, C., Tyler, W., Parra, L.C., Bikson, M., 2015. The tolerability of transcranial electrical stimulation used across extended periods in a naturalistic context by healthy individuals (No. e1574). PeerJ PrePrints. https://doi.org/10.7287/peerj.preprints.1097v2
28. Sarantos, C., Bekritsky, J., **Khadka, N.**, Bikson, M., Adusumilli, P., 2015. Design of Wireless Intra-Operative Pulse Oximeter With Reticulated Pressure-Sensitive Head1. J. Med. Devices 9, 030934-030934–2. https://doi.org/10.1115/1.4030600
29. Seibt, O., Truong, D., **Khadka, N.**, Huang, Y., Bikson, M., 2019. Computational Finite Element Method (FEM) forward modeling workflow for transcranial Direct Current Stimulation (tDCS) current flow on MRI-derived head: Simpleware and COMSOL Multiphysics tutorial. bioRxiv 704940. https://doi.org/10.1101/704940
30. Shin, D.W., Fan, J., Luu, E., Khalid, W., Xia, Y., **Khadka, N.**, Bikson, M., Fu, B.M., 2020.

In Vivo Modulation of the Blood-Brain Barrier Permeability by Transcranial Direct Current Stimulation (tDCS). Ann Biomed Eng 48, 1256–1270. https://doi.org/10.1007/s10439-020-02447-7

31. Shin, D.W., **Khadka, N.**, Fan, J., Bikson, M., Fu, B.M., 2016. Transcranial direct current stimulation transiently increases the blood-brain barrier solute permeability in vivo. pp. 97881X-97881X–10. https://doi.org/10.1117/12.2218197
32. Zannou, A.L., **Khadka, N.**, FallahRad, M., Truong, D.Q., Kopell, B.H., Bikson, M., 2019a. Tissue Temperature Increases by a 10 kHz Spinal Cord Stimulation System: Phantom and Bioheat Model. Neuromodulation. https://doi.org/10.1111/ner.12980
33. Zareen, N., Shinozaki, M., Ryan, D., Alexander, H., Amer, A., Truong, D.Q., **Khadka, N.**, Sarkar, A., Naeem, S., Bikson, M., Martin, J.H., 2017. Motor cortex and spinal cord neuromodulation promote corticospinal tract axonal outgrowth and motor recovery after cervical contusion spinal cord injury. Experimental Neurology 297, 179–189. https://doi.org/10.1016/j.expneurol.2017.08.004